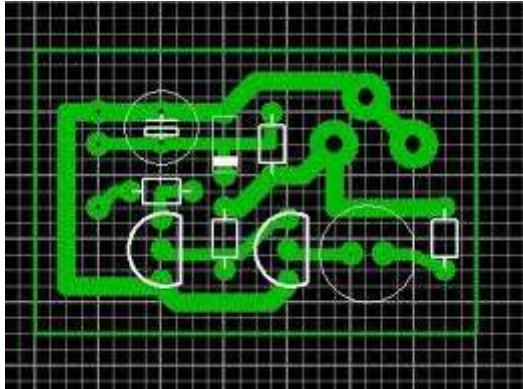


E.A. KERIMOV



**READING OF INFORMATION AND
PHOTOELECTRIC PHENOMENA IN ELECTRONIC
DEVICES BASED ON MULTILAYER METAL-SILICON
SILICIDE SEMICONDUCTORS**

Baku-2024

UOT 621.383.5

E.A. KERIMOV

**READING OF INFORMATION AND
PHOTOELECTRIC PHENOMENA IN ELECTRONIC
DEVICES BASED ON MULTILAYER METAL-SILICON
SILICIDE SEMICONDUCTORS**

E.A. Kerimov. Reading of information and photoelectric phenomena in electronic devices based on multilayer metal-silicon silicide semiconductors. Baku: 2024 – 345 p.

Reviewers:

- Professor of the Department “Automatics, telecommunications and energy” of Azerbaijan Engineering University

E.J. Qurbanov

- Head of the Department “Radioelectronic and aerospace systems”, Professor B.Q. Ibrahimov

Scientific editor:

Professor G.B. Ibragimov

The monograph describes the main types of photodetector designs for spectral regions from ultraviolet to near-infrared. The basic parameters of multielement photodetectors of different types based on different semiconductor materials are given. The features of construction of photodetectors, new directions of their development, including matrices with internal scanning, are described.

CONTROLLER

INTRODUCTION.....	8
--------------------------	----------

PART 1

CHAPTER I. PHOTODETECTORS OF IR RADIATION ON SCHOTTKY BARRIER DIODES

1.1. Ways to increase quantum efficiency of semiconductor photodetectors.....	10
1.2. Schottky matrix design and operation modes	26
1.3. Parameters of Schottky matrix receivers.....	48
1.4. Visible and infrared radiation.....	54
1.4.1. Thermal radiation.....	55
1.4.2. Radiation passing through the atmosphere.....	57
1.4.3. Optical input windows and image filters.....	58

CHAPTER II. BASIC TYPES OF PHOTODETECTORS

2.1. Radiation receivers. General characteristics.....	62
2.2. RRs with external photoelectric effect.....	64
2.3. Photoconductive RRs.....	64
2.4. Photovoltaic receivers or receivers with p-n junction..	67
2.5. Receivers with Schottky barrier.....	69
2.6. Depleted layer.....	71
2.7. Detectability and threshold flux.....	72
2.8. Signal and noise.....	77
2.9. Components of noise.....	82
2.10. Current and volt sensitivity. Dynamic range.....	83
2.11. Linear infrared image receivers.....	86
2.12. Scanning methods.....	87

CHAPTER III. MATRIX IMAGE RECEIVERS

3.1. Solid-state television photoelectric transducers (TSPEPs).....	90
3.2. Charge transfer devices.....	92

3.3. Problems of creating IR CCDs. IR receivers based on CCDs with Schottky barrier diodes.....	95
3.4. Low temperature techniques for working with cooled RR.....	96
3.5. Low temperature thermometry.....	100
3.6. Temperature control and stabilization in nitrogen level cryostats (region $T \geq 800K$).....	101
3.7. Optical systems for aerospace RRs.....	103
3.8. Mirror OS.....	105
3.9. Antireflective coatings.....	108

CHAPTER IV. CHARGE-COUPLED DEVICES

4.1. CCD devices.....	109
4.2. Spectral characteristics of CCDs.....	124
4.3. Dark current.....	129
4.4. Sensitivity inhomogeneity.....	131
4.5. Noise.....	131
4.6. Antiblooming, or resistance to local over lighting.....	133

CHAPTER V. BASIC TYPES OF PHOTODETECTORS

5.1. Limiting characteristics of receiver systems.....	138
5.2. Chaotic nature of photon distribution.....	139
5.3. False signals.....	140
5.4. Mode of limitation by fluctuations of signal and fluctuations of background radiation.....	141
5.5. Receivers of radiation with signal accumulation.....	143
5.6. Calculation of parameters of receiving systems. Scanning systems.....	146

CHAPTER VI. CONFIGURATION OF MATRIX FPU'S

6.1. Charge injection devices.....	155
6.2. Charge-coupled devices.....	164
6.3. Hybrid structures.....	166

6.4. Basic characteristics of photonic receivers.....	168
6.5. Impurity photoresistor.....	170
6.6. Reliability of semiconductor based radio electronic devices.....	173
6.7. Interaction of a quantum system with external radiation.....	180

PART 2

CHAPTER VII. PROSPECTS FOR THIN-FILM SOLAR CELLS.....	186
7.1. Ways to analyses the efficiency of solar energy conversion.....	191
7.2. Theoretical study of polycrystalline solar elements....	199
7.3. Formation technology and properties of microcrystalline silicon used in solar batteries.....	210

CHAPTER VIII. CARRIER TRANSPORT MECHANISMS AND DARK VOLT-AMPERE CHARACTERISTIC OF SOLAR CELLS.....	217
8.1. Roll-to-roll technology for manufacturing solar cell modules.....	222
8.2. Solar elements with p-i-n structure.....	227
8.3. Effect of temperature and radiation on solar cell parameters.....	233
8.4. Increasing the stability of basic parameters of solar cells based on disordered semiconductors.....	241

CHAPTER IX. PHOTOELECTRIC PHENOMENON IN AMORPHOUS SEMICONDUCTORS.....	246
9.1. Study of optical properties of thin films by 4-probe method.....	252
9.2. Theoretical calculation of photocurrent generated in silicon-based solar elements.....	259
9.3. Emission processes in α -Si:H based solar elements....	269

9.4. Optical absorption in amorphous hydrogenated silicon.....	276
9.5. Thin-film solar modules based on amorphous and microcrystalline silicon.....	283
9.6. Cyclic method of deposition of a-Si:H layers by processing in hydrogen plasma.....	289
9.7. Influence of thermal treatment on the properties of nanostructured films α -Si:H.....	296
9.8. Basic parameters of solar elements based on IrSi.....	305
9.9. Radiation effects in IrSi-Si based microcircuits.....	309
9.10. Energy diagram of the iridium silicide-silicium structure, problems of silicon nanoelectronics and their solutions.....	316
9.11 Effects of ionizing radiation on the parameters of semiconductors.....	328
LITERATURE.....	335

INTRODUCTION

The main types of photodetector designs for spectral range from ultraviolet to near-infrared are described. The basic parameters of multielement photodetectors of different types based on different semiconductor materials are given. Features of construction of photodetectors, new directions of their development in military science, including matrixes with internal scanning are stated.

The content of the monograph allows to feel the progress in the creation of such systems, which was made possible by solving a number of material science problems, mainly related to the manufacture of photodetectors of the near and infrared - range. The appearance of cheap, small-sized, easy-to-use and reliable element base not only caused the modernization of previously developed information devices but also promoted the wide introduction of various purpose optoelectronic systems based on new physical principles.

Of course, with such a wide range of problems addressed in one monograph it is impossible to achieve exhaustive completeness of coverage of any particular issue. However, the author did not set himself this goal. Their main task was to give a generally accessible presentation of the main content of the devices in question. In my opinion, the authors have succeeded in this task. Despite the schematic nature, which is inevitable in such cases, the presentation of material allows to clearly understand the basic physical ideas that underlie the functioning of a particular device, to understand the technical and technological factors that limit its parameters. Therefore, this monograph will be of interest primarily to those who are new to modern optoelectronic devices. The concentration of the material on the basis of the general idea of describing the principles of functioning of known devices is the main

difference between this book and most publications on the subject, which focus on special issues of design and application.

The monograph can be used as a textbook for students, graduate students and engineering-technical workers related to the creation and use of semiconductor devices in optoelectronic equipment.

PART I

CHAPTER I. PHOTODETECTORS OF IR RADIATION ON SCHOTTKY BARRIER DIODES

1.1 Ways to increase quantum efficiency of semiconductor photodetectors

The use of radiation receivers in infrared systems requires high homogeneity of sensitivity of receiving elements, because otherwise the geometric noise increases sharply (fig.1.1) [1]. If in scanning systems the dispersion of sensitivity of receiving elements can be significantly reduced by working in time-delay and summation mode or by using special electronic schemes of sensitivity alignment by average brightness of the observed image, in non-scanning systems, due to a significantly larger number of elements in the matrix, such relatively simple methods of sensitivity alignment are difficult to use.

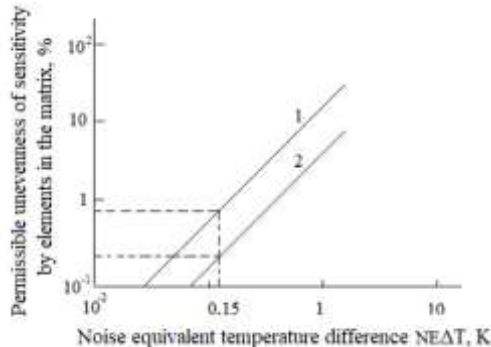


Fig. 1.1. Relationship between the non-uniformity of sensitivity by elements in the matrix and the value of the equivalent NEAT temperature difference noise at temperature, in the wavelength range of $3\div 5\mu\text{m}$ (1) and $8\div 14\mu\text{m}$ (2)

Geometric noise of multielement matrices is eliminated by using two reference radiating surfaces with high and low emission levels, with subsequent digital processing of signals of each receiving element using a special algorithm [2-4].

When eliminating the geometric noise, to provide an equivalent temperature difference of 0.1^0 K, provided that the temperature interval of the objects perceived by the receiving device is in the range $286 \div 306^0$ K, the digital sensitivity equalization system must have at least 12 digits [5].

Some strict requirements on speed and digit capacity are imposed on digital signal processing system to provide the sensitivity equalization and exclude the geometric noise in multielement radiation receivers with a large number of elements, and thus, to create conditions for the operation of the receiver in a non-scanning mode.

There is a fundamentally different way to eliminate geometric noise - to create multielement radiation receivers based on such physical mechanisms of conversion of radiation into electrical signal, which provide a very high homogeneity of individual matrix elements. The process of conversion of optical radiation to electric charge on Schottky barriers refers to such physical mechanisms [6-8].

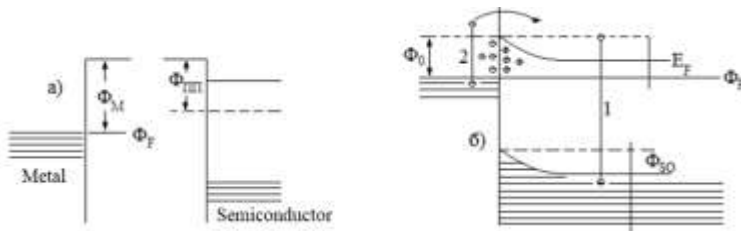


Fig. 1.2. Energy diagrams of metal-semiconductor n-type contact in the absence of metal-semiconductor contact (a) and after bringing them into contact establishing equilibrium (b); E_F is Fermi level [10].

In a Schottky barrier, i.e. a potential barrier in the boundary layer of metal-semiconductor contact, depending on the ratio between the values of the electron yield work in the metal F_M and in the semiconductor F_{SC} , electrons, as a result of internal emission, can move from the metal to the semiconductor (at $F_M < F_{SC}$) or vice versa (at $F_M > F_{SC}$) until thermodynamic equilibrium occurs and Fermi levels on both sides of the contact, coincide. Fig.1.2a shows zone diagrams of metal contact with an n-type semiconductor, for the case: $F_{SC} < F_M$ [9].

Upon contact, some of the electrons from the semiconductor pass into the metal. Near the contact, a united near-contact layer is formed in the semiconductor, a region of spatial charge of uncompensated positive donor ions arises, the electric field of which, prevents further transitions of electrons from the semiconductor to the metal, zones are curved upward by the value of the equilibrium surface potential F_{S0} . If we neglect the role of surface states, the value of $F_{S0} = F_M - F_{SC}$ [11].

Under the influence of radiation in such a structure two types of electronic transitions can take place (fig. 1.2b). At absorption of a photon in a semiconductor, generation of an electron-hole pair (1) takes place; in this case, as well as in a usual p-n photodiode, separation of carriers of different sign by transition field takes place and photoelectromotive force – foto EMF. At absorption of a photon in the metal, if the excited electron appears at a high energy level sufficient to overcome the potential barrier at the boundary between the metal and the semiconductor, there is an internal photoemission of an electron from the metal into the semiconductor (2). To overcome the potential barrier in the transition from metal to semiconductor, the kinetic energy of the excited electron must be greater than the barrier height F_0 , equal, as seen in Fig. 1.2b, $F_0 = F_{S0} + E_F$. Here E_F is the energy distance between the Fermi level and the bottom of the semiconductor conduction band. In other words,

the height of the barrier is equal to the difference between the yield work of the metal and the electronic similarity of the semiconductor. The long-wave boundary of the photoelectric effect at type 2 electronic transitions, by selecting appropriate materials, can be shifted to the infrared region of the spectrum. At the same time, it is clear that the long-wave boundary of process 1 cannot be less than the energy of the semiconductor's band gap and from this point of view, the photodetector with Schottky barrier does not differ from p-n photodiodes or own photoresistors made of the same semiconductor material. Thus, the greatest interest, in terms of creating IR receivers from silicon, is the process 2, i.e. photoresist from metal to semiconductor. Therefore, only these devices will be considered below.

To eliminate the influence of surface states on the height of the potential barrier F_0 Schottky diodes are made by chemical reaction to form silicides that have metallic conductivity. Such metals include, for example, palladium and platinum. In this case, the Schottky barrier occurs at the interface. The advantage of such a barrier is that its properties are not affected by surface defects - oxides and impurities on the surface of the semiconductor. By selecting the material it is possible to provide such a barrier height, which determines the sensitivity of the receiver in the required range of the infrared spectrum (Table 1.1) [12-15].

The same table shows the values of the corresponding long-wave limits of the photoeffect λ_0 for type 2 electronic transitions in photodetectors based on these barriers. The value of λ_0 is related to the height of the potential barrier F_0 by the known relation directly obtained from the equality $h\nu_0 = F_0$, where λ_0 is measured in micrometers (μm), F_0 in electron volts (eV), and $h\nu_0$ is the energy of the quantum corresponding to λ_0 :

$$\lambda_0 = 1.24/F_0 \quad (1.1)$$

Table 1.1.

Silicide	F ₀ , eV	λ ₀ , μm	Silicide	F ₀ , eV	λ ₀ , μm
TiSi ₂	0,52	2,4	Pd ₂ Si	≈ 0,34	≈ 3,6
WSi ₂	0,47	2,64	Pt ₂ Si	≈ 0,35	≈ 3,65
NiSi	0,46	2,7	PtSi	0,19-0,2	6,0
			IrSi	≤ 0,18	7,0

Experiments and theoretical calculations show that the spectral dependence of the quantum yield Y of the internal photoemission from metal to semiconductor in Schottky diodes can be described by the so-called refined Fowler formula:

$$Y = c \frac{(h\nu - h\nu_0)}{h\nu} \quad (1.2)$$

$$R = c_1 \left(1 - \frac{\varphi_0 \lambda}{1,24} \right) \frac{A}{Vt}$$

where c - is the quantum photoemission coefficient, the absolute value of which depends on the geometrical, optical, and electrical parameters of the detector. Figure 1.3 shows the experimental dependence of the quantum yield observed at IrSi barriers, expressed as a linearized Fowler formula:

$$\sqrt{Y \cdot h\nu} = \sqrt{c} \cdot (h\nu - h\nu_0) \quad (1.3)$$

Here it should be emphasized that IR photodetectors based on Schottky diodes differ from traditional intrinsic or impurity IR receivers in the shape of their spectral response.

Quantum yield of receivers based on internal photoeffect (photoresistors or p-n photodiodes) does not depend on quantum energy at energies higher than threshold value at all and is close to unity. For Schottky diode receivers, the quantum yield

increases monotonically with the quantum energy at energies greater than the threshold [16].

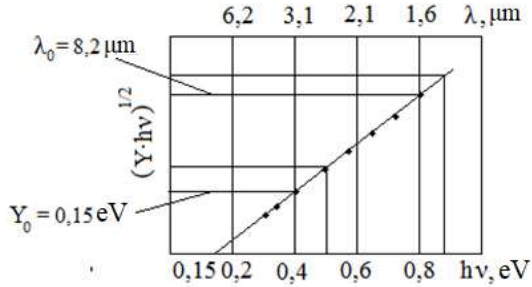


Fig. 1.3. Dependence of $(Y \cdot h\nu)^{1/2}$ on photon energy, for photodiodes with Schottky barrier of IrSi, $c = 5\% / \text{eV}$

This effect must be taken into account when calculating those characteristics of the receiving systems, which depend on the spectral characteristics of the receiving device (optimal spectral range, threshold characteristics with respect to non-monochromatic radiation, etc.).

The main processes of radiation detection by a Schottky receiver are absorption of photons in the silicide layer and internal photoemission of carriers from the metal into the semiconductor, so the value of the coefficient c , and therefore the quantum yield and photosensitivity of these diodes are determined mainly by electronic and optical processes in the metal silicide, but not in the semiconductor [17]. In addition, it is also essential that the photosignal is associated with the emission of the main current carriers into the semiconductor through a potential barrier. Therefore, the photosensitivity of Schottky diodes in the first approximation does not depend on such semiconductor parameters as doping degree and impurity compensation level, as well as on the lifetime of non-basic

carriers. This eliminates the main reasons that cause uneven sensitivity in multielement matrices, the main one in Schottky matrices being the scatter of geometric sizes of the sensitive elements (in relative value it is a fraction of a percent) [18-20].

In addition to high uniform sensitivity, Schottky receivers are characterized by much less stringent requirements on the electrical parameters of silicon. Since the silicon substrate is not involved in the process of photogeneration of current carriers, the same silicon used to manufacture integrated circuits can be used for Schottky diodes [21].

Two noise mechanisms are essential for Schottky receivers: shot noise, caused by fluctuations in the thermoelectron emission current across the barrier, and background noise, caused by fluctuations in the number of photoelectrons excited by background radiation incident on the receiver [22].

The dark current of thermionic emission I_m depends on the temperature. This dependence is described by Richardson formula:

$$I_m = A \cdot A^* \cdot T^2 \cdot \exp\left(-\frac{e\Phi_0}{kT}\right) \quad (1.4)$$

where T - is the detector temperature in Kelvin, e is the electron charge, k is the Boltzmann constant, A^* - is the Richardson constant (its theoretical value for hole emission in silicon is $32A\text{-sm}^{-2} \text{K}^{-2}$), A is the detector area.

As the temperature decreases, the average value of the thermoelectronic emission current and its fluctuations decrease. Therefore, at some sufficiently low temperature, the predominant noise mechanism will be background noise.

In [23] it is shown that the condition of predominance of background noise over all other sources of noise in photovoltaic receivers (P_V), including Schottky photodiodes, is fulfillment of the relation:

$$R_0 \cdot A \gg \frac{2kT}{e^2 Y(\lambda) Q_F(\lambda)} \quad (1.5)$$

where $R_0(\text{Ohm})$ and $A(\text{sm}^2)$ are, respectively, the dark resistance and detector area; $Q_F(\lambda)$ is the photon background flux density at wavelength $\lambda < \lambda_0(\text{sm}^{-2} \cdot \text{s}^{-1})$ and $Y(\lambda)$ is the quantum yield of the detector at that wavelength.

For a Schottky receiver, for which:

$$R_0 = \left. \frac{\partial I}{\partial U} \right|_{U=0} = \frac{kT}{eA^*T^2} \exp\left(-\frac{eF_0}{kT}\right). \quad (1.6)$$

This condition, when integrated over all wavelengths, takes the form:

$$\frac{kT}{eA^*T^2} \exp\left(-\frac{eF_0}{kT}\right) \gg \frac{2kT}{e^2 \int_0^{\lambda_0} Y(\lambda) Q_F(\lambda) d\lambda} \quad (1.7)$$

Inequality (1.7) determines the output temperature of the Schottky-receiver in the OF* mode, depending on the long-wave limit of photosensitivity (Fig. 1.4).

In Fig. 1.4, the output temperature is taken as the temperature at which the shot noise of thermoelectronic emission equals the background noise; the cases considered approximately correspond to the maximum and minimum real values of the intensity of background irradiation; the dots in the figure show experimental results for some silicides.

Figure shows that as to the optimum operating temperatures (in this case the temperatures of reaching OF*) Schottky receivers are considerably inferior to usual photon receivers on narrow-gap semiconductors, for which in the 3÷5 microns window they are achieved with thermoelectric coolers (150÷190⁰ K), and in the 8÷14 microns window they are close to liquid nitrogen temperature ($\approx 80^0$ K).

When quantifying the working temperatures of Schottky receivers it should be taken into account that to obtain the best sensitivity in the window of atmospheric transparency, their long-wave sensitivity boundary should be greater than the long-wave boundary of the usual photodiode.

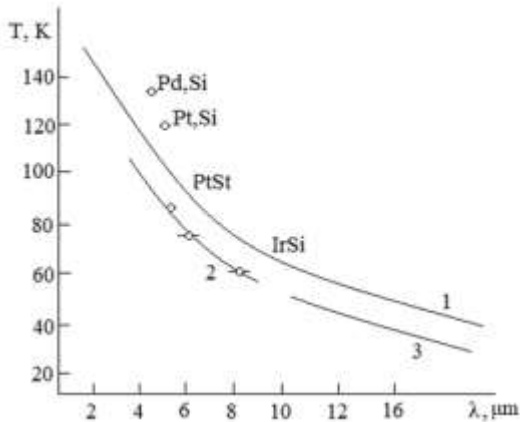


Fig. 1.4. Calculated dependences of temperature of Schottky receivers output to OF* mode on the longwave limit of photosensitivity λ_0 at different intensity of background radiation, when background radiation falls on a sensitive element within hemisphere and in the spectral range from 0 to λ_0 (1), at 30° and $\Delta\lambda = 3\div 5 \mu\text{m}$ (2), and at 300° and $\Delta\lambda = 8\div 14 \mu\text{m}$ (3)

Therefore, as a Schottky receiver working temperature, for $3\div 5 \mu\text{m}$ transmittance window, 80°K , and for $8\div 14 \mu\text{m}$ window, $T \leq 40^\circ \text{K}$ [24-28].

When Schottky receiver operates in OF* mode, its noise is determined by the intensity of background radiation, as for conventional photoresistors or photodiodes. The RMS value of the background noise depends on the average intensity of the background flux incident on the receiver:

$$\sqrt{\Delta n_{sh}^2} = \int_{\nu_0}^{\infty} Y(\nu) \cdot \overline{Q_F(\nu)} d\nu; \quad (1.8)$$

where, $\sqrt{\Delta n_{sh}^2}$ - RMS value of fluctuations of photoelectron concentration (photoboles), - average photon flux density with frequency of background radiation falling on a sensitive element; $\nu_0 = F_0/h$ [29].

Using the known technique, we can obtain an expression for the spectral detectability of the Schottky receiver in the OF* mode:

$$D^*(\lambda) = c \left(\frac{h\nu - h\nu_0}{h\nu} \right)^2 \cdot \left(\int_{\nu_0}^{\infty} c \frac{(h\nu - h\nu_0)^2}{h\nu} \cdot \overline{Q_F(\nu)} \cdot d\nu \right)^{-\frac{1}{2}} \quad (1.9)$$

The dependences calculated by equation (1.9) for some values of Schottky barrier height, $c = 10\%$ eV and $T_F = 290^0$ K are shown in Fig. 1.5; here, for comparison, similar dependences for the usual photon receiver of radiation with quantum efficiency equal to one and with the same values of the long-wave limit are given.

The figure shows that Schottky receivers have significantly lower values of $D^*(\lambda)$ at wavelengths close to the long-wave boundary compared to conventional receivers.

To increase the detectability of Schottky receivers operating in the OF* mode, as with conventional photonic receivers, the intensity of the background flux is reduced by cooled apertures or filters of the required working spectral interval (fig. 1.6) [30-33].

The analytical expressions, according to which the dependences shown in Fig. 1.6 are calculated, can be obtained by opening the integral in equation (1.9), according to the corresponding wavelength interval. It is obvious that in absolute value, the integral detectability, as well as the spectral

detectability, of Schottky receivers is much smaller than that of conventional photonic receivers.

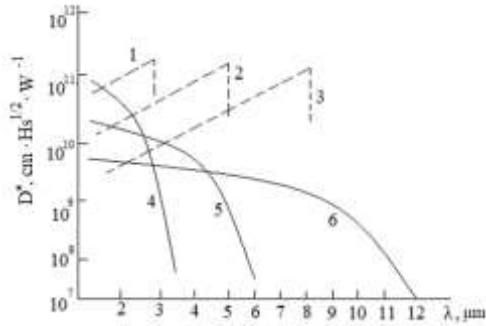


Fig. 1.5. Spectral dependence of the reduced detectability of photoresist (curves 1 - 3) and Schottky photodiodes (curves 4 - 6) at F_0 , equal to 0.1 (curves 3, 6), 0.2 (curves 2, 5) and 0.3 eV (curves 1, 4)

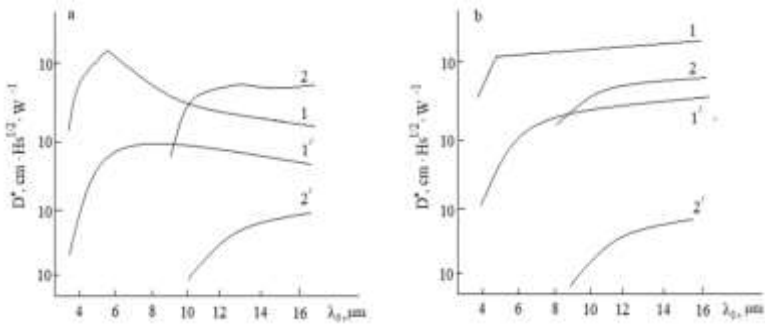


Fig. 1.6. Dependence of integral value $D^*(\lambda)$ on the position of the Schottky diode (curves 1, 2) and p-n photodiodes (curves 1, 2) long-wavelength limit of photosensitivity in the transparency window $\Delta\lambda = 3-5 \mu\text{m}$ (curves 1, 1') and μm (curves 2, 2'), when the background radiation falls in the whole wavelength range $0-\lambda_0 \mu\text{m}$ (a) and in the windows $\Delta\lambda(\delta)$

Their dependence on the position of the long-wave limit of photosensitivity also differs: if for conventional receivers the shift of λ_0 beyond the long-wave limit of the signal radiation transmittance window does not at best reduce the detectability, then for Schottky receivers, the maximum value of integral detectability is achieved only when λ_0 is greater than the long-wave limit of the corresponding transmittance window.

Thus, for a window of $3\div 5\text{ }\mu\text{m}$, the maximum value of integral detectability corresponds to $\lambda_0 = 7\text{ }\mu\text{m}$ in the case when the background radiation hits the sensitive element throughout the spectral region from 0 to $\lambda_0\text{ }\mu\text{m}$ and for $\lambda > 20\text{ }\mu\text{m}$ - when the background radiation lies in the same spectral region as the signal radiation. Obviously, this feature of Schottky receivers is determined by a special kind of spectral dependence of the quantum yield of the internal photoemission (see equation 1.2), when increasing the long-wavelength limit leads to increasing the quantum efficiency in a given wavelength interval, which is not observed in conventional receivers. Thus, in Schottky receivers, the detectability in atmospheric transparency windows can theoretically be increased by using materials that provide a lower potential barrier height, but the cooling temperature of the sensing element must also be reduced [34].

From comparison of curves a and b of Figure 1.6, it would seem that traditional photonic radiation receivers (for example, PVs at p-n junctions) have a significant advantage over Schottky diodes in terms of limiting sensitivity. However, this is true only for "lightweight" receivers, but not for devices with signal accumulation.

When operating a receiver with signal accumulation in the OF mode, the signal-to-noise ratio is determined by the square root of the product of the signal accumulation time T_v and the quantum efficiency η (for Schottky receivers the quantum output Y). Therefore, for a Schottky receiver, the small value of the quantum output when operating in the charge accumulation

mode can be compensated for by increasing the signal accumulation time. In multielement receivers with a CCD reader, the T_V value is mainly determined by the limited capacity of potential wells of the CCD register [35].

During operation in ground level background conditions the receivers with quantum efficiency close to unity, due to overfilling of potential wells of the CCD readout register, cannot provide a signal accumulation more than $\approx 10^{-4}$ s for a 3-5 μm window and 10^{-3} s for an 8-14 μm window, i.e. less than a TV frame duration. Therefore, when using a Schottky diode matrix in non-scanning receivers operating in the television standard, it is quite feasible to compensate the small value of the quantum output with a large signal accumulation time ($T_V \approx 4 \cdot 10^{-2}$). To provide such compensation, the condition must be fulfilled:

$$T_V \cdot \eta / p - n_{diode} = T_V \cdot Y_{Schottky-diode} \quad (1.10)$$

The maximum signal accumulation time that can be realized in the system is determined by equality:

$$T_V^{max} = \frac{n_0}{\int_0^{\lambda_0} Y(\lambda) \cdot Q_F(\lambda) d\lambda} \quad (1.11)$$

n_0 - is the maximum capacity of the CCD-register well and depends on the wavelength limit of photosensitivity (Fig. 1.7) [36].

From Fig. 1.7 it is seen that for Schottky detectors the potential well with electron density $n_0 = 10 \text{ sm}^{-2}$ is filled with background radiation at temperature $TF = 290^0 \text{ K}$ for 0.1 s when the receiver operates in the window of 3÷5 μm and for $\approx 10^{-2}$ s when operating in the window of 8÷14 μm [37].

Thus, the value of signal accumulation time for Schottky receivers can be increased in $10^2 \div 10^3$ times in comparison with

usual photon radiation receivers and consequently to provide the fulfillment of the relation (1.10).

The possibility to compensate a small value of quantum output of Schottky diodes by a large value of accumulation time in the signal accumulation mode is physically quite obvious, because, as well as for conventional receivers, the number of accumulated carriers, and therefore the noise equal to the square root of this number, in both cases is n_0 and determined by the capacity of the potential well of the CCD-register [38].

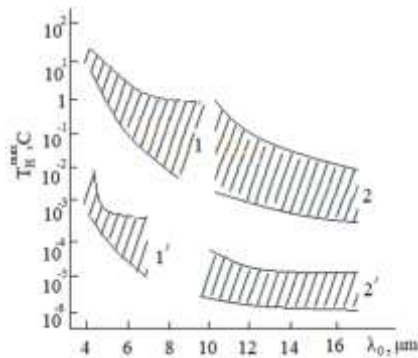


Fig. 1.7. Dependence of maximum accumulation time on the long-wave limit of photosensitivity for Schottky diodes (regions 1, 2) and p-n photodiodes (regions 1', 2') for transparency windows $\Delta\lambda = 3 \div 5 \mu\text{m}$ (regions 1, 1'), and $\Delta\lambda = 8 \div 14 \mu\text{m}$ (regions 2, 2') at different intensity of background radiation (see Fig. 1.4) and potential well capacity $n_0 = 10 \text{ sm}^{-2}$

To compare receivers with signal accumulation, using Schottky receivers and ordinary photodiodes on the limiting sensitivity let's assume that conditions for realization of T_V^{max} are created in them. The signal accumulated by the photosensitive element, under the influence of signal emission, is equal:

$$n_S = A_{f.e} \cdot T_V \cdot \int_{\lambda_1}^{\lambda_2} \eta(\lambda) Q_S(\lambda) d\lambda \quad (1.12)$$

where $A_{f.e}$ - is the area of the photosensitive element; $Q_S(\lambda)$ is the spectral density of the photon flux of the signal radiation incident on the sensitive element; $\lambda_1 \div \lambda_2$ is the spectral region in which the signal radiation is registered [39].

The rms value of the background noise is determined by the square root of the number of accumulated electrons caused by background radiation:

$$n_{Sh} = \left[A_{f.e} \cdot T_V \cdot \int_0^{\lambda_0} \eta(\lambda) \overline{Q_F(\lambda)} d\lambda \right]^{\frac{1}{2}}. \quad (1.13)$$

The threshold flux density of the signal radiation, corresponding to the signal-to-noise ratio at the output of the photosensitive element, equal to one, in this case, is equal:

$$E_{th} = \frac{\left(\int_{\lambda_1}^{\lambda_2} \frac{hc}{\lambda} Q_S(\lambda) d\lambda \right) \left(\int_0^{\lambda_0} \eta(\lambda) \overline{Q_F(\lambda)} d\lambda \right)^{\frac{1}{2}}}{(T_V \cdot A_{f.e})^{\frac{1}{2}} \cdot \int_{\lambda_1}^{\lambda_2} \eta(\lambda) Q_S(\lambda) d\lambda} \quad (1.14)$$

To calculate the maximum accumulation time T_H^{\max} (equation 1.11), the threshold exposure is calculated as follows:

$$E_{th} = \frac{\int_{\lambda_1}^{\lambda_2} \frac{hc}{\lambda} Q(\lambda) d\lambda n^{1/2}}{T_H^{\max} A_{f.e}^{1/2} \int_{\lambda_1}^{\lambda_2} \eta(\lambda) Q_S d\lambda} \quad (1.15)$$

For simplicity, it is assumed that the areas of the sensitive element and the cell, in which the charge is accumulated, are equal. From the dependences calculated by equation (1.15) it is clear that in systems (fig. 1.8) with Schottky receivers, the same values of threshold irradiance can be obtained as with conventional p-n photodiodes.

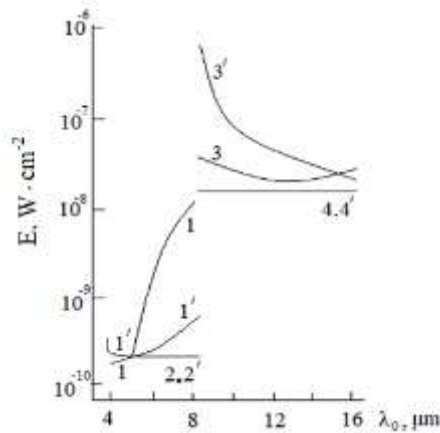


Fig. 1.8. Dependence of Schottky threshold irradiance of receivers (curves 1' - 4') and p-n photodiodes (curves 1 - 4) on the longwave limit of photosensitivity at the maximum accumulation time in the atmospheric window, $\Delta\lambda = 3 \div 5 \mu m$ (curves 1, 1', 2 and 2') and $\Delta\lambda = 8 \div 14 \mu m$ (curves 3, 3', 4 and 4'), when the background radiation falls on the receiver in the region of $0 - \lambda_0 \mu m$ (curves 1, 1', 3 and 3') and only in the window $\Delta\lambda$ (curves 2, 2', 4 and 4') the background temperature is $290^0 K$; cooled apertures limiting the flux apertures are not used

Thus, a Schottky receiver operating in a charge accumulation background-limited mode is essentially not a low-sensitivity receiver, but an inertial receiver of radiation, and its "inertia" is such that it allows its application in non-scanning receiver systems with a frame duration close to a television frame [40]. Summing up the physical mechanism of Schottky receivers we can draw the following conclusions:

- the investigated mechanism of converting optical radiation into electrical signal provides high uniformity in sensitivity of individual elements of a multielement radiation

receiver, and is characterized by moderate requirements to the quality of the semiconductor material (silicon).

- at present Schottky receivers are probably beyond competition by this parameter among all known multielement radiation receivers: small (more than an order of magnitude, compared to photoresistors and p-n photodiodes) quantum efficiency in signal accumulation mode can be compensated by an increase of accumulation time [41].

The main disadvantage of Schottky receivers, due to the special kind of spectral sensitivity, is the need to cool down to lower operating temperatures than for conventional photoresist or p-n photodiodes operating in the same spectral range [42]. Nevertheless, in the atmospheric transparency window corresponding to $3\div 5\text{ }\mu\text{m}$, Schottky receivers have quite acceptable operating temperatures in the liquid nitrogen region ($\approx 800\text{ K}$) [43].

1.2. Schottky matrix design and operating modes

Parameters of multielement IR receivers on Schottky diodes, depend both on characteristics of the sensing element itself, and on the device and mode of operation of the matrix. To increase quantum efficiency of Schottky diodes in the operating wavelength range, it is necessary to increase the long-wavelength limit of photosensitivity, which in turn is determined by the height of the Schottky barrier. The Schottky barrier depends on the metal yield strength and the electronic affinity of the semiconductor. The metal Schottky yield work of PtSi barrier metal diodes is 0.27 eV, which corresponds to a long-wavelength photosensitivity limit of $4.6\text{ }\mu\text{m}$ [44-47].

To reduce the Schottky barrier height, it is made thinner (in the direction perpendicular to the transition surface) and conditions for tunneling of photo-excited carriers through it are

created. In order to facilitate the tunnelling of photocarriers the silicon has to be additionally doped with a thin layer of ions near the silicon-metal silicide interface. The material of the doRRng layer is taken in such a way that its conductivity is the same as that of the substrate. The right dosage of the dopant ions provides a noticeable reduction of the barrier height. The thallium doRRng lowered the PtSi barrier height from 0.267 to 0.223 eV and thus shifted the long-wavelength limit of photosensitivity from 4.6 to 5.5 μm (fig. 1.9).

Increasing the long-wavelength limit by only 20%, resulted in a $5.6 \div 9.1$ -fold increase in Schottky diode quantum efficiency, in the $3.4 \div 4.2 \mu\text{m}$ range [48]. If a photosensitive element is made in the form of "optical cavity", the quantum efficiency of Schottky receivers can be significantly increased (fig. 1.10).

First Schottky photodiodes made of metal silicides had rather thick metal layer (about 60 nm) and very low quantum efficiency at low quantum efficiency.

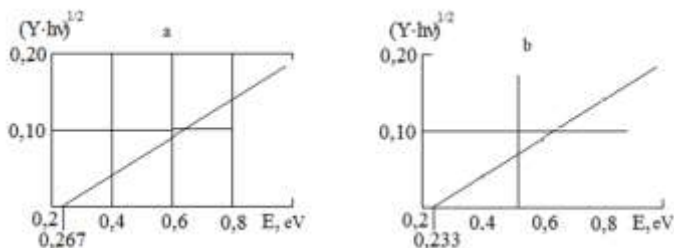


Fig. 1.9. Dependence of $(Y \cdot hv)^{1/2}$ on photon energy for Schottky diodes of PtSi without doRRng (a) and with thallium doRRng (b)

By creating a Schottky receiver in the form of an 'optical cavity' with a thin layer of silicide, the quantum photoemission coefficient C is increased.

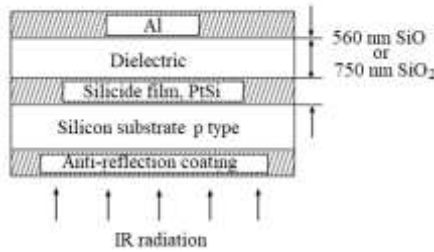


Figure 1.10. Schottky diode photosensitive layer structure as an "optical cavity"

Optical absorption is increased by multiple reflections of the rays in the 'cavity'. And the "cavity" is formed by the aluminium mirror and antireflection layers and the efficiency of internal photo-emission of hot holes from a thin layer of silicide into the silicon substrate, due to their multiple reflection at the silicide-semiconductor interface. It is clear that for emission of hot hole (electron) into semiconductor, the momentum of photo-excited carrier in the direction normal to the silicide-silicon interface must correspond to such kinetic energy which is higher than the Schottky barrier height Φ_0 . The result is a reflected hot hole from the interface. This changes the angle between the direction of motion of the photocarrier and the normal to the silicide-silicon interface.

Obviously, the momentum in the direction of the normal is proportional to the cosine of this angle, and with multiple reflections, the probability of internal photoemission increases (fig. 1.11).

So the coefficient C grows. All this is taken into account by introduction of G , which is equal to the ratio of emission probabilities in thin $P_m(h\nu)$ and thick $P(h\nu)$ layers of silicide:

$$G = P_m(h\nu)/P(h\nu) \quad (1.16)$$

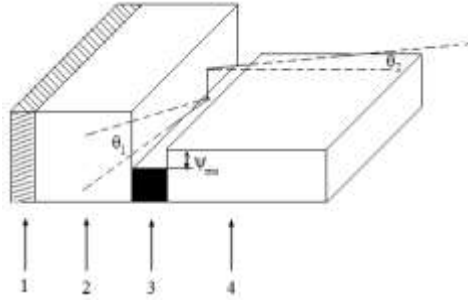


Fig. 1.11. Graphical representation of "hot" hole re-reflection processes at a silicide-semiconductor interface: 1 - aluminum mirror; 2 - dielectric; 3 - silicide; 4 - semiconductor, $\theta_1 > \theta_2$

From the physical considerations it turns out that the coefficient is the higher the higher the number of possible reflections of the hot hole from the surface of the silicide-semiconductor [49].

Assuming that with each re-reflection the energy of the hot hole is conserved, the reflection angle is uncorrelated with the incidence angle, and the dissipation of hole energy by collisions with phonons and reflections at the boundaries of the silicide film can be described by the average length of energy dissipation by the hot carrier L (in the direction perpendicular to the layer surface). The number n of possible re-reflections depends on the hot hole energy E , the thickness of the silicide layer t and the value of L :

$$\text{Exp}\left(-\frac{2nt}{L}\right) = \Phi_0 \quad (1.17)$$

It is clear that the photoemission gain G must increase with the ratio L/t , and this dependence must be different for different photon energies $E = h\nu$. The analytical dependence of $G(t, L, \lambda)$ is shown graphically in fig. 1.12.

It can be seen from the figure that for different wavelengths the gain reaches a maximum at different values of the ratio L/t . The maximum value of G is obtained only when all the hot photocarriers are emitted into the silicon substrate (i.e. $P_m(h\nu) = 1$). Thus:

$$G_{max} = \frac{1}{P(h\nu)} \quad (1.18)$$

The calculated sensitivity for an idealised diode with a thin layer of platinum silicide (fig.1.13) can be regarded as the theoretical limit of photosensitivity of a Schottky diode, when the radiation is fully absorbed in it and all photocarriers take part in the photodetector formation.

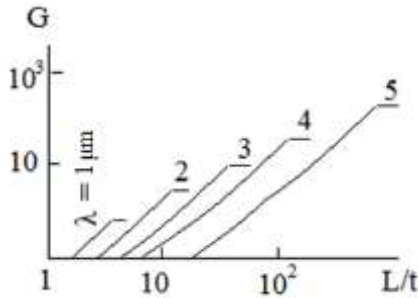


Figure 1.12. Dependence of emission gain G on L/t ratio, at different wavelengths

For the photodiode in question, for example, the theoretical limit is 5 times higher than for a Schottky photodiode with a thick PtSi layer at wavelength $\lambda = 1 \mu\text{m}$ and almost 10^2 times higher, at wavelength $\lambda = 5.3 \mu\text{m}$ [50].

In the "optical cavity" of a Schottky diode photosensitive structure, the degree of radiation absorption depends on the thickness of the silicide layer, and the thickness of the dielectric material (figure 1.14) [51].

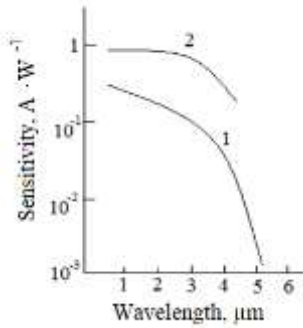


Figure 1.13. Spectral dependence of photosensitivity of a Schottky diode of PtSi with a thick silicide layer (curve 1) and an idealised photodiode of PtSi with a thin silicide layer (curve 2) at $G = G_{\max}$ and total absorption of radiation in the photosensitive layer

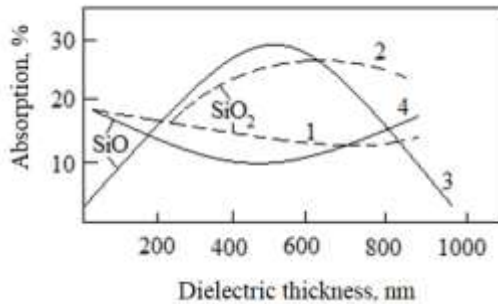


Fig. 1.14. Radiation absorption in "optical cavity" of photosensitive Schottky diode structure at wavelength $4 \mu\text{m}$ as a function of dielectric layer thickness. 1, 2 - dielectric) SiO_2 ; 3, 4 - dielectric SiO_x ; 1, 4 - without aluminum mirror layer; 2, 3 - with aluminum mirror layer

This means that by selecting (for example, by calculating by Fresnel formulas) the optimum thickness and dielectric layer

material, one can significantly (several times) increase the absorption of radiation in the silicide layer and thereby increase the quantum yield of photoemission of Schottky diodes.

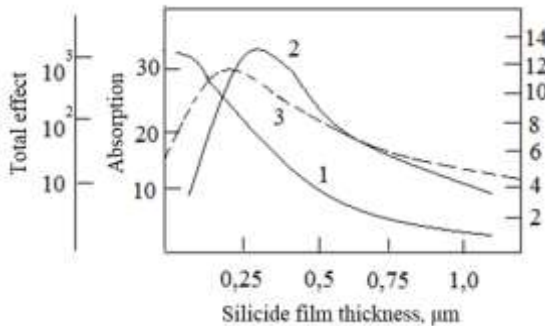


Figure 1.15. Dependence of emission gain (curve 1), absorption intensity (curve 2) and total effect expressed as the product of these quantities (curve 3) on the thickness of the PtSi layer (in units inverse to the absorption coefficient), for a Schottky photodiode

As can be seen from Fig. 1.15, the maximum value of quantum yield is achieved when the thickness of the silicide layer is equal to the inverse of its absorption coefficient.

Comparison of parameters of thickness optimized PtSi-receivers with receivers of previous releases shows that the optimization allows increasing the sensitivity at a given wavelength by 20÷30 times (by increasing the optical absorption, - by 3.5 times and by increasing the gain G - by 9.2 times).

It should be borne in mind, however, that such an increase in sensitivity has only been obtained for individual, better elements. On average, the sensitivity of Schottky receivers is still below these values.

Figure 1.16 shows experimentally measured temperature dependences of dark-current of Pd₂Si and PtSi Schottky receivers and dependences for thermoelectronic emission current, calculated from Richardson formula (1.4), at activation energy values of 0.199 and 0.378 eV respectively.

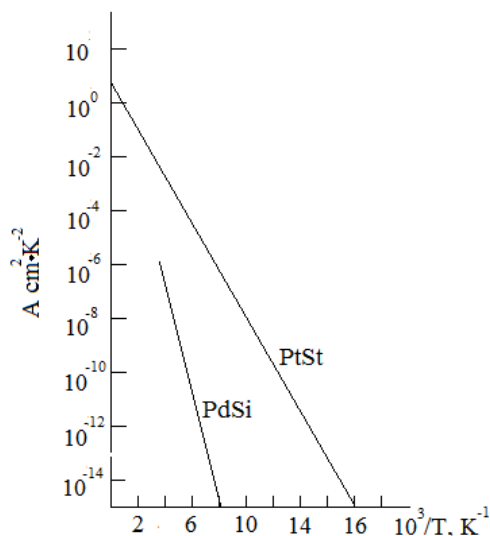


Figure 1.16. Temperature dependences of the dark current of PtSi and Pd₂Si Schottky diodes

The value of Richardson constant A^* for these diodes differs from the theoretical value of $32 A \cdot cm^{-2} K^{-2}$ and is equal to 53 and $10 A \cdot cm^{-2} K^{-2}$, respectively.

The photosensitive element in the form of a Schottky barrier "optical cavity" is formed by depositing a thin film of metal (about 60 nm thick), for example, palladium, through the windows in the oxide film on the surface of boron-doped silicon p-type (up to $10 \div 50 \text{ Ohm} \cdot cm$). After applying CCD-reader register contacts between silicon and metal silicide a Schottky

diode is formed by means of a heat treatment at $593 \div 923^0$ K. Then the remaining platinum layer is removed so that the thickness of the silicide layer is $2 \div 10$ nm, a dielectric layer is deposited and, on top of that, aluminium. On the reverse side of the substrate, a transmittance layer is deposited to reduce the reflection coefficient of the surface on which the registered radiation falls [52].

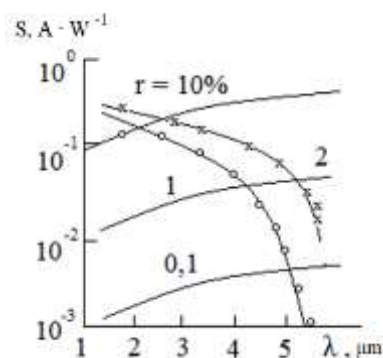


Fig. 1.17. Spectral characteristics of the photosensitivity of PtSi diodes at 8 h (curve 1) and 10 min (curve 2) heat treatment time; $\varphi_1 = 0.218$ and $\varphi_2 = 0.190$ eV, respectively

Studies of PtSi diodes developed by RCA have shown that the magnitude of the dark current depends on the duration of the heat treatment to which the diode is subjected during manufacturing. With increasing the heat treatment time, the dark current in the diode decreases, but, at the same time, the quantum efficiency and sensitivity of the diode decreases (Fig. 1.17).

Experiments have shown that the best ratio of quantum efficiency to dark current density is achieved with a heat treatment time of 8 hours [53].

Photodetectors made of Schottky diodes are monolithic structures. In the considered photodetectors conversion of

optical radiation into electric signal and its primary processing occur in the same semiconductor: in silicon. The primary processing of photodetection of Schottky receivers consists of element-by-element reading and output of the signal to a common output. Surface or covert channel CCD registers are used for this purpose.

One of the first simplest schemes for connecting Schottky receivers to a CCD shift register, is shown in Figure 1.18.

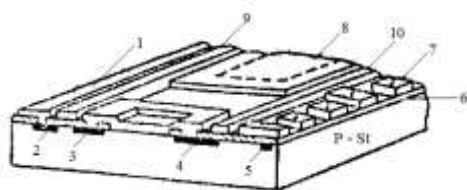


Figure 1.18. Schottky photodiode connection diagram with CCD register: 1 - reset bus; 2 - n+ reset channel; 3 - n-diffusion region of reset channel; 4 - n+ diffusion region of readout channel; 5 - p+ stop channel; 6 - oxide; 7 - three-phase CCD shift register; 8 - photosensitive element; 9 - reset gate; 10 - readout gate

This structure works in two modes:

- 1) with background signal subtraction;
- 2) without background signal subtraction.

When the background signal is not subtracted, the reset channels are not used, as they are not involved in the operation of the device. If a high potential is applied to the first phase electrode of the shift register, a potential well will form below it. A positive potential is then applied to the readout gate, creating a potential U_a under the gate electrode and on the floating diffusion region of the readout channel (figure 1.19).

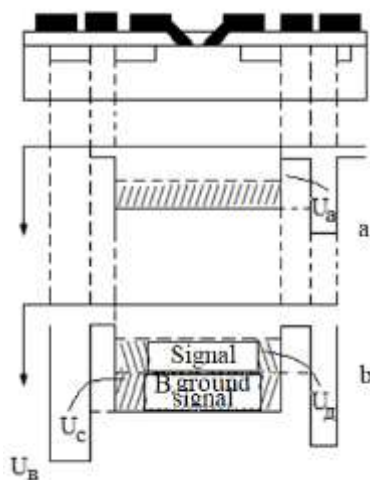


Figure 1.19. Schematic diagram explaining the Schottky photodiode operation without background subtraction (a) and with background subtraction (b)

In the Schottky barrier region, a charge builds up and passes into the deeper potential well below the first phase electrode of the readout register. The charge, which is a signal packet, is transferred in the usual way to the output of the shift register to form a video signal once the reading pulse at the gate is terminated. As soon as the charge is read out, the metal electrode of the Schottky diode is placed under the floating potential U_a . A signal charge is built up on this electrode and this charge is read out in the same way in the next frame.

The potential well of the shift register, with this reading method, transfers all the charge accumulated by the photosensitive element. This process can be carried out in the following ways:

- 1) through optical excitation by radiation from the object being registered;
- 2) by excitation by background radiation.

In the first mode (with background signal subtraction), the difference signal is used as the signal charge. The signal taken as the basis is between the charge accumulated by the cell and the charge due to background radiation exposure. The difference signal is the same for all photosensitive cells in the matrix. It contains no useful information about the observed object and therefore may not participate in the formation of the video signal. Subtraction of the constant background signal is performed by means of a reset channel (fig. 1.18, 1.19). A high positive potential applied to the reset signal bus forms a potential (depth -) well below the reset bus (fig. 1.19b). As soon as the frame ends, a reset pulse U_c is applied to the gate. This pulse sets the potentials of the diffusion regions of the reset and readout channels. All charge accumulated by the photosensitive region of the receiver is transferred to the potential well below the reset bus and removed. This charges the Schottky Photodetector to a floating potential U_c , i.e., prepares it for charging during the next frame. Before the reset pulse is applied to the readout gate, a pulse is applied at the end of the signal integration time. At this time it sets the surface potential under the gate equal to U_d . The charge that resides in the potential well below the Schottky barrier is placed above this level and flows into the potential well below the shift register electrode. By selecting the value of the potential U_d the following condition is ensured: only the charge which carries information about the change of the emission to be registered in relation to the average level of the background flux must be transferred to the reading register to form the video signal. After the termination of the readout pulse, the remaining constant background charge is removed by opening the reset gate. Thus:

- 1) the image contrast is significantly improved,
- 2) the limited phase shift register capacitance is used more fully (to provide a larger dynamic range of the receiving device) [54].

The main advantage of Schottky diode array compared to other multielement arrays is the high uniformity of sensitivity of the receiving elements. This process is characteristic of the conversion stage of optical radiation to electrical charge directly in the photosensitive element. The full uniformity of sensitivity of the photodetector matrix also depends on the uniformity of the signal reading process of the individual elements. Above said, the read-out mode without background signal subtraction is preferable. Signal non-uniformity in the matrix can be caused by non-uniformity of the charge density in the oxide and the thickness of the oxide film. The non-uniformity is also affected by non-uniformity of the alloying impurity concentration in the silicon. This phenomenon causes variations in individual element capacitance and surface potential under the gates. In non-background subtraction mode, the same gate is used to set the initial floating potential of the sensing element and read the potential after the signal charge builds up. In this case, a possible difference in the values of the set floating potential between the different cells does not lead to a variation in the level of the read signal. This is because it is only determined by the difference in potential before and after charge build-up. In background subtraction mode, the initial value of the floating potential in each cell is set by the reset gate and the read potential, by the read gate. In this case, variation in level of potential being set by either gate, leads to variation in readout signal and thus, to non-uniformity of matrix elements in sensitivity [55].

In radio electronics, other signal readout circuits are used, such as direct injection circuits (figure 1.20).

In such circuits, the photosensitive element is directly connected to the source of the effective MOSFET. Some negative voltage U_1 is maintained via a surface channel gate G_1 on a Schottky photodiode. When an optical signal accumulates, the charge generated by the radiation being registered is collected in the potential well below electrode G_3 , with a hidden

channel. After accumulation, gate G_4 opens and the accumulated charge is transferred under the phase one electrode F_1 of the CCD shift register.

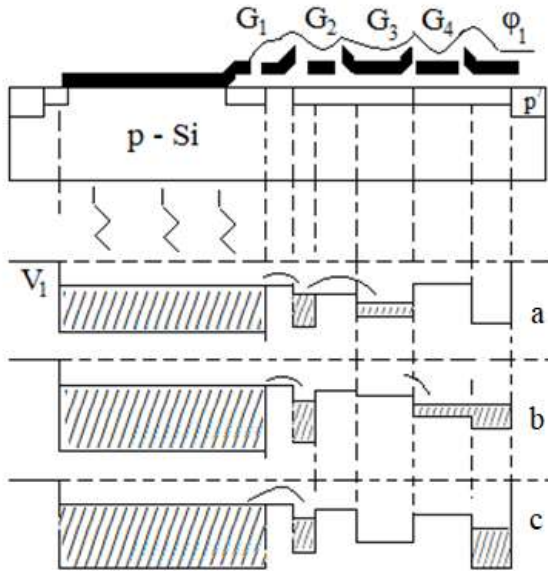


Figure 1.20. Scheme for connecting a Schottky photodiode to the input of a CCD register by direct injection

After the accumulated charge is transferred to the CCD register, the gate G_4 closes. Further, an accumulation potential is applied to electrode G_3 , and the cell is now ready for signal accumulation in the next frame. A special feature of the circuit in question is the elimination of noise caused by periodic voltage switching on the Schottky diode. In this case the Schottky diode is under the same voltage all the time.

This voltage is selected to minimize diode leakage currents and increase the sensitivity of the Schottky diode. A feature of this circuit is that the capacity limiting signal storage

time is not determined by the Schottky diode capacity, but by a larger capacity of the CCD register [56].

Sensitivity of receivers using multiple-element matrix Schottky diodes, as well as other multiple-element receivers, depends on the ratio of the area, occupied directly by photosensitive surface, to the whole receiver area, including the reading structure. When using CCD registers as a readout system, a multi-element receiver includes the following elements: shift register signal buses, read gate electrodes, charge transfer electrodes, stop-channel areas, etc. Because of this, the relative proportion of photosensitive area in multiple-element Schottky matrices (sometimes called the fill factor), is small. For example, in one of the first two-element Schottky diode matrixes, it was only 16.4%. By reducing the size of the readout structure elements, stop-channels and other non-photosensitive areas, it was possible to increase the fill factor, while maintaining a sufficiently large dynamic range of the readout structure. In a recent RCA development, for example, a matrix of 160x244 Schottky diodes achieved a fill factor of 39%. A simplified schematic of the sensing element of this matrix is shown in figure 1.21.

Further reductions in the size of the non-photosensitive areas of the matrix are envisaged, which is expected to increase the fill factor to a maximum of 83%.

It is possible to increase the fill factor by using CCD structures, with channels in the form of meanders, as a readout device. In this case, the readout consists of two electrodes Φ_1 and Φ_2 and a readout gate G (figure 1.22) [57].

As in matrixes with conventional CCD-reader registers, during the time while the frame charge is accumulated at the Schottky diode capacity, at the end of each frame, the charge is transferred via gate G to electrode Φ_1 , and from there, during the next frame, in series, via electrodes Φ_1 and Φ_2 , is transferred to the output reading device.

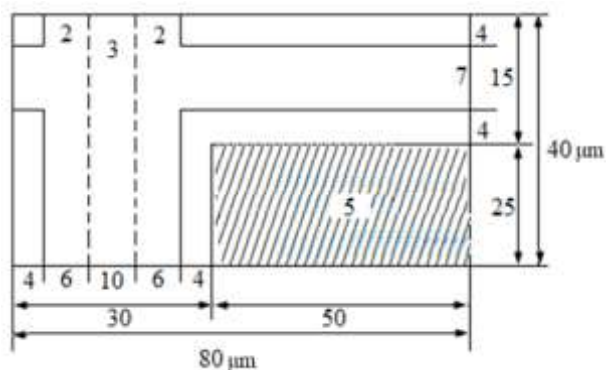


Fig. 1.21. Simplified schematic of a Schottky matrix cell of 160x244 elements, with a total cell area of 50x25μm and a fill factor of 39%: 1 - n- protective ring; 2 - stop-channels; 3 - transmitting CCD register with a hidden channel; 4 - silicon gates; 5 - photosensitive area of DSh

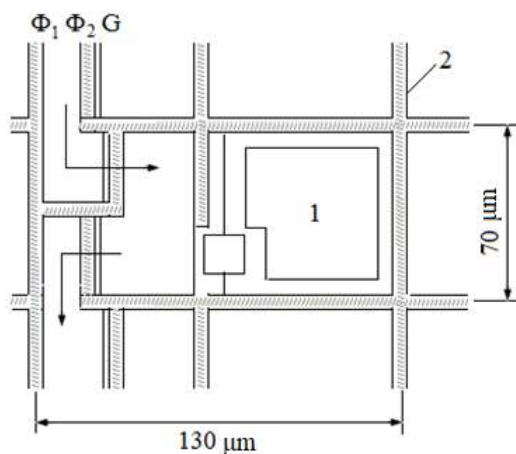


Figure 1.22. Photosensitive matrix Schottky diode cell topology with increased fill factor: 1 - photosensitive element; 2 - stop-channel diffusion region

The directional transfer of charges over channels Φ_1 and Φ_2 is ensured by a special silicon doRRng profile under these electrodes Φ_1 and Φ_2 . In such a scheme, the fill factor in a two-coordinate matrix of 64x64 elements, increases to 23%. With further process improvements, Fujitsu estimates that this factor could be increased to 57%.

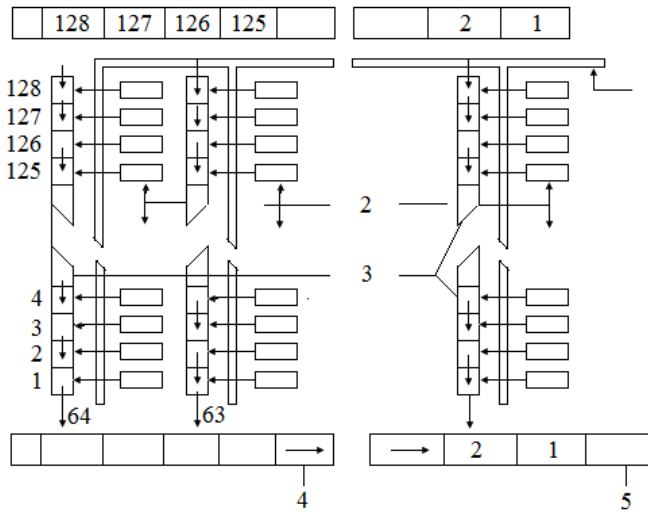


Figure 1.23. Schottky matrix schematic of RCA cell size:
1 - transmit gate; 2 - Schottky diodes; 3 - CCD column registers;
4 - CCD output register; 5 - output amplifier

Figure 1.23 shows the 64x128 element Schottky matrix structure developed by RCA.

The charges accumulated by the detectors are read by means of parallel columns and a serial output CCD register. During the loopback of the indicator unit, the signal accumulated by each sensing element is transferred to the corresponding cell of the column registers. Then, during the reverse stroke along the line, the signals of one row of parallel registers in the

columns are simultaneously fed into the cells of the output serial register. As the indicator sweeps along the line, these signals are fed to an output amplifier located on the same silicon crystal as the Schottky matrix itself and further, to signal processing devices placed outside the focal plane of the receiver.

This Schottky matrix (figure 1.24a) is an improved version of the previous model (figure 1.18) and operates in a background-subtraction-free mode. The matrix cells are separated by p⁺ regions; the n region of the CCD column register cell forms a protective ring around the sensing element preventing back current emissions. The charge transfer from the Schottky diode to the CCD-column register is accomplished by a gate with a surface channel formed by the n⁺ region. During the integration time, a sufficiently high potential is applied to the transfer gate to isolate the Schottky diode from the column CCD cell. In the region of the silicon substrate, under the silicide layer, photogenerated carriers (holes) accumulate under the influence of the registered radiation.

At the end of the integration time, a readout pulse is applied to the transfer gate and the accumulated charge is transferred to the hidden-channel CCD, the Schottky diode is recharged to potential 2 (figure 1.24b). At the end of the read pulse, a potential barrier is formed (potential 1 equal to the substrate potential) and the conditions for starting the next integration period are provided. This Schottky matrix cell structure also prevents the spreading of charge to neighbouring cells due to a strong optical signal (so-called 'blooming', causing a deterioration of the modulation transfer function of the receiver).

The intense optical signal shifts the Schottky diode in the forward direction, the photocarriers no longer accumulate in the substrate under the silicide layer, the excess charge flows into the hidden-channel CCD-register cell. Before the next integration period, the cell is fully restored to operation, while

the CCD column register must have sufficient capacity to store the entire saturation signal, which in turn reduces the Schottky matrix fill factor [57-60].

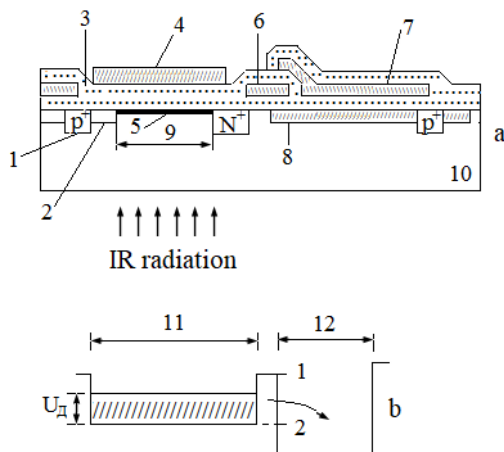


Figure 1.24. (a) - cross section of Schottky matrix element [64x128 elements] and (b) - potential diagram explaining its operation: 1 - p⁺ stop channel region; 2 - N guard ring; 3 - SiO₂ layer; 4 - aluminum layer; 5 - PtSi layer; 6 - transmit matrix gate; 7 - transmit CCD-column register gate; 8 - N latent channel of CCD-column register; 9 - active Schottky diode region; 10 - p⁻ silicon substrate; 11 - substrate region under silicon layer; 12 - potential well of CCD-column register

Significant increase of Schottky matrix filling factor is achieved by reading the charge stored in a Schottky diode not through CCD-registers, but by injecting it into a signal bus, similar to CCD structures on narrow-gap semiconductors. In this case a multi-element matrix contains horizontal and vertical shift registers, horizontal buses for polling elements of a selected row, vertical signal buses, MOSFET keys to connect the polled

column and a matrix of photosensitive elements, each consisting of a photosensitive Schottky diode itself and a MOSFET key (Figure 1.25) [61-63].

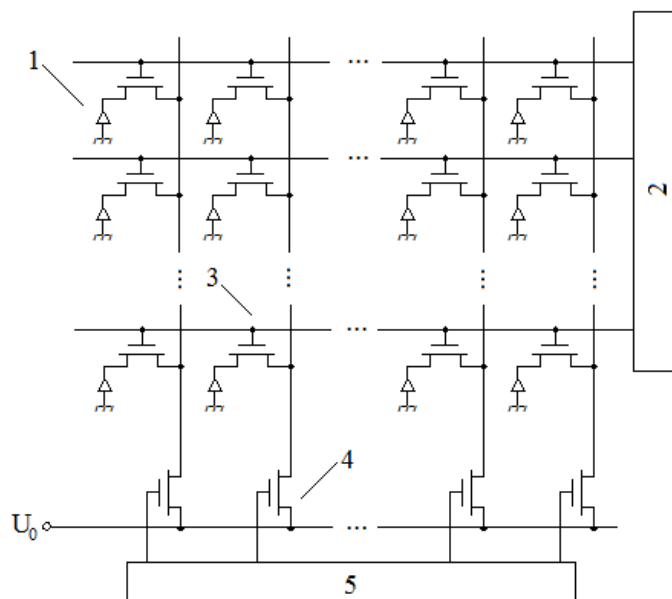


Figure 1.25. Schottky matrix device with a reading structure in the form of MOS-keys: 1 - Schottky diodes; 2 - vertical shift register; 3 - vertical MOS - keys; 4 - horizontal MOS - keys; 5 - horizontal shift register

Before the signal accumulation starts, the Schottky diodes are charged to a certain negative potential U_0 . After the accumulation time has elapsed, a vertical shift register is used to connect the selected line of sense elements to the signal buses and a horizontal shift register is used to connect the signal vertical buses in turn to the common signal readout bus. The output signal is proportional to the charge injected by the selected element into the signal bus. Developed by Mitsubishi

64x64 - element matrix PtSi Schottky diodes with MOS switches has a fill factor of 56% [21]. The increase in fill factor is achieved by reducing the surface area occupied by the signal buses compared to parallel shear CCD registers [64].

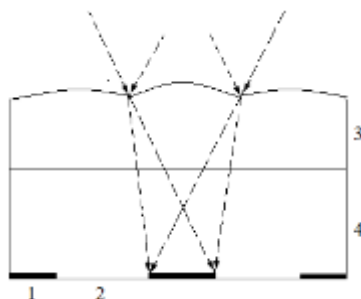


Fig. 1.26. Schematic diagram of radiation propagation in a photosensitive matrix with a refractive optical plate: 1 - photosensitive surface; 2 - insensitive surface (CCD register area); 3 - optical plate; 4 - multielement monolithic matrix

To increase the fill factor of a matrix, an optical refractive plate made of an IR-transparent material (silicon, germanium) that is placed in direct contact with the surface of the matrix through which the receiving elements are illuminated can also be used. This plate must change the course of the beams in such a way that the radiation is focused only on photosensitive areas of the matrix (figure 1.26) [65].

In their usual topology (fig. 1.23), the distance between the sensitive elements is large only in one coordinate, and in another, these elements are located very close to each other, so that the "dead zones" area is small and the direction of the beams, can only be changed in one plane. For this reason, a refractive optical plate has a variable profile only in one section and is plane-parallel in the other (perpendicular) section. The radius of curvature of the surface in the variable profile section

is determined by the size of the sensitive elements of the matrix, the aperture angle of the beam incident on the multi-element matrix and the refractive index of the material of which the refractive plate is made.

For example, for an aperture angle of 45° and a sensing element matrix of size $55 \times 59 \text{ } \mu\text{m}$ (distance between the centres of the neighbouring elements is $160 \text{ } \mu\text{m}$), the radius of curvature is $197 \text{ } \mu\text{m}$, with a total thickness of the refractive plate of silicon and monolayer of silicon of the multielement matrix being $261 \text{ } \mu\text{m}$. A refractive surface with these parameters can be obtained by machining the silicon with a diamond cutting tool. Because of the high refractive index of germanium, the radius of curvature in a germanium refractive plate can be made large, however, germanium is a more brittle material and therefore machining its thin layers, even more difficult [66].

The use of refractive plates at the input of a multielement receiver allows the elimination of "dead zones", increasing the fill factor and thereby increasing the sensitivity of matrices almost twofold. In addition, the ability to redistribute the detected radiation from insensitive areas to photosensitive areas opens up greater opportunities for the design of highly sensitive arrays, since the requirement of providing a large fill factor ceases to be a defining parameter. Obviously, this method of increasing the fill factor can be used not only for multielement matrices on Schottky diodes, but also for other matrices, where part of the focal plane, is not photosensitive. In the future, as the manufacturing process of silicon multielement matrices improves, the need for special refractive plates may disappear, because the irradiated surface of the monolithic layer of the multielement receiver can be immediately given the desired profile. In this case, the sensitivity of the matrices will additionally increase due to the elimination of losses of the registered radiation at the boundary between the refractive plate and the monolithic surface [67-69].

1.3. Parameters of Schottky matrix receivers

Dependence of signal/noise ratio for one-dimensional ruler of 256 photosensitive elements on PtSi diodes on radiation intensity of absolutely black body at temperature 500^0 K in spectral region $3,4\div 4,2\text{ }\mu\text{m}$ was investigated; signal integration time - 35 ms. The irradiation was performed through the silicon surface. Since the surface is not enlightened, the reflection loss was as high as 30%.

A signal-to-noise ratio of unity was obtained at an irradiance of $4,5\cdot 10^{-7}\text{ W}\cdot\text{sm}^{-2}$, which corresponds to an individual cell limit sensitivity of $8\cdot 10^{-12}\text{ W}$. The signal increased linearly with irradiance, up to values of $10^{-3}\text{ W}\cdot\text{sm}^{-2}$.

The dynamic range was $5\cdot 10^3$ and the operating temperature of the sensitive elements was 80^0 K . The sensitivity non-uniformity of the elements in the ruler, equal to 0,55%, was determined only by the accuracy of compliance with the geometric dimensions of the sensitive elements. The modulation transfer function obtained with a 25×50 element matrix is shown in fig. 1.27. The MPF value at Nyquist frequency is 60% [70].

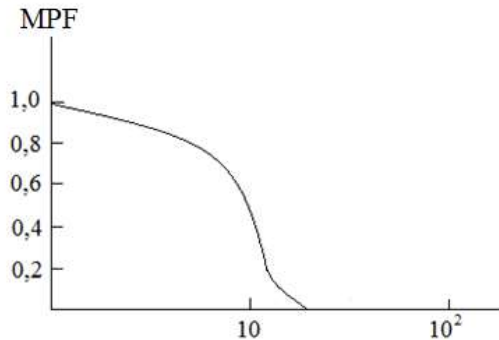


Figure 1.27. Normalised modulated Schottky transfer function in a 25×50 element linear matrix; Δ - Nyquist limit

Sensitivity of two-dimensional matrix of 64x64 elements on PtSi diodes with MOS switches was determined at temperature 77⁰ K and accumulation time, - 19 ms. The injected signal charge was measured by an external preamplifier, due to which, the main source of noise was induced by the coaxial cable connecting the matrix input with the preamplifier.

Under these conditions, the sensitivity of the matrix versus background irradiance difference at 3000 K and ABT at 500⁰ K was $3,5 \times 10^7$ V/W, with a RMS noise value of 5 mV and a dynamic range of 48 dB. The sensitivity with respect to the difference in temperature of the ABT was also measured.

At a background temperature of 300⁰ K, the sensitivity was 10,5 mV/K, which for the above RMS noise value, corresponds to a temperature difference equivalent noise of 0.48⁰ K. Tests have shown that the matrix has no dead elements, the RMS value of the element sensitivity variation is 1.8% and is mainly determined by the flux shielding of the input window. By using this matrix in an optical system with an entrance puRRI diameter of 50 mm and relative aperture of f/1, a thermal image of low-contrast objects in an atmospheric transparency window of 3 to 5 μm is obtained.

By irradiating the photosensitive structure from the side of the silicide layer, images of objects in the spectral range of 0,4÷5,2 μm can be obtained. In the wavelength range up to 1,1 μm (the limiting wavelength of silicon), the radiation detection mechanism is the intrinsic absorption of photons in silicon and the photocarrier separation by the Schottky diode transition field; above 1,1 μm , the absorption of radiation in the silicide layer causes an intrinsic photoemission of photo carriers from metal to semiconductor.

If the thickness of the silicide layer is less than 10 nm, the Schottky matrix, in the visible and near-infrared ranges, is comparable in quantum efficiency to silicon solid-state image transducers [71-72].

Experimental estimation of receiver parameters based on two-dimensional matrix (32x63 elements) of PtSi Schottky diodes for optical system with relative aperture $f/2,0$, at frame frequency 60 Hz and operating temperature 800 K was carried out. At this temperature, due to the dark current, the cell accumulated ≈ 109 electrons per frame time. RMS noise of the cell in the matrix (without taking into account geometrical noise) was $\approx 1,3 \cdot 10^3$ electrons, with RMS noise of the reading CCD-register, $180 \div 250$ electrons per 1 cell. Absolute sensitivity of the photodetector reached $4 \cdot 10^4$ electrons per 1° K at small temperature changes relative to the background 3000 K, which corresponds to the equivalent temperature difference of $0,033^\circ \text{ K}$ for the given value of mean square noise. Such high threshold sensitivity however was not realised in the receiver because of the geometrical noise which was not caused by the scatter of the sensitivity of the individual elements (the RMS value of the scatter was 0,2 to 0,5%) but because of the absolute value of their dark current (charge). Since this geometrical noise is additive, it can be appreciably reduced by subtracting the signal of some reference frame from the signal of the observed frames. In this case, however, temporal noise of the reference frame is converted into spatial noise, which limits the threshold characteristics of the device. With additive correction for dark current variations using only one reference frame signal, the minimum resolvable temperature difference at $1/5$ of the Nyquist frequency was less than $0,1^\circ \text{ K}$. It is argued that by using a reference frame averaged over several reference frames as a signal, the MRI value can be improved by a factor of 2 to 3. The dynamic range of the receiver was 70 dB [73].

A 64x128 element sensor has similar performance. At a frame rate of 60 Hz, using a germanium optical system having an entrance area of 175 mm in diameter and a relative aperture $f/2,35$, the matrix sensitivity was 6.5 mV/K (or $1,3 \cdot 10^4$ electrons per 1° K) for small temperature increments at 300° K relative to

the background. The matrix output voltage at a signal from the 300⁰ K background is 235 mV, the peak noise value (excluding geometric noise) is 1,75 mB (0.29 mV - RMS value); correspondingly, the noise equivalent temperature difference is 0,045⁰ K. The receiver made on the basis of this matrix has small dimensions (35x12,5 sm), high reliability, relatively low cost and provides 0,1⁰ K resolution of the temperature difference, which is enough for most industrial applications. There is no opto-mechanical scanning node. The receiver unit under consideration can be used with a special unit that enables conversion of the Schottky matrix output voltage to a television standard.

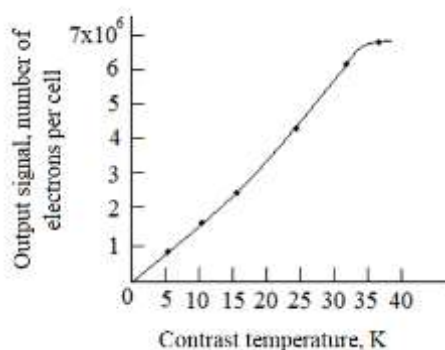


Figure 1.28. Dependence of output voltage of a 160x244 Schottky matrix of PtSi decomposition elements on the contrast temperature relative to 300⁰ K background

A thermal imaging camera has been developed based on the PtSi, a 160x244 element matrix. The matrix, mounted in a 32-RRn ceramic housing, is installed in a Dewar and cooled to a temperature of 77⁰ K with liquid nitrogen. To improve image quality, a special electronic device is used to eliminate the

additive component of geometric noise. In this case, the background signal averaged over 16 consecutive frames is used as a reference frame. Frequency of the frames is 30 Hz. Each frame consists of two interlaced fields of 160×122 decomposition elements. Experimentally determined dependence of sensing element signal on contrast temperature of the object with respect to 300^0 K background for 1/2 optical system (fig. 1.28) and RMS noise, with respect to number of accumulated electrons (fig. 1.29) [74-75].

The temperature sensitivity of the chamber was 2×10^4 electrons per 1^0 K. It was seen that already at the number of accumulated electrons $\approx 10^4$, matrix noise is determined by fluctuations of this value. Under matrix noise measurement conditions (cooled aperture corresponds to f/2.5 aperture) the dark charge is $1,2 \cdot 10^3$ electrons per element, at a frame duration of 1/30 s [76].

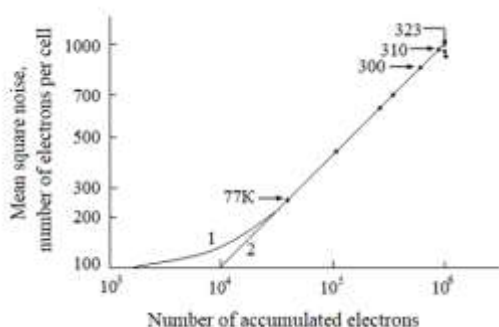


Figure 1.29. Dependence of the RMS noise of a Schottky diode on the number of elements accumulated: 1 - experimental dependence; 2 - theoretical limit for shot noise

Multi-cell receivers on Schottky diodes were used in a non-scanning receiver of a thermal homing head (TGS) of a new generation antitank missile. The missile is designed to be

manually launched by a single operator and operates in a "fire and forget" mode, where the operator does not have to track or aim the missile after firing.

IR receiver is placed in a biaxial gyrostabilized gimbal and consists of optical lens system nodes with relative aperture $f/3$ (entrance aperture diameter 173 mm) and photodetector. The field of view of the optical system is 55° and the angle of change of direction of the optical axis of the system in a suspension is within 25° . The photodetector consists of 64×128 elements of PtSi Schottky matrix, with the working wavelength range of 1 - 5 microns. The photodetector matrix is placed in a dewar and cooled with a Joule-Thomson refrigerator to a temperature of $\approx 85^\circ \text{ K}$, the power dissipated by the Schottky matrix at this temperature is $\approx 20 \text{ mW}$. To reduce the background illumination of the photosensitive elements, a set of cooled apertures and a cooled optical filter are installed at the input of the photodetector. To correct field curvature, a lens is placed in the focal plane; there is no special optical-mechanical scanning unit. Tests have shown that this TGS fully satisfies the requirements [78].

A 512×2 element Pd₂Si Schottky diode array cooled to 120° K has been used for space research of the Earth's surface and imaging of objects in reflected beams in the short-wave IR $1,1 - 2,5 \text{ } \mu\text{m}$ range [79]. The cost per Schottky diode in an oversized matrix is expected to be 0,03 – 0,15 dollars. However, the total cost of an IR receiver on a Schottky matrix will be much higher than that of a solid-state image converter in the visible range, due to the need for IR-transparent optics, a receiver cooling system and special electronic video signal processing devices.

Developers of a new generation of IR receiver systems, using multielement receivers, are faced with a very serious problem: the uneven sensitivity of individual elements in the matrix and the associated geometrical noise. Multielement

receivers, in which photosensitive elements are silicon diodes with Schottky barrier, and conversion of optical radiation into electrical signal is made by internal photoemission at the silicon-metal silicon interface, allow one of the simplest ways to solve this problem [80].

Multi-cell matrices based on Schottky diodes outperform all other types of such matrices in terms of uniformity of sensitivity. Low requirements for semiconductor material quality, allow using standard silicon IC manufacturing technology to produce Schottky receiver arrays. In receiver devices with optical signal accumulation, Schottky receivers are as sensitive as conventional receivers with InSb or HgCdTe sensing elements. They are also comparatively inexpensive and allow the use of virtually convenient refrigeration devices. The first models of non-scanning IR-receiving devices with rather high parameters were created on their base [81].

Good cost-performance parameters of Schottky matrixes themselves, and also the receiver devices on their basis, make such receivers of radiation one of the most perspective, at creation of non-scanning thermal devices on 3÷5 microns range which on quality of thermal image are not inferior to TV, have temperature resolution less than 0,1⁰ K and are suitable for application in THS of small-sized rockets.

1.4 Visible and infrared radiation

The relation between wavelength and frequency of electromagnetic radiation can be written as follows

$$c = \lambda \nu \quad (1.19)$$

where λ is wavelength, μm ; ν is frequency, Hz; c is the speed of light, $3 \cdot 10^8 \text{ m} \cdot \text{s}^{-1}$.

In table 1,4, for point sources of electromagnetic radiation, parameters of energy quantities are presented.

A point source of radiation, the concept is ideal. In fact, all sources are extended. In practice, at large distances, the irradiance from a point source located at a large distance to an object is calculated by the formula:

$$E = I/d^2, \text{ W}\cdot\text{sm}^{-2}\cdot\text{ster}^{-1} \quad (1.20)$$

1.4.1 Thermal radiation

Heated bodies are characterized by a continuous distribution of radiation. In the wavelength spectrum, there is a single maximum whose position depends on the temperature of the source. Such sources are called heat sources and these bodies are normally in a state of thermodynamic equilibrium. The radiation from a flame or electric discharge in gases is not continuous in spectrum but is concentrated in narrow intervals: lines and bands. Such sources are called selective sources [82].

A fundamental concept in the study of thermal radiation is that of the black body (BSE). A jet-black body absorbs all the radiation falling on it at any wavelength.

$$W_\lambda = \frac{2\pi hc^2}{\lambda^5} \cdot \frac{1}{e^{ch/kT\lambda} - 1} \quad (1.21)$$

The formula (1.21) is usually written as follows

$$W_\lambda = \frac{c_1}{\lambda^5} \cdot \frac{1}{e^{c_2/\lambda T} - 1} \quad (1.22)$$

where W_λ is the spectral density of radiation, $\text{W}\cdot\text{sm}^{-2}\cdot\mu\text{m}^{-1}$; λ is the wavelength, μm ; h is Planck's constant, ($6.62 \times 10^{-34} \text{ W}\cdot\text{s}^2$); Absolute temperature in $^\circ\text{K}$; c -velocity of light, ($3 \cdot 10^8 \text{ m}\cdot\text{s}^{-1}$); $c_1 = 2\pi hc^2 = 3,74 \cdot 10^4 \text{ W}\cdot\text{sm}^{-2}\cdot\mu\text{m}^4$; $c_2 = ch/k = 1,44 \cdot 10^4 \mu\text{m}\cdot^\circ\text{K}$, k - Boltzmann constant, ($1,38 \cdot 10^{-23} \text{ W}\cdot^\circ\text{K}^{-1}$).

Figure 1.30 shows the spectral density of ABT radiation in the temperature range from 500 to 900⁰ K.

It can be seen that the total radiant flux emitted by BHT increases rapidly with increasing temperature. The law of this increase can be obtained by integrating Planck equation (1.21):

$$W = \int_0^{\infty} W_{\lambda} d\lambda = \frac{2\pi^5 k^4}{15c^2 h^3} \cdot T^4 \cdot \sigma \quad (1.23)$$

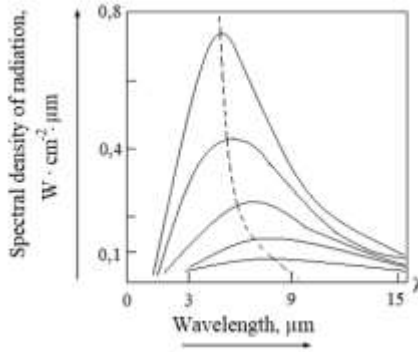


Figure 1.30. Spectral density of BHT emission in the temperature range from 500 to 900⁰ K

Equation (1.23) is called the Stefan-Boltzmann law. As can be seen from (1.23), the total radiation of the ABB increases in proportion to the absolute temperature T^4 . If you differentiate the Planck equation, you get the Wien's law of displacement:

$$\sigma = 5,67 \cdot 10^{-12} \text{ W} \cdot \text{sm}^{-2} \cdot \text{K}^4$$

$$\lambda_{\max} \cdot T = a \quad (1.24)$$

where, λ is the wavelength at which the maximum wavelength distribution of spectral density of radiation is observed; $a = 2898 \text{ } \mu\text{m} \cdot ^0\text{K}$.

It is known from quantum mechanics that thermal radiation is a flux of - photons (Bosev quanta). The energy of a thermal photon is equal to:

$$hc/\lambda = 1,99 \cdot 10^{-19} / \lambda, \text{ W} \cdot \text{s} \quad (1.25)$$

i.e. $1.0 \text{ W} = 5 \cdot 10^{18} \text{ photons} \cdot \text{s}^{-1}$.

1.4.2. Radiation passing through the atmosphere

To design an infra-red system, we usually solve the problem of creating an apparatus according to the scheme shown in figure 1.31.

Next, we will show that a modulator in the circuit is only necessary when using linear receivers. For television matrix receivers, a modulator is not needed. It should be taken into account that almost always (with the exception of the space-to-space case) the radiation from a target passes through the Earth's atmosphere. The radiation is either attenuated or attenuated altogether by scattering and absorption by ozone, carbon dioxide and water vapour molecules.

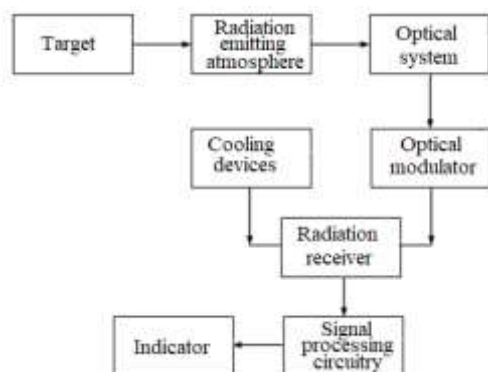


Figure 1.31. Scheme of problem solving

The spectral transmittance of atmospheric radiation, shown in figure 1.32, is measured on a horizontal 1.8 km track at sea level.

The ozone layer at an altitude of about 80 km retards ultrashort ultraviolet radiation. There are transparency windows in the atmosphere, which are standardised in the International Photometric System (IPS), by $\lambda \pm \Delta\lambda$:

- In the visible and early near-infrared bands: B, V, R, I - up to $1.2\text{ }\mu\text{m}$;
- H - range - $(1,6 \pm 0,1)\text{ }\mu\text{m}$;
- K - range - $(2,2 \pm 0,3)\text{ }\mu\text{m}$
- L - range - $(3,6 \pm 0,45)\text{ }\mu\text{m}$
- M - range - $(4,6 \pm 0,5)\text{ }\mu\text{m}$;
- N - range - $(10,0 \pm 2,0)\text{ }\mu\text{m}$;
- Q - range - $(20,0 \pm 0,4)\text{ }\mu\text{m}$.

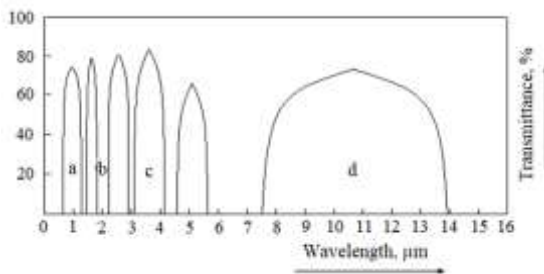


Figure 1.32. Spectral transmission of atmospheric radiation: a - normal ultraviolet, 0.2 to $0.4\text{ }\mu\text{m}$ and visible range, 0.45 to $0.8\text{ }\mu\text{m}$; b - near-infrared, 0.8 to $2.6\text{ }\mu\text{m}$; c - mid-infrared, 2.9 to $6.0\text{ }\mu\text{m}$; d - far-infrared, 8.0 to $14.0\text{ }\mu\text{m}$

Between the transparency bands there are bands of total absorption of IR radiation by the atmosphere. Absorption is mainly due to carbon dioxide CO_2 : $2.6 \div 2.9\text{ }\mu\text{m}$; $4.2 \div 4.4\text{ }\mu\text{m}$ and water vapour H_2O : $5.0 \div 8.0\text{ }\mu\text{m}$ [83]. Aerospace image receptors use one or the other band of transmission or absorption, depending on their purpose.

1.4.3 Optical input windows and image filters

Image receptors which need to be deeply cooled must be isolated from the external environment by placing them in a device called a "cryostat". We will talk about cryostats in more detail in a special section.

Cryostat is a device, in which various phase transformations in gases, liquids or solids are used to provide thermostats at various cryogenic temperatures. In order to allow radiation to pass through, the cryostat is fitted with optical input windows which have the necessary radiation bandwidth. They are also provided with -cooled image filters to form a given operating wavelength bandwidth of the IR receiver. Table shows the most common materials that are used to manufacture the optical input windows of cryostats.

Table 1.1

Materials for cryostat optic entrance windows

Material	Bandwidth, μm	Refractive index
Fused quartz CI	0,3÷4,5	1,43
Leucosapphire	0,3÷5,5	1,67
Irthran-2 (ZnS)	0,8÷15	2,20
Silicon	1,06÷15,0	3,42
Germanium	1,7÷25,0	4,00

The materials listed in the table 1.1 are used to manufacture optical discs of appropriate cross-section, which can withstand vacuum pressure of the atmosphere inside the cryostat with a diameter up to 0.5÷0.6 m. It should be noted that for the visible range quartz of KU and KV grades is also suitable. Monocrystalline germanium is commonly used in the infrared (especially long range) grades GMO-1, GMO-2, GMO-3 and others. They differ from each other only by ingot diameter of initial monocrystal [84].

Due to its high refractive index ($n = 4$), germanium has some disadvantages. For this reason, germanium windows are enlightened by covering them with half-wavelength and quarter-

wavelength layers of transparent material in a given range. In doing so, the coating material has a lower refractive index. Cooled filters are usually made with germanium [85].

The indices (ε , α , ρ , τ) given in table should be considered in more detail. According to Kirchhoff's laws, bodies do not radiate energy in their transparency band. Absorption coefficient:

$$\alpha_{\lambda} = 1 - \tau_{\lambda} - \rho_{\lambda} \quad (1.26)$$

where, τ_{λ} is the transmittance coefficient; ρ_{λ} is the absorption coefficient.

The absorption coefficient is equated to the spectral coefficient of thermal radiation ($\alpha_{\lambda} = \varepsilon_{\lambda}$), i.e. to the spectral degree of blackness. TyRRcal values of ε , α , ρ , and τ are given in table 1.2.

The data in the table 1.2 are averaged from spectral measurements in the range from 2 to 25 μm (CI quartz and leucosapphire, to 6 μm). It is convenient to use a stainless steel disk coated with a thick layer of black matte enamel KS-818 as a cold ABB. The coefficient of thermal radiation of the steel ABB simulator thus obtained, $\varepsilon \geq 0.95$. And to simulate heated ABB, a sRRral heater with a temperature sensor is attached to the rear side of the steel disc.

Table 1.2

TyRRcal values of ε , α , ρ , and τ

Sample material	Optical characteristics			Thermal emission coefficient, ε
	τ	ρ	α	
Germanium GMO GMO	0,49	0,44	0,07	0,13
Quartz CI	0,69	0,15	0,16	0,75
Leucosapphire	0,49	0,24	0,27	0,60

The sun is hot ABB - with a temperature of 6040^0 K ($\lambda_{\text{max}} = 0.48 \text{ } \mu\text{m}$). Jet and rocket nozzles are regarded as grey bodies ($\varepsilon = 0.9$). Materials with low emissivity include well-polished gold, with $\varepsilon \leq 0.02$ and copper, with $\varepsilon \leq 0.05$. For this purpose, the most commonly used globar is a straight tungsten rod in a casing with a radiation aperture, which is cooled with cold water (glabar operating temperature: $T_{\text{gl}} = 1400^0 \text{ K}$). For television tests, the type A source most commonly used is a tungsten filament with a temperature $T = 2856^0 \text{ K}$ [86].

CHAPTER II. BASIC TYPES OF PHOTODETECTORS

2.1 Radiation receivers. General characteristics

IR-radiation receivers are designed to convert energy. Converted infrared radiation is transformed into: blackening of photoemulsion, voltage, electric current, etc. Let's take a look at the main characteristics of IR receivers.

Sensitivity - is the ratio of the change in electrical quantity at the receiver output caused by incident radiation to the quantitative characteristic of that radiation.

Current sensitivity S_I - the measured electrical value of the RR is the strength of the photocurrent.

Volt sensitivity S_V - measured sensitivity when calculating the RR output voltage.

Integral sensitivity - sensitivity to non-monochromatic radiation of a given spectral composition.

Monochromatic sensitivity S_λ - is the sensitivity to monochromatic radiation with wavelength λ .

Static sensitivity - is the ratio of constant values measured at the input and output of a radiation receiver.

Differential sensitivity - is the ratio of small increments measured at the input and output of the radiation receiver.

Quantum yield (for PhDs and other RRs with external photoelectric effect) - is the ratio of the number of photoelectrons escaping from the photocathode into vacuum to the number of photons incident on the photocathode.

Quantum efficiency (for solid-state television photovoltaic transducers) - is the ratio of the number of photogenerated carriers in a semiconductor to the number of incident photons. Quantum yield for solid-state television photovoltaic transducers (SSTPhT) (defined as the ratio of absorbed photons to the number of photogenerated charge carriers), always $\equiv 1$.

Detectability is used when comparing several RRs. The RR with the highest output at a given irradiance is assumed to have the best sensitivity. However, when RRs are compared on their ability to detect the minimum radiation flux, the receiver with the lowest $P_{t.s.}$ value, i.e. the flux equal to the flux which causes the RR to output a signal equal to its own noise, is considered the best receiver. In this case, Jones used the inverse of $P_{t.s.}$ - the detectability of D:

$$D = \frac{1}{P_{t.s.}}, W^{-1} \quad (2.1)$$

Theoretical and experimental studies have shown that the detectability of D, is inversely proportional to the square root of the RR area, i.e:

$$D\sqrt{S_{el}} = const, \quad (2.2)$$

where, S_{el} is the sensing area of the RR, sm^2 .

The noise at the RR output contains many harmonics of different frequencies and it follows that the detectability of D depends on the frequency bandwidth of the measuring instrument. Knowing that the band related noise voltage is frequency independent (an assumption well checked in practice) it follows that the D varies as the inverse of the square root of the frequency band (Δf). Using this, Jones introduced a value of D^* referring to a frequency bandwidth of $\Delta f = 1Hz$ and a RR area of $1sm^2$:

$$D^* = D(S_{el} \cdot \Delta f)^{1/2} = \frac{(S_{el} \cdot \Delta f)^{1/2}}{P_{t.s.}}. \quad (2.3)$$

In the equation, the value of D is measured in $sm \cdot Hz^{1/2} \cdot W$; S - is sm^2 ; Δf is Hz; D^* is the specific detectability [87].

2.2. RR with an external photoelectric effect

The external photoelectric effect was discovered by Hertz in 1887. It was not until 15 years later that Einstein explained the phenomenon.

The energy of a photon is calculated using the formula:

$$E = h\nu = hc/\lambda \quad (2.4)$$

The photon, is absorbed by the photocathode, and gives its kinetic energy to the metal electron. As a consequence, the electron can overcome the work of escape and escape into the vacuum. Thus, the kinetic energy of the photoelectron, is equal to:

$$E' = mv^2/2 = h\nu - \varphi = hc/\lambda - \varphi \quad (2.5)$$

where, φ - is the work of exit of the photocathode surface.

The lowest work of escape among metals (1.9 eV), is in cesium. Since the photon energy depends on the frequency, there is a concept of "redshift boundary" for the photoelectric effect:

$$\lambda_c = 1,24/\varphi,$$

where, φ is measured in eV. Nowadays antimony-zeum and semitransparent photocathodes are created, the quantum yield of which reaches 10÷12% of cesium, and the "red border" is 0,65 μm . In modern photocathodes, the "red edge" is somewhat larger.

2.3. Photoconductive RR

In semiconductors operating in the IR range, various types of internal photoelectric effects occur. In these semiconductors

the electrical resistivity at $T = 300^0 \text{ K}$, ranges from $1 \cdot 10^{-2}$ to $1 \cdot 10^9 \text{ Ohm} \cdot \text{sm}$. Thus, we can say that semiconductors are between good conductors ($\approx 1 \cdot 10^{-6} \text{ Ohm} \cdot \text{sm}$) and insulators (from $\approx 1 \cdot 10^{14} \text{ Ohm} \cdot \text{sm}$ to $\approx 1 \cdot 10^{22} \text{ Ohm} \cdot \text{sm}$). From these considerations it follows - at absolute zero ($T = 0^0 \text{ K}$), pure and perfect crystals of most semiconductors become insulators. Their characteristic semiconductor properties are found at:

- 1) heat exposure;
- 2) the presence of impurities;
- 3) presence of defects.

Intrinsic conductivity. If we exclude the region of ultra-low temperatures, high purity semiconductors exhibit the so-called intrinsic conductivity - to be distinguished from impurity conductivity of less pure samples. In this case, we introduce the notion of the temperature region of natural conduction of a semiconductor, the region of temperatures where the electrical properties of a semiconductor are not significantly affected by the presence of impurities in the crystal. Fig. 2.1 shows a diagram explaining the occurrence of intrinsic conductivity in semiconductors. It is obvious from the diagram that there is no conduction at $T = 0^0 \text{ K}$.

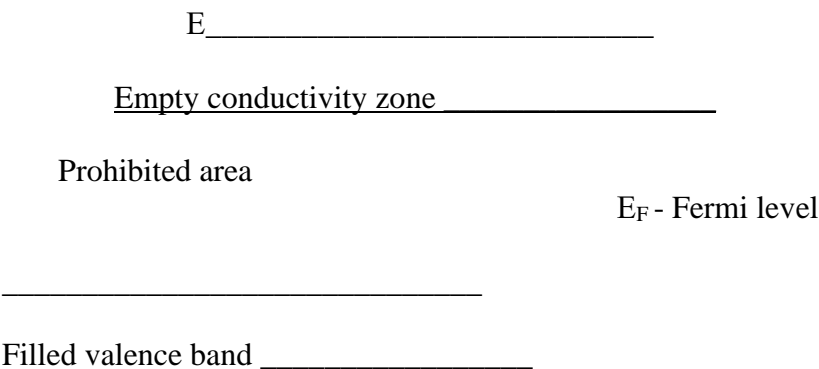


Figure 2.1. Schematic of electronic energy zones

When the valence band is full, all states of the conduction band are free. When the temperature increases, the conductivity of the semiconductor increases. This phenomenon is caused by thermal excitation of electrons, causing them to move into the conduction band, where they can move around. And in their place in the valence band, positively charged “holes” remain.

In the presence of an electric or magnetic field, the holes move in the same way as electrons, but in the opposite direction. In an unadulterated semiconductor, the transition of an electron into the conduction zone creates an electron-hole pair of charge carriers, i.e., conduction is increased. This is roughly how germanium and silicon behave. When the temperature of a semiconductor is below its own conduction region, its electrical properties are determined by the impurities. In this case we are talking about impurity or non-impurity conductivity. The valence electrons gain energy from the photons, and this energy is sufficient to create electron-hole pairs. As a result, the conductivity changes under the influence of photons. Such photodetectors are called photoresistors.

We considered phenomena, which are based on the external photoelectric effect, where there is a long wavelength limit. In photoresistances, there is also a long-wavelength limit, beyond which there is insufficient photon energy to create a vapour. Threshold wavelength:

$$\lambda_c = 1,24/E_d \quad (2.6)$$

All of our known intrinsic conductivity receivers have an $E_d \geq 0.18$ eV (at $T = 300^0$ K), so the red edge is $\lambda_c \geq 7.0$ μm . Semiconductors with intrinsic conductivity include: indium arsenide, lead selenide, germanium, lead sulphide, indium antimonide, silicon.

In order to shift the threshold towards longer wavelengths, materials with a narrower band gap are needed. The most

common means of lowering E_d is by doRRng the base material with other materials. When reducing the E_d by doRRng, the semiconductors produced are called non-potential or impurity semiconductors. In a non-essential semiconductor, the conductivity is determined by just one type of carrier: electrons in n-type materials and holes in p-type materials.

2.4. Photovoltaic receivers or receivers with p-n junction

Let's consider a scheme (fig. 2.2), where a photovoltaic RR is shown. As it can be seen from the figure, photovoltaic RR contains p-n junction (E_F - Fermi level; N_a - acceptor concentration; N_d - donor concentration; W - volume charge zone).

There is no bias applied to the p-n junction. If a reverse bias $U_{r.b.}$ is applied to the p-n junction (figure 2.3), the energy diagram will change. In this case, the E_F will be lower in the n-junction.

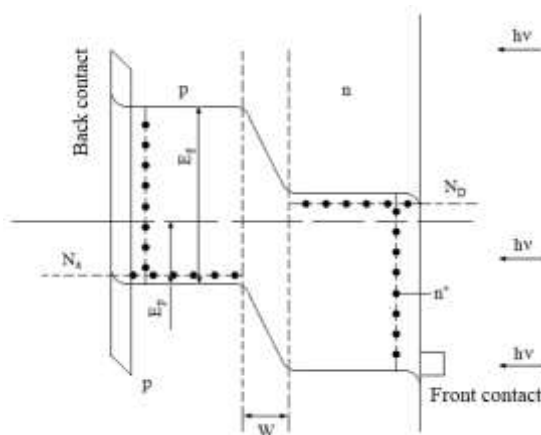


Figure 2.2. Photovoltaic RR with p-n junction

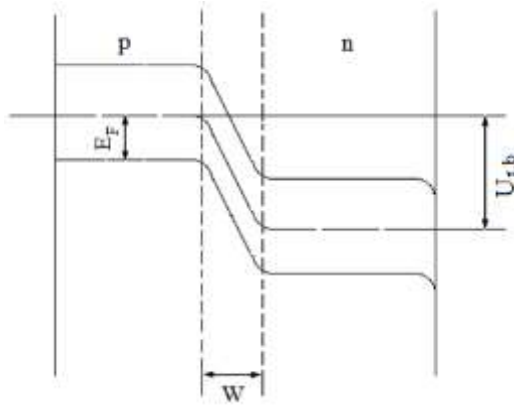


Figure 2.3. Energy diagram for reverse bias $U_{r.b.}$

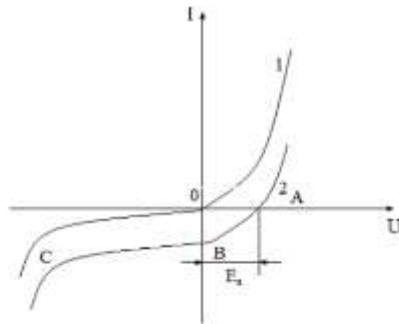


Figure 2.4. Volt-ampere characteristic of a photovoltaic RR (receiver of radiation is shielded from incident radiation)

Figure 2.4 (curve 1) shows the volt-ampere characteristic of a photovoltaic RR. In this case the RR is shielded from incident radiation. The incident photons shift curve 1 to position 2 and the result is the photo emf E_a . The graphs show that during the operation of a flat RR, the position of the operating point can be chosen over a wide range of bias voltages. In the first case, we select the operating point A as the operating point. In this

case, the voltage drop across the RR, corresponds to an open circuit mode. A voltmeter with a large resistance can be included in the circuit to measure the voltage drop across it. This voltage drop corresponds to the power of the voltage drop. In the second case, load the RR with a low resistance, ammeter. In this case, the operating point will be point B - the so-called short-circuit mode. In the third option, we apply a reverse bias to the RR - this corresponds to point C. The RR then becomes a high impedance element and the signal voltage is taken from a load resistor which is connected in series with the RR [89].

If the photovoltaic RR is short-circuited then it has maximum sensitivity, with zero bias voltage - this corresponds to point B. The photovoltaic RR is a self-generating device that does not need a power supply. It has been proven that the noise of photovoltaic RRs is lower than that of photoresistors (by 40%). This phenomenon is explained by the fact that in photoresistors, the generation-recombination noise (GRN) is generated by carriers of both signs, while in photovoltaic RR, only one sign is generated.

2.5. Schottky barrier receivers

In 1938, Schottky suggested that the potential barrier is created by a stationary spatial charge in the semiconductor rather than by an intermediate chemical layer between the metal and the semiconductor. The energy diagrams for a metal-semiconductor n-type contact are shown in figure 2.5.

Let the metal and the n - type semiconductor are not connected and are not in thermodynamic equilibrium. A diagram of this phenomenon is shown in figure 2.5,1. When they are electrically connected, some charge will flow from the semiconductor to the metal and thermodynamic equilibrium will be established. Then the Fermi levels in both materials will equalize. Because the E_F in the semiconductor will decrease

relative to the metal E_F by an amount equal to the difference of the corresponding works of yield.

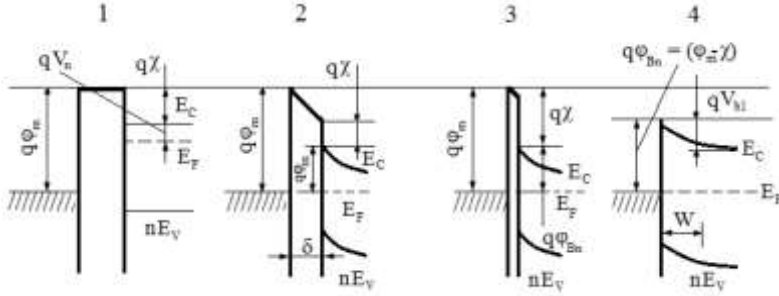


Figure 2.5. Energy diagrams of metal-semiconductor n-type contact

For metal, the work of output is equal to $q\phi_M$. In a semiconductor, the work of output is $q(\chi + V_n)$. The value $q\chi$ is called the electron affinity. The value of electron affinity is found as the difference between the energy for the conduction zone E_C and the electron level in the vacuum, and qV_n is the position of the Fermi level in the forbidden zone of the semiconductor. The difference $q\phi - q(\phi + V_n)$, is called the contact potential difference (Fig. 2.5, 2). As δ decreases, the negative charge on the metal surface increases and an equal positive charge is formed in the semiconductor (fig. 2.5, 3). Since carrier concentrations are relatively low, this positive charge is distributed in some region near the semiconductor surface. If δ becomes comparable to the interatomic distance and the gap becomes permeable to electrons, we have a limiting case (fig. 2.5, 4). The barrier height in this case, is equal to the difference between the yield work of the metal and the semiconductor [90]:

$$q\phi_{Bi} = q(\phi_m - \chi) \quad (2.6)$$

where ϕ_{Bi} is the contact potential difference.

2.6. Depleted layer

When a metal is brought into contact with a semiconductor, the valence conduction band of the semiconductor occupies a certain energy position in relation to the Fermi level of the metal. Fig. 2.6 shows (at different offsets) zone energy diagrams of metal-semiconductor n-type contacts: a) at thermodynamic equilibrium; b) at direct bias; c) at reverse bias.

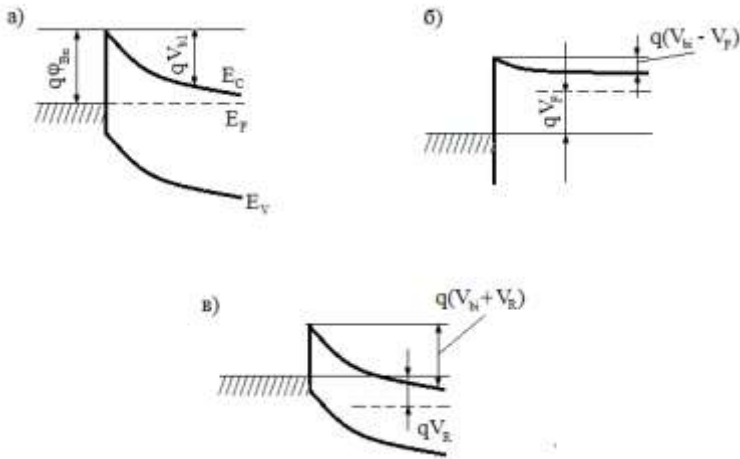


Figure 2.6. Zone energy diagrams of metal-n-type semiconductor contacts

Figure 2.7 illustrates the Schottky barrier energy diagram with respect to the electron level in a vacuum: $\Delta\phi_R$ - barrier lowering at reverse displacement; $\Delta\phi_F$ - barrier raising at forward displacement; $q\Phi_{Bn}$ - barrier height at thermodynamic equilibrium; $q\Phi_{B0}$ - barrier height in absence of field.

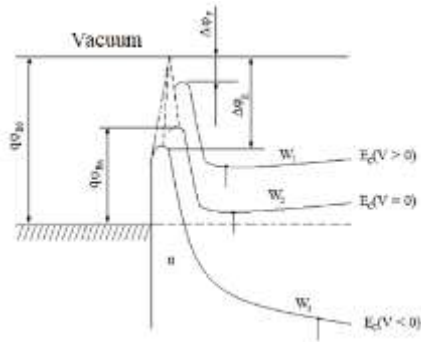


Figure 2.7. Schottky barrier energy diagram relative to the electron level in a vacuum

From the diagrams shown in fig. 2.7 it is clear that in the vicinity of the metal in the semiconductor a special layer with depletion of the basic carriers is formed. The electron in the metal, under the action of the incident photon acquires energy greater than the height of the potential barrier $\Delta\phi_{Bn}$ and enters the semiconductor, creating a photocurrent.

2.7. Detection capacity and threshold flow

A limitation of the sensitivity of radiation receivers is its noise. Noise has a number of components. First consider the signal flux. When the radiation power from a circuit is small, W_λ fluctuates. The law of dispersion of fluctuations may be applied to it.

Einstein proved in his works that the variance of fluctuations, or the mean square of the deviation $\overline{\Delta E^2}$ from the mean photon energy \bar{E} , obeys the following relation:

$$\overline{\Delta E^2} = \overline{E^2} - (\overline{E})^2 = kT^2 \frac{\partial \bar{E}}{\partial T} \quad (2.7)$$

By identifying, $\overline{E_C W_\lambda}$ we differentiate equation (2.2), and obtain the following expression:

$$\frac{d\overline{W_\lambda}}{dT} = \frac{2\pi h c^2}{\lambda^5} \cdot \frac{e^{ch/kT\lambda} \cdot \frac{ch}{k\lambda} \cdot \frac{1}{T^2}}{\left(e^{ch/kT\lambda} - 1\right)^2} = \frac{2\pi h^2 c^3}{\lambda^6} \cdot \frac{1}{kT^2} \cdot e^{-\frac{ch}{kT\lambda}}$$

Substituting this expression into (1.34), we obtain:

$$\overline{(\Delta W_\lambda)^2} = \frac{2\pi h^2 c^3}{\lambda^6} \cdot e^{\frac{ch}{kT\lambda}} \quad (2.8)$$

For the infrared range, at $T = 80 \div 900^0$ K, this value is very small. In this case, the noise is not determined by fluctuations in the special flux (for a flux from a point ABB distant by ∞), but by the standard deviation from the mean value $\overline{W_\lambda}$. Einstein proved that: $\overline{\varepsilon^2} = 2\chi T^2 \frac{d\overline{E}}{dT}$, where ε is the photon energy, Boltzmann identified $2\chi = k$.

In fact \overline{W} is $\overline{W(\lambda, T)}$. The fraction of energy falling in the interval $\lambda_{\max} \pm \Delta\lambda$ will be small in the small solid angle (where, $\Delta\lambda \rightarrow 0$, with $\varepsilon < 1$), and since differentiation is performed only on T the round (partial) derivatives $\frac{\partial E}{\partial T}$, can be replaced by straight lines:

$$\overline{\Delta E^2} = kT^2 \cdot \frac{d\overline{E}}{dT}$$

Einstein proved that the variance of the fluctuation, the deviation from the mean value of the \overline{n} number of photons, satisfies the relation:

$$\overline{\Delta n^2} = \overline{n} \quad (2.9)$$

Thus, the mean square fluctuation of the photons, will be:

$$\sqrt{\Delta n^2} = \sqrt{n} \quad (2.10)$$

Note relations (2.9) and (2.10). They are extremely important for determining the threshold sensitivity of RR. The expression (2.9) proves that small photon fluxes obey a Poisson distribution. Let's return to formula (2.1). Here the notion of specific D^* of detectability is introduced. We find the minimum flux value P_{th} , at which the output signal is equal to RR noise. The value Δf can only be calculated when an electrical measurement circuit is necessarily connected to the RR. The bandwidth of this circuit, is determined by the time constant, RR:

$$\Delta f = 1/2\tau. \quad (2.11)$$

On the RR, together with the radiation flux from the measuring circuit, the background flux falls. The irradiance of the background flux, E_b , is many times greater than the irradiance of the target on the P_C/S_{el} element (P_S -signal flux from the target, the projection of which is preferably equal to the area of the RR element). This projection is called the scattering circle of the optical system (OS) and forms the image of the target on the RR element. Ideally, it is necessary that:

$$S_{el} \approx \frac{\pi}{4} d_c^2, \quad (2.12)$$

where, d_c^2 is the OS scatter circle.

Consider the brightness of the background B_f on which the target is observed. Then in the focusing plane of the optical system, the irradiance from the background is: $B_f \cdot \pi \cdot \sin^2 A$; where, A is the exit aperture angle of the lens. The background brightness is calculated as follows:

$$E_f = \frac{\pi}{4} \cdot \tau \cdot \left(\frac{D}{F'}\right)^2 \cdot B_f, \quad W \cdot sm^{-2}, \quad (2.13)$$

where τ – transmittance OS; D - diameter of entrance pupil OS; F' - focal length OS.

Now, using formula (2.6), let's calculate the flux falling on PI from the radiation of ABB, located from RR not at infinity, but at some distance (fig. 2.7). R - distance from ABB to RR; D - diameter of entrance pupil; α - angle constricted by D ($R \gg D$).

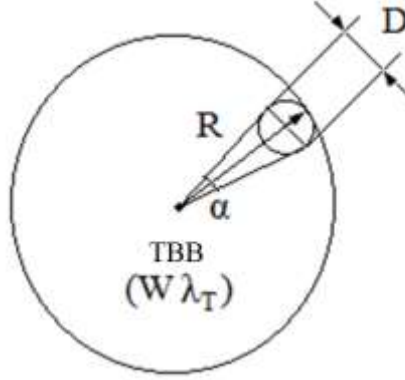


Figure 2.7. The flux reaching the RR from the incident ABB radiation at distance R

At a small solid angle α , equal to $(\pi/4) \cdot (D^2/R^2)$ the energy falling through the OS onto the RR is calculated as follows:

$$R_{\lambda_{max}}^{\alpha} = \frac{\pi^2 hc D^2 \tau}{2 R^2 \lambda_{max}^5} \left(e^{hc/kT\lambda_{max}} \right)^{-1}. \quad (2.14)$$

For ABB the value $\left(e^{hc/kT\lambda_{max}} \right)$ is found from the conditions: $\lambda_{max} = 3-14 \mu m$ and not very high temperatures, $T =$

80-900⁰ K. In this case $\left(e^{hc/kT\lambda_{max}}\right) \gg 1$. By performing some transformations, we obtain:

$$R_{\lambda_{max}}^{\alpha} = \frac{\pi^2 h c \tau}{2 \lambda_{max}^5} \left(\frac{D}{R}\right)^2 \cdot e^{-hc/kT_{max}}$$

Conclusions:

1. The spectral density of radiation hitting the radiation receiver is proportional to the entrance pupil area of the optical system and inversely proportional to the square of the distance to the source;

2. The incident flux in the PI focusing plane is independent of the focal length of the optical system.

The following equation can be written for η the quantum efficiency of a RR:

$$\eta = \frac{\overline{Ne^f}}{N_f} \quad (2.15)$$

In equation (2.15) $\overline{Ne^f}$ - the average number of photogenerated carriers; $\overline{N_f}$ - the average number of photons incident on the RR surface. The value P_{th} . corresponds to the number of incident photons from a useful signal equal to the noise:

$$\overline{Ne_{nop}^c} = \sqrt{\eta_{max} (\Delta N_f)^2 \cdot S_{el}} = \sqrt{\overline{N_f} h_{max} S_{el}}.$$

It is known that, photon energy $E = h\nu = hc/\lambda_{max}$, hence $\overline{Ne_{th}^c} = P_{th} \frac{\lambda_{max} \eta_{max}}{hc}$, then:

$$P_{th} = \frac{hc}{\lambda_{max}} \sqrt{\frac{\overline{N_f} S_{el}}{\eta_{max}}}. \quad (2.16)$$

Taking formula (2.1) $D^* = D(S_{el}\Delta f)^{1/2} = \frac{(S_{el}\Delta f)^{1/2}}{P_{th}}$ and $\Delta f_{g.r.n}$ - frequency bandwidth of the generation-recombination noise from the background, we obtain:

$$P_{th} = \frac{\sqrt{S_{el}\Delta f_{g.r.n}}}{D^*} \quad (2.17)$$

Since the fluctuations from the strong flux are very small, the background irradiance, which creates a signal at the RR output, thresholds the sensitivity of the RR:

$$P_{th} = \frac{hc}{\lambda_{max}} \sqrt{\frac{S_{el}N_f}{\eta_{max} \cdot 2T_H}} \quad (2.18)$$

here, $\Delta f = \frac{1}{2T_H}$ - the equivalent noise bandwidth of the generation-recombination noise of photogenerated carriers from the background. In this case there are no other noise $\sqrt{N_f}$ components, according to (2.9) the background flux fluctuation. We call this mode the RR sensitivity limitation by background fluctuations.

Normalized threshold D^*_{BLIP} sensitivity of RR is defined as D^* of radiation receivers with $\eta = 1$ in the whole spectral band of its sensitivity. And also noise determined only by fluctuations of the flux falling from the background; - Background Limited Infrared Photoconductors - extreme sensitive mode (achievable only in an ideal receiver) [91].

2.8. Signal and noise

When we read a signal from a data logger connected to the PI output, we have a set of random signal values from which we sample. At the output of the amplifier the electrical signals obey a Gaussian normal distribution. For the distribution of random variables x , the Gaussian differential law is of the form:

$$P(x) = \frac{1}{\sigma\sqrt{\pi}} \exp\left\{-\frac{[x-M(x)]^2}{2\sigma^2}\right\} \quad (2.19)$$

In the process in question, the mathematical expectation or mean value of a random variable, in our case the signal, is the sum of the products of all possible values of x_i by their corresponding probabilities P_i :

$$(x) \sum_{i=1}^n x_i p_i \text{ или } M(x) = \frac{\sum_{i=1}^n x_i p_i}{\sum_{i=1}^n p_i} \text{ т. к. } \sum_{i=1}^n p_i = 1 \quad (2.20)$$

The mathematical expectation for a continuous random variable is calculated as follows:

$$M(x) = \int_{-\infty}^{\infty} x p(x) dx. \quad (2.21)$$

The variance of a discrete random variable is the mathematical expectation of the square of the deviation of the value of the random variable from its mathematical expectation:

$$D(x) = M\{[x - M(x)]^2\} = \sum_{i=1}^n [x - M(x)]^2 P_i = M(x^2) - [M(x)]^2 \approx \frac{\sum_{i=1}^n [x - M(x)]^2}{n-1}.$$

The value $(n-1)$ is written only when the number of realizations in the sample ≤ 25 .

The variance of a continuous random variable can be calculated using the formula:

$$D(x) = \int_{-\infty}^{\infty} [x - M(x)]^2 P(x) dx = \int_{-\infty}^{\infty} x^2 P(x) dx - [M(x)]^2 = \sigma^2 \quad (2.22)$$

Let a number of RR (e.g. photoresistors) be placed on the same substrate. Figure 2.8 shows a RR with electrical (ohmic) contacts. Each RR consists of: a PdS, PdS or HgCdTe film having electrical (ohmic) contacts 2 at the edges of the films; a common bus 3; individual outputs 5 at the other ends connected

to a shift register 6; an amplifier 7 and an oscilloscope 8 having a line extraction unit and an electronic memory tube. In the circuit, the photoresistor is supplied with a bias voltage from source 4. This entire eight-element ruler is made using the same technology.

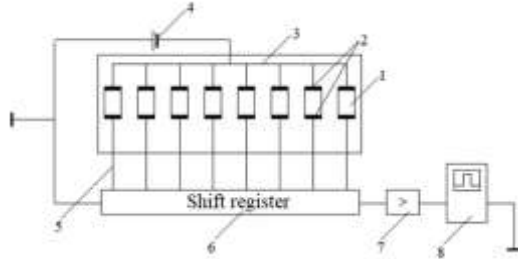


Figure 2.8. RR with electrical (ohmic) contacts

Next, it is cooled in an optical cryostat to a temperature of $T=170^0$ K. With the output optical window of the cryostat closed using a metal shutter, the intrinsic noise of the PI is measured from the ruler elements.

The mathematical expectation for all PI elements is taken to be zero. And if the condition ≥ 25 arbitrary realizations of the output signal readout are satisfied, then we will see on the oscilloscope (fig. 2.9) the readout corresponding to the variance of the intrinsic noise.

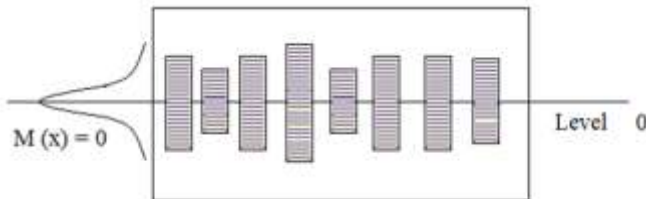


Figure 2.9. Sampling set corresponding to intrinsic noise variance

The reason for this is the variation in film RR parameters. Each element has a different intrinsic noise value. The probability of occurrence of a particular signal value during the instantaneous realization is governed by Gaussian law [92] (fig. 2.10).

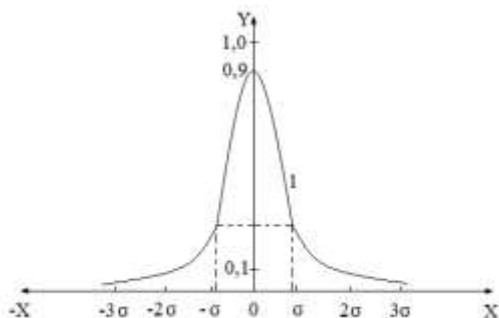


Figure 2.10. Own noise of each RR element

As can be seen from the figure, the Gaussian curve is symmetrical about the OY axis. The RMS deviation of the signal amplitude is plotted on the OX axis. The deviation of the amplitude $\sigma = \sqrt{D(x)}$ is taken from the individual element from an average value of zero. The RMS value of the eigen-noise is $\sigma_{e.n.}$.

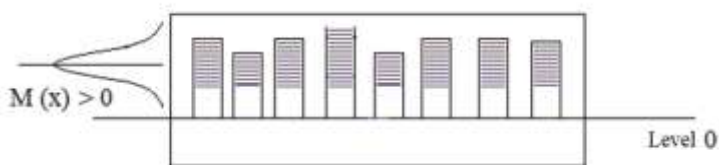


Figure 2.11. Picture on the oscilloscope screen

In the next step, open the cold shutter and project a flux of infra-red radiation onto the ruler elements. The infrared radiation flux must be within the spectral sensitivity of the RR.

In this case the picture corresponding to figure 2.11 appears on the oscilloscope screen.

Taking average values of the signal from the elements, we can make sure that they correspond to the same exposure of receivers to infrared radiation (with different threshold sensitivity of the elements).

At each vertex of the signal pulse there are noticeable "noise tracks" determined by the total noise from RR, generation and recombination of photogenerated charge carriers, radiation fluctuations:

$$\sigma_n = \sqrt{\sigma_{n.o}^2 + \sigma_{g.r.n}^2 + \sigma_{n.f}^2} \quad (2.23)$$

In formula (2.23), the main contribution to the total noise is the generation and recombination noise due to the background IR illumination. The Gaussian curve shown in figure 2.12 for the case shown will have an offset in the positive direction of the signal amplitude.

The signal-to-noise ratio is denoted by ψ :

$$\psi = U_s / \sigma_n. \quad (2.24)$$

In order to detect targets reliably, the following condition is necessary: the value of ψ must be as large as possible:

$$\psi \geq 6 - 12$$

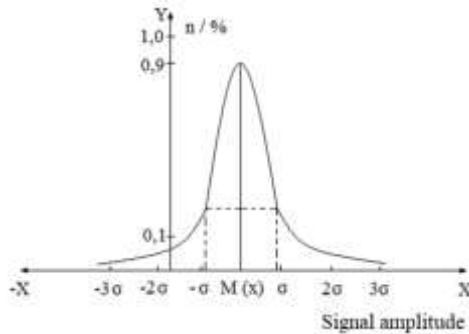


Figure 2.12. Gaussian curve

The exact value of the σ_n total noise of the radiation receivers, is determined by the formula:

$$\sigma_n = \sqrt{\sigma_{n.o}^2 + \sigma_{n.f}^2 + \sigma_{g.r.n}^2 + \sigma_{n.u.s}^2 + \sigma_{n.u.d.s}^2} \quad (2.24)$$

The formulae are marked: $\sigma_{n.u.s}$ - sensitivity non-uniformity; $\sigma_{n.u.d.s}$ - noise from the non-uniformity of the dark signal. The last two components are deterministic. They can be subtracted by computer processing of the video signal.

2.9. Noise components

The noise components are different for different PI:

1. Thermal noise. The variance of this noise in the Δf band can be calculated using the formula:

$$(\overline{V_T})^2 = 4kTR\Delta f, \quad (2.25)$$

where, R is the equivalent noise resistance.

When dealing with photoresistive and photovoltaic solid-state RR, in deep cooling, thermal noise is usually neglected.

2. Generation and recombination noise. In semiconductors at intermediate frequencies, generation and recombination noise is a major source of noise. Generation and recombination noise is noise associated with fluctuations in the generation and recombination of charge carriers.

3. Radiation (photon) noise. In the Δf frequency band at T_b background temperature, the dispersion of fluctuations in the radiation power from the background, and the $\epsilon_{e.f}$ emission factor, at the RR are calculated as follows:

$$\Delta\Phi_r^2 = 8\epsilon_{e.f}kT_f^5\sigma S_{el}\Delta f. \quad (2.26)$$

2.10. Current and volt sensitivity. Dynamic range

The current and volt sensitivities are of utmost importance in determining the magnitude of the output signal from a RR. For photoresistors based on PdS, PdSe or PdSe typical values of current (or ampere-watt) sensitivity S_I are achieved $1\text{-}2 \cdot 10^5$ for matrices with $T_{\text{cadr}} = 0.1$ s. And photodiode receivers have volt-watt sensitivity – S_V (W/Vt).

For any RR the most important parameter is the dynamic range. This range covers the region of input flux values in which the linear (or close to it) dependence of the input signal on the value of the background irradiance or input flux is maintained. Most commonly, dynamic range is defined as the ratio of U/σ_n : the ratio of the signal saturation of the light-signal characteristic, to the RMS value of the RR noise. If the irradiance at the OS entrance pupil from the background exceeds the corresponding irradiance at the OS entrance pupil 100-1000 from the target, the situation is greatly complicated. The background irradiance at the entrance pupil of an OS creates the irradiance in the OS plane of focus on the RR surface and is calculated using formula 2.26. In turn, it depends on the focal length F .

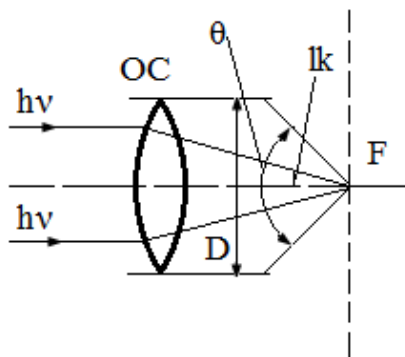


Figure 2.13. Large output aperture OS

In addition to the external background, an instrumental internal background is also observed. Because, with uncooled OS and the inlet optical part of the RR cryostatic device, forms a "gray" cavity. The "grey" cavity has a temperature $T = 300^0 \text{ K}$ (figure 2.13).

For an OS with a large output aperture, the value of the internal background also depends on the focal length, which can be determined by the formula:

$$A = D/2F \quad (2.26)$$

If, θ - is half the viewing angle of the RR surface from any point in the space of the RR posterior segment, then the solid angle Ω in which the background radiation of the OS posterior segment is absorbed is equal:

$$\Omega = \pi \cdot \sin^2 \theta. \quad (2.27)$$

In the geostationary orbit (about 40000 km) the typical values at $\psi \geq 3$ for the IR receiver required to detect the 1st stage of ICBM launch have the value $P_{th.} = 5 \cdot 10^{-13} \text{ W/element}$. The irradiance from the background of the daytime Earth ($E_F \approx 1 \cdot 10^{-6} \text{ W/sm}^2$), and the hardware background ($E_F \approx 1 \cdot 10^{-6} \text{ W/sm}^2$) is taken into account. If we take an element with area $S = 30 \times 30$ microns, then from the total background on the PI, gets a flow equal to $RF \approx 2 \cdot 10^{-11} \text{ W/element}$.

Thus, we obtain: dynamic range should be not less than 120. With values $\psi \geq 6-10$ usually required, it should be ≥ 1000 . The required dynamic range margin should be at least 100 times larger. To select targets and give target indications, it is necessary to operate with values $\psi \geq 10-100$.

Now it is necessary to determine the signal-to-noise ratio for the considered case in the bands $2.7 \text{ } \mu\text{m}$ and $4.3 \text{ } \mu\text{m}$. The background (external and internal) irradiance at:

1) in the 2.2 μm band, we will take it to be $E_{F2,7} = 2 \cdot 10^{-6} \text{ W/sm}^2$,

2) in the 4.3 μm band, we take it as $E_{F4,3} = 2 \cdot 10^{-5} \text{ W/sm}^2$.

In this case, $P_{\text{nor},2,7}$ relates to $P_{\text{nor},4,3}$ as 1:5, since $P_{\text{nor},2,7} \approx 5 \cdot 10^{-13} \text{ W/element}$, $P_{\text{nor},4,3} \approx 2 \cdot 10^{-12} \text{ W/element}$. Knowing that, $E_{\text{phot},2,7} = 7.4 \cdot 10^{-20} \text{ C}$; $E_{\text{phot},4,3} = 4.6 \cdot 10^{-20} \text{ C}$; and the element area will be $S_{\text{el}} = 1 \cdot 10^{-5} \text{ sm}^2$. Then we find: $1 \text{ W}_{2,7,\mu\text{m}} \approx 1,3 \cdot 10^{19} \text{ photon/element} \cdot \text{s}$, $1 \text{ W}_{4,3\mu\text{m}} \approx 1,3 \cdot 10^{19} \text{ photon/element} \cdot \text{s}$. Quantum efficiency of diodes based on Schottky barrier $\eta = 0.01$ at 2.7 μm (PtSi) $\eta=0.01$, at 4.3 μm (PdSi). Thus $P_{f,2,7} = E_{f,2,7} \cdot S_{\text{el}} = 2 \cdot 10^{-11} \text{ W/element}$; $P_{f,4,3} = E_{f,4,3} \cdot S_{\text{el}} = 2 \cdot 10^{-10} \text{ W/element}$.

Energy contrast - defined as the ratio of $P_f/P_s = 50$ at $\lambda = 2,7 \mu\text{m}$ and $P_f/P_s = 100$ at $\lambda = 4,3 \mu\text{m}$. At $\eta = 0.01$, the background charge is $Q_{f,2,7} = 1,3 \cdot 10^{19} \text{ photons/s} \cdot 0.01 \text{ e/photon} = 2 \cdot 10^{-11} = 1,3 \cdot 10^6 \text{ e/s}$. Hence it follows that a saturation charge will accumulate in 1s if a CCD pit is used as a storage device. In order to have dynamic range margin of at least 10, we limit the accumulation time to 0.1s. If we take $\sigma_{f,2,7} = 100 \text{ e/sample}$ of signal, then during this time $P_{\text{nor},2,7} = 5 \cdot 10^{-13} \text{ W/cell}$ will accumulate $\sigma_{c,2,7} = 6,5 \cdot 10^3 \text{ electrons}$ [93].

2.11. Linear infra-red image receivers

The following materials are mainly used for the manufacture of linear IR receivers:

- PdS due to:

1) high quantum efficiency in the range up to 3,0 μm (up to $25 \div 30\%$),

2) The need for moderate cooling ($\approx 170^0 \text{ K}$), to ensure good detectability,

3) high ampere-watt sensitivity (up to $(1-2) \cdot 10^5 \text{ A/W}$).

- PdSe has the same advantages as PdS. Its spectral sensitivity, however, is up to 5.0 μm .

- $\text{Hg}_{0,8}\text{Cd}_{0,2}\text{Te}$ - this material, at temperatures $T = 40 - 60^\circ \text{K}$, has high sensitivity in the range of 8 to 12 μm . When cooled to a temperature of 170⁰ K in another component, it has success in the range of 3,0 to 5,0 μm . This material is exceptionally cost-effective.

Linear receivers can be manufactured using planar technology. In this case, substrates with high thermal conductivity (sapphire, beryllium oxide).

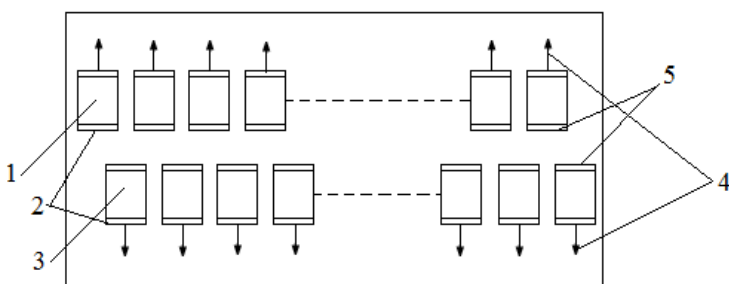


Fig. 2.14. (1) - photosensitive elements of the 1st ruler; (3) - photosensitive elements of the 2nd ruler shifted by the element step; (5 and 2) - common busbars; (4) - individual signal outputs from the elements

We attribute this phenomenon to the fact that linear IR receivers are mounted on cooling devices. In this case the devices have a minimum thermal resistance of the contact area of the ruler substrate and the cold lead. Figure 2.14 shows a typical design for a linear IR receiver (photoresist).

When scanning in the gaps between the elements, no target skipping is ensured by shifting the elements between the 1st and 2nd rulers by half a step. An amplifier is connected to each isolated element. Similarly, we can implement linear receivers of photovoltaic type (photodiode rulers).

2.12. Scanning methods

IR rulers include between 64 and 6000 elements. So, a ruler is a photoelectric transducer. It forms one side of a television frame. To get a complete picture, the image of the television frame line is scanned in the second coordinate. Thanks to technological progress we have at the moment a great number of ways of scanning both one-dimensional (for rulers) and two-dimensional (for mono-element RR) images.

Until recently, the US Air Force was equipped with DLIR (Down Looking Infrared) type night vision systems. The cadmium-mercury-tellurium compound line is cooled to the normal boiling point of nitrogen ($77,4^0$ K). It is positioned strictly perpendicular to the axis of motion of the aircraft. The image of the terrain is scanned by the movement of the aircraft. Currently, US aircraft are equipped with FLIR (Forward Looking Infrared) systems. The ruler is usually positioned vertically and the scanning is carried out horizontally. The result is a forward looking infrared night vision indicator. First, for convenience, let's look at the simplest mirror scanning scheme (figure 2.15). In the scheme, a scanning mirror is placed in front of the optical system at an angle to the field of view. The second method of scanning is scanning in image space (fig. 2.16).

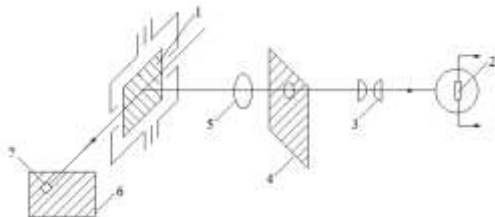


Figure 2.15. Schematic of two-coordinate scanning of objects in space: 1 - scanning mirror; 2 - PI; 3 - condenser; 4 - aperture; 5 - OS; 6 - field of view; 7 - OS instantaneous field of view

In spite of technical difficulties, scanning of images in space is more advantageous when using an OS with large diameter. This is because huge scanning mirrors placed in front of the OS disturb the spatial stabilization of the spacecraft. In addition, they require compensation to preserve the total angular momentum.

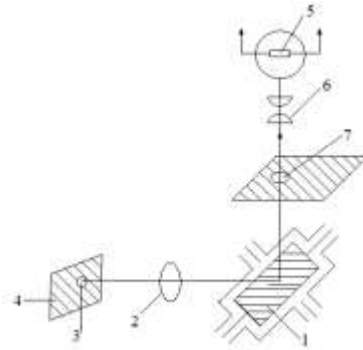


Figure 2.16. Scans - in image space: 1 - scanning mirror; 2 - OS; 3 - OS instantaneous field of view; 4 - field of view; 5 - PI; 6 - condenser; 7 – aperture

The developers of the IMEWS (Integrated Missiles Early Warning System) system on the DSP (Defence Support Program) satellites (~ 40000 km) have pioneered an excellent scanning method. The satellite carries an image sensor that faces the Earth and is stabilised by rotating around an axis at a speed of 10 rp/m. If a line of 6000 elements rotates around element 1, a circular television infra-red frame can be formed in the focusing plane of the radiation receiver. In this case the diameter of the line scan is 12000 elements.

CHAPTER III. MATRIX IMAGE RECEIVERS

3.1 Solid-state television photovoltaic transducers (SSTPHT)

SSTPHT solid-state television photovoltaic transducers are ultra-large integrated circuits (VLSIs) with the number of photosensitive elements from 170×128 up to 512×512 in one matrix. Figure 3.1 shows a schematic diagram X – Y with SSTPHT organization: a) - matrix diagram; b) - structure.

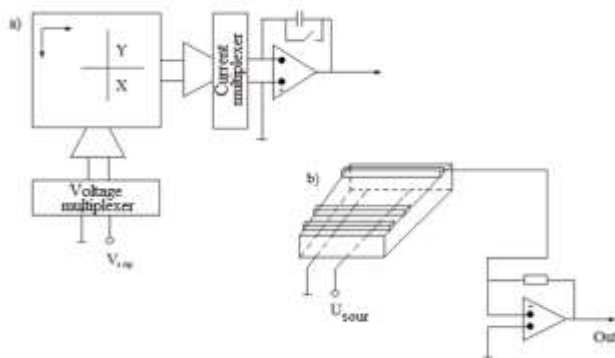


Figure 3.1. Scheme with X - Y organization SSTPHT

In the circuit, the voltage multiplexer is a pulse generator. The pulses are fed alternately to all Y-buses of the matrix by means of a shift register and a system of high-speed micro-power keys.

In order to register the output, signal the current multiplexer, using a shift register and a system of current keys, connects the X-buses alternately to the output of the operational amplifier with deep feedback.

The simplest and cheapest SSTPHTs used today are based on compensated germanium and lead sulphide.

To compensate, copper doped germanium-based matrices are used with a high degree of accuracy using doping with source antimony. In order to bring the dark currents to zero and to increase the impurity conductivity of the germanium crystal to near dielectric level, cooling is performed to a temperature of $77,4^0\text{ K}$ ($T_{H,KN2}$).

The ampere wattage sensitivity of the SSTPHT based on compensated germanium is as high as $(1-2) \cdot 10^5\text{ A/W}$. It does so in the wavelength range of $(2-3)\text{ }\mu\text{m}$, with a photoelectric inertia of fractions of a second.

When infra-red radiation up to $3.0\text{ }\mu\text{m}$ hits the surface of the SSTPHT matrix, the plate resistance at the X and Y intersection where the IR image is projected decreases dramatically. Then, the operational amplifier, must capture the electrical signal corresponding to the target. The system considered is considered coordinate-sensitive. All elements of the X - Y matrix are displayed on the screen of a video monitoring device (VMD) with corresponding coordinates. The disadvantage of primitive SSTPHTs is: 1) inertia; 2) low quantum efficiency, equal to $\sim 1\%$, at $2.0\text{ }\mu\text{m}$ and $\sim 0.1\%$, at $3\text{ }\mu\text{m}$ [94].

And the advantage of SSTPHT on impurity germanium, we can consider a huge dynamic range, which reaches $\sim 1 \cdot 10^7$, and it allows to register signals at the ratio of irradiance from the background, to irradiance from the target, approximately $\sim 1 \cdot 10^3$. But in this case complex signal processing is required, which uses RAM from the background illumination and other real-time inter-frame operations. Cooling on board the SSTPHTs we examined to nitrogen temperatures is done using sublimation cold accumulators or closed-loop microcryogenic systems (MCSs).

After germanium, the second popular material for manufacturing matrix SSTPHTs, is palladium sulphide PdS. The fabrication scheme for PdS-based SSTPHTs is similar. Despite

this, the quantum efficiency of PdS-based SSTPHT at 2,7 μm , reaches 25÷30%. Such characteristics significantly increase the detectability of PdS-based SSTPHT. Another important advantage is the possibility of PdS-based SSTPHT operation at $T = 170^0 \text{ K}$, which is easily achieved by means of passive radiation cooling systems (PCOs). Since PdS is a semiconductor, it has $\eta \approx 25\%$.

3.2. Charge transfer devices

There are several names of charge transfer devices:

- 1) CCDs - charge transfer devices;
- 2) CCDs - charge-coupled devices;
- 3) CPPD - charge transfer photodetectors;
- 4) FPGA - charge-coupled photodetectors.

Since the middle of XX century, this area of microelectronics received its intensive development. At that time engineers-physicists prepared both ideological and technological basis. When the effect of charge transfer along the surface of semiconductor was discovered, there was already a deep understanding of physical phenomena taking place in metal-dielectric-semiconductor structures which were the basis for CCD. And the fabrication methods for such structures were already known. Before them, VLSIs based on field-effect transistors with isolated gates were successfully developed. Further, we will consider methods of constructing: 1) complex photodetectors (FPU) containing an OS, 2) cooled FPU in an optical cryostat and cooling systems that can be placed on aircrafts, missiles and spacecrafts [95]. A schematic of the CCD is shown in figure 3.2.

When a CCD operates in standard television mode (25÷50 fps), both the accumulation section and the storage section have 512x288 elements each. Storage section in TV mode, must be shielded from light. When the accumulation time ends ($\sim 25 \text{ ms}$)

there is a rapid parallel vertical transfer of all 288 lines to the storage section.

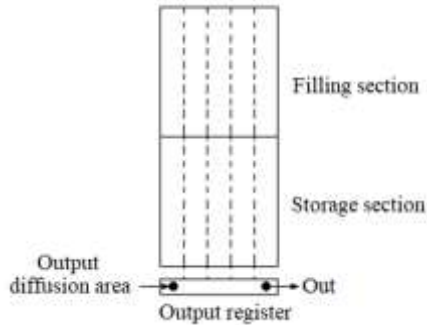


Figure 3.2. CCD matrix

Then, the accumulation section is emptied again. Now the potential pits in the cells, are ready for accumulation of the next frame. From the storage section a sequential line-by-line output of the previous frame is performed. This process is done by means of an output register with a transistor. The transistor is equipped with a floating gate and reset transistor. In order to avoid a charge overflow between all 512 vertical registers, it is implemented as follows: areas (channels) with stop diffusion are implemented in both sections, which create a potential barrier between the vertical registers.

The register frequency in broadcast mode = 50 MHz. When operating in "low-frame rate" mode, with long accumulation time - which is most often used in spacecraft and astronomy - both sections are used for accumulation. In this case, readout is performed with the shutter closed, the so-called "pulse mode". In low-frame mode accumulation time ranges from one to tens of minutes, and the readout register frequency, from 500 Hz to 3÷5 kHz. Naturally, the noise frequency bandwidth $\Delta f_{n.f.b.}$ is narrowed. With $\eta = 25\%$, the photodetector can register a flux of 15÷20 photons.

CCDs come in two types: surface and bulk 'hidden' charge transfer channels. When the charge is transferred on the surface, low impedance n-type silicon is used. When the surface layer is thin, a p-type surface charge transfer channel is formed. If the flux to be registered is small and the output register is also shielded from light, an additional charge of $\approx 1000\bar{e}$ is introduced into the register. This additional charge is called the "fat zero". This ensures a high transfer efficiency, otherwise there is simply nothing to transfer.

In the second case, we use a p- or n-type flint. And a deepened n- or p- channel for charge transfer is created by ion doping of phosphorus or boron into the surface layer. On this surface layer radiation falls. In this case the bulk channel is not impoverished with minor carriers, i.e. a "fat zero" input is no longer necessary. Thus, magnitude σ_n of CCD with surface channel of charge transfer, by $\sqrt{1000} \bar{e}$ greater than the value σ_n of CCD with volumetric channel.

CCDs function by means of three-phase control. A system of polysilicon bars, which create potential pits for charge accumulation and organize charge transport, covers the entire surface of the sensitive semiconductor. Polysilicon has a low transmittance in the blue spectrum region of $0.45 \div 0.40 \mu\text{m}$. Virtual Phase CCDs are also available. Instead of a third polysilicon electrode, a doped ion layer is introduced that creates a permanent well. This region of silicon is open to light, therefore the performance of V-phase CCDs is significantly higher in the blue spectrum region: $\eta = 15 \div 20\%$ at $\lambda = 0.40 \mu\text{m}$, and the spectral sensitivity extends to $0.2 \mu\text{m}$ [96].

3.3. Problems in the design of IR CCDs. IR receivers based on CCDs with Schottky barrier diodes

Below is a typical technical characteristic of a small-frame CCD ($T \leq 800\text{K}$).

- Saturation voltage is 0.6 V;
- dark signal voltage reduced to saturation voltage - 1.1%;
- irregularity of sensitivity - 5,2%;
- dynamic range - $1100 \div 1600\%$;
- energy threshold illuminance - $3,2 \cdot 10^{-10} \cdot 10 \text{ W/sm}^2$;
- modulation depth when transmitting 200 TV lines - 62%;
- RMS value σ_n (surface channel) – $100 \bar{e}$ /sampling;
- σ_n (volumetric channel) - $22 \div 32 \bar{e}$;
- Pit capacity - $2.1 \cdot 10^6 \bar{e}$;
- quantum efficiency in the spectral interval $\Delta\lambda = 0,4 \cdot 0,8 \mu\text{m}$ is $16 \div 22\%$.

Attempts to create high-quality IR CCDs based on impurity conduction of Si, so far have not given positive results. Therefore, in recent times, hybrid devices based on CCD ICs are used as multiplexer. A photodiode array based on PtSi-Si Schottky barriers, $T \leq 80,0^\circ \text{ K}$, is implemented on the multiplexer. The temperature value is taken from the consideration that the barrier is very low and the dependence of the dark background on $T: U_c \approx (T^2)$. Platinum silicide is used as a metal and is formed by thermodiffusion after vacuum deposition of platinum onto the exposed areas of the CCD silicon cells.

On Schottky barrier diodes based on platinum silicon, the spectral sensitivity of the infrared CCD, extends from $1.06 \mu\text{m}$ to $5,5 \mu\text{m}$. Of course, in this case the receiver is irradiated through a silicon substrate. The value of quantum efficiency at the spectral sensitivity maximum reaches $\eta = 1\%/2 \div 3 \mu\text{m}$.

We have so far given typical threshold fluxes at $2.2 \mu\text{m}$ and background irradiance, when observing a target against a daytime background. In this case $P_{th} = 5 \cdot 10^{-13} \text{ W/cell}$; $E_F = (1 \div 2) \cdot 10^{-6} \text{ W/sm}^2$, and $\psi = 3 \div 6$. At and capacitance of potential well of CCD cell $\eta = 1\%$, background fills the well for $t_H \cdot A_c \leq 0,1 \text{ c time}$, i.e. the signal grows up to U_{nac} . Then, the useful signal is smaller than σ_n . To detect a signal with $\psi \geq 3 \div 6$, it is necessary

to accumulate not on the cell but in an external memory that has a capacity up to $25\div 30$ frames. In real-time operation, where we deal with broadband amplifiers, they must be ultra-low noise. If we take Schottky barrier diodes based on iridium silicide, in the $8\div 12\text{ }\mu\text{m}$ range and $T_p \leq 30\div 40^0\text{ K}$ then $\eta = 1\%$. To ensure interference immunity in the $8\div 12\text{ }\mu\text{m}$ range, space communication lines are used on-board calculator on spacecraft [97].

3.4. Low Temperature Techniques for Cooled RR

Let's assume that we have made experimental samples of different PI (SSTPHT, CCD or CCD based on Schottky barrier diodes). If we need to switch CCDs in standard TV mode ($25\div 50$ frames), we need: 1) dia projector with a lamp certified as type A source (2856^0 K); 2) set of TV oscilloscopes with line extraction units and storage tube 3) power supply unit for CCDs and VKU. For convenience, all this equipment is combined with a computer. And in advance we make up a program for measuring CCD parameters.

In RR work with cryogenic cooling we proceed somewhat differently. First, laboratory-research cryostats are designed and manufactured. In these cryostats using liquid nitrogen we can cryostasis CCDs of low-frame mode in range of $220\div 80^0\text{ K}$ up to $\Delta\lambda = 3\div 6$ microns, photoresist lines or matrixes, at the level of $170\div 77,4^0\text{ K}$ if they are on PdS, PdSe or Hg-Cd-Fe working up to 5,0 microns. If we work with PIs on triple bonds in the range $T = 80\div 40^0\text{ K}$, we have to design a helium temperature-controlled cryostat (or use a gas cryogenic machine (two-stage), working according to the Stirling cycle).

A cryostat is a device which provides thermostatic control through various phase transformations in gases, liquids or solids. If enough liquefied gases are available, the problem of cryostatting any RR can be solved in any desired temperature range,

using a set of two cryogenic liquids: 1) from 100 to $(60\div 65)0\text{K}$ - using only liquid nitrogen ($T_{\text{H.K}} = 77,35^0\text{ K}$); 2) 60 to 1.2^0 K - with liquid helium ($T_{\text{H.K}} = 4,2^0\text{ K}$).

Fig. 3.3 presents a schematic diagram of helium cryostat construction for optical investigations. Although the normal boiling point of nitrogen is $77,35^0\text{ K}$, and that of helium, $(4\div 4,2)^0\text{ K}$, when using these liquids we perform temperature regulation and stabilization in optical cryostats within the above limits.

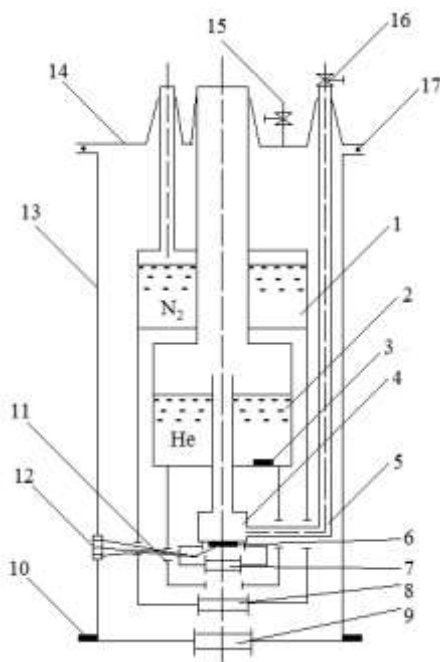


Figure 3.3. Helium cryostat for optical research

Cryostats with temperature control according to Swenson's method and its modifications are mainly used in space research (fig. 3.3). The diagram shows: 1 - nitrogen tank; 2 - helium tank; 3 - cryopump; 4 - heat exchanger with vaporized

or liquid helium intake; 5 - vaporized helium drainage pipe; 6 - SSTPHT; 7 and 8 - cooled filters; 9 - inlet window; 10 - flange for installation in optical system; 11 - cooled diaphragm; 12 - hermetic connector; 13 - vacuum body; 14 - upper flange with filling spigots; 15 - vacuum valve; 16 - needle valve; 17 - seal.

By pumping helium vapour through a needle valve, the SSTPHT temperature is regulated and stabilised within a range of $6\div 8$ to $\sim 80^0$ K. A pressure stabiliser, the manostat, is used for this purpose.

If work is carried out at temperatures above , instead of liquid helium, liquid nitrogen is used in tank 2. Then cryostat construction can be considerably simplified, i.e. it can be made with one tank.

In laboratory practice, work on a telescope with such traditional designs, in spite of wide distribution of the considered cryostats, is very difficult. For this purpose optical cryostats are specially executed, which ensure stability of mutual arrangement of all elements of the photoreceiving device. The photodetector is located in the rear working section of the optical system. The optical system has the ability to be adjusted as well as the ability to operate with the window down, up, etc.

Figure 3.4 shows an optical cryostat that can operate in an astrophysical observatory environment. The figure shows: 1 - leucosapphire inlet window; 2 - vacuum casing; 3 - STEF supports; 4 - birch activated carbon (BAU) based cryopump; 5 - working chamber; 6 - nitrogen container; 7 - vacuum valve; 8 - vapour drain; 9 - external connector of PCGS-50 type; 10 - socket for filling of liquid nitrogen; 11 and 12 - steam inlets for vaporous nitrogen; 13 - flange for installation of cooling window; 14 - indium collapsible joint; 15 - photodetector.

When compared to single element RR or small rulers, the SSTPHT (CCD) is a hybrid integrated circuit (HIC). A HIC is a non-compact circuit that cannot be cryostatized simply by holding it against a cold lead. To cool and cryostat such

photodetectors, circulating cooling with vaporised nitrogen vapour is used. The vapour temperature is equal to the temperature of the walls of the working chamber 5, i.e. it is not necessary to measure the temperature of the HIC.

The leucosapphire exit window has a diameter of 80 mm and the cooled leucosapphire window has a diameter of 60 mm. A germanium plate, GMO-1 grade, is pressed onto the leucosapphire and has a diameter of 60 mm. The resulting combination forms an IR bandpass filter from 1,7 to 5,5 μm K and L -bands of the MFS. When pouring liquid nitrogen and during operation, the filler neck 10 is made hermetically sealed, otherwise liquid air will condense in chamber 5. Cryostats are made of stainless sheet steel of X18H9T brand and of thin-walled tubes of OX18H9T steel grade with the help of constructional materials. The presented materials possess the lowest thermal conductivity: $\lambda_{\text{stainless steel}} \approx 1 \text{ W/sm}\cdot\text{K}$; $\lambda_{\text{glass}} \approx 0,008 \text{ W/sm}\cdot\text{K}$; $\lambda_{\text{Cu}} \approx 4\div 5 \text{ W/sm}\cdot\text{K}$; $\lambda_{\text{glass}} \approx 0,008 \text{ W/sm}\cdot\text{K}$; $\lambda_{\text{glass plastic}} \approx (2\div 3)\cdot 10^{-3} \text{ W/sm}\cdot\text{K}$.

The metals Au, Ag, Al have high thermal conductivity. And of the dielectrics, the best values are in:

- quartz, $\lambda_{\text{SiO}_2} = (0,5 \div 1) \text{ W/sm}\cdot\text{K}$;
- leucosapphire $\lambda_{\text{Al}_2\text{O}_3} = (1 \div 2) \text{ W/sm}\cdot\text{K}$;
- beryllium oxide $\lambda_{\text{BeO}} = (1 \div 2) \text{ W/sm}\cdot\text{K}$.

The cryostat shown in fig. 3.4, does not require a high-vacuum pumping condition. Before pouring, into the cryostat, it is pumped out with a mechanical or zeolite fore vacuum pump to a pressure $P \leq 5 \cdot 10^{-2} \text{ Tor}$. Then, by closing valve 7 and into container 6, liquid nitrogen is poured. Almost instantly, using BAU-based cryopump 4, pressure $P \leq 5 \cdot 10^{-2} \text{ Tor}$ is established in the vacuum cavity of the cryostat. This pressure is sufficient to ensure reliable vacuum thermal insulation of all cooled parts. The cryostat is very handy when working with ground-based telescopes of the Kassegren system. In these cases, it works in the position with window 1 upwards. In this case the branch pipe

10 is closed and the vapour outlet of evaporating nitrogen is made according to the scheme 12. The capacity of the cryostat is 3÷4 litres of liquid nitrogen, and this ensures normal pump operation for 6÷8 hours. When the cavity is heated to 300⁰ K the cryostat with BAU angle self regenerates [98].

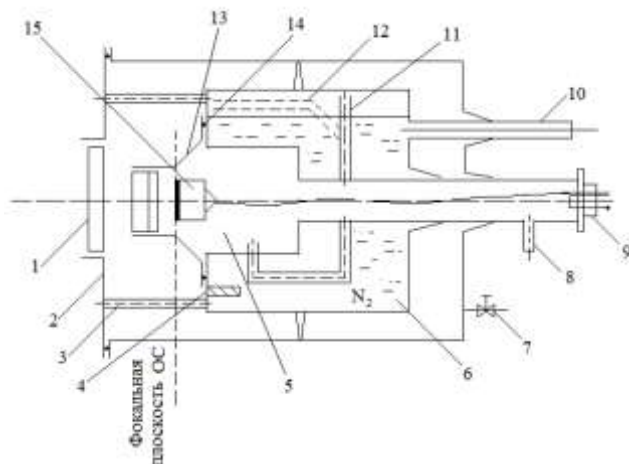


Figure 3.4. Nitrogen optical cryostat

3.5. Low temperature thermometry

In the temperature range from the triple nitrogen point 63,15⁰ K to 300⁰ K, chromel droplet, chromel-alumel and copper-constantan based thermocouples are commonly used. Resistance thermometers based on germanium or gallium arsenide single crystals can also be used. One of the temperature gauges is attached to the isothermal surface, next to the RR. Shielding is applied to insulate the warm parts of the cryostat from thermal radiation. In the cryostat shown in fig. 3.4, the temperature is not measured as it is guaranteed at T_{H,K} 77,35⁰ K.

And thermometry at helium and hydrogen temperatures, are not considered. Of all the RR, they are of interest only to single element thermal receivers (bolometers) which, as image receptors, have no need.

3.6. Temperature regulation and stabilization in nitrogen level cryostats (region $T \geq 80^{\circ} \text{ K}$)

The simplest method of thermal regulation, is the adjustable thermal bridge method (figure 3.5). In the figure: 1 - container N_2 ; 2 - thermal bridge ; 3 - heater; 4 - cold-wire pad; 5 - cooled screen; 6 - temperature sensor; 7 - RR.

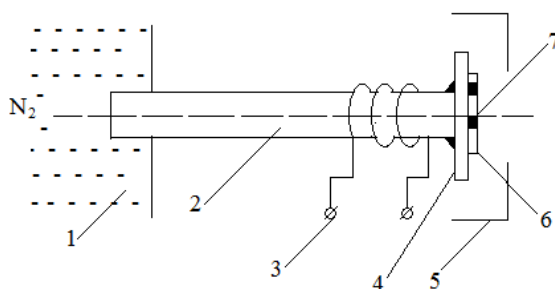


Figure 3.5. Thermal bridge

The required materials for the thermal bridge are selected on the basis of the initial setpoint temperature difference. First, the RR and the temperature sensor are brought into good thermal contact with the cooling conductor, then the tracking system with feedback, according to the temperature sensor 6, switches the heater 3 on and off. In this case, shielding of the whole device with a low-temperature screen is applied. We leave only the aperture for the falling signal flow. Let's note that very effective is Swenson method, which consists in circulation of liquid or

vaporized cryoagent through heat exchanger, which in its turn is built into RR holder (fig. 3.6).

From the vaporiser 8 the evaporated nitrogen is supplied to the heat exchanger 5 of the cooling duct 4, equipped with a heater 6 and a tracking system with feedback from the temperature sensor.

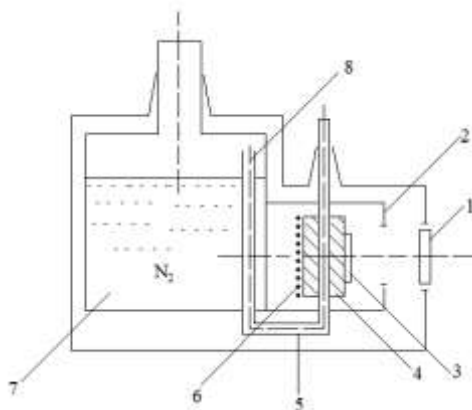


Figure 3.6. Heat exchanger built into PI holder: 1 - inlet window; 2 - cooled diaphragm (with hood); 3 - PI; 4 - cold pipe; 5 - heat exchanger; 6 - heater; 7 - nitrogen container; 8 - steam trap

The incoming vapour pressure is regulated by heating a piece of vapour pipe at the inlet to the cryostat. We can now say that we have mastered the technique and technology of regulating and stabilizing the temperature in cryostats, and are ready to begin work on investigating the parameters of any RR.

3.7. Optical systems for aerospace PI

Without an optical system (OS) - one cannot imagine an IR system. The task is to project a target image onto the PI, which is located in the focusing plane of the OS. All IR systems

with linear and matrix IR receivers are equipped with ultra-luminous OS with a relative aperture (the ratio of the entrance pupil diameter to the focal length) close to unity. This is due to the very small size of the ICS liners and matrixes, which must provide for a sufficiently large OS angle of view.

In general, the angle of view, at a given focus, is entirely determined by the size of the RR ("field" aperture, which is located at the edges of the photosensitive field of the RR). Two types of angle are distinguished: 1) "full" angle of view - the angle constricted by the entire area of the RR and 2) "instantaneous" angle of view - the angle constricted by a single "pixel". The pixel is the value defining the resolution of the whole receiving system. In most cases the pixel size, is conjugate to the scattering circle of the OS. The NATO military standard for high-resolution infrared systems in full field of view is 6000x6000 elements.

For any OS, an important characteristic is the diameter of the "scattering circle" with a given percentage (ratio) of energy concentration in the spot. The spot is an image in the focusing plane of the point infrared source. And the point infrared source is distant to infinity. This situation is to be simulated by means of a large collimator and a miniaturised monocellular IR receiver. With this IR receiver the energy concentration coefficient of the spot is measured (figure 3.7) [99].

For an OS lens the "diffraction limit" value - the minimum size of the scattering circle - must be calculated. In this case, the concentration factor value is $0.8 \div 0.9$ and is determined by unrecoverable diffractions. And in fact each OS has different types of aberrations - image distortions caused by non-ideality of the optical system (i.e. there is a blurred image): geometric, chromatic and diffractive.

If one examines the illuminance distribution in the focusing plane, it is a Gaussoid of rotation. When the OS is at the diffraction limit when the wavelength is $3,0 \mu\text{m}$, the diameter

of the scattering circle of an ideal lens with an energy concentration factor of $80 \div 90\%$, is $20 \mu\text{m}$. With fast lenses, this is extremely difficult to achieve. For this reason, a mirror with a spherical surface is used to achieve the objective [100].

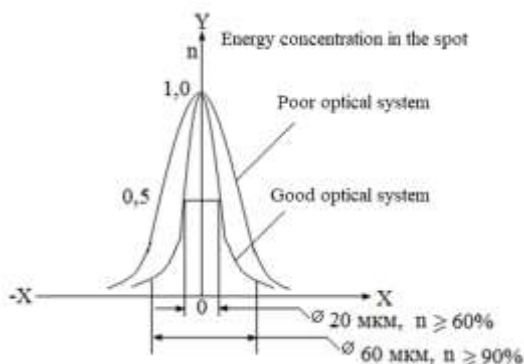


Figure 3.7. Energy concentration coefficient in the spot

In practice, we determine the resolving power of the OS and thus of the whole IR system by means of the scattering circle. Clearly, with a smaller scattering circle, the threshold sensitivity of the IR system will be higher. So, the scattering circle, or more precisely its diameter, is called the "quality" of the optics.

Below we will give you a description of the most common and advanced OS's that are designed to work with linear and matrix IR receivers.

3.8. Mirror OS

For the normal operation of large ground-based telescopes, a Newton single-mirror system is placed in them. Placed on the BTA (large azimuthal telescope), the parabolic mirrors have a diameter of 6 m. A RR is placed at the upper end of the "tube" and an observer $F = 25 \text{ m}$ in the main focus. Multi-

mirror OSs and also lens compensators and projection lenses are used on spacecraft, missiles and aeroplanes because of inconvenience of RR location in direct focus in front of mirror. We present schemes: Newton's double mirror OS (fig 3.8) and Cassegrain's double mirror OS. (fig. 3.9). Here: 1 - parabola, 2 - hyperbola. For removal of the secondary focus F' outside of the primary (main) mirror, increasing its diameter, the secondary mirror is brought nearer to the main mirror.

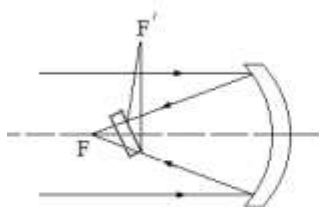


Figure 3.8.
Two-mirror OS
Newton

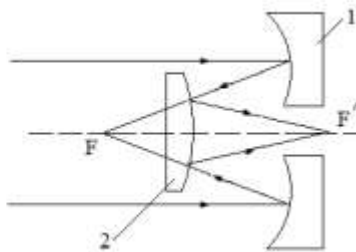


Figure 3.9.
Two-mirror OS
Cassegrain

As a result, one gets rather big "blind" spot in the center of the primary mirror collecting a luminous flux. To eliminate spherical aberrations we use hyperbolic mirrors instead of spherical mirrors, but still there are chromatic aberrations. And to eliminate them we do as follows. We set a projection lens in the aperture in the blind spot of the main mirror and reduce the secondary mirror by moving it closer to the primary focus F .

Figure 3.10 shows the Kassegren OS with a chromatic aberration compensation projection lens. 3.10 shows a Cassegrain OS with a chromatic aberration compensation projection lens. In this case, the secondary focus is moved to the convenient plane of the F_1' radiation receiver.

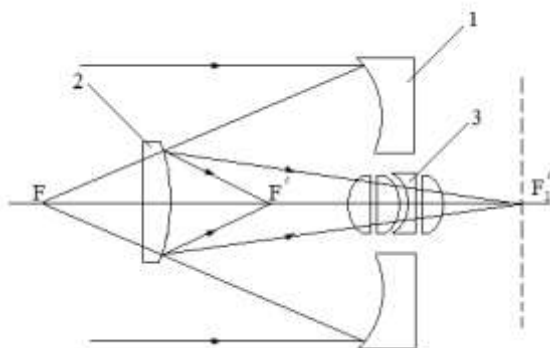


Fig. 3.10. Kassegren's OS with projection lens: 1 - primary mirror; 2 - secondary mirror; 3 - projection lens

The OS under consideration transfers (projects) the secondary focus F' into the RR plane. Germanium lens lenses with antireflection are usually made of GMO grade, τ of such lens, is $\approx 0,5$ and the mirrors of the system are coated with polished aluminum.

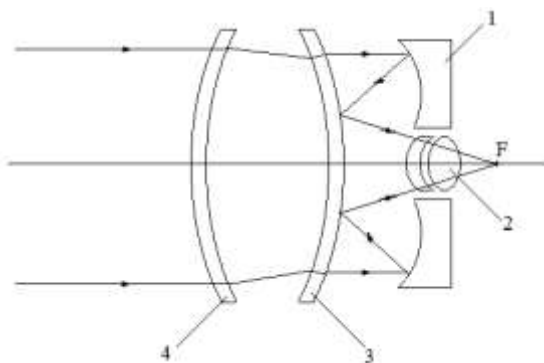


Figure 3.11. Maksutov OS: 1 - Main mirror; 2 - Compensator; 3 - Semi-reflective meniscus

The reason for the reduced effective area of the main mirror is the presence of a blind spot. Some Cassegrain OSs are made with diffraction quality for spacecraft and a diameter $D = (0.5 \div 0.6)$ m.

In thermal homing heads, simple germanium lens lenses are often implemented. Figure 3.11 shows the OS on the Maksutov system, which has the best performance. The telescopes of the Maksutov system, are compact and have a small diameter.

When installing a Maksutov OS on a thermal seeker head, the meniscus 4 is the fairing and sealing element of the missile head. Among large-diameter space telescopes, the Schmidt telescope has the best performance in the USA, which is shown in figure 3.12.

RR with a Schmidt telescope with the following characteristics are placed on spacecraft located on geostationary orbits: $L = 1,0$ m; $F = 1,5$ m and field of view angle $16 \div 17^\circ$. From an altitude of 40000 km this is almost half the Earth. Schmidt systems also have a disadvantage: the focal surface is not flat. It is convex, with a diameter equal to its focal point, and is very difficult to manufacture [101].

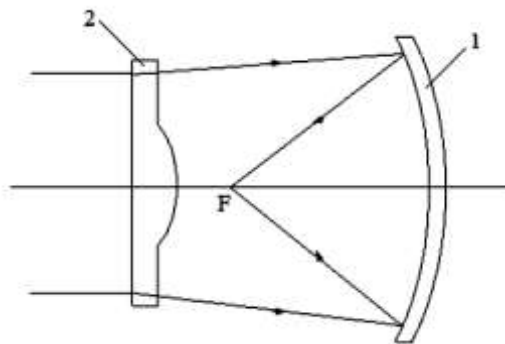


Figure 3.12. Schmidt telescope

3.9. Antireflection coatings

There are two conditions attached to antireflection coatings used in optical materials:

1. The refractive index of the coating, n , must be equal to the root square of the refractive index of the optical material.

2. the optical thickness at which the minimum reflection is to be achieved must be $\lambda/4$.

The main antireflection materials used at OS are as follows: ZnS, GeO₂, TiO₂, MgF₂.

CHAPTER IV. CHARGE-COUPLED DEVICES

4.1. CCD devices

As we mentioned above CCDs are functional electronics products, for this reason they cannot be represented as a set of transistors or capacitors. In electronics the principle of charge coupling is very simple and is based on two equally fundamental premises: 1) like-minded charges repel, and 2) the fish is always looking for the deepest place. Take an MOS capacitor (metal-oxide-semiconductor). If we remove drain and source from the MOSFET, we are left with a MOSFET capacitor, i.e. just an electrode separated from silicon by a dielectric layer. For convenience, we assume that our semiconductor is of the p-type. In other words, the concentration of holes in equilibrium conditions is much (a few orders of magnitude) higher than that of electrons.

What will happen if a positive potential is applied to such an electrode (gate)? And the answer - "nothing will happen, since the dielectric does not conduct electricity" - is not true, since an electric field can penetrate through the dielectric. The electric field created by the electrode penetrates the silicon through the dielectric. The field repels the mobile holes and a depleted region, a volume of silicon that is free of basic carriers, is created. If the parameters of semiconductor substrates that are typical for CCDs are taken into account, this region is about 5 μm deep. And the electrons, suddenly in some way (let's say as a result of photogeneration) will be near this region attracted, to the gate. The electrons accumulate at the oxide-silicon interface directly below the shutter. In this case they merge into a pit, which we quite officially call the potential pit (fig. 4.1a).

Naturally, the electrons, as they accumulate in the well, will partially neutralize the electric field created in the semiconductor by the gate. Further, they can compensate for it

completely, due to the fact that the entire electric field will only fall on the dielectric. Everything will return to its original state - but with one exception, a thin layer of electrons will form at the interface.

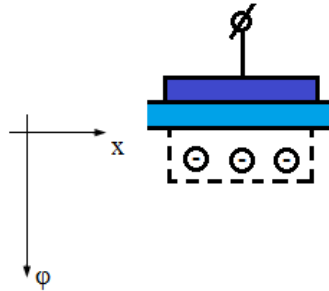


Figure 4.1a. Potential well formation when voltage U is applied to the gate

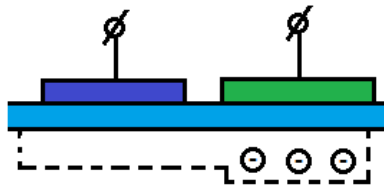


Figure 4.1b. Overlapped potential pits of two closely spaced gates. The charge overflows into the pit where the potential well is deeper

Now, next to the first gate, we place another gate, the second one, and apply a positive potential to it as well, and a higher one than to the first gate (fig. 4.1.b). In this case, if the gates are close enough, their potential wells will unite and the electrons in one potential well will go to the next one.

So, if we have multiple gates, by applying the appropriate control voltages to them we transmit a localized charge packet along such a structure. The most remarkable property of CCD is the self-scanning property. It consists of controlling several gates of any length with only three clock busses.

It is now clear that three electrodes are sufficient to transmit charge packets: 1) transmitting, 2) receiving and 3) isolating, which separates the receiving and transmitting electrodes from each other. In this case, the homonymous electrodes can be connected to each other to form a single tract bus. This bus requires only one external lead (fig. 4.1c). The result is a simple three phase shift register on a CCD. Figure 4.1d shows the clock diagrams of such a register.

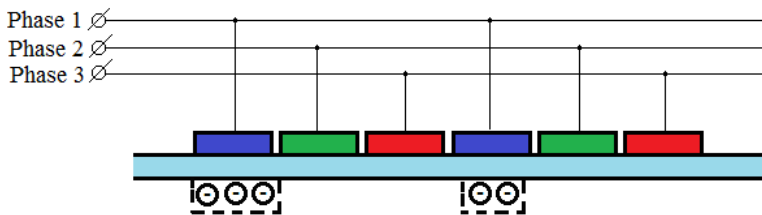


Figure 4.1c. The simplest three-phase CCD register

Figure 4.1d. The control clock diagrams of a three-phase register are three meanders shifted by 120°

For normal operation of a three-phase register at any given time, there is a high potential on one clock bus and a low potential on the other. When a potential rises on one busbar and falls on the other (previous busbar) the charge packets are transferred (shifted) to one register element.

To localize the charge packets in the transverse direction we form stop channels. The stop channels are narrow strips with

an increased concentration of the main alloying impurity running along the transfer channel (fig. 4.1e).

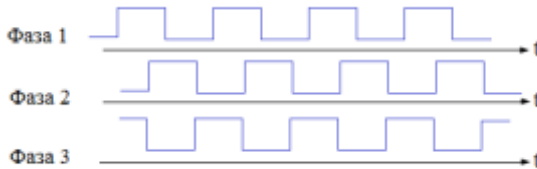


Figure 4.1d. The clock control diagrams for the three phase register are three meanders shifted by 120°

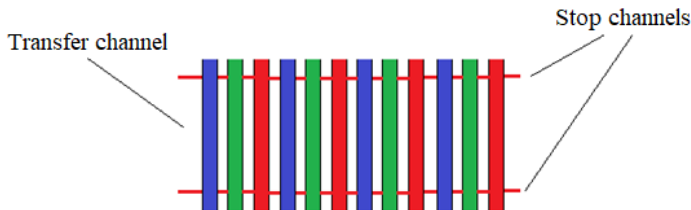


Figure 4.1e. Top view of the register. The transfer channel in the lateral direction is limited by the stop - channels

The exact voltage at which the gate will form a depleted region underneath depends on the concentration of the doping impurity. It is clear that the higher the concentration of the impurity, i.e. the more holes in the semiconductor, the harder it is to banish them deep down. In other words, the higher the threshold voltage, the lower the potential in the potential well.

It takes time to fully transfer the charge from one well to the next. At high clock frequency (and for TV standard it is 7-13 MHz in the readout register, depending on the number of elements horizontally) this time may not be enough. The value that indicates how much of the charge packet is transferred to

the next CCD cell is called the transfer efficiency, and is denoted by ϵ . In electronics the associated inefficiency value $\eta = 1 - \epsilon$ is often used. Frequency constraints are another half of our problem. The problem is that for the CCD structure discussed so far, all events take place in a very thin (tens of angstroms) region at the oxide-silicon interface. Even on the most perfect crystal substrate structure, the interface breaks the homogeneity of the crystal. From solid-state physics we know that when the homogeneity of the crystal lattice is disturbed in the forbidden zone, allowed energy levels arise. With this disturbance, the resulting energy levels form a quasi-continuous spectrum. Now, among these, there are some that are capable of trapping electrons from the conduction band (the trap). This time, after which the captured electron will return back to the conduction band, depends on the energy of the trap (and the absolute temperature). In this case, there is no charge above a given interface point, which means that some of the trapped electrons are released and emit an electron back into the conduction zone. When another charge packet arrives - they instantly fill up to release the trapped electrons again after that charge packet has left. In doing so, the freed electrons go into another charge packet, which comes later.

During the emission of electrons from the traps back to the conduction band, as with any thermal process, thermodynamic fluctuations take place. This introduces a transfer noise in the cell charge distribution. Electrons trapped in a deep level with a long emission time may not return at all (fixed losses - they are especially noticeable in the transport of small charge packets). Further, there is intense dark current generation through the quasi-continuous trap spectrum. The thermal process of spontaneous formation of electron-hole pairs, is considered to be an unavoidable process. It occurs at temperatures other than absolute zero, and the presence of levels in the band gap dramatically increases its probability.

The disadvantages associated with the surface transfer channel have been completely eliminated by physics engineers from the Dutch firm Philips. They suggested using a CCD with a hidden channel. This solution turned out to be so successful, and since then all CCDs are produced only with a hidden channel. The covert channel technology differs from a usual one in that it involves creating a thin (about 0,3-0,5 μm) layer of silicon on the surface with the opposite conductivity as the substrate. At the same time, the concentration of the impurity is such that it can be completely depleted when a voltage is applied to it through a suitable contact.

For convenience we assume that the hidden channel has a homogeneous impurity concentration over its entire depth. When the hidden channel is completely depleted there remains an uncompensated charge of the dopant impurity. In this case, the depleted region will extend into the substrate, just as it does for a CCD with a surface channel. Then the uncompensated impurity charge will be negative in the substrate. If the bulk charge distribution is stepwise, then, as follows from the Laplace equation, the potential distribution will be piecewise parabolic with the maximum potential lying at some depth from the interface (fig. 4.2a). We have solved the problem. Now the signal electrons gather exactly in the region of potential maximum and neutralize as they accumulate impurity atoms (red line in fig. 4.2a) without reaching the surface. We have eliminated all negative points connected with the interaction of the charge packet with the interface. Note also that the channel potential at the maximum is proportional to the doping dose of the channel. In modern materials the degree of lattice perfection is very high. At the moment, the transport efficiency in CCDs with a hidden channel reaches in the best devices remarkable values of 99.9999 % (in other words $\eta = 10^{-6}$ per transfer), which means that the distortion of inefficiency after a thousand transfers is only 0,1 %.

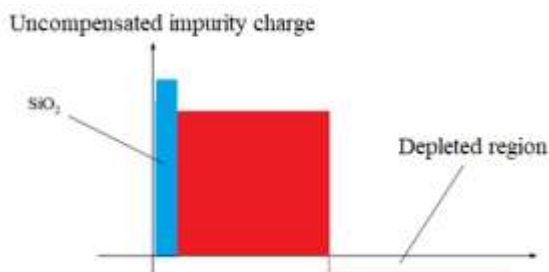


Figure 4.2a. Charge distribution in the hidden channel

These results are achieved not only because of extremely low density of traps in the semiconductor volume. These results are greatly influenced by the fact that the transfer occurs at some distance from the gates.

Clearly, in this case, two-dimensional effects become noticeable - the electric field of one gate penetrates under the neighbouring one and creates a drift component of the transfer (a pulling field). This process draws the charge much faster than simple thermal diffusion, and we hardly notice the frequency efficiency limitations in the frequency range typical of TV matrices.

There is another difference to surface-channel CCDs: the control voltage levels for hidden-channel CCDs are bipolar. So the barrier voltage is negative. And at a certain value of barrier voltage potential at the interface reaches zero and does not change further, because the holes from the stop-channel fill the surface.

The holes short-circuit the surface to the stop and shield the channel from further changes in the electric field of the gate. The phenomenon in question is called surface potential fixing (RRn). It is used in: 1) virtual phase CCDs, 2) multi - RRn phase devices. Let us add that the hidden channel cannot be closed, at fixation, further change of the channel potential stops (aig. 4b).

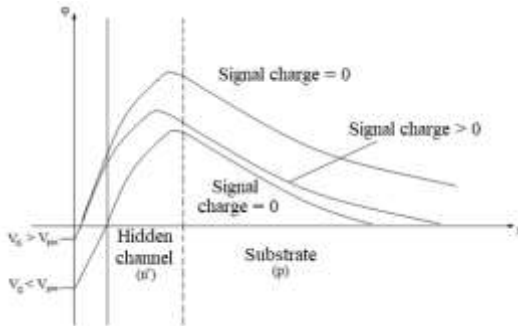


Figure 4.2b. Potential distribution in a CCD with a hidden channel; with no signal charge; with a signal charge and with surface potential fixation

Now, we need to make a two-dimensional matrix out of a single register. Let's first explain what a standard black and white television signal actually looks like and by going deeper into this or that TV standard, we'll look at the general principles of signal formation.

Figure 4.3 is a schematic representation of a TV signal. The TV signal contains video signals of individual lines. Lines separated by a return interval (line blanking interval), which is necessary to ensure that the electron beam, both in the kinescope and in the transmitting camera, has time to return to the beginning of the next line.

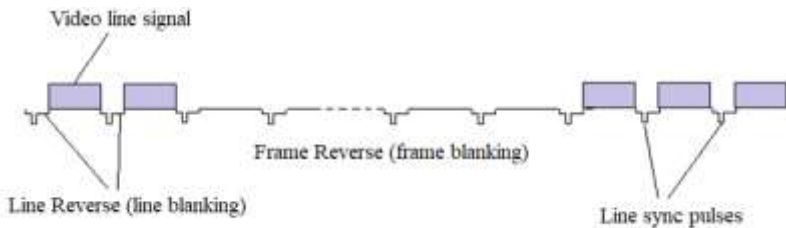


Figure 4.3. Diagram of a TV signal

In this interval, a line sync pulse is applied. Levels: sync pulse 0V, video black level 0,33 V, quench =0.3V, video signal (white level) = 1,00 V.

After the signals of all lines of the same field have been transmitted, a frame blanking interval is formed. Lines are still formed so as not to disrupt the kinescope's line sweep circuitry, and no video signal is formed. At the end of the frame extinguishing interval, the straight frame starts for the next field. The standard adopted in Europe is:

- the period of line sweep is 65 μ s,
- duration of forward stroke along the line - 52 μ s,
- duration of back stroke on a line - 12 μ s,
- frame dwell time - 25 lines.

Each field has 312,5 lines, of which 287,5 are active. In other words, there is a video signal (the appearance of half a line is explained by the fact that the total number of lines in the frame for interlaced scanning is odd - 625).

Consider the structure of a two-dimensional CCD matrix. Figure 4.4a shows its simplest version. In this variant one can distinguish two vertical shift registers on the CCD that make up an accumulation section and a storage section with an equal number of rows (each row of a section is formed by one triplet of electrodes), a horizontal shift register and an output device.

So how does this structure work? During a forward pass through the frame, the accumulation section stands still. This means that it is supplied with constant voltages that form potential pits only under one electrode of each triplet. Let this be under the first phase electrode (VS1). It should be noted that potential pits are formed in all elements of all rows in the section. The accumulation cells are horizontally separated by stop channels, which are highlighted in red in the picture. When the image is projected onto the accumulation section, photogeneration - the formation of electron-hole pairs - is induced.

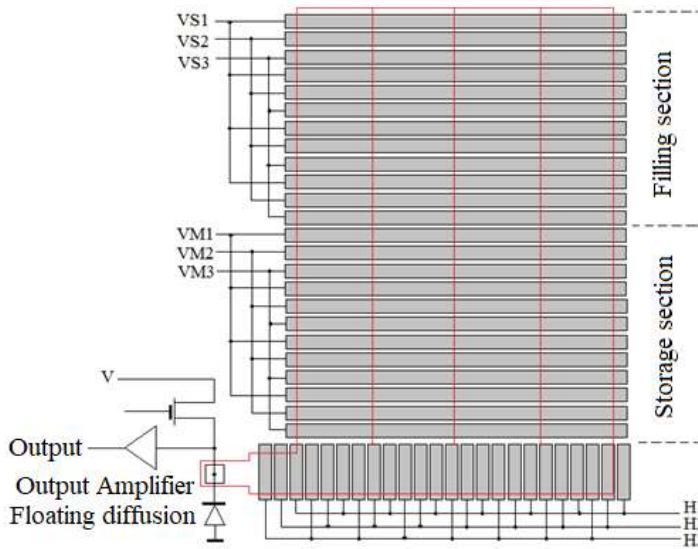


Figure 4.4a. The simplest structure of a two-dimensional CCD matrix

Then photogenerated electrons remain in the potential well, holes, respectively, escape to the substrate or along the surface into the stop-channels. At the same time, under the action of photons the charge - relief is accumulated in the cells. This means that each cell accumulates a charge proportional to its illumination and accumulation time.

When the forward stroke across the frame ends, clock pulses are applied to both sections. These cause synchronous charge transfer, and it is important (all shown in the figure) that both sections form a continuous shift register [102]. As soon as a cycle equal to the number of rows in each section (each row is formed by three electrodes) ends, the entire accumulated charge relief is moved to the memory section which is closed to light, i.e. the accumulation section will be cleared of charge.

The process of transferring section to section is all too fast (in fact, it takes a small fraction of the frame-back time). Then, during the next accumulation cycle (this is the next frame back frame field), the accumulation section is accumulated by the next image frame. In this case, during the line reversal, from the memory section the charges are transferred line by line to the horizontal register (each register element has a charge relationship with the corresponding column of the memory section, and one line is transferred at a time). The charges are then output to the register output for the forward stroke time, and form a video signal.

Recall that the first matrices looked like the one shown, with the electrodes formed from metal. In order to ensure charge coupling and complete charge transfer from gate to gate, the gap between them cannot be large. This results in extremely low sensitivity: indeed, almost the entire area of the cell is opaque to light. If the gap is 2 microns wide and its total length for the whole matrix is several meters, it is very likely that the metallic phases short circuit each other which leads to a loss of the matrix operability.

To eliminate these difficulties K. Seken and M. Thompsett of Bell Labs have suggested using polycrystalline silicon electrodes, transparent in almost the entire visible range. In this type of device three layers of polysilicon, each for its own phase, are applied sequentially to the substrate to form a three-phase electrode system. These silicon levels are oxidized after the electrode pattern is formed. Clearly, the oxidation of the polysilicon does not change the thickness of the sub-gate dielectric. For this reason, the dielectric in modern devices is made in two layers: oxide + silicon nitride (Si_3N_4). This technology has made devices with polysilicon shutters more sensitive than vacuum tubes and even photo emulsion. In addition, growing on each layer of polysilicon insulating oxide (fig. 3.5, above) the probability of interfacial closure is sharply

reduced and the interfacial gap is reduced to interfacial oxide thickness = 0,2 microns.

Let's talk about the advantages and limitations of CCDs in general and this structure. The advantages of moving from vacuum devices to IS with high degrees of integration are obvious and need no comment. The first to note is the hard screen. The screen is created in tubes using a scanning electron beam and its geometric quality depends on many factors: linearity of scanning voltages, stability of supply voltages, temperature effects. In solid state electronic devices the image is specified with high accuracy during fabrication of the device structure. So, the geometric distortion of the resulting image is only determined by the quality of the optics.

The rigid raster also has the following advantages: 1) absence of microphonic effect (i.e. change of parameters of the electrovacuum device due to acoustic influence); 2) insensitivity to magnetic fields. Unless special measures are taken, distortions in the tubes may arise even from changes in its position relative to the Earth's magnetic field. Another advantage is the absence of a burnout effect. In excessively bright light, everything in the tubes went to burn-out, i.e. a long-lasting and sometimes irreversible change of the photocathode parameters. The resulting image of that source (and a negative one at that) could still be observed for a long time, even without opening the lens. Another unpleasant effect, which refers to tubes (by the way, also to photoresist matrixes), we can consider completely absent in CCD - the inertia. We have all seen the tail that stretches behind the image of a bright bulb when the camera is panned. That's how the inertia of the tube comes out, if the illumination of a given point of the photocathode disappears, the signal from it does not go down instantly. A very different phenomenon occurs in CCD matrices - the accumulated signal charge is completely removed when the frame is transferred, and by the

beginning of the next exposure the accumulation section is as good as new [103].

If we compare CCDs with solid-state devices with coordinate addressing, they greatly benefit in signal homogeneity. Because, all charge packets are detected by one amplifier (in devices with CA each column has its own amplifier - with its own gain). In addition to the same charge-voltage conversion for all charge packets, the CCD amplifier is characterized by a much lower noise as compared to a matrix with CA.

Another advantage is that the entire area of the accumulation section is photosensitive, i.e., the fill factor is 100%. Because of this characteristic of the instruments, they are considered to be a monopoly in astronomical research, and in general, wherever there is a struggle for sensitivity [106].

For all its simplicity, the frame-transfer CCD has one major disadvantage: the frame-transfer (FTR) itself. During KP, the magnitude applied to the clock frequency sections is typically a few hundred kHz.

This is due to the high phase capacitance (up to 10000 pF) of the electrodes have distributed parameters (RC), and the clock pulses, which at high frequency may simply not reach the middle of the electrode. So, the KP takes a significant amount of time - fractions of a ms. If we consider that during KP the accumulation section is always illuminated, then the bright areas of the image contribute to someone else's charge packet in the short time that KP takes to pass through them.

Thus blur - a vertical trail of bright portions of the image the size of an entire frame - appears on the signal. A mechanical shutter is used to combat this phenomenon, or the light source is simply removed. In digital cameras, rather simple image-processing algorithms are implemented to eliminate blur. To solve the problem of blur in a radical way, devices with interlinear transfer (IP) are used.

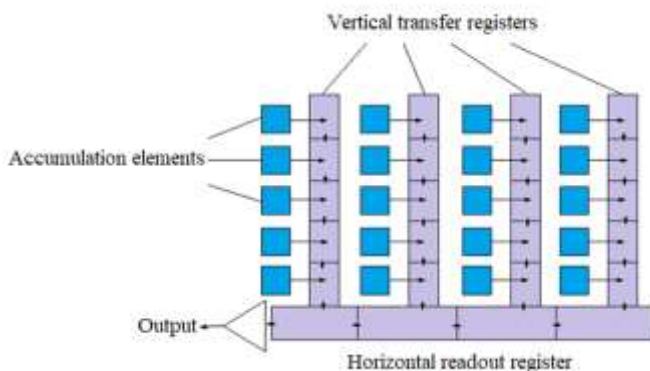


Figure 4.4b. Devices with interlinear transfer

At the moment, devices with MF dominate the market of consumer video equipment (fig. 4.4b).

Comparing MP with KP we can be convinced: in MP the functions of the charge accumulation and its transfer are separated. The elements, where the charges are accumulated (as a rule, photodiodes - they also have the capacitance and are able to accumulate the charge!) transmit them to the light-enclosed CCD - the transfer registers.

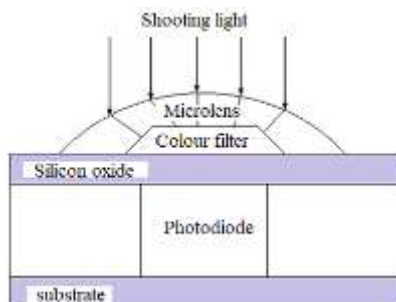


Figure 4.4c. Additional memory section to a matrix with MP

This means that the transfer section is as if inserted into an accumulation section. In this case, charge transfer of the entire frame takes place in a single clock cycle and, therefore, there is no blurring associated with the transfer. There is one last step left to take, which is related to distortions arising from carriers generated deep within the substrate in the transfer channels. To eliminate this, another memory section with the appropriate number of elements is added to the MF matrix (fig. 4.4c).

The smudges in such a matrix with line-frame transfer (LFP) are very small. If we compare MP matrices with SCP matrices, the fill factor is about half as much. That's because about half of the photosensitive surface area is blocked from light. To increase photon collection efficiency, we use a micro-grid - an array of small lenses. The micro-grid is formed very simply: matrix structures are formed on the plate and a layer of optical fusible plastic is applied to their surface. Then, by photolithography, insulated squares are cut out of the plastic and laid over each element. The gaps between the individual squares are kept small. By heating the plate, the plastics are then adjusted, and the surfaces of the individual squares become close to a spherical shape. The squares, which are spherical in shape, focus the light arriving on their surface precisely onto the photosensitive element of the matrix.

4.2. Spectral response of CCD

It's time to talk about the parameters and characteristics of CCDs. First, we will talk about spectral characteristics - the dependence of the output signal on wavelength. Or in other words, quantum yield - number of photoelectrons per one photon of incident radiation.

When determining the spectral response (SR) of a CCD we take into account, and multiplicatively, two factors: 1) light transmission through the electrode structure; 2) photogeneration

caused by light absorption directly in the semiconductor (internal quantum yield). Let us start with the second one. The absorption of photons in the semiconductor is described by a quantity called the absorption coefficient. This quantity is the inverse of the length at which the intensity of radiation drops by a factor e . Photogeneration is caused only by photons having energy exceeding the band gap width, i.e. about 1.2 eV, which corresponds to a wavelength just over 1.05 μm (near infra-red range). It is clear that at longer wavelengths the photons are simply not absorbed and consequently do not contribute to the output signal. Red boundary of photoeffect in silicon appears at $\sim 1.05 \mu\text{m}$. The absorption coefficient gradually increases with decreasing wavelength: at $\lambda = 1 \mu\text{m}$ the light is damped by e times by 100 μm , at $\lambda = 0.7 \mu\text{m}$ (red) by 5 μm , and at $\lambda = 0.5 \mu\text{m}$ (green - blue) by 1 μm .

Earlier we said that the depth of the depletion layer (the depth to which the electric field of the gate extends into the semiconductor) is about 5 μm . In this case, for light which is entirely absorbed within this layer (at a wavelength of less than about 0.6 μm), the internal quantum yield will be nearly 100%, because, there is an instantaneous separation of electron-hole pairs due to the action of the electric field. At long wavelengths a large proportion of photons are absorbed in the neutral substrate. From here carriers can get into potential wells only by thermal diffusion. Consider the fact that the substrate itself has heterogeneous properties.

Almost all European devices are based on epitaxial substrates. Thickness of these epitaxial layers is 10-12 μm . Russian CCD's are made on substrates with internal heterostructure - in special process, the defects of crystal lattice are driven deep into the substrate. In this process, the surface layer, approx. 20 μm thick, becomes defect-free. The lifetime of the free carriers outside the surface layer, in both of these cases is extremely short, and they do not enter the potential wells. This fact, further

reduces the internal quantum yield of the CCD for the long wavelength region of the spectrum.

At very short wavelengths (less than 270 nm) the energy of photons is sufficient to generate two electron-hole pairs. The intrinsic quantum yield for them, can exceed 100%. And for shorter wavelengths the absorption coefficient becomes so large and the absorption length so small that the contribution of surface recombination cannot be neglected. This means that the born pairs recombine before they have time to separate. In the short wavelength region the intrinsic quantum yield also decreases.

Consider the phenomenon associated with the transmission of light by the electrode structure. Figure 4.5 (top) schematically shows a cross section of a three-phase CCD with polysilicon gates.

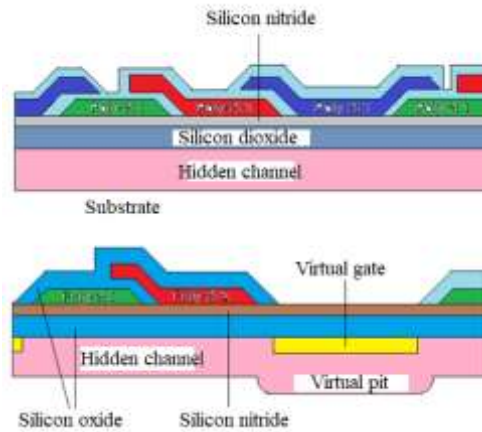


Figure 4.5. Cross-section of a three-phase CCD with polycrystalline silicon electrodes (top) and with a virtual phase (bottom)

Photons entering the semiconductor pass through several layers with different optical characteristics. And light

interference is observed [105]. The electrodes are made of semi-crystalline silicon, and the silicon is completely opaque in the wavelength range up to 430-450 nm (blue and violet). Figure 6 shows the LC of a conventional three-phase CCD with polysilicon gates as the red line. Using photodiodes in MF and ICP matrices significantly improves CCD's MRR, especially in the short wavelength part of the spectrum, because the problems associated with the electrodes simply disappear. Because of this fact, such devices work successfully in broadcast and consumer colour television cameras. And in cameras of applied and scientific direction, which are dominated by devices with control, there should be applied completely other approaches. The easiest and simplest approach is to apply a phosphor - a special substance transparent to long waves. The phosphor converts short wavelength light into longer wavelength quanta.

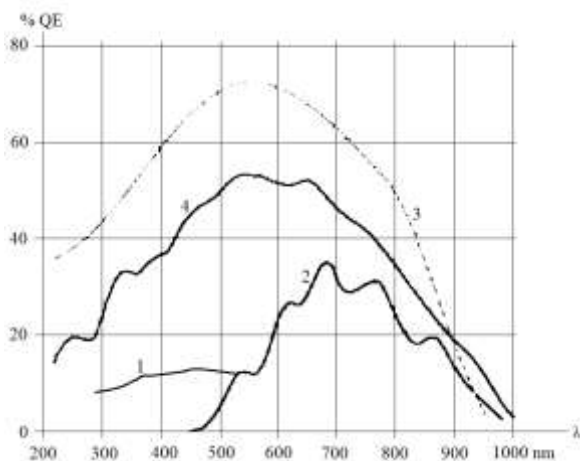


Figure 4.6. Spectral characteristics of absolute quantum yield: CCD with phosphor coating (1), conventional CCD (2), with illumination from backside of substrate (3), with virtual phase (4)

Using this technique expands the CCD CCD into the blue and UV region of the spectrum (shown in figure 4.6 in yellow (1)). 4.6 shown in yellow (1), and does not affect the mid- and long-wavelength portion of the CCD. This method also has its disadvantages: the most important disadvantage is the limited temperature range of such a device. Since phosphor coatings cannot stand deep cooling (I as the author had to see what such coating turns into after cooling down to -100°). And in the study of electronic equipment to work with deep cooling (the reasons for which we will talk) - we have to work very often. In electronics research, however, deep cooling is very common - and the reasons for this will be discussed later.

The second method is the most labour-intensive and expensive and consists in that the CCD crystal, already after manufacture, is reduced to a thickness of $10\text{ }\mu\text{m}$ or less with the light falling on the reverse side of the substrate, which is specially treated.

With such a thin substrate the carriers reach the potential wells, and the total absence of electrodes in the circuit ensures that practically all the light penetrates the silicon, except for reflection losses.

With a quantum efficiency of 90% (green curve in fig. 4.6) the spectral range extends from 180 to 950 nm. Although expensive, such arrays are used in most major astronomical projects. This includes the Hubble Space Telescope, recently built by the Southern European Observatory with several telescopes.

A third method - using virtual phase to improve spectral characteristics - was proposed by Jaroslav Hinecek at Texas Instruments for the US Galileo project to launch a spacecraft to Jupiter. The essence of the method is this: one of the electrodes of an ordinary CCD is replaced with a fine p-type layer (virtual shutter) directly on the silicon surface. In this case the silicon surface is closed to stop channels (Hinecek modified biphas

CCD but I am closer to virtual-phase CCD derived from conventional three-phase - see fig. 4.5 below). Under the virtual gate, the channel dose is slightly higher than under the clock gate. Now we, together with you, will remember what we said about CCDs with a hidden channel. And we were talking about fixing of the surface potential and dependence of the depth of the potential well on the channel dosing. The structure that has a virtual gate closed to the substrate does not differ from the fixation state in a conventional CCD with a hidden channel. By selecting the channel doping dose in the virtual well region as desired, the channel potential in the virtual well will become the average between the well and the barrier under the clocked electrodes. The conditions for clocked charge transfer are maintained.

Compared to conventional CCDs, the advantage of this structure is that about half of the cell area is free of polysilicon. This results in high sensitivity in the blue and UV region of the spectrum (theoretically even up to soft X-rays). The high sensitivity is achieved with illumination from the front side of the substrate, and this has a positive effect on their price. It should be noted that CCDs with virtual phase relate in principle to Multi - RRn Phase (MRP) devices, which we will discuss below, where dark current is discussed.

Mention here of virtual phase CCDs is not groundless. It is the research of this type of devices that I have been engaged in for many years. These devices, based on CCDs with a virtual phase, have been used for many years in the orientation systems of Russian spacecraft, and with their help a detailed image of Halley's comet was obtained for the first time in the world under the VEGA project.

Now it is time to talk about other CCD parameters (we have already talked about transfer inefficiency and spectral characteristics). We will discuss both the parameters themselves and the measures used to improve them.

4.3. Dark current

As we already mentioned the result of spontaneous generation of electron-hole pairs, the dark current is an unavoidable phenomenon - however it can and should be dealt with. Research has shown that the theoretical value of the dark current in silicon (if only direct generation through the band gap is taken into account) is extremely small. In fact the dark current in CCD is determined by one important phenomenon: it is a two stage generation through intermediate energy levels in the band gap. Clearly, with low concentrations of these levels, the dark current is small. And the concentrations of these levels are determined by:

- 1) the quality of the original silicon;
- 2) the purity of the reagents and the degree of perfection of the technology.

At the interface these levels are known to be plentiful. The reason for this is the fact that it gives a noticeably larger contribution to the dark current than the volume. The difference between MPR devices and conventional CCDs is that the channel dose is increased under one of the clock phases. This means that the channel potential at fixation will also be higher. Thus, even if on all phases, the gate voltage is of such a magnitude that the surface potential can be fixed. Then in the transfer channel the potential relief will be preserved and thus there will be a localized accumulation of charge packets. In this case the surface is closed to the substrate and is completely excluded from the dark current generation process.

Currently typical room temperature dark current values for the best European CCDs are a few hundredths of a nA/sm², in other words several hundred electrons per cell per second. Clearly, for broadcast and consumer TV (20 or 40 ms accumulation time), this dark current is unnoticeable. But for scientific applications, where we register fluxes of a dozen of

photons per cell, even such a low dark current is undesirable. Indeed, in small-frame systems, e.g., fluorescence microscopy, the accumulation time reaches minutes. In astronomy, on the other hand, when we obtain the spectrum of a 20th magnitude star - hours. In this case, matrix cooling is applied. The dark current, like any thermodynamic process, strongly depends on the absolute temperature.

Research shows that for every 7-8 degrees drop in temperature it decreases by about half. For deep cooling (in astronomical systems) nitrogen cryostats are used. In them the matrixes are cooled down to -100°C . In simpler systems thermo electronic cooling using Peltier batteries is used. These are capable of providing a 70°C drop in temperature at 5 to 6 volts. This results in a crystal temperature of -40°C . At the crystal temperature of -40°C the dark current is reduced to one electron per cell per second. Peltier batteries are so compact that they are mounted directly in the same housing together with the CCD crystal. The cooled devices considered are produced both in the USA (e.g., by S1Te Technology or Hamamatsu Photonics) and in Europe (EEY, UK) [108].

Since the characteristic of CCDs is highly linear, in digital systems based on them, it is possible to simply memorise the dark signal and then subtract it from the resulting signal.

4.4. Sensitivity heterogeneity

Due to the fact that CCD cells have unequal sensitivity, even at absolutely homogeneous illumination they have different signal (geometric noise effect). Value of this non-uniformity usually does not exceed 1-5% (for different types of devices), therefore, in usual TV cameras we ignore it. Since in scientific systems, photometric accuracy is required, rather simple non-uniformity correction algorithms are applied. Sensitivity of each individual element is a fixed value and for its

correction at even illumination we memorize signals from all elements of the device. Preliminarily, we use them as correction coefficients, carrying out dark current correction at all subsequent exposures.

4.5. Noise

Let's start with the fact that the light flux itself is noisy. That is, the number of photoelectrons accumulated in the cell is determined to the square root of their number (Poisson statistic). For example, a charge packet of 10000 electrons will fluctuate from frame to frame with a standard deviation of 100 electrons. The dark signal, and therefore the total (light + dark) is subject to exactly the same statistics. This, however, does not remove the problem of CCD noise reduction proper, because often one has to work with signals of a dozen photons per cell (fortunately, not in TV systems). For good quality devices where dark current and transport inefficiencies are low, the dominant noise source will be the output device. Again, refer back to fig. 4a and look at the output device. This consists of a readout capacitance, usually a diode, reset transistor Q_1 , and an output amplifier (usually a two stage high input impedance source repeater). The output device works like this. A reset pulse connects the diode to V_{REF} reference, then the reset transistor closes and the diode is floating, i.e. its potential can change when a charge is applied to it - and it changes with the next charge transfer cycle in the register. This change in potential is transmitted to the output of the device via the amplifier.

So, a fundamental property of the key-capacitor system (in case of CCD it is transistor Q_1 and floating diffusion) is that every time after opening of a key the initial potential of reading capacitance will be different. And the RMS value of this noise (called the setting noise) is $(kT/c)^{1/2}$, and the equivalent noise charge is $(kT/c)^{1/2}$, where k is Boltzmann constant, T is absolute

temperature, and c is the capacitance of the reading node. At room temperature, the setting noise charge is $400 c^{1/2}$, where c is in picofarads. The signal itself is proportional to $1/s$. Thus, the smaller the capacitance on which the charge is detected, the greater the signal to set noise ratio for a given readout. This is where CCDs have an advantage over previous sensors, where the charge from a single element went to a common busbar for the whole column. The readout capacitance in modern CCDs is as low as 0,01-0,03 pF, which corresponds to a setting noise level of about 40-70 electrons. For many applications this level of noise is acceptable, but a method exists that allows it to be almost completely eliminated. This method was proposed by N. White and others from Westinghouse in 1974, and is called double correlated sampling. Let's consider again when setup noise occurs: after opening of the reset transistor (note again, that "after" does not mean "because of"; the cause of the setup noise is in the fundamental thermodynamic laws), but before the charge enters the floating diode.

Receipt of signal charge causes only change of floating diffusion potential and if pre-stored voltage of setting noise, it can be easily subtracted from resulting signal and thus it (noise) completely eliminated. Double correlated sampling method became actually standard method of signal preprocessing for all low-frame systems, operating at relatively low clock frequencies, and in many TV cameras as well.

This leaves only the noise of the output amplifier itself. It has two components: so-called $1/f$ noise, inherent in MOSFETs, whose spectral density, as the name implies, increases at low frequencies and is strongly dependent on process refinement, and thermal noise in the transistor channel, which has a uniform (white) spectrum. The $1/f$ noise is largely suppressed by a double-correlated sampling circuit which acts as an upper-pass filter and the extent of the suppression depends upon the ratio of the clock frequency of the noise density spectral response.

Typically the output amplifier design is optimized to achieve the lowest equivalent noise charge for a given application. The total equivalent noise charge also depends on the CCD clock frequency. For modern devices, an output amplifier noise figure of 3-6 electrons (when cooled) is typical at around 100kHz, and a figure of 2 electrons is reached in the best devices. Since the saturation charge (maximum value of the charge packet, transmitted without distortion) is usually 200-500 thousand electrons, the dynamic range of a CCD reaches about 100-110 dB; that's about 18 or 19 bits. By the way, the dynamic range of audio-CDs is only 16 bits.

4.6. Antiblooming, or resistance to local over-lighting

Those who have found the energy to read this point will probably remember the observation that because of the phenomenon of surface potential fixation the hidden channel cannot be closed. What will happen in the CCD cell when the charge in it will grow and grow? Let's go back to fig. 2. It shows that as the signal charge grows in the potential well the potential of the channel in it decreases and when it reaches the potential in the channel by neighboring electrode, the charge will just start to overflow through this unlocked part of the channel to the neighboring cell - and in both directions. This shows up in an image as a vertical blurring of the bright parts of the image. This phenomenon is called optical blooming, and while in low light detection systems it can be accepted (due to low probability of encountering it and possibility to change blooming time), in TV cameras it is absolutely unacceptable.

Blooming can only be combated by developing a special cell design. The first method (horizontal antiblooming) consists in that along each column of photosensitive cells a narrow drainage area is laid out, which is under a high positive potential and separated from the potential pit accumulating a signal charge

by some barrier, the potential of the channel in which (sometimes controlled by a separate shutter) is higher than in the locked channel separating the cells from each other. In this case the excess charge will overflow into the drain and no signal distortion will occur in neighboring cells. If a special antiblooming control gate is used, it is possible to force the charge from the storage cell even without overflowing it, which is nothing less than electronic exposure control.

The cost of horizontal anti-blooming is some reduction in the fill factor (the drain area, clearly, cannot contribute to the signal), and an increase in cell size, which for devices with a small cell size is unacceptable. In TV matrices, where the cell size is typically less than 10 μm , another, very sophisticated method is used to combat blooming - vertical anti-blooming. In this case, the drain area is not next to but below the storage cell, hence no increase in cell area is required. The cell here has a structure not just $n+p$ as in a conventional hidden channel, but $+pn-$, with the middle p -layer serving as a "substrate" and the n -layer itself as the antiblooming drain. As one can guess, in the absence of charge the vertical potential distribution in such a structure with a stepwise approximation of the impurity-depth distribution will be piecewise-parabolic with one maximum and one minimum potential and, if the doping parameters of the layers are chosen correctly (and if they are carefully observed during fabrication!), the excess charge from the cell will drain down rather than to the side. The price for this, besides the complex technology, is a strong decrease in IR sensitivity of the device (most of IR photons, if you remember, are absorbed at a considerable depth from the surface) and some decrease in the red region, which is, however, quite acceptable. The loss of IR sensitivity for color TV devices is not a big deal.

The variety of CCDs is not limited to the types discussed in this review. For example, CCD line cards are widely used - both for reading one-dimensional images (e.g., bar codes) and in

systems where there is a mechanical scan on a single coordinate. The simplest examples are the fax machine and the scanner. Less obvious applications are systems for observing the Earth's surface from spacecraft or aircraft.

Where the motion of the vehicle itself in relation to the Earth is used. Typically, photodiodes serve as storage elements; readout registers are located on either side of the storage element line (bilinear organization for odd-numbered and even-numbered elements, respectively). The range of rulers available today is quite wide and the number of elements ranges from 1024 to 8192.

A variety of devices for systems with mechanical scanning are VZN devices - with time delay and accumulation. Their organization is identical to single-section CCDs with KP, but they differ in the vertical clocking mode: the section is clocked continuously, and the clock frequency is chosen such that the rate of movement of the charge relief is equal to the rate of image movement; thus, each image element contributes to the same charge pack, which, obviously, increases the sensitivity of VZN in comparison with conventional rulers by a number of lines. It is the VZN that is widely used in space-based instruments for observing the Earth's surface.

The number of lines in such devices ranges from 64 to 256, and the number of horizontal elements ranges from 1024 to 4096. But image receptors are not the only application for CCDs. For example, by adding an electrical signal input device to the CCD register, we get an analog delay line, and the delay time is determined by both the number of register elements and the clock frequency, and therefore can be easily changed.

Next. Not only floating diffusion can be used as a charge packet register element, but also a floating gate characterized by non-destructive readout, i.e. we can obtain a register with taps. Such registers are the basis of transversal filters, widely used for example in radar signal processing.

It cannot be said that CCDs have now reached perfection, although tremendous progress has been made in manufacturing technology over the years. The range of products includes both miniature 3-by-5- μm element format arrays (one of the latest Sony products) and giant crystals with 5,000-by-5,000 element format and crystal size of almost 8-by-8 cm (DALSA, Canada). Not far off also is the advent of single-chip devices in 8,000 by 8,000 elements format, whereas nowadays super-sized devices (those astronomers are insatiable...) are assembled from two or four separate crystals mounted back-to-back on a common base.

Of course, CCDs also have their own problems. The most serious of them is a specific, unlike anything else manufacturing technology and extremely stringent requirements for the homogeneity of the initial silicon and the degree of perfection of the technological process. If in the production of digital devices the variation of parameters on a wafer can reach several times without noticeable impact on the parameters of obtained devices (because the work is done with discrete voltage levels), in CCD, a change of, say, 10% alloying impurity concentration is already noticeable in the image. The size of a crystal and impossibility of reservation (like in the case of VLSI) adds its own problems, so the defective areas lead to the inoperability of the whole crystal. Another specific limitation is the inherently sequential output, while in some applications (e.g., optical guidance systems or spacecraft attitude control devices) it is more convenient to have random sampling sensors. As a result, in recent years, there has been considerable interest in so-called active RRxel sensors (APS), which are manufactured using standard CMOS technology. While inferior to CCD technology, these devices are progressing rapidly. The future is likely to see a degree of separation between the "footprints" of each of these classes of devices, or perhaps something entirely new [107].

Sony has recently announced the Microblock CCD, a colour CCD matrix and CCD control and video processing

chipset mounted in a single housing with an integrated plastic lens. The output is a standard TV signal. The size of the color camera is 18,3 by 18,3 by 7.3 millimeters. We all remember what a TV camera looked like 10-15 years ago.

CHAPTER V. BASIC TYPES OF PHOTODETECTORS

5.1. Limit characteristics of receiving systems

The measure of quality of any receiving system is the ratio of information transmitted by this system to the information contained in the incident light flux. The quality of a system is influenced by factors of internal and external origin. Internal factors, which are determined by the intrinsic properties of the system, including various kinds of noise, will be discussed in the following sections. External factors are due to the quantum nature of light. It is the external factors that determine the requirements that a receiver system must satisfy when its intrinsic noise is small and it operates in a mode limited by fluctuations in the signal or background radiation.

The information that a finite portion of light carries is limited by the discreteness of the light quanta and the presence of false signals, that is, false visual images, which may be due to the chaotic nature of the photon distribution and not to the object itself.

Discreteness of light quanta. Suppose we want to image a black spot on a white background, the size of which is such that when placed densely on the image field N spots are reduced. The white background can be represented by a set of small white dots of equal size. Each white spot would correspond to the visual effect produced by a single photon in some generalized visual system. The question arises: what is the smallest number of white dots required to represent a single black spot on a uniformly white background? If the white spots are uniformly white, then $N - 1$ spots will be both necessary and sufficient. Suppose now that the reflection coefficient of the spot is 99% with respect to the reflection coefficient of the background, in other words, it is necessary to represent a gray spot with a contrast of 1% (the contrast is defined as a share of the

brightness of the background). Since, according to the adopted assumption, each white point is identified with a single photon, a total of $100N - 1$ points are required in order to represent a grey spot. In this case each image element contains exactly 100 points except for one element which contains 99 points. From the given reasoning it follows, that to image small elements with low contrast many photons are required.

5.2. Chaotic nature of photon distribution

The photon emission process, being stochastic, can be characterized by mean and variance. The square root of the variance is called the standard deviation or the error. For a random process described by a Poisson distribution, the standard deviation is equal to the square root of the mean. Thus, if signal is the average number of photons reaching a test elementary site, and noise is the standard deviation from this value, then the signal-to-noise ratio is n_0 . It should be noted that the term "signal" is often understood as the difference between the average numbers of photons falling on the test element and the surrounding elementary sites of the same size. In the previously discussed example, the image of one grey area, which is 99% of the brightness of the surrounding background, requires 100 white dots (photons) per image element defined as the area of the grey area. If we take into account the random distribution of photons it will appear that in reality the numbers of photons falling on the areas of different image elements are distributed around the mean value (100) so that the standard deviation equals $(100)^{1/2}$ or 10. In this case the signal to be detected is 0,1 i.e. much less than unity, which is often taken as a signal discrimination threshold against a fluctuating background. It is possible to increase the signal to noise ratio to unity, if the average number of photons falling on an image element is increased from 10^2 to 10^4 .

5.3. False signals

Fluctuations due to noise are of the same physical nature as the signal. Therefore, in order to detect a real signal against a false signal, it must exceed the noise level by several times. The required excess can be estimated by knowing the statistical distribution of noise fluctuations. The probabilities of occurrence of noise fluctuations exceeding the average background value by $k = 1; 2; 3; 4; 5; 6$ contain 10 elements. In this case there are 10^5 possibilities of false signal occurrence. If it is necessary to reduce the total number of false signals to a value less than unity, then according to the above mentioned data the signal amplitude should exceed the standard deviation by 4-5 times.

Now we get the general expression for the total number of photons which are necessary for the detection of the contrast element C with a given signal to noise ratio. If the average number of photons incident on the test spot is n_0 , the noise is $n_0^{1/2}$, the signal is Cn_0 and the signal to noise ratio is $Cn_0^{1/2}$. Assuming this value to be k we obtain $n_0 = k^2/C^2$ and the required total number of photons:

$$N_{ph} = Nk^2/C^2 \quad (5.1)$$

where, N is the total number of elements in the test image.

The presence of this multiplier is due to the discreteness of light quanta. In order to obtain images with good resolution the number of image elements should be in the range of 10^6 - 10^7 . Multiplier $1/C^2$ is related to contrast and reflects both the random nature of photon distribution and the requirement of protection against false signals.

Dividing the left and right parts of obtained expression to the total image area we get the relation characterizing an ideal

receiving system, which properties are determined by photon noise:

$$n_{ph} d^2 C^2 = k_l^2 \quad (5.2)$$

where, n_{ph} is the number of photons falling on 1 sm^2 ; d is the linear size of an image element. The image element is to be understood as the minimum resolvable element with a given contrast. Important consequences of the obtained expression:

- for a given photon flux density, the size of the minimum resolvable element is inversely proportional to its contrast;
- the concept of "resolving power" of a system only makes sense if the contrast of the test item is specified;
- signal-to-noise is meaningful for a system only if the size of the test item is specified;
- the considerations in this section apply equally to any region of the spectrum.

5.4. Mode limited by signal fluctuations and background radiation fluctuations

Under conditions where the intrinsic noise of the system can be neglected, any change in the output signal will only be caused by a change in the photon flux from the signal source. This mode is called the signal fluctuation limitation mode (CL mode), because in this case only the random nature of the photon emission processes limits the minimum power which can be detected by a given photodetector. This mode is characteristic for receivers of visible and ultraviolet radiation. Maximum capabilities of IR radiation receivers are achieved in the mode of limitation by fluctuations of background radiation (OΦ mode).

Background radiation sources are most often objects with a temperature close to room temperature. Equilibrium power of black body radiation at a temperature of 300 K has a

maximum near the wavelength of 10 μm . In this case the photon flux density is comparable to that of bright sunlight, fig. 5.2.

At 3 μm photon flux density is close to photon flux density in room light, and at 1 μm it is below the absolute visual threshold, which explains the minor role of background radiation fluctuations for receivers in the visible range.

The visibility of objects in the infrared region of the spectrum is complexly dependent on the characteristics of the artificial lighting used, the flux of their own radiation, their emissivity and their temperature difference.

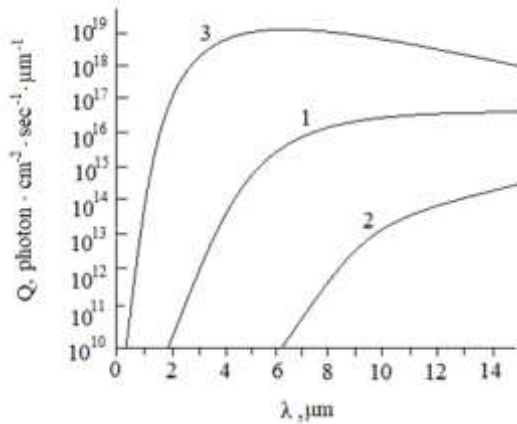


Figure 5.2. Spectral dependencies of photon flux density at different temperatures: 1 - 300 K; 2 - 100 K; 3 - 900 K

For objects visible due to their own emission and having the same emissivity, the contrast is defined by the expression:

$$C = \frac{h\nu}{kT} \frac{\Delta T}{T} \cdot 100\% \quad (5.3)$$

where, ΔT is the temperature difference between the object and its environment. A temperature difference of 1⁰ C creates a

contrast of about 10% at wavelengths around $1\text{ }\mu\text{m}$ and 1% at $\lambda \sim 10\text{ }\mu\text{m}$ [108]. From the above data, it follows that thermal imaging systems, unlike the receiving systems of visible range, should be optimized for recording low contrast images in conditions of strong background radiation.

5.5. Radiation receivers with signal accumulation

A feature of photodetectors used in modern IR systems is the accumulation of the optical signal directly in the photosensitive matrix and not in the electronic processing of the signal, as it is done in circuits with instantaneous receivers. Instantaneous matrix structures operate without charge accumulation in a steady-state photocurrent mode. Therefore, the switching time of the interrogated element τ , i.e. time of its connection to the power supply, must be not less than intrinsic time constant of the photodetector. Increasing the number of elements in the structure n leads to a proportional increase of the frame time $t_k = n\tau$.

In receivers with "instantaneous" action the recorded signal is proportional to the intensity of radiation, in receivers with accumulation - to the product of the intensity of radiation and time of exposure. The noises of the photodetector system under conditions when the intrinsic noise of the FPU can be neglected in comparison to the noise of the background radiation are proportional to the accumulation time to the power of $1/2$. Thus, increasing the accumulation time improves the signal-to-noise ratio and the detectability of the receiving system.

In scanning systems, the exposure time is determined by the duration of one or more image decomposition elements; in non-scanning systems, it is determined by the frame duration, so the accumulation mode is most effective in non-scanning systems [109].

The principle of storage structures is based on the charge and discharge processes of an external capacitance or, preferably, the capacitance of the photosensitive element itself, such as a photodiode, Schottky diode or MDF capacitor. If a reverse bias voltage is applied to the p-n junction, a bulk charge will accumulate in the effective capacitance of the junction. If the circuit into which the p-n junction is connected is then opened, the capacitance of the depleted region will be discharged by the generation-recombination current. For Si diodes and MOS structures time constants of the discharge process on the order of a few seconds at room temperature are typical. When such structures are illuminated by radiation generating free carriers, the process of capacitance discharge is accelerated, and the rate of discharge is proportional to the illumination level. If the optical discharge current prevails over the thermal discharge current, e.g., by lowering the temperature, the amount of charge removed at a given time from the vessel is proportional to the integral of the photon flux and the time from the start of discharge to the measurement of charge on the vessel. Thus, by periodically registering the charge required to recreate the initial voltage (or charge) conditions on the capacitance of the structure, it is possible to measure the intensity of the flux of registered radiation.

It should be noted that the accumulation mode is the usual operating mode of multielement image receivers for the visible spectrum. However, the implementation of this mode for IR systems is associated with significant difficulties. A specific feature of IR range is intensive background radiation and low thermal image contrast in the focal plane of the optical system. The contrast flux of photons in the spectral intervals of 3-5 and 8-14 μm in relation to the total radiation flux at a background temperature of 300 K and a temperature difference between the object and background $\Delta T = 1$ K is only $8 \cdot 10^{-5}$ and 10^{-3} respectively. Contrast enhancement can be achieved by using

cooled filters that only allow the background radiation to pass in the spectral region where the signal radiation lies. Another effective way to increase contrast is to subtract the background signal. This increases the dynamic range of the received signal and the accumulation time. The latter is especially important in cases where the storage cell capacities are limited and the signal must be read frequently enough to avoid potential pit overflow and signal saturation [110]. The high level of background radiation in the IR range determines the existence of another problem associated with the use of multielement photoreceivers (PhR) - a significant "geometrical" noise, fundamentally absent in receiving systems with a single-element receiver. The variation of the absolute sensitivity of individual elements in the matrix, even by fractions of a percent, leads, due to the large constant component of the signal, to the appearance of structural noise on the thermal image that is many times greater than the intrinsic noise of an individual element. In scanning systems, the sensitivities of individual elements can be averaged over several elements in the matrix. To accomplish this, a time-delay and accumulation (TDA) mode is usually used. In this mode, the polling of the PhR elements is synchronized with the scanning process so that each image decomposition element is recorded in turn by several elements of its corresponding row or column of the PU matrix, then the values are averaged. In non-scanning systems, the VZN mode cannot be used. In order to obtain the same threshold sensitivity in a non-scanning system operating in the 8-14 μm wavelength range as in a comparable scanning system, the nonuniformity of sensitivity of individual elements should not exceed 0,1%. With current PhR fabrication techniques, this requirement is only feasible for Schottky diode arrays.

Thus, the direct use of standby thermal image acquisition devices in non-scanning IR systems is difficult. The receiver array must work in conjunction with efficient processing

circuitry that provides real-time processing of large amounts of information to equalize the sensitivity of the individual matrix elements.

5.6. Calculation of receiver systems. Scanning systems

Let's assume that at a distance L from an optical system with effective entrance pupil area A_0 and focal distance F there is an extended source of radiation which is an absolutely black body at the temperature T_1 .

The spectral flux of radiation collected by an optical system and incident on a radiation receiver:

$$P(\lambda) = \frac{R(\lambda, T_1) A_0}{\pi L^2} L^2 \omega = \frac{R(\lambda, T_1) A_0}{\pi} \omega, \quad (5.4)$$

and the signal taken from the receiver:

$$U_s = S(\lambda) \frac{R(\lambda, T_1) A_0}{\pi} \omega \quad (5.5)$$

where, $S(\lambda)$ is the absolute volt sensitivity of the receiver, V/W; $R(\lambda, T_1)$ is the spectral flux density of blackbody radiation at temperature T_1 , W/sm² - μm ; ω - is the instantaneous field of view of the receiving system (aperture angle of a single receiver element).

Signal-to-noise ratio for non-monochromatic radiation:

$$\frac{U_s}{U_N} = \frac{A_0 \omega}{\pi U_N} \int_0^\infty S(\lambda) R(\lambda, T_1) d\lambda. \quad (5.6)$$

Usually the reduced detectability is used instead of the absolute volt sensitivity $S(\lambda)$:

$$D^* = (A \Delta f)^{1/2} \frac{1}{p_{th}}, \quad (5.7)$$

where, A – is the area of the sensing element, hereafter assumed to be square with side a for simplicity; Δf – is the bandwidth of the electronic signal-noise amplification path; h is the energy flux of radiation at which the signal-to-noise ratio is unity. Since, by definition, $S(\lambda) = U_S / p_S$, then:

$$p_{th}(\lambda) = \left(\frac{U_S}{S(\lambda)} \right)_{U_S=U_N} \quad (5.8)$$

and

$$D^* = (\lambda) = \frac{\sqrt{A}\sqrt{\Delta f}}{U_N} S(\lambda). \quad (5.9)$$

В этом случае выражение (5.6) для отношения сигнал – шум принимает вид:

$$\frac{U_S}{U_N} = \frac{A_0 \omega}{\pi} \frac{1}{\sqrt{a^2 \Delta f}} \int_0^\infty D^*(\lambda) R(\lambda, T_1) d\lambda. \quad (5.10)$$

The optimum electronic bandwidth of an opto-electronic instrument depends on the purpose of the receiving system as well as the spectral characteristics of the signal and noise. Usually a filter with a bandwidth matching the bandwidth of the signal is used. As a first approximation, the bandwidth Δf can be assumed to be related to the time per decomposition element of the observed thermal pattern τ_e by the relation:

$$\Delta f = c / \tau_e \quad (5.11)$$

where, c - is some constant of the order of unity.

Given that, the angle of the instantaneous field of view is equal to the angular size of the sensitive element of the radiation receiver:

$$\omega = a^2 / F^2 \quad (5.12)$$

We obtain that the difference signal determining the contrast of the thermal image of the target with temperature T_1 on the background with temperature:

$$\frac{\Delta U}{U_N} = \frac{A_0 \alpha \tau_e^{1/2}}{\pi F^2 c^{1/2}} \cdot \int_0^\infty D^*(\lambda) \{D^*(\lambda) [R(\lambda, T_1) - R(\lambda, T_0)]\} d\lambda \quad (5.13)$$

For small temperature contrasts $\Delta T = T_1 - T_0 \ll T_1, T_0$ the difference in the integrand can be replaced by the differential difference $[dR(\lambda, T)/dT] \Delta T$ and the expression for the thermal contrast will look like:

$$\frac{\Delta U}{U_N} = \Delta T \frac{A_0 \alpha \tau_e^{1/2} D_{max}^*}{\pi F^2 c^{1/2}} \cdot \int_0^\infty S(\lambda) \frac{dR(\lambda, T)}{dT} d\lambda \quad (5.14)$$

where, $D_{max}^* = D^*(\lambda)/S(\lambda)$, $S(\lambda)$ - is the relative spectral response of the radiation receiver.

The time τ_e per decomposition element is determined by the frame duration t_k and the ratio between the values of the instantaneous field of view ω and the total field of view Ω :

$$\tau_e = (m\omega/\Omega) \cdot t_k \quad (5.15)$$

where, $n = M \times N$ - is the total number of elements in the multi-element receiver matrix; M - is the number of rows; N - is the number of columns.

Thus, the contrast signal:

$$\frac{\Delta U}{U_N} = \Delta T \frac{D_{max}^* A_0 \omega}{\pi F} \cdot \left(\frac{nt_k}{c\Omega} \right)^{1/2} \int_0^\infty S(\lambda) \frac{dR(\lambda, T)}{dT} d\lambda \quad (5.16)$$

When designing a receiver system, the frame duration t_k , the total field of view Ω , the instantaneous angle of view ω , and the temperature difference ΔT of the object in the background are usually set based on the purpose of the system. The value of

the parameter c is also set, as it is determined by the functional purpose of the system. Thus, only the values of A_0 , F , $D^*(\lambda)$ and n can be varied during the design of the receiver system to provide a given signal-to-noise ratio.

Increasing the size of the optical system's aperture A_0 leads to a drastic increase in the mass and dimensions of the receiver, which is not always acceptable. Decreasing the focal length while keeping A_0 constant leads to increasing aberrations in the optical system, making it more complex and the negative effects associated with it. Therefore, the relative aperture A_0/F of the optical system of the receiver is actually a pre-determined value. In properly designed receiver systems the value of the reduced detectability $D^*(\lambda)$ of the receiver is close to or equal to the maximum possible value determined by the fluctuations of the background radiation (OB or BLIP mode):

$$D_f^*(\lambda) = \frac{\lambda}{2hc_0} \left(\frac{\eta_0}{Q_B} \right)^{1/2} \quad (5.17)$$

where, h - is Planck's constant; c_0 - is speed of light; η_0 - is quantum conversion efficiency of radiation; Q_B - is intensity of background radiation, falling on sensitive element. All parameters (except for h) controlled by the designer are equal or close to their maximum values and the only possibility for modern receiver systems to increase significantly the signal to noise ratio is to increase the number of elements n in the multi-element receiver.

If we do not take into account the peculiarities of manufacturing and functioning of multielement receivers, which will be considered in the following chapters, and assume that a developer has at his disposal multielement receivers with any desired number of elements, the maximum possible number of elements in a matrix will be determined by the particular application of matrices in the receiving systems.

One of the basic conditions that must be fulfilled in a properly designed receiving system is that the noise of the receiving element dominates the noise of the subsequent electronic readout and amplification circuitry. In deriving the equation for the contrast signal, it has been assumed that this condition is met. The bandwidth Δf , in which noise accumulation occurs, is determined by the sampling frequency of the elements in the matrix. The latter, in turn, depends on the frame time and the number of elements in the matrix to be sampled during the frame time. As a consequence, the maximum number of elements in a matrix is automatically set when the initial data in the form of frame time t_k and preamplifier noise level is specified by a developer [111].

5.7. Non-scanning systems

To describe the photoelectric characteristics of accumulated receivers it is customary to use parameters that are very close in their definition to those of instantaneous receivers. By analogy with the given detectability of instantaneous receivers (4.9) the marginal sensitivity of accumulated receivers is characterized by the value

$$T^*(\lambda) = \left(\frac{A}{t_i}\right)^{1/2} \frac{S(\lambda)}{U_N} \quad (5.18)$$

where, t_i is the time of charge accumulation in the sensitive element. Comparing (5.18) and (5.9) we see that the parameter "accumulation time" t_i of the non-scanning system corresponds to the parameter $\tau/c = 1/\Delta f$ of the scanning system. If the first one is actually equal to a frame time, the second one, defined by equation (5.15), depends on the number of elements in the matrix and tends to i_k - when the number of matrix elements approaches the number of the image decomposition elements.

The introduction of $T^*(\lambda)$ instead of $D^*(\lambda)$ makes it possible to use the above expressions describing the characteristics of scanning systems to describe the corresponding characteristics of non-scanning systems. Thus, instead of equation (5.10) defining the signal-to-noise ratio in a scanning system, we have:

$$\frac{U_S}{U_N} = \frac{A_0 \omega}{\pi} \cdot \left(\frac{t_i}{A} \right)^{1/2} \int_0^\infty T^*(\lambda) R(\lambda, T_1) d\lambda \quad (5.19)$$

and instead of equation (5.14), which determines the contrast of the thermal image of an object with respect to the background at $\Delta T \ll T$,

$$\frac{\Delta U}{U_N} = \Delta T \frac{A_0}{\pi F^2} \cdot (A t_i)^{1/2} T_{max}^* \int_0^\infty S(\lambda) \frac{dR(\lambda, T)}{dT} d\lambda \quad (5.20)$$

where, $T_{max}^* = T^*(\lambda)/S(\lambda)$, $S(\lambda)$ - is the relative spectral response of the radiation receiver.

Like instantaneous receivers, receivers with signal accumulation reach the maximum possible sensitivity in conditions, when their noise is determined by fluctuations of background radiation, i.e. they operate in OF mode. In this case the noise (measured by the number of electrons) is equal to the square root of the number of charge carriers accumulated by the photosensitive cell due to absorption of the background radiation flux AQ_B :

$$U_N = (\eta_0 \cdot t_i \cdot A \cdot Q_B)^{1/2} \quad (5.21)$$

If the cell is irradiated by an energy stream of radiation from an object

$$p_S = (hc_0/\lambda) \cdot Q_S \cdot A \quad (5.22)$$

the cell accumulates a signal (also measured by the number of electrons):

$$U_S = \eta_0 \cdot t_i \cdot A \cdot Q_S(\lambda) \quad (5.23)$$

then from the expression:

$$T^*(\lambda) = \left(\frac{A}{t_i}\right)^{1/2} \frac{S(\lambda)}{U_N} = \left(\frac{A}{t_i}\right)^{1/2} \frac{1}{p_S} \frac{U_S}{U_N} \quad (5.24)$$

we obtain the values of $T^*(\lambda)$ under conditions restricted by background fluctuations:

$$T_f^*(\lambda) = \left(\frac{A}{t_i}\right)^{1/2} \frac{\lambda \eta_0 t_i A Q_S(\lambda)}{h c_0 Q_S A (\eta_0 t_i A Q_B(\lambda))^{1/2}} = \frac{\lambda}{h c_0} \left[\frac{\eta_0(\lambda)}{Q_B} \right]^{1/2} \quad (5.25)$$

Putting $T^*(\lambda)$ in equations (5.19) and considering (5.4) and (5.22), we obtain:

$$\left(\frac{U_S}{U_N}\right)_f = \frac{A_0 t_i^{1/2}}{\pi A^{1/2}} \int_0^\infty \eta_0^{1/2}(\lambda) \frac{Q_S(\lambda)}{Q_B^{1/2}} d\lambda \quad (5.26)$$

Equation (5.26) shows that an accumulated receiver can provide a high signal-to-noise ratio in background-limited mode if the signal accumulation time is long.

The most important factor that determines the maximum value of the accumulation time is the filling time of the potential well t_0 where the charge is accumulated. The filling time in turn depends on the capacity of the potential well and the rate of its filling. In the case when the filling time required for a given threshold sensitivity (or a given noise-to-signal ratio) exceeds the potential pit filling time t_0 , a given threshold sensitivity

cannot be fulfilled by the accumulated receiver considered without taking special measures to avoid overfilling of the potential pits.

Potential well filling time of TIR-cell can be estimated by formula:

$$t_0 = N_{\max}/\eta_0 \cdot Q_\lambda \cdot \sin^2 \theta \quad (5.27)$$

where, $N_{\max} \approx 10^{12} \text{ el} \cdot \text{sm}^{-2}$ - is the maximum electron density that can be accumulated in the silicon MOS capacitor; Q_λ - is the spectral density of blackbody radiation at 300 K, equal to $\approx 6 \cdot 10^{15} \text{ photon} \cdot \text{sm}^{-2} \cdot \text{s}^{-1} \cdot \mu\text{m}^{-1}$ at $\lambda = 4 \mu\text{m}$ and $\approx 1,7 \cdot 10^{17} \text{ photon} \cdot \text{sm}^{-2} \cdot \text{s}^{-1} \cdot \mu\text{m}^{-1}$ at $\lambda = 12 \mu\text{m}$ respectively (fig. 1): θ - is the aperture angle within which the background radiation hits the receiver. Estimates show that the potential pit filling times for receivers of the short-wave and long-wave windows of the IR-atmosphere transparency differ by a factor of tens, for example, as $\approx 10^{-2} \text{ s}$ and $\approx 4 \cdot 10^{-4} \text{ s}$ at $\lambda = 4 \mu\text{m}$ and $12 \mu\text{m}$, respectively. Even more different are the filling times of potential wells of near-infrared and visible radiation receivers, since in the visible range of the spectrum the intensity of the ambient background radiation itself is very small at a temperature of 300 K.

If the receiver system is intended to detect an object with minimum temperature difference ΔT on the background, which radiates as an absolutely black body with temperature T_0 , the value of accumulation time t_i required to realize a given signal-to-noise ratio $\Delta U/U_N$ must be less than the time of filling of potential pits by background radiation.

The particular effect of intense background radiation on the performance of multielement radiation receivers with signal accumulation must be emphasized. In matrices with signal accumulation, as in instantaneous multi-element matrices, the constant component of the background radiation causes the appearance of "geometric" noise, associated with differences in

the sensitivity of individual matrix elements. But it also determines the rate of filling of potential pits and hence the maximum possible signal accumulation time. For receivers with signal accumulation, careful shielding with cooled apertures must be ensured, and the aperture angle at which the background radiation hits the sensing element must not significantly exceed the aperture angle at which the object radiation is collected on the radiation receiver [112].

CHAPTER VI. CONFIGURATION OF MATRIX PHOTO-RECEIVING AMPLIFIERS (FRA)

Solid-state multi-element radiation receivers are divided into two classes: with coordinate sampling and with sequential charge transfer. The operation of modern receivers of the first class is based on the use of charge injection devices (CIC), the second class - on the use of charge-coupled devices (CCD).

6.1. Charge injection devices

Surface channel solid-state image receivers which use charge injection and charge transfer within individual photosensitive cells to read, store and scan. The simplest charge injection device is an MOS capacitor. When a voltage is applied to the capacitor and the near-surface region of the substrate is depleted of carriers, the nonessential carriers generated by the light are collected and stored in the surface inversion region. If the voltage is then removed, the stored charge is injected into the substrate and recombines. The magnitude of the injected charge can be determined by measuring the current in the external circuit during injection.

For $x - y$ addressing, each photosensitive matrix cell has two separate electrodes (line and column). In the storage state, the signal charge accumulates under both electrodes of the cell. To read out the signal charge, a zero potential is applied to the selected column and line buses. This injects a charge into the substrate from the photodetector cell located at the intersection of the column and row data. In all other zero potential column and row cells, the signal charge flows under the row or column electrode respectively. By measuring the current flowing in the external circuit during injection, the magnitude of the signal charge packets accumulated in the cells of the CIC matrix can be determined. This method of reading is called injection

sensing. Injection sensing is an information decay process because the injection frees the sensitive matrix cells from the accumulated charge. Variations of the injection readout are the sequential and pre-injection methods.

Another method of determining the amount of stored charge is based on measuring the change in potential of one of the electrodes of the cell when the signal charge is transferred from under the electrode of the adjacent capacitor. The transfer can be carried out in parallel in all sensing elements of any selected string. In parallel for all elements of a string it is also possible to perform an injection operation that removes the signal charge. This method of reading can be called transfer reading, it is non-destructive because the read and inject operations are performed separately. After the read operation, the signal charge packets can either be left in the matrix or injected into the substrate. Variations of this reading method are the parallel injection method and the line reading method. Let us consider as an example the sequential injection method, the schematic of which is shown in fig. 6.1 [113].

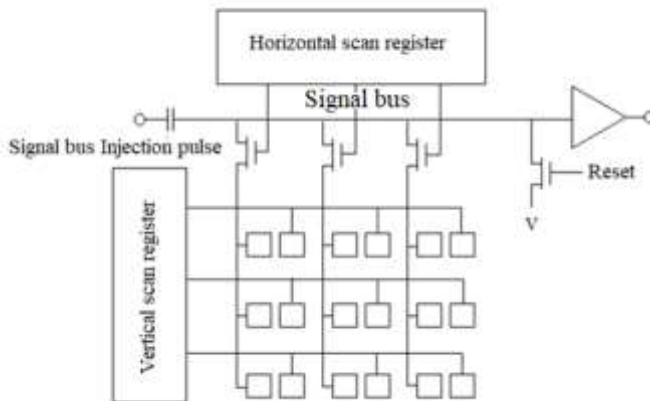


Figure 6.1. Schematic diagram of the sequential injection method

To determine the magnitude of the signal charge, the change in the floating signal bus potential during injection, connected by a horizontal scan register to one of the matrix columns, is measured.

When the vertical scan register is used to set the bullet potential on the selected string busbar, the charges in the cells of that string will flow under the column electrodes. This is followed by setting the reference potential on the signal busbar and the "selected" column busbar connected to it. A control pulse is then applied to the signal bus via the isolation capacitance and the signal charge in the selected cell is injected into the substrate, resulting in a change of signal bus potential which is amplified by the output preamplifier. Thus, all cells of a given row are polled while the other column buses of the matrix are connected in series to the signal bus. A zero potential is then set on the next line bus and the above process is repeated.

The main challenge in creating two-dimensional CCD arrays is to ensure 100% exchange of stored charge between the two electrodes of the photosensitive cell. A method similar to the 'fat zero' method used in CCD shift registers can be used to improve the exchange. In this case the surface states are always filled with charge carriers and do not affect the process of charge transfer from one potential well to another.

Another problem that arises when using CCD arrays is that the readout speed of the signal accumulated in the photodetector cells of a matrix must be relatively high. In most cases the manufacturing process for a given narrow band material is unsuitable to ensure that the required scan registers, sampling keys and preamplifier can be manufactured on the same chip as the photodetector cells.

In such an environment, said framing elements as well as SZN registers or other signal processing devices are fabricated on separate silicon crystals using standard technology. Since the SZN operation in such systems is performed on a single chip,

the CIC matrix must be fully interrogated in a single line shift time. In such cases the required readout rate may require the preamplifier bandwidth to be too wide. In such cases, it may be efficient to use a separate preamplifier per matrix column.

Another possible difficulty in using CIC receivers is the rather large output capacitance of the matrix, consisting of the intrinsic capacitance of the signal bus, the total cell capacitance of the connected column and the stray capacitance. The large value of output capacitance causes small value of noise voltage at the preamplifier input, corresponding to the given noise charge in the cells of the CIC - matrix, because $V = Q/C$.

Consequently, the preamplifier must have a sufficiently small equivalent input noise voltage so that the overall noise response of the whole system is determined by fluctuations in the background radiation. Combined with the requirement for a wide enough bandwidth, this can be a very demanding requirement on the preamplifier.

The compatibility of MOS - memory cores with LRD provides ample opportunities for creating energy-independent high-density information writing MDs. One of the most important issues to be solved during the creation of devices with a storage element MOS - capacitor is the recording of the amount of charge stored in the structure. At this time, the written information should not be scattered, the power used should be minimal, and the pace of information reading should be as high as possible. The article is devoted to the analysis of methods of reading information in a memory device based on MOS-LRD, which can be applied during the creation of different types of fillers.

Experimentally, the counting mode was studied in a 4-stroke LRD-register-based charger based on p-type silicon with an MOS-capacitor next to each electrode. Diffusion area was used to introduce the charge into the register, and the output signal was recorded by means of a linear amplifier (fig. 6.2).

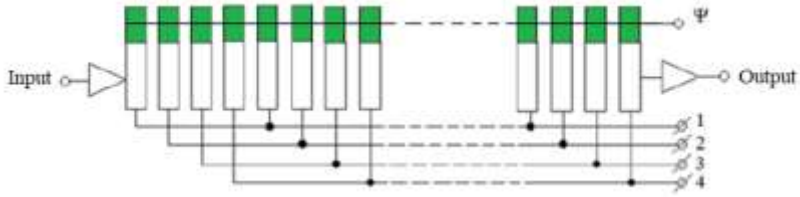


Figure 6.2. Schematic of the MD-charger based on the MOS-LRD

MOY - charge of any sign written into the structure can be stored for any time in the traps in silicon nitride. We will consider that when a negative voltage of sufficient amplitude is applied, the positive charges captured by the traps correspond to a logical zero, and when a positive voltage is applied, the capture of the negative charge (non-main charge carriers) corresponds to a logical unity. The applied load MOY – changes the boundary voltage of the structure, so the capacitance of the potential hole created when a depletion voltage is applied to the structure will be different in the logic zero and logic one states. MOY – the maximum load of non-main carriers that can be stored in the structure:

$$Q_{max} = c_g \cdot S \cdot (U - U_{boun.})$$

where, U is the stress applied to the structure, $U_{1boun.}$ – MDS (metal-dielectric-semiconductor) – the boundary voltage of the structure, c_g – the specific capacitance of the dielectric, S – the area of the element. The difference between the charges stored in the states of logical one and logical zero can take the following value:

$$\Delta Q_{max} = c_g \cdot S \cdot (U_{1boun.}^1 - U_{1boun.}^0)$$

Several methods based on the estimation of the storage capacity of the memory element are shown for counting information in MOS-LRD. In the conducted work, it is proposed to fully fill the charger with the load with the help of the HC,

and then to bring the charger under the MOS - elements by applying a depleting voltage. Thus, the depleting voltage can be selected in such a way that the charge in the case of a logical unit cannot remain under the electrode and is recombined. After some time, by applying clock pulses in a suitable sequence, the information load can be removed from the LRD and counted with the help of an amplifier. One of the main disadvantages of this method is the very small effect and the possibility of trapping the charge if it has not recombined. Other methods require the presence of additional elements in the structure, such as an injector and a control electrode, which leads to an increase in the area occupied by the circuit.

We have proposed and implemented a method that removes the requested load in all cases, this method does not require additional elements and has the same effect as the effect of the register of the LRD. Let's look at the request process of the filler, whose structure is shown in figure 6.3.

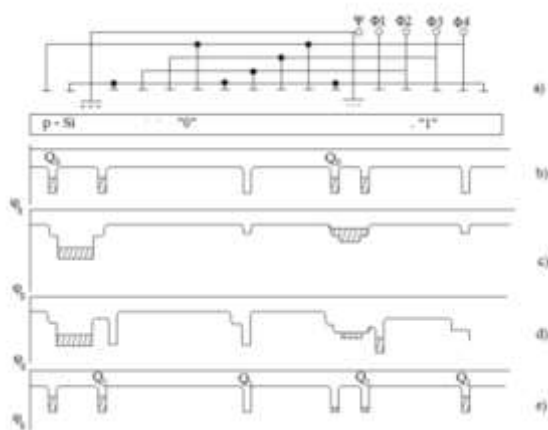


Figure 6.3. Cross-section of the structure and time diagrams of the profile of the surface potential in the process of counting information

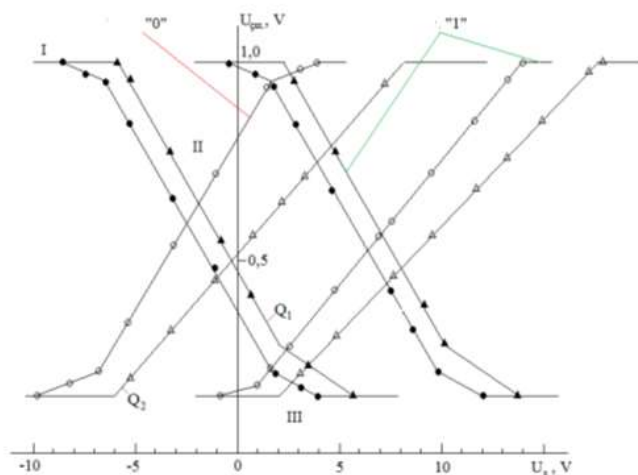


Figure 6.4. Dependence of the output voltage on the counting voltage in the cases of logical zero and logical one: $\Delta \blacktriangle$ – experiment; $\bullet \circ$ – calculation

Here, Ψ -MOS– capacitors are located near the Φ_1 – transport electrode. When the charging charge is given clock pulses to the LRD register, it is brought under the Φ_1 electrode (fig. 6.3 b), then the voltage on the transport electrode decreases to the U_d – support value, and at the same time, a depleting pulse is given to the Ψ – electrode (fig. 6.3 c). After the distribution of the asking charge between the Φ_1 – and Ψ – electrodes, a U_r – amplitude clock pulse is applied to the Φ_2 – electrode (fig. 6.3 d). A part of the charge, depending on the value of $U_{m.z.}$ – voltage of the planar zones, will flow into the potential hole under the Φ_2 – electrode, while the other part will remain under the Ψ - electrode and will arrive at the output with a delay of one period of the clock frequency (fig. 6.3 e).

Let us denote the load that arrives first at the output by Q_1 , and the load that is delayed by one period by Q_2 . Depending

on the value of Q_0 - asking charge, U_d - supporting voltage, U_s - counting voltage applied to Ψ - electrode, the ratio of the areas of Φ and Ψ electrodes, $U_{m.z.}$ - plane zone voltage, the load can be distributed in different ways. Figure 3 shows the calculated and experimental dependences of the output signal on the counting voltage at fixed values of Q_0 and U_d . curves have three characteristic areas. In area I, the surface potential under Ψ is less than the uneven surface potential under Φ_1 , and all charge flows under Φ_2 ($Q_1 = Q_0$, $Q_2 = Q_1$). With the increase of Φ_Ψ - surface potential, the distribution of Q_1 and Q_2 - charges (area II) occurs. U_s and U_d - for each value of external voltages, the value of loads in this area can be found from the following expression:

$$Q_1 = Q_0 - Q_2$$

$$Q_2 = c_\Psi S_\Psi \left\{ U_s - U_{m.z.} + \frac{eN_a \epsilon_s}{c_\Psi^2} - \frac{1}{c_\Psi} \left[2eN_a \epsilon_s (U_s - U_{m.z.}) + \left(\frac{eN_a \epsilon_s}{c_\Psi^2} \right)^2 \right]^{\frac{1}{2}} - U_d + \frac{eN_a \epsilon_s}{c_\Phi^2} - \frac{1}{c_\Phi} \left[2eN_a \epsilon_s U_0 + \left(\frac{eN_a \epsilon_s}{c_\Phi} \right)^2 \right]^{\frac{1}{2}} \right\}$$

where N_a is the dopant concentration and ϵ_s is the dielectric permittivity of the semiconductor.

When $S_\Psi c_\Psi (\varphi_\Psi - \varphi_\Phi) = Q_0$, the whole load will be delayed by one clock period, i.e. $Q_1 = 0$, $Q_2 = Q_0$ (field III). $\Delta U_{m.z.}$ - the quantitative assessment can be carried out by comparing the values of Q_1 and Q_2 to any support level or between themselves. The most convenient counting method is the counting method that provides the maximum difference of the signal in the case of logical zero and logical one, and the maximum deviation of the design parameters and supply voltages from the nominal values. We will assume that the working point, that is, U_s , U_d and Q_0 is chosen so that $\Delta U_{m.z.}$ change does not move this point out of the linear field of characteristics. The dispersion of the output signal from the comparison of Q_1 and Q_2 will take the following form:

$$\Delta Q_{12} = \Delta Q_{in} = \Delta(Q_1 - Q_2) = \Delta Q_0 + 2[(\varphi_\psi + \varphi_{m.z.} - \varphi_\Phi) \Delta S_\psi c_\psi + c_\psi S_\psi (\varphi_\psi + \varphi_{m.z.} + \varphi_\Phi)]$$

and the maximum of the signal difference in case of logical zero and logical one:

$$Q_{in}^0 - Q_{in}^1 = S_\psi c_\psi \Delta U_{m.z.}$$

will be dispersion of the output signal when comparing Q_1 with the reference signal:

$$\Delta Q_1 = \Delta Q_0 + (\Delta \varphi_\psi + \Delta \varphi_{m.z.} - \Delta \varphi_\Phi) S_\psi c_\psi + (\varphi_\psi + \varphi_{m.z.} - \varphi_\Phi) \Delta S_\psi c_\psi$$

When comparing Q_2 with the reference signal:

$$\Delta Q_2 = \Delta Q_1 - \Delta Q_0$$

The maximum value of the output signal:

$$Q_{in} - Q_d = (S_\psi d_\psi \Delta U_{m.z.})/2$$

Thus, the maximum value of the output signal is obtained between Q_1 and Q_2 , and the smallest dispersion of the output signal is obtained when comparing it with the reference signal of Q_2 . For a more reliable count, the following condition must be met:

$$Q_{in}^0 - Q_{in}^1 - \Delta Q_{in} > Q_{boun.}$$

where, $Q_{boun.}$ is the boundary sensitivity of the amplifier. At the time of writing, the planar zones are $U_{m.z.}$. The change in the value of the voltage should be such that the following condition is met when comparing Q_2 and Q_1 :

$$\Delta U_{m.z.} > \frac{Q_{boun.} + \Delta Q_{12} - Q_0}{2c_\psi S_\psi} + (\varphi_\psi - \varphi_\Phi)$$

If Q_2 is compared to the reference level ($Q_0/2$):

$$\Delta U_{m.z.} > \frac{2(Q_{boun.} + \Delta Q_2)}{2c_\psi S_\psi} + (\varphi_\psi - \varphi_\Phi)$$

If we use the comparison of (11) and (12) and (5) and (8), the following considerations are obtained: if $Q_{boun.} > \Delta Q_0$, the information count is from the comparison of Q_1 and Q_2 ; if $Q_{boun.} < \Delta Q_0$ is more favorable than the comparison of Q_2 with reference signal. If MOS – the size of the capacitor core is 25

μm^2 and $\Delta U_{\text{m.z.}} = 4 \text{ V}$, the limit sensitivity of the amplifier should be 0.12-0.13 pKl. The voltage U_0 is selected in such a way that it is possible to store the requested charge Q_0 , that is, the condition $c_\phi U_0 \geq Q_0$ is satisfied.

In the process of counting, the maximum value of the quick effect $\varepsilon Q_0 n = Q_{\text{boun.}}$ ε - determined from the expression is limited by the ineffectiveness of transport. Here, n is the number of load carrying cycles. In my counting process, the power dissipated in the crystal is not that great, since the questioner fills 10-15% of the potential hole of the LRD. The quantity εe can be estimated from the formula $P = N f_T Q_0 U_T$: where, N is the number of clocks, f_T is the clock frequency. In our case, the power dissipated during the counting of one bit of information for a frequency of 1 MHz is 5 mW.

6.2. Charge-coupled devices

Charge-coupled devices are used to create matrix IR-FRA in two basic configurations (fig. 6.5a, fig. 6.5b).

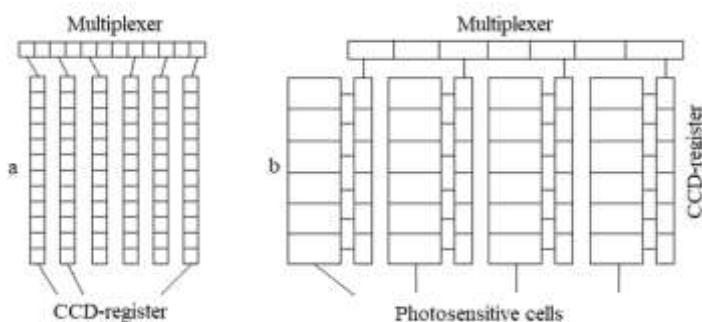


Figure 6.5. CCD based matrix ROM configurations

In the first case (fig. 6.5a) the MDS-shift register cells simultaneously act as photosensitive elements. Such

configuration provides high density filling of a focal plane of the receiver.

In systems with mechanical image scanning along the CCD matrix the shift registers carry out SZN mode of signal processing. In this case, the SZN operation and detection are carried out on a common chip, so in such a system, there is no pre-multiplexing of the signal. As a consequence, the CCD receivers of this configuration require a significantly lower readout rate than the FRA receivers.

The speed of the output register, on which the signals from the outputs of each SPE-register are applied, must be m times (where m is the number of columns of the matrix) faster than the speed of the SPE-registers. If technological constraints do not allow for such fast registers with high charge transfer efficiency in a narrow band material, the output register is manufactured on a separate silicon crystal using standard technology.

The output signals of the SZN-registers have a sufficiently large amplitude and are characterized by a relatively high signal to noise ratio (as a consequence of the SZN processing). In addition, the output capacitance of the SZN-registers is quite small. Therefore, a significant disadvantage of this CCD receiver design is only a large number of interconnections.

In CCD receivers usually aim for possibly high charge capacity of CCD-register cells, especially in systems designed to operate with strong background radiation, due to the fact that the background signal is added at each stage of SZN-processing. CCD receivers are free of this disadvantage because a variable component of the signal can be separated before the SPD processor. The second configuration based on charge-coupled devices (fig. 6.5 b) differs in that the radiation detection is performed in separate photosensitive cells (not necessarily TIR) connected to CCD registers, which carry out SPD signal processing in systems with mechanical image scanning. Matrices in this configuration are more complex because they

contain a number of additional elements that communicate between the detectors and the CCD, and provide a lower density of photosensitive elements in the focal plane. On the other hand, they allow for separation of the variable signal component, background suppression and some other processing between the detectors and the CCD registers. The dynamic range of the system is extended because the background signal no longer accumulates in the CCD-register cells. In this case it may also be appropriate to use an output multiplexer on a separate crystal.

6.3. Hybrid structures

The above considered FPU's with series charge transfer are analogues of silicon FPU's in the visible range and, in principle, can be fabricated as monolithic structures based on narrow-band semiconductors. However, the efficiency of charge transfer in CCD registers made of narrow-band semiconductors is much lower than in silicon, which leads to a decrease in sensitivity of FRA with an increase in the number of elements in the matrix. As a consequence, monolithic charge transfer semiconductor arrays in the infrared spectrum range have a smaller number of elements than silicon CCD arrays in the visible spectrum range. The limitations of low charge transfer efficiency in narrow-band semiconductors do not apply to hybrid structures with sequential charge transfer or to matrices with coordinate sampling. In hybrid structures, charge packet transfer takes place in silicon registers with high charge transfer efficiency and radiation detection takes place in a matrix of radiation receivers based on a narrow-band semiconductor or impurity silicon.

In multielement receivers assembled according to a hybrid circuit, the conversion of an optical signal into an electrical signal and its subsequent processing takes place separately in two constituent parts made of different materials. The detection of optical radiation takes place in a matrix of photosensitive

elements made of narrow-zone semiconductors. The primary signal processing step consists of polling the photosensitive matrix elements one by one, multiplexing the channels and amplifying the signal, and uses a dedicated processor based on silicon (CCD structures or MOS switches for two- or single-coordinate addressing).

An advantage of the hybrid multi element matrix system is that the detection and readout structures can be optimized separately. To create photosensitive structures it is possible to use the material that best meets the operational requirements in terms of operating temperature, spectral sensitivity range, geometry of sensitive elements, and to read signals it is possible to use the material with the most mature technology for CCD structures and MOS switches, with low noise level, wide dynamic range and low power dissipation. The operating temperature of hybrid structures can be increased compared to monolithic structures because they can use photodiodes with small dark currents as photosensitive elements.

The main technological challenges in creating multi-cell receivers using hybrid circuitry arise at the stage of connecting the sensing element to the corresponding input of the silicon processor. This connection must carry out not only electrical, but also thermal and mechanical connection of photosensitive matrix and reading structure. It is this step that is decisive in the technology of hybrid structures and determines the maximum number of elements in the matrix.

Two main methods are used to combine the photosensitive matrix and the reading silicon structure:

- Edge-metallization by directly applying photosensitive material to the silicon crystal;
- Inverted mounting (flip - chip method) using contact columns of soft metal, e.g. indium.

In edge-metallization the electrical contact between the output of the photosensitive element and the input of the silicon

readout structure is made by sawed metal contacts. This structure is typically used to create one-dimensional arrays with gaps between the elements of approximately 25 μm .

For two-dimensional arrays, the method of "inverted" mounting is more commonly used. In this process, the matrix of photosensitive elements and the silicon structure are fabricated and inspected separately, then the indium columns are applied and then mechanically bonded together using thermal compression.

The more the coefficients of thermal expansion of the photosensitive material and silicon differ, the fewer elements can be incorporated into the matrix. For example, photosensitive matrices made of lead chalcogenides (PbS , PbSe , PbTe) having the coefficient of thermal expansion $20 \cdot 10^{-6} \text{ K}^{-1}$ (for silicon $\text{CTE} = 2 \cdot 10^{-6} \text{ K}^{-1}$) are compatible with the silicon reading structure with the number of elements not exceeding 10^2 .

As an IR-transparent substrate on which photosensitive material is deposited by liquid-phase epitaxy or molecular beams, BaF_2 , InAs or CdTe are commonly used. IR-transparent substrates can also be used. In this case electric contacts to photosensitive elements are formed on the same side of a substrate, on which radiation falls.

6.4. Basic characteristics of photonic receivers

Photonic receivers used in IR systems must meet certain requirements.

1. The spectral range of photosensitivity of a photodetector is given by the inequality $\lambda < \lambda_{\text{th}}$ and is determined by the excitation energy of electrons in the photosensitive material. For intrinsic and impurity photodetectors $\lambda_{\text{th}} = 1,24/\Delta E$, where λ is measured in micrometers and ΔE in electron volts. For Schottky diode receivers, $\lambda_{\text{th}} = 1,24 \varphi_0$, where φ_0 is the height of the

potential barrier equal to the difference between the metal yield work and the electronic affinity of the semiconductor.

2. The maximum operating temperature to which a photon radiation receiver must be cooled is determined by the requirement that the receiver must operate in a mode where its characteristics are determined by background radiation (background-limited mode - BLM).

3. For a receiver to operate in the BLM mode, it is necessary that the Johnson noise is negligibly small compared to the generation-recombination background noise.

4. For a receiver operating in BLM mode to have the best threshold characteristics, it is necessary that the quantum conversion efficiency η_0 be the highest, close to unity.

Conditions 1 and 4 are rather obvious, so let us consider in more detail only conditions 2 and 3. The optimum operating temperature of IR receivers is the temperature of the sensing element that provides the best parameters of the receiving system for the given application and, first of all, the best threshold sensitivity.

The best threshold sensitivity is achieved with the lowest possible noise level. The principal intractable noise in semiconductor photodetectors is generation and recombination noise.

Other noise can either be eliminated completely or significantly reduced in one way or another. For this reason, the optimum operating temperature for a receiver is the temperature at which the generation-recombination noise is lowest.

6.5. Impurity photoresistor

The total noise of a photoresistive radiation receiver, referenced to a unit frequency band $\Delta f = 1$, is described by the expression:

$$I_N^2 = 4e \left(e\eta_0 Q_B A G^2 + eR_T A d G^2 + \frac{kT}{eR} \right) \quad (6.1)$$

where, e - charge of electron; Q_B - intensity of photon flux, falling on the receiving pad of sensitive element; $\eta_0 Q_B$ - speed of optical generation of charge carriers in photosensitive element; A - area of sensitive element of receiver; G - photoelectric gain, equal to the number of current electrons in external circuit, divided to one absorbed photon; R_T - speed of thermal generation of free carriers in photoresistor volume; d - thickness of photosensitive element in direction of radiation propagation. The first term in (6.1) takes into account the generation-recombination noise resulting from the optical generation of free carriers; the second term, the generation-recombination noise of thermal generation; the third term, the Johnson noise. Current sensitivity including photoelectric gain:

$$S_i(\lambda) = (e\eta_0\lambda/nc_0) \cdot G \quad (6.2)$$

From (6.1) and (6.2) it follows that the reduced detectability of the photoresistor is equal:

$$D^*(\lambda) = \frac{\lambda}{hc_0} \frac{\eta_0}{\left(\eta_0 Q_B + R_T d + \frac{kT}{e^2 G^2 R A}\right)^{1/2}} \quad (6.3)$$

Under conditions where the photodetector noise is determined by generation-recombination noise only:

$$D^*(\lambda) = \frac{\lambda \eta_0}{2hc_0} \left(\frac{1}{R_T d + \eta_0 Q_B} \right)^{1/2} \quad (6.4)$$

the assumption made fulfils the condition of paragraph 3, i.e:

$$\eta_0 Q_B \gg \frac{kT}{e^2 G^2 R A} \quad (6.5)$$

For impurity resistors it is usually true because their dark resistance at low temperatures is very high. The impurity resistor is usually used in circuits with a small load resistance, and as the photoresistor noise decreases, the Johnson noise of the load resistance begins to appear earlier than the Johnson noise of the photoresistor dark resistance. The rate of thermal generation of free current carriers in an impurity photoresistor (assume for certainty that the photoresistor is made of a semiconductor with hole conductivity):

$$R_T = \frac{P_0}{\tau} = \frac{N_A - N_D}{2q} \cdot N_v B_r \cdot \exp\left(-\frac{\Delta E_A}{kT}\right) \quad (6.6)$$

where, P_0 - concentration of free holes; τ - lifetime of holes; N_A , N_D - concentrations of acceptors and donors; N_v - effective density of states in valence band; B_p - hole recombination factor; q - degeneration factor of acceptor levels; ΔE_A - ionization energy of acceptor impurity; k - Boltzmann constant; T - temperature of sensitive layer.

Thus, for a doped photoresistor, the reduced detectability under conditions where the photodetector noise is determined by the generation-recombination noise is equal:

$$D^*(\lambda) = \frac{\lambda \eta_0^{1/2}}{2hc_0} \left[\frac{(N_A - N_D) dN_v B_r \exp\left(-\frac{\Delta E_A}{kT}\right)}{2\eta_0 q} + Q_b \right]^{1/2} \quad (6.7)$$

As can be seen from (6.7), at high temperatures, the first term in the subcorrelated expression dominates and the photodetector operates in a mode in which its detectability is determined by the rate of thermal generation of free charge carriers, $D^*(\lambda)$ being a function of temperature. As the temperature decreases, the intensity of thermal generation decreases, the first summand of the chaining expression decreases, and the value of $D^*(\lambda)$ increases.

At low temperatures, the second term dominates; the detectability in the first approximation does not depend on the temperature and is only determined by the intensity of the background radiation. In these conditions, the receiver operates in the background limiting mode (BLM mode or BLIP mode) and $D^*(\lambda) = D\lambda^*(Q_B)$. The graph of dependence of D^* on temperature is shown in fig. 6.6. The temperature at which the optical and thermal carrier generation rates are equal can be taken as the optimum receiver temperature T_0 .

By equating the terms in the sub-rectified expression (6.7), we find:

$$T_0 = \frac{\Delta E_A}{k} \left[\ln \frac{(N_A - N_D) dN_v B_r}{2\eta_0 q Q_B} \right]^{-1} \quad (6.8)$$

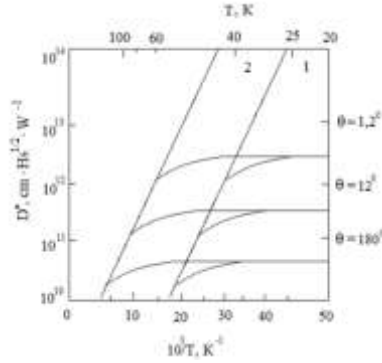


Fig. 6.6. Temperature dependences D^* for impurity Ge(Hg) photoresistor (1) and native HgCdTe alloy photoresistor (2) at different background radiation intensities determined by aperture angle θ [114].

At the optimum temperature, the reduced detectability is $2^{1/2}$ times lower than the maximum possible value:

$$D_{\lambda}^*(Q_B) = \frac{\lambda}{2hc_0} \left(\frac{\eta_0}{Q_B} \right)^{1/2}$$

The main factor determining the temperature T_0 is the impurity level ionization energy ΔE_A .

The lower the ionization energy and the higher the long wavelength limit of photosensitivity λ_0 , the lower the optimum operating temperature T_0 . Considering $\lambda_0 = 1,24/\Delta E$ from (6.8) we can get:

$$T_0 \lambda_0 \approx 1,24 \left[k \cdot \ln \frac{(N_A - N_D) d N_v B_r}{2 \eta_0 q Q_B} \right]^{-1} \quad (6.9)$$

The optimum operating temperature is the higher the background illumination level Q_B . An increase in the background illumination level not only decreases the absolute value of the reduced detectability, but also increases the

temperature at which the receiver enters the BLM mode. The value of T_0 depends on the characteristics of the semiconductor material of which the sensing element is made, and in the first place, on the B_r recombination coefficient. The value of T_0 does not depend on impurity concentration because $\eta_0 \approx (N_A - N_D)d$ and consequently, the right side of equation (4.3) does not include impurity concentration. In order to increase the operating temperature, the semiconductor material with the lowest recombination coefficient should be used. Among all known mechanisms of charge carrier recombination in semiconductors, radiative recombination, Auger recombination and recombination with phonon emission are the most important. The minimum achievable value of B_r and, consequently, the limit (maximum) value of T_0 is determined by the emissive recombination process. Naturally, this limit value T_0 corresponds to the given operating conditions, i.e. wavelength range $\lambda < \lambda_0$ and the background illumination level Q_B .

6.6. Reliability of semiconductor based radio electronic devices

Since the radio-electronic and electronic devices of modern space vehicles have tens of millions of complex devices, the problem of increasing the reliability of these devices is of great importance. The most important of the quantitative characteristics of reliability is the intensity of rejections. In this case, failure is understood as an event resulting in the product's malfunctioning. The property of an electronic device maintaining its ability to work for a certain period of time is called fail-safe. This property is characterized by the probability $p(t)$ of fail-safe operation during the time period t .

Determining the reliability of electronic devices is considered one of the important issues during the operation of

space vehicles. Reliability is the property of the object performing the given functions during its activity within the given limits according to the given modes, conditions of use and mode, maintenance, repair, and maintenance.

The probability of failure is determined from the following expression:

$$p(t) = \frac{n(t)}{N},$$

where, $n(t)$ is the number of active devices at any time; N – the total number of primary devices tested; $n(t)/N$ is the probability of failure of an individual radio-electronic device at any time t . The intensity of rejections $\lambda(t)$ characterizes the intensity of device failure and is determined by the following expression:

$$\lambda(t) = \frac{\Delta n}{(N - d)\Delta t},$$

where, Δn is the number of failures of devices during the time of small Δt ; N – total number of tested devices; $d - \Delta t$ is the number of devices that have given up before the start of the time interval. The probability of working without refusals and the intensity of refusals are related to each other as follows:

$$p(t) = \exp \left[- \int_0^t \lambda(t) dt \right].$$

The intensity of rejections $\lambda(t)$ for electronic devices has three characteristic time intervals (figure 6.7). The initial time interval (region I) corresponds to rapid failures, the reasons for which are the manifestation of hidden manufacturing defects. The second region of time (II) corresponds to the normal operation period, when the value of $\lambda(t)$ changes little compared to the period of initial rejections. In the third time zone (III zone), the intensity of rejections increases again due to the wear of devices. In this area, rejections due to changes in device parameters prevail. The grid required for one rejection is related to the average time $\lambda(t)$ as follows: grid = $1/\lambda$.

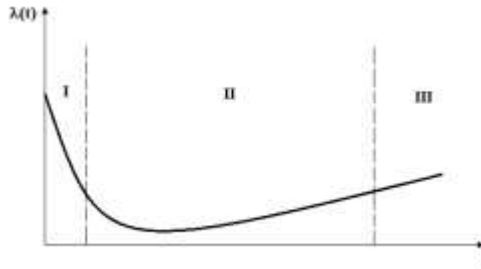


Figure 6.7. Rejection intensity $\lambda(t)$ for electronic devices

$\lambda = 5 \cdot 10^6 \text{ h}^{-1}$ and $t = 5000 \text{ h}$ when $\lambda_t = 2.5 \cdot 10^{-2}$ then $p(t) = p(5000) = 0.975$; $t_{or} = 2 \cdot 10^5$ hours, that is, the working life of the device should be 20,000 hours for bi-examination.

Reliability indicators determine the longevity of devices - a parameter that determines the period of guaranteed functionality of radio-electronic devices during their operation. Rejections according to the nature of the change of parameters of radioelectronic devices can be divided into two large groups:

- 1) catastrophic (sudden) characterizing the impulsive (jump) change of device parameters;
- 2) conditional rejections characterizing the intermittent change of parameters.

The first type of rejection usually leads to a complete loss of functionality of devices. In the second case, the device can maintain its functionality either completely or partially, but its parameters significantly deviate from the initial or complex values over time. Catastrophe waivers, which refer to unconditional waivers, are typically conditioned by design or technology deficiencies as well as heating conditions. Structural defects that lead to catastrophic failures may be due to the fact that the materials of the device elements have different coefficients of thermal expansion, which leads to mechanical failure of contacts and cracking of semiconductor crystals. This manifests itself more in powerful devices. In order to prevent

such defects, they place thermocompensating materials between individual elements of the structure.

In high-frequency devices, mainly in semiconductor devices, the dimensions of the electrodes are measured in μm . The outputs of such devices are created from thin ($\sim 8 \mu\text{m}$) wires that cannot be made homogeneous due to their length. As a result, internal outputs may break or burn. When long internal outputs are used, burning out of the outputs also occurs in case of a significant change in temperature and violation of the technology of soldering the contacts. In addition to the breaking and burning of outputs in electronic devices, it is also possible to puncture the connections and oxidize the layers, as well as short circuit. All these processes cause a short circuit between different electrodes. The reason for the punctures is due to the violation and imperfection of technologies, improper operation related to the observation of the operating modes of the devices. An example of the imperfection of technologies in planar transistors is the presence of microscopic holes that cause holes in the oxide layer. After the addition process, the presence of dust on the surface of the photoresistor leads to the formation of holes in the places where they are located.

Let's examine the main reasons for the occurrence of catastrophic failures, since the reliability of the devices in the circuit during improper operation of the devices depends not only on its specific reliability, but also on the operating conditions. 70% of all semiconductor device failures are caused by improper operating conditions. An example of improper operating modes is the use of devices in modes above the maximum allowable mode. One of the most important parameters that determine the reliability of the device is the power dissipated by the switch in the device, the ambient temperature and the maximum allowable temperature determined by the heat exchange between the environment and the switch.

An increase in the power dissipated by the device will lead to heating of the device elements. An increase in temperature leads to an increase in the share of specific electrical conductivity in the doped semiconductor. As a result, at a certain temperature, the electron-hole transition generally ceases to exist. The lower temperature at which the main properties of the device are maintained is taken as the maximum allowable temperature. The transition temperature is determined by the semiconductor material (silicon, germanium, gallium arsenide, etc.) and its doping degree. Highly doped semiconductor devices (eg, tunnel diodes) have a maximum allowable junction temperature ($T_{\max.k}$), while lightly doped semiconductor devices (eg, high-voltage diodes) have the lowest temperature ($T_{\min.k}$). In order to increase reliability in practice, it limits the ambient temperature in the range of 30...40 °C, and the operating power P_{\max} is less than half of the maximum power.

The maximum allowable voltage between the electrodes of devices is often decided significantly lower than the breakdown voltage of the junction: to the possibility of breakdowns that can occur both in the volume and on the surface of the semiconductor; the effect of the absence of requirements for the multiplication of charge carriers in the collector junction on the current transfer coefficient; due to the presence of technological defects (inhomogeneity, external connections) of the semiconductor material. The maximum allowable values of the currents are determined from the condition of heating of the transition, taking into account the inhomogeneity of the material. Catastrophic rejections account for 15...20% of the total number of rejections. The vast majority of rejections are due to the gradual change in the settings of the devices. Conditional rejections are caused by physical and chemical processes in the volume and surface of semiconductor devices. In semiconductors, volume processes that lead to unacceptable changes in parameters do not play a big role. The change of

parameters of semiconductor devices is related to the processes taking place on the surface. Changes in surface states lead to significant changes in reverse currents, transmission coefficients, and breakdown voltages of semiconductor devices. One of the main factors that determine the instability of the electrophysical properties of semiconductors is the presence of moisture. In order to prevent moisture from falling on the surface of the semiconductor, the housings of the devices are hermetically sealed and a moisture absorbent (sorbent) is placed inside the housing: silica gel or almyugel. Another reason for the instability of the surface properties is related to the movement of ions of alkali metals (sodium, calcium, potassium) in the oxide layer. The surface density of these ions is 10^{14} ions/cm². These ions create dynamic volume charges in the silicon dioxide layer that affect the properties of the junctions and the parameters of the devices.

Thus, the impact on the operating conditions of the facilities is manifested in the intensity of both disaster and conditional rejections. For transistors, such an effect can be given in the form of dependences shown in figure 2. The figure shows the effect of the normalized temperature T_n and the scattered power P_k on the quantity λ (P_{kmax} is the maximum permissible power in the collector). The value of the normalized temperature is determined from the following expression:

$$T_n = \frac{T_{oper.} - T_{ac.}}{T_{max} - T_{ac.}},$$

here, $T_{oper.}$ - working temperature; T_{max} - maximum permissible temperature; $T_{ac.}$ - is the temperature at which the drop of the electrical mode begins.

Thus, during long-term and uninterrupted operation of the devices, it is considered more appropriate to take the operating modes as low as possible below the maximum allowable values.

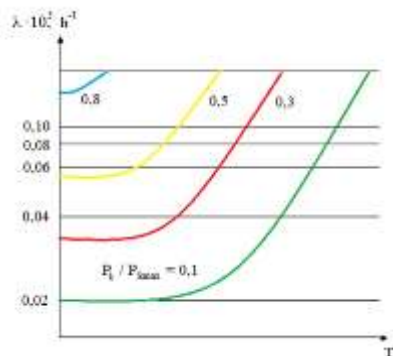


Figure 6.8. Effect of normalized temperature T_n and scattered power P_k on quantity λ

In the end, we can talk about specific values of the intensity of rejections of electronic devices. Region I in figure 6.8, which corresponds to the start-up period, varies from unity to several hundreds of hours for different electronic devices. A noticeable increase in the intensity of rejections corresponding to the aging period is not observed for semiconductor devices (fig. 1, region III), which proves the longevity of such devices. Rejections $\lambda(t)$ during normal operation and in nominal modes (fig. 1, region II) are 10^{-7} - 10^{-3} h^{-1} for diodes and transistors, and 10^{-5} - 10^{-4} h^{-1} for electronic lamps 1 is.

6.7. Interaction of a quantum system with external radiation

If the quantum system is in a state of thermodynamic equilibrium, this system absorbs external radiation energy, so that the number of transitions from lower levels to higher levels is greater than the number of reverse transitions. In order to achieve amplification of light (electromagnetic waves) in the medium, it is important that the number of transitions occurring with energy radiation exceeds the number of transitions

occurring with energy absorption. For this, the state of thermodynamic equilibrium must be disturbed.

In thermodynamic equilibrium, the number of radiation transitions from the upper state to the lower state (N_2) is equal to the number of radiation absorption transitions from the lower state to the upper state (N_1). The number of transitions N_2 is determined by the product of the probability of one transition to the occupancy of the energy level E_2 [11,28]:

$$N_2 = n_2(W_{21} + w_{21}) = g_2(\rho_V B_{21} + A_{21}) \exp \left[-\frac{E_2}{kT} \right].$$

Analogous to the number of induced transitions from the lower state to the higher state, the number of transitions that determine energy absorption is given by:

$$N_1 = n_1 W_{12} = g_1 \rho_V B_{12} \exp \left[-\frac{E_1}{kT} \right],$$

where n_1 and n_2 are the number of particles located in E_1 and E_2 levels, respectively; g_1 and g_2 are statistical weights of levels 1 and 2.

The relationship between the coefficients A_{21} , B_{21} , B_{12} is found from the thermodynamic equilibrium condition when $N_1 = N_2$. Most of the active substances used in quantum electronics are multilevel systems. However, as a rule, despite the large number of levels involved in the process of laser radiation generation, many active media can be conventionally divided into three or four working level systems, so that in the process of population inversion and radiation generation, a set of three or four energy levels is actually formed. participates. Such a collection of levels can form energy bands (eg levels 3 in fig. 1a and b).

So, the active environment can be conventionally called three- or four-level. Let us first consider the condition for obtaining population inversion in a three-level quantum system (figure 6.9a). Auxiliary radiation acts in the frequency range of the ν_{13} transition and forces atoms or molecules of the active substance to move from level 1 to level 3, which is wider. After

a certain period of time, the particles pass from level 3 to the 2nd metastable level (relaxation transition), whose lifetime without radiation is several orders of magnitude greater than the lifetime of the 3rd level [39].

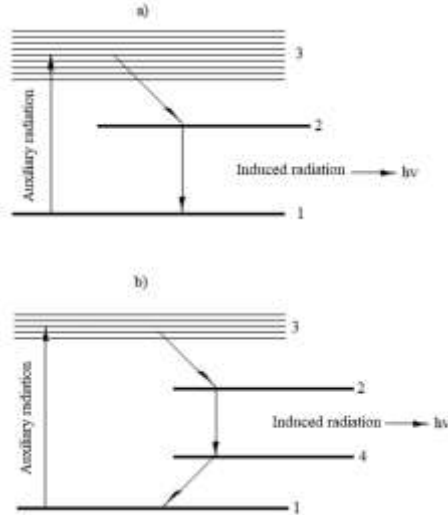


Figure 6.9. Energy bands created by a set of energy levels

As a result, the accumulation of particles in the second level occurs and the settlement inversion is realized ($n_2 > n_1$). From the solution of the kinetic equations for n_2 and n_1 , it is important to satisfy the following conditions to obtain the settlement inversion under the condition of minimal auxiliary radiation:

$$\tau_{31} \gg \tau_{32}; \quad \tau_{21} \gg \tau_{32},$$

where τ_{31} and τ_{21} are the time of spontaneous transitions and τ_{32} is the relaxation time between the corresponding levels.

The first inequality is that particles that go to level 3 under the influence of auxiliary radiation must go to level 2 without returning to level 1. According to the second relationship, the particles in level 2 should stay in this level for

a longer time than in level 3, which causes particles to accumulate in level 2 of the radiative transition 2 – 1 (metastable level). The three-level system has a number of disadvantages, such as the presence of a large number of spontaneous 2 – 1 transitions in addition to induced transitions, such as the large power of auxiliary radiation [44].

Circuits with four energy levels have many advantages over three-level circuits (figure 6.10).

An additional fourth level of energy is located between the first and second levels of the three-level scheme. In order to get population inversion in the four-level scheme, the excited particles must pass from level 3 mainly to level 2, that is, the condition $\tau_{32} \ll \tau_{31}, \tau_{34}$ is fulfilled. In addition, the inequality $\tau_{21} > \tau_{24}$ must be satisfied. This shows that transition 2 – 4 is more likely than transition 2 – 1 and the lifetime of particles in metastable level 2 is significantly longer than the lifetime in level 4, i.e., $\tau_{24} > \tau_{41}$.

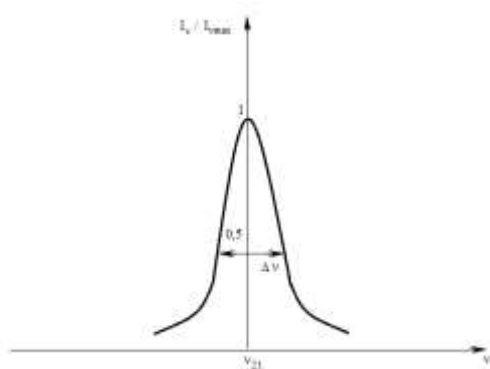


Figure 6.10. Settlement inversion in a four-level scheme

During the analysis of the process of interaction of the quantum system with external radiation, it is assumed that the width of E_1 and E_2 energy levels is equal to zero and the amplification occurs only at one frequency ν_{21} . However, in

reality, radiation occurs in any frequency band determined by the increase in the width of the energy levels. The power radiated by the quantum system is maximal at any frequency $\nu_{21} = (E_2 - E_1)/h$ (corresponding to energies $E_{1,2}$) and decreases on both sides of this frequency. The frequency dependence of the spectral intensity I_ν of radiation (absorption) is called the spectral line of radiation (absorption). A typical dependence of $I_\nu = f(\nu)$ is given in figure 6.10. The width of the spectral line ($\Delta\nu$) is the frequency interval at the boundaries of which the power of the radiation decreases from the maximum value to half.

It is clear that the quantity $\Delta\nu$ is determined by the width of the energy levels: $\Delta\nu = (\Delta E_2 + \Delta E_1)/h$, where ΔE_2 and ΔE_1 are the energy widths of levels 2 and 1, respectively. The smallest width of a spectral line is called the natural width. It is determined by the probability of natural or spontaneous radiation and has a value from several Hz to several MHz. The Doppler effect has a noticeable effect on the growth of the width of the spectral lines, so that the atoms, molecules, and ions radiating inside the gas either move in the crystalline lattice of the solid body or dance in different directions at random speeds. As a result, a frequency shift will occur in proportion to the speed of displacement of the indicated particles relative to the observer.

In such a case, the spectral line will be the sum of the spectral lines of all the particles of the considered system - and for a certain frequency, it will be proportional to the number of particles with the resonant frequency added to this sum. The expansion due to non-overlapping resonance frequencies of different microparticles is called inhomogeneous expansion. If the average dispersion of resonant frequencies of microparticles is greater than the width of the spectral line determined by the homogeneous broadening of the lines of each atom and the system as a whole, inhomogeneous broadening will prevail [52].

Strong broadening of spectral lines also results from particle collisions, population of energy levels, and other factors. The total width of the spectral line in the optical range can exceed several hundred MHs.

As a result of the expansion of the induced radiation energy received due to the settlement inversion, it is distributed along the entire width of the spectral line. Settlement inversion in different types of lasers is created by different methods. The process of creating inverse population in quantum systems is auxiliary radiation. Quantum systems capable of amplifying electromagnetic radiation should in principle have two main elements – an active medium and an auxiliary radiation source that provides population inversion.

If a plane electromagnetic wave propagates in the x-axis direction in an inverse populated active medium, calculations show that the intensity of the wave $I = \rho v$ (v is the speed of the electromagnetic wave) (the density of the energy flow) at any section $x = \text{const}$ within the active medium ($0 \leq x \leq L$) from the following relation is set:

$$I = I_0 \exp \left\{ \left[B'_{21} \left(\frac{h\nu}{v} \right) \left(n_2 - \frac{g_2 n_1}{g_1} \right) - \beta \right] x \right\},$$

where I_0 is the intensity of the wave at the entrance of the active medium (at the cross-section $x = 0$), β is a constant characterizing the value of losses per unit length in the active medium (for example, scattering due to inhomogeneities, defects in crystals, etc.) (fig. 6.11).

The coefficient $B'_{21} = B_{21}/(2\pi\Delta\nu)$ is proportional to the B_{21} – Einstein coefficient ($\Delta\nu$ is the width of the contour of the spectral line). The parameter that determines the gain of a wave per unit length is defined as:

$$\alpha = B'_{21} \left(\frac{h\nu}{v} \right) \left(n_2 - \frac{g_2 n_1}{g_1} \right).$$

When inverse settlement exists $n_2 > g_2 n_1 / g_1$, the intensity of the wave increases exponentially as it propagates through the medium. It can be seen from expression (4) that when $x = L$, that

is, the intensity at the output of the active medium is equal to $I_0 \cdot e^{(\alpha-\beta)L}$.

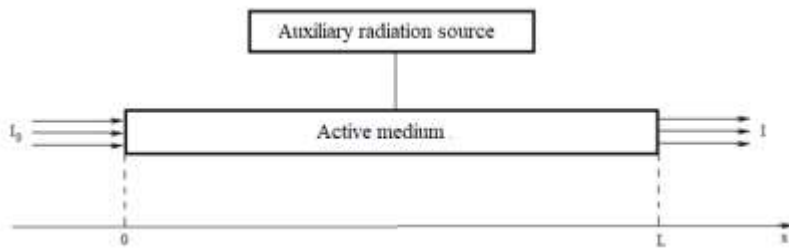


Figure 6.11. Quantum systems capable of amplifying electromagnetic radiation – an active medium and an auxiliary radiation source providing population inversion

In other words, settlement inversion increases exponentially with overstrength. The last two expressions take into account amplification factors related to the width $\Delta\nu$ of the spectral line contour.

PART 2

7. PROSPECTS FOR THIN-FILM SOLAR CELLS

A characteristic feature of mankind's technical activity in the second half of the twentieth and early twenty-first centuries is the rapid growth of energy consumption. It is estimated that by the middle of the XXI century the energy needs of mankind in comparison with the current level of consumption (~ 13 TW) will more than double (~ 30 TW), and by the end of the XXI century will more than triple (~ 46 TW). - will more than triple (~ 46 TW). This is due, firstly, to the growth of the world economy as a whole (up to 4 times by 2050), and the dramatic economic growth of developing countries such as China and India, whose population is 2/3 of the world population. Second, it is associated with a marked increase in the world's population. By 2050, the population of the Earth will reach 10-11 billion people.

The increase in energy production has so far been mainly due to the use of fossil energy sources - oil, natural gas, coal, nuclear fuel. However, it is impossible to satisfy further growth of energy consumption only through the use of fossil sources.

At the same time, traditional energy sources are being exhausted. Geophysicist King Hubert was one of the first to build a model of depletion of world oil reserves and on its basis predicted the peak of oil production in the USA (approximately in 1970). He also predicted the peak of world oil production (around 1995), but this prediction did not come true. Nevertheless, most experts believe that it is only a matter of time before the increase in global energy demand exhausts traditional energy resources by the middle of this century. Technological progress, development of new hard-to-reach deposits (deep-sea and polar deposits, bitumen sands) will only push back the exhaustion of resources. It should be understood that even if the

reserves of traditional energy resources are not completely depleted, there will be an acute shortage of them and a sharp rise in prices. The problem cannot be solved by nuclear energy either, as uranium reserves are limited.

The next problem is related to environmental and thermal pollution of the Earth, which may lead to irreversible climate change. There is pollution of the atmosphere as a result of fuel combustion, ocean and land by oil, radioactive elements as a result of accidents with catastrophic global consequences. The latest example is the accident on an oil production platform in the Gulf of Mexico in 2010. Coal, the deposits of which are quite large, as energy carrier does not meet modern environmental requirements. "Clean" methods of its utilization are being actively developed, but this leads to an increase in the cost of the energy produced. There is also a serious problem of radioactive waste utilization.

Thermal pollution of the Earth occurs when burning any type of fuel: the concentration of CO_2 in the atmosphere increases, which contributes to the "greenhouse effect". With increasing growth of energy production through fuel combustion, including nuclear power, the safe limit of temperature increase on the Earth may be reached already in the XXI century.

Finally, there is the major challenge of energy security, which encourages the diversification of energy sources used.

The need to combat these problems will require many countries and, above all, industrialized countries, to incur significant costs and radically reduce the use of hydrocarbon raw materials. As a result, it is estimated that these reasons will not allow meeting the growing needs of the world energy industry at the expense of fossil energy sources in 10-15 years.

Thus, at the beginning of the XXI century, the world energy industry has faced the need to dramatically change the structure of the sources of energy consumed.

According to the figurative definition of Fatih Birol, chief economist of the International Energy Agency (IEA), if the current rates of energy consumption growth are maintained, by 2030 it will be necessary either to find "six new Saudi Arabias" or to bet on other energy sources.

Most analytical studies by academic scientists and scientists from fuel and energy companies suggest a significant (up to 30%) increase in the share of non-conventional renewable sources over the next 20-30 years.

Renewable energy sources are sources based on permanently existing or periodically occurring energy flows in the environment.

According to the UN classification (1978), non-conventional and renewable energy sources include the following:

- 1) peat;
- 2) biomass energy, which is obtained from various wastes: agricultural, forestry, municipal and industrial;
- 3) energy plantations. These include agricultural crops, tree and shrub and herbaceous vegetation;
- 4) wind energy;
- 5) energy from the sun;
- 6) energy of water flows on land, used in mini and micro hydroelectric power plants - hydroelectric power plants with a capacity of less than 1 MW;
- 7) medium and high potential geothermal energy (hydrothermal and vapor-hydrothermal sources);
- 8) energy of seas and oceans - tides, currents, waves, temperature gradient, salinity gradient;
- 9) low-potential heat energy of the earth, air and water, industrial and domestic wastewater.

Developed countries have been investing billions of dollars annually in the development of alternative energy sources for many years. There are state programs to support the

development of renewable energy sources. However, at present, renewable (alternative) energy sources cannot yet compete with traditional energy sources. Their total share in the total volume of energy consumed is 8-10% percent, but it will increase significantly by 2020, as shown in figure 7.1.

The main reason for non-competitiveness is economic - the high cost of generated energy.

In addition, all renewable energy sources have limitations related, for example, to the location of the site, the presence of certain climatic conditions, are characterized by either limited potential or significant difficulties in widespread use [6].

One of the most attractive and promising renewable energy sources has always been considered photovoltaics, i.e. direct conversion of solar energy into electrical energy. The sun can supply the growing energy needs for many hundreds of years. The total amount of solar energy reaching the Earth in an hour exceeds the amount of energy consumed by mankind in a year.

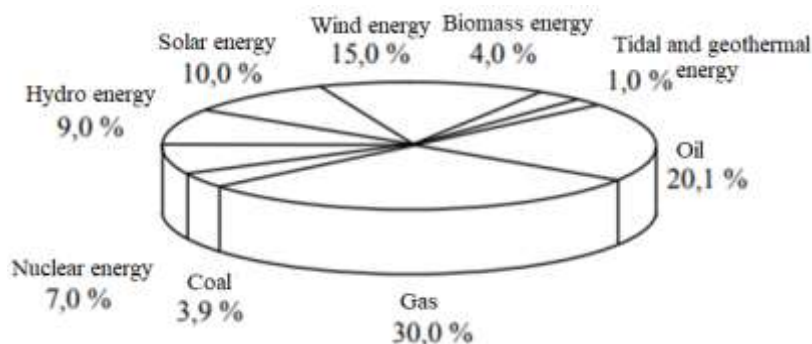


Fig.7.1. Structure of global energy consumption in 2020

Over the last 20-30 years, the growth rate of solar energy has averaged about 25%. According to forecasts, in the XXI

century the development of solar energy will remain the main among all alternative sources. It is estimated that by 2050 solar energy can provide 20-25 % of the world's energy production, and by the end of the XXI century solar energy should become the dominant source of energy with a share reaching 60 % [4,5].

Despite significant growth rates and impressive estimates of the prospects of solar energy, the amount of electricity currently generated by photovoltaics is small compared to other renewable energy sources. The main barrier preventing the widespread adoption of solar cells is the high cost of the electricity they produce [6]. Today it is the most expensive type of electricity, almost completely subsidized by the states.

The price of electricity generated by photovoltaics ranges from 20 to 65-euro cents/kWh. The price of electricity generated by conventional energy sources is currently between 2- and 3.5-euro cents/kWh and is projected to increase to 5-to-6-euro cents/kWh by 2020. Thus, in order for photovoltaics to compete with fossil energy sources, the price of the electricity it generates must be reduced by a factor of about 5-10. For this purpose, it is necessary to develop efficient, cheap technologies and designs of photovoltaic converters (PVs). A promising direction for reducing the cost of PV-generated electricity is the development of thin-film solar cell (SC) technology based on amorphous hydrogenated and microcrystalline silicon [7]. The price of produced electricity is determined, first of all, by the cost of the material from which the SE is made and the costs of the technological process of production of the SE. The main material for manufacturing solar cells at present is crystalline silicon, as it is the basic material of all solid-state electronics, and its production is perfected.

The main disadvantage of crystalline silicon-based SEs is their high cost, as 50% of the total cost of these elements is the cost of Si substrate. In the manufacture of this type of SEs, high quality raw materials are used, the production of which is

currently very energy-consuming. Total losses of silicon as a result of its processing and cutting are high. Due to the fact that monocrystalline and polycrystalline silicon are indirect-zone semiconductors and their absorption coefficient is low, for effective absorption of sunlight the thickness of FEPs made of them should be hundreds of microns. This leads to significant silicon consumption and high cost of solar cells.

Thus, it seems promising to create thin-film solar cells based on amorphous hydrogenated and microcrystalline silicon instead of expensive crystalline silicon. Thin-film technology has great potential for reducing the cost of solar modules. The rate of decrease in the production cost of thin-film solar modules is much higher than that of modules based on crystalline silicon.

In addition, thin film technology has a number of specific applications that are impossible or difficult with crystalline semiconductors (flexible modules, translucent modules, etc.). One of the advantages of thin film technology is obtaining layers of amorphous hydrogenated and microcrystalline silicon at low temperature. This makes it possible to create semiconductor structures on flexible substrates. SEs on flexible substrates are lightweight, mounted on any surface and can be used for making bags, covers, embedded in clothes, etc. Translucent modules of different colors are used, for example, to decorate buildings. Finally, a significant advantage of thin-film technology is the possibility of creating device structures on very large areas. The production of thin-film photovoltaic converters is expected to increase significantly after 2010.

7.1. Ways to analyses the efficiency of solar energy conversion

It is assumed that the charge carrier collection factor η_Q is independent of the applied bias voltage. However, in many real elements, and especially in heterojunctions with

inconsistent crystal lattice parameters, the η_Q decreases at forward displacement, which leads to a decrease in f_r (duty cycle of the voltage-ampere characteristic) and $U_{0,C}$ (idle voltage). Analysis of this question is difficult due to the nonlinearity of the equations and the lack of specific data on the properties of the material in the depleted layer.

Considering the variation of the η_Q in variations of the applied voltage as perturbations with respect to the characteristics of the ideal element makes it possible to predict the features of the transfer process of photogenerated charge carriers without resorting to solving the transport equation in the depleted layer under non-equilibrium conditions. Since this method of analysis is based on the linear superposition of dark current and photocurrent in the depleted layer, it is approximate. In many cases, it can be used with simple consideration of perturbations related to all components and factors in the expression for the collection coefficient and arising from variations in the bias voltage and wavelength of light.

The irradiation and temperature values are characteristic of the cosmic use of photovoltaic converters, enclosed in the ranges $P_S/P_{S0} = 0,03 \div 2$ (here P_S is the irradiation created by sunlight, and P_{S0} is the solar irradiation at the border of space and the Earth's air atmosphere) and from -125 to $+140^0$ C, corresponding to the orbits of Jupiter and Mercury. For a surface photovoltaic system with radiation concentrators, the irradiation can exceed the $10^3 \cdot P_{S0}$ when adjusting the temperature so that it does not exceed the temperature of the heat discharge by more than $5 \cdot 10^0$ C (which, if it is necessary to obtain useful thermal energy, can be maintained at a level of $T > 100^0$ C).

In some types of solar cells with heterojunction, elements with a MIS-structure and, in particular, on the basis of Cu_xS - CdS , variations in the density of the reverse saturation current of the J_0 and the diode coefficient A (or one of these parameters)

are observed when the radiation level or wavelength changes. This effect is most pronounced when the thermal exchange of charge carriers is slowed down between trap centers located in or near the transition region in the zone conduction or valence zone (i.e., the so-called slow states); it is possible to change the degree of filling of traps and, therefore, their charge when exposed to lighting. Silicon elements have this effect at least [1,2].

The change in J_0 and A can be caused by the absorption of light by states near the interface, in the volume of material at the junction or in the dielectric layer of MIS-structured elements, in which case the distribution profile of the concentration of charge carriers in the junction can be changed. In Cu_xS -CdS-based elements, variations in J_0 and A are associated with a change in illumination of the concentration of ionized donors or acceptors, which in turn affects the width of the depleted layer, the shape of the potential barrier in the transition region, and finally the process of carrier transfer through the transition.

It is known that the same impurity centers cause photocurrent of CuS-doped cadmium sulfide with similar spectral and temperature characteristics, however, in elements with a Cu_xS -CdS structure, transition processes are not the result of photocurrent alone.

The existence of differences between the dark dependence of $\lg J$ on U and $\lg J_{\text{SC}}$ on $U_{0,C}$, measured at variable irradiation, indicates that J_0 and A are associated with the level of light flux. The data for homogeneous transition silicon solar cells are shown in fig. 7.2.

However, since the irradiation varies widely in these measurements, it is usually impossible to determine which parameter (J_0 or A) is changing. In addition, this method does not allow separating the following effects: changes in J_0 and A , as well as the dependence of the charge carrier collection coefficient on the bias voltage $H(V)$. However, the dependence

of $\lg J_{SC}$ on $U_{O.C}$ is not affected by series resistance if its value is small. In Cu_xS - CdS based solar cells, the variation of the parameters J_0 and A is so significant that the light and dark volt-ampere characteristics overlap.

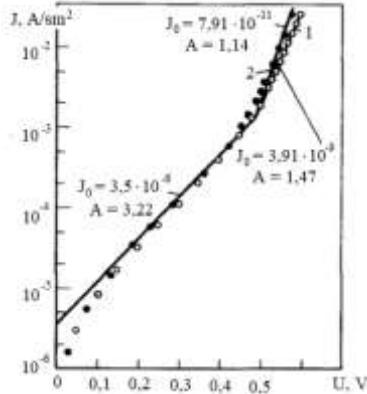


Fig. 7.2. Dark volt-ampere characteristic (1) and dependence of J_{SC} on $U_{O.C}$ (2) for a silicon solar cell with p-n junction of NASA ground reference cell having 13.6% efficiency under AM1 conditions

More complete qualitative information about changes in J_0 and A can sometimes be obtained by comparing the dark volt-ampere characteristic with a similar characteristic corresponding to a constant irradiation level (shifted with respect to the previous curve by the total photocurrent density - J_L). In the data selected for analysis, only high values of currents should be used due to the large error of J_L measurements. In this case the $H(V)$ dependence will appear very weakly, otherwise its influence should be taken into account theoretically.

When radiating the temperature dependence of the solar energy conversion efficiency, the similar dependences J_{SC} , $U_{O.C}$ and f_f can be considered separately.

The dependence of J_{SC} on temperature is mainly due to the relationship between the latter and the diffusion length of non-basic charge carriers $L = (\mu k T \tau / q)^{1/2}$. If a solar cell has a high initial value of the collection coefficient η_Q , changes in L at different temperatures do not affect it significantly [3,4]; only in cells with low initial η_Q , changes in L can significantly affect J_L . With this in mind, let us consider the effect of temperature on L and J_L .

The complex relation between the lifetime τ of non-main charge carriers and temperature is due to the fact that τ is influenced by the mutual position of the energy levels of recombination centers and Fermi quasi-levels, as well as by the temperature dependence of the capture cross sections of these centers. A simple example is a donor-type recombination center with energy level E_i and capture cross section σ_n (due to the Coulomb interaction), which decreases with increasing temperature in proportion to T^{-2} . Consequently, $\tau_{n0} = 1/(N_r \cdot \sigma_n \cdot v_{th})$ varies proportionally to $T^{3/2}$ (v_{th} is the average thermal velocity of charge carriers).

Calculations performed using the Shockley-Reed relation show that the electron lifetime τ_n at 300 K slowly increases with increasing temperature until n_i reaches the value $N_A \cdot \tau_{n0} / \tau_{p0}$. The presence of a strong temperature dependence of n_i (when its values exceed $N_A \cdot \tau_{n0} / \tau_{p0}$) leads to the fact that τ increases almost exponentially with increasing T . The experimentally observed change in τ_n in silicon is a smooth increase in τ_n with increasing T (roughly proportional to $T^{1.5}$ at $T \approx 300$ K under low-injection conditions).

The nature of the temperature dependence of the charge carrier mobility is determined by the main scattering mechanism. For example, if the scattering of carriers on acoustic phonons prevails, the mobility changes proportionally to T^{-m} , where in the simplest case $m = 1.5$. At a low level of silicon doping, the observed variations of μ can be described

approximately by $\mu \sim T^{-2}$, and therefore L is almost independent of temperature. In the case of GaAs, however, an increase in T is accompanied by a more pronounced increase in L due to the stronger dependence of τ on T .

A small shift of the optical absorption edge with temperature variations causes a change in J_{SC} (which can be found for any particular solar radiation spectrum). This change is relatively small (e.g., for Si $(\Delta J_{SC}/J_{SC})/\Delta T \approx 0.03\%/^{\circ}\text{C}$). In addition, a small increase in J_{SC} with increasing temperature is a consequence of the change in the light absorption coefficient itself with temperature variations [5].

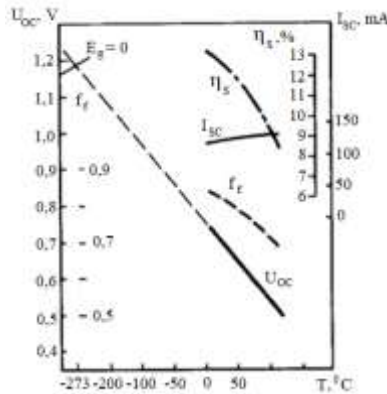


Fig. 7.3. Temperature dependences of the photovoltaic parameters of an experimental silicon solar cell with an area of 4 cm^2 at $P_S = 140 \text{ mW/cm}^2$. The curve $U_{O.C}(T)$ is extrapolated to $T = 0 \text{ K}$

According to experimental data for most high-quality silicon solar cells J_{SC} is almost constant and slightly increases with increasing temperature. An example of temperature dependence of J_{SC} is shown in fig. 7.3.

The decrease of $U_{O.C}$ and f_f with increasing temperature is mainly caused by the change of n_i ; J_0 increases exponentially

as T increases, which leads to an almost linear decrease of $U_{O.C}$ with increasing T. In general, for the region located on one side of the homogeneous transition, at $A = 1$, the relation is true:

$$U_{O.C} = \frac{kT}{q} \ln \left(\frac{J_{SC}}{J_0} \right), \quad (1)$$

at

$$J_0 = \sqrt{\frac{D}{\tau}} \cdot \frac{n_i^2}{N_A} = BT^3 \cdot \sqrt{\frac{D}{\tau}} \cdot \exp \left(-\frac{E_g}{kT} \right), \quad (2)$$

where the parameters practically independent of temperature are generalized in the form of constant B. Equation (1) can be represented in the form:

$$U_{O.C} = \frac{E_g}{q} - \frac{kT}{q} \cdot \ln \left(\frac{\sqrt{\frac{D}{\tau}} T^3 B}{J_{SC}} \right). \quad (3)$$

Here, the term of the equation defined by the logarithmic function is greater than zero, and its change with temperature variations is insignificant. An example of the temperature dependence of $V_{O.C}$ is shown in fig. 2.

The temperature dependence of $U_{O.C}$ is often used to estimate the effective barrier height in experimental photovoltaic devices. Thus, with the help of (3) for the Shockley diode region located on one side of the transition, when extrapolating the measured $U_{O.C}$ dependence on T to the point $T = 0$ K by the value of the segment cut off on the temperature axis, the value of E_g/q is determined.

Usually, f_f decreases quite sharply with increasing temperature, as shown in fig. 7.4.

The solar energy conversion efficiency of silicon-based homogeneous junction cells, determined using the relation: $\eta_s = U_{O.C} \cdot J_{S.C} \cdot f_f / P_s$, reaches its maximum value at temperatures from -150 to -100°C ; at temperatures close to 25°C , the efficiency changes at a rate $\Delta \eta_s / \Delta T \approx -0.05\% / ^\circ \text{C}$ (see fig. 7.3). The data allow us to compare theoretical and experimental temperature dependences of photovoltaic parameters of silicon solar cells.

Since GaAs tends to show a sharper increase of L with increasing temperature, the maximum η_s value of GaAs-based solar cells corresponds to higher temperatures (-100 to -50⁰ C). As can be seen from fig. 3, at temperatures near 25⁰ C, the efficiency decreases at a rate $\Delta\eta_s/\Delta T \approx -0.033\%/^{\circ}\text{C}$.

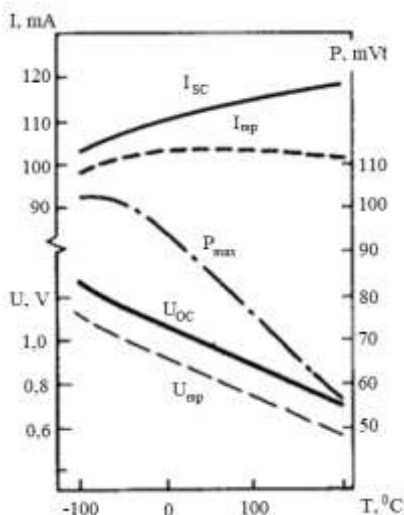


Fig. 7.4. Temperature dependences of photovoltaic parameters under AM0 conditions at $T = 25^{\circ}\text{C}$ of a solar cell based on AlGaAs - GaAs with $\eta_s = 16.4\%$

Temperature dependences of photovoltaic parameters of other types of devices with heterojunction or Schottky barrier, in which the current flow is associated mainly with thermal injection of charge carriers, are qualitatively similar to the considered ones. In heterojunctions at elevated temperatures, η_s usually increases quite sharply with increasing bandgap width of the narrow-gap semiconductor. Therefore, wide-gap materials are more suitable for use in combination with radiation concentrators and in high-temperature systems of other types.

If the process of current flow is at least partially caused by tunnelling of charge carriers, as it happens in solar cells based on Cu_xS - CdS and with MDS-structure, it is believed that $U_{0,c}$ and f_f may depend on temperature to a lesser extent. The temperature dependences of the photovoltaic parameters of cells with MDS-structure are currently not sufficiently studied.

When cells operate at low temperature, special problems arise: if the mobility of charge carriers is determined by their scattering by charged impurities, a significant decrease in L and, consequently, J_{SC} is possible. At low temperatures, contacts may lose their ohmic properties, leading to a significant decrease in f_f . In silicon solar cells, the latter problem is largely eliminated due to the creation of a p^+ -layer on the back surface (via Al diffusion).

7.2. Theoretical study of polycrystalline solar elements

We will consider the optical phenomena in ultra-thin films mainly from the point of view of their influence on the efficiency of photoelectric conversions in thin-film solar cells. The thickness of the CdS layer can be calculated by determining the difference between the wavelengths of the interference maxima (minima). In the spectral dependence of the absorption coefficient of the same layer, a sharp absorption edge smaller than that of single crystals is observed. This phenomenon is related to the result of the combined effect of several effects:

- first, scattering on the face textured surface of the layer whose reflection and emission coefficients are changed; this effect becomes stronger when the size of the grains is compared to the length of the incident wave;
- secondly, optical scattering in the voids and grain boundaries inside the layer;

- third, non-specific absorption of light due to high concentration of defects near grain boundaries;
- fourthly, the possibility of changing the optical absorption coefficient due to the presence of strong electric fields at the intergranular boundaries (France-Keldysh effect).

As an example of a number of different interesting optical effects in thin films, we can show the typical dependence of the optical emission of a CdS thin film with a mirror surface. In the considered material, the reflection coefficient under the condition $h\nu > E$ (about 19%) is very close to the value determined by the following expression:

$$R = \frac{(n_r - 1)^2}{(n_r + 1)^2},$$

where n_r is the refractive index.

The incoherent nature of scattering and the non-mirror image of reflection and emission in thin polycrystalline layers make it difficult to measure the optical characteristics of the layers. Data obtained with conventional spectrophotometers using small-aperture (about $f/10$) receivers relate only to the specular component of the emission. Such a layer will also give a useful addition to the scattered light in the solar cell used. This problem can be overcome by using large aperture receivers or integrating spheres [12].

The main tool used to measure the thickness and optical constants of polycrystalline layers is spectroscopic ellipsometry. The high accuracy of this method allows to detect not very large changes in the optical constants of the material caused by the influence of intergranular boundaries.

Due to the fact that the solution of the three-dimensional equation of charge transport in a polycrystalline material is very complicated to estimate the relationship between the useful duty factor of the solar cell, the sizes of the grains and other parameters of the material, various simplifications are made in the calculation models. Figure 7.5 compares the estimates of

various simplified models with the experimental results. In many cases, free charge carriers exist in the grain ($2W \ll \gamma$) [25,38].

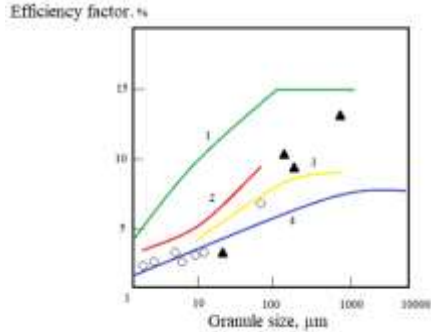


Figure 7.5. Comparison of experimental results with evaluations of simplified models and dependence of η on γ : curves 1, 2, 3 and 4 - results of theoretical calculations; o - and ▲ - experimental results

One of the models assumes that $S \rightarrow \infty$ and all photogenerated carriers falling into the truncated region (region width W) do not add significantly to the current in the external circuit. Therefore, the effective grain size is $\gamma_{\text{eff}} = \gamma - 2W$. The average diffusion length $\bar{L} = (D\tau)^{\frac{1}{2}}$ was calculated analogously to the above formula and is used to estimate j . The scheme of such dependence (dependence of η on γ) is given in figure 7.5.

If the shape of the granules is cylindrical, numerical methods are used to solve the three-dimensional equations of load transport. The solar cell quantity j is calculated as the sum of the currents in the quasi-neutral region of the grain. Here, $S \rightarrow \infty$ and $S = 0$ in the closed region of the p - n transition. The images obtained as a result of calculating the distribution of the concentration of excess charge carriers during illumination of Si

and GaAs-based Schottky barrier solar cells are shown in figure 7.6 [49].

According to the model, even if the value of J undergoes a slight change during straight shifts in the p-n transition (when there is variation of the shift), the change in the values of S is not noticeable. For Schottky barrier solar cells, the no-load voltage $U_{y.d.}$ values are calculated from the point of view that the properties of these walls are not affected by the presence of inter-crystallite boundaries. In another model, an empirical formula is used to determine the sum of contributions to the total current of photogenerated charge carriers in the entire area of a grain with a rectangular cross-section. The integration is carried out taking into account the spectral composition of the illumination and the above expressions (the expression is true under the condition that there is no shear stress at the boundary of the hardened layer ($x = x_p$):

$$j_n(x_p) = \frac{q\Gamma(\lambda)}{\left(1 + \frac{1}{\alpha L_n}\right)} = J_L,$$

$$L_+ \approx L_n \left[\left(\frac{\varepsilon}{\varepsilon_c} \right) + 1 \right]^{-1}; \quad L_- \approx L_n \left[\left(\frac{\varepsilon}{\varepsilon_c} \right) + 1 \right],$$

in these terms: j_L – density of photocurrent generated during monochromatic radiation; L_+ and L_- are “across-field” and “against-field” diffusion lengths, respectively; L_n – diffusion length of charge carriers when there is no field; Γ – photon flood density; $\varepsilon_c = kT/(qL_n)$ – is called critical field voltage. $j = j_n + j_p$. With the help of these statements $j_{q.q.}$ - the density of the short-circuit current is estimated depending on the size of the grain. Further measurements of $j_{q.q.}$ in polycrystalline silicon with grain size $\gamma > 100 \mu m$ of solar cells prove the correctness of the theoretical results.

The results of the experiments show that when the grain size increases from 100 to 1000 μm , there is a noticeable increase in the output characteristics of solar cells: $j_{q.q.}$ about 8 times; volume recombination rate $U_{y.d.}$ about 6-7 times; And η

increases by about 30-32%. Such typical relative changes apply to polycrystalline solar cells. Apparently $j_{q,q.}$ and $U_{y,d}$'s changes are almost the same. Experiments show that with a decrease in the size of the grains, the addition of $A \approx 2$ to the diode current of the mechanism, correspondingly, to the diode coefficient, increases sharply.

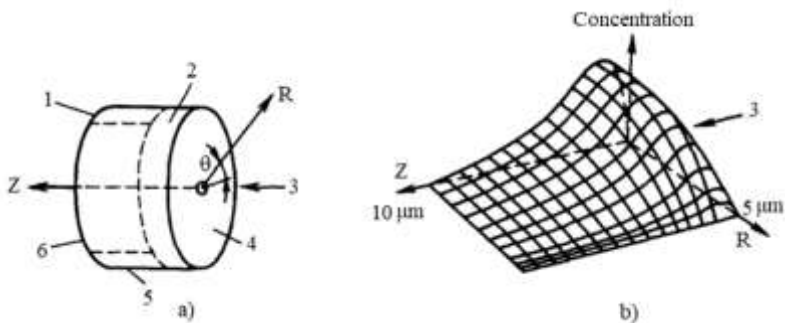


Figure 7.6. Images obtained as a result of the calculation of the distribution of the concentration of excess charge carriers during the illumination of Schottky barrier solar cells: a – model of the grain in Lanza and Hovel calculations; b – distribution of the concentration of excess charge carriers in a 10 μm -thick GaAs grain; 1 – hardened region near the intergranular boundary; 2 – the calcified area of the Schottky barrier; 3 – photon flood; 4 – Schottky barrier; 5 – grain boundary; 6 – rear contact

Several innovations to polycrystalline solar cells were reported by Card and Young. They fixed the recombination rate S at grain boundaries and considered the effect of radiation on the height of the intercrystallite potential barrier and recombination while calculating the average lifetime $\bar{\tau}$ in the polycrystalline absorbing layer. $U_{y,d.}$ and $j_{q,q.}$ was evaluated by taking into account the average life time $\bar{\tau}$ in the usual

expressions $\bar{L} = (D\bar{\tau})^{\frac{1}{2}}$ and $j = qG\bar{L}$. Here, G is the rate of homogeneous generation. We think that the main drawback of this model is the assumption of homogeneity of the generation throughout the volume of the grain. Therefore, the theoretical and experimental results coincide at small grain sizes (when the active additive is provided by layers with small x). At a large value of the size of the grains, η takes low values (figure 7.1).

In the pair model, as in the previous model, the procedure of averaging recombination centers located at the inter-crystallite boundary is equivalent to locating these centers throughout the entire volume of the semiconductor. However, at this time, the effects of truncated layers of the intergranular boundary and illumination on recombination at the boundary were not taken into account. The following expression is used for the average lifetime of non-major charge carriers in cubic grains with a grain size equal to γ :

$$\bar{\tau} = \frac{\gamma}{6\sigma vN}.$$

where, σ is the charge carrier capture cross section.

During experimental measurements of silicon materials, the appropriate empiric relation $\bar{\tau} \cong 5 \cdot 10^{-6} \gamma$ (γ is expressed in centimeters) is satisfied in most cases within the condition $0.2 < \gamma < 10^3 \mu\text{m}$. The expression of $\bar{\tau}$ at the infinite rate of surface recombination on the backside of the layer, the semiempirical dependence of charge carrier mobility on γ , and the usual solutions of the diffusion equation are used to estimate j_L . The addition of annealed layer current to j_L (about 8 mA/cm^2) can be estimated from the following relation:

$$j_L \cong q\Gamma_0[1 - \exp(-\alpha W)]M,$$

where $M = 1$ when $\bar{\tau} \geq \tau$; and when $M = \bar{\tau}/\tau$, $\bar{\tau} < \tau$. τ is the time for the charge carriers to pass through the truncated layer. Γ_0 is the density of the photon stream on the frontal surface of the solar cell.

The dependence of the complete j-current on γ is presented in figure 7.7.

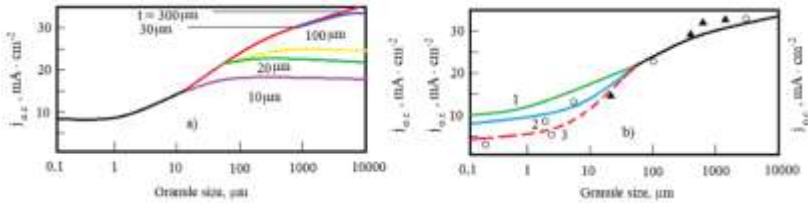


Figure 7.7. Dependence of $j_{q,q}$ on grain size γ at different thicknesses of polycrystalline Si layer (a); Effect of $j_{q,q}$ on fence height and creepage (b): symbols depicting experimental results correspond to figure 2. 1 – stiffness is stable; 2 – the stiffness is changed; 3 – decrease in the height of the fence

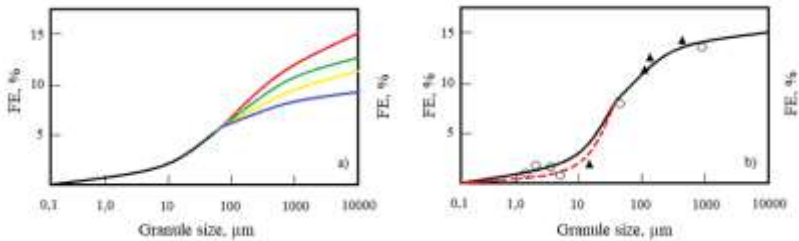


Figure 7.8. The effect of the grain size on the efficiency of the silicon solar cell: a) in different thicknesses of Si polycrystalline layers; b) cases where there is an effect of reducing the height of the potential barrier in the p-n junction (black curve) and cases where this effect is not present (red curve). Symbols showing experimental results correspond to figure 3

The calculation is done using regular expressions for diocs. During the calculations, it is assumed that the volt-ampere characteristics are affected by the recombination-generation

mechanism at small grain sizes, and by the injection-diffusion mechanism at large values of γ . The obtained results are given in figure 7.8. To explain the difference between the experimental and computational dependences (at small values of γ), it is proposed that the truncated region of the p – n junction during illumination is significantly reduced due to the capture of charge carriers in the defect levels (fig. 7.8b) in this region.

Another model is the Fossum and Lindholm model. In this model, the influence of inter-crystallite boundaries in the truncated regions of p-n junctions is taken into account. If the E_{Fn} and E_{Fp} - Fermi quasi-levels of electrons and holes are constant in the entire truncated region (including the region crossing the crystallite boundary), the following expression can be used to estimate the recombination current:

$$S_{eff} = \frac{1}{4} (S_n S_b)^{\frac{1}{2}} \left[\frac{N_A}{n_p(x, W)} \right]^{\frac{1}{2}},$$

where, $n_p(x, W)$ is the concentration of charge carriers at the boundary of the truncated layer during illumination; N_A is the concentration of acceptors; S_n and S_b are the electron and grain boundary recombination rates, respectively.

It is necessary to take into account that the charge carriers are three-dimensional in the entire region of width W , but in large electric fields and in the diffusion current, the Fermi quasi-levels can be considered as planar zones, so: $E_{Fn} - E_{Fp} = qU$. The rate of recombination at the surface

$$U \cong (S_p S_n)^{\frac{1}{2}} \left(\frac{n_i}{2} \right) \exp \left(\frac{E_{Fn} - E_{Fp}}{2kT} \right),$$

The current density of each grain can be determined by multiplying the surface area A of the inter-crystallite boundary in the truncated layer of the p-n junction.

During the calculation of recombination, grains were also not taken into account. Diode coefficient - for the maximum rate of recombination was equal to two due to the presence of quasi-equilibrium stationary levels at the intergranular

boundary. Using this and other similar arguments, an expression including the $\exp(qU/2kT)$ limit for recombination at the edges of single-crystalline $\text{Al}_x\text{Ga}_{1-x}\text{As}$ heterojunctions was derived. When estimating the recombination surface area, the "interaction length" is used, not the value of W .

The current density of each particle passing through the truncated region of the p-n junction is determined by the following expression:

$$j = \frac{I}{\text{area}} = \left(\frac{U}{2}\right) \frac{4\gamma W}{\gamma^2} = q(S_n S_p)^{\frac{1}{2}} \left(\frac{W n_i}{\gamma}\right) \exp\left(\frac{qU}{2kT}\right).$$

From the analysis of experimental results (above) on polycrystalline solar cells with p-n junction, whose grain sizes vary in the range of $0.2 \leq \gamma \leq 6 \mu\text{m}$, it is obtained that the calculated and experimental values for j_0 measured in the non-illuminated branch of the volt-ampere characteristic are in full agreement. As a rule, the dependence of the characteristics of solar cells on the average value of the grain size is analyzed. Another important parameter is the surface area of the intergranular boundary. In materials characterized by a certain distribution according to the size of the grains, grains with smaller sizes have a large value of the surface-to-volume ratio, which causes a sufficient increase in the parameter called average grain size [52].

The two-dimensional problem of charge transport in polycrystalline silicon solar cells is solved with the help of ECM. A simplified Shockley-Reed-Hall expression is used to account for recombination at the intercrystallite boundary. In addition to recombination at the intergranular boundary, this process is observed in the n- and p-layers on the back and front surfaces of the solar cell. Apart from the temperature interpretations, the importance of the work carried out is that dependences are obtained as a result of the variation of the angle between the inter-crystallite boundaries and the planes of the p-n transition, as well as the Poisson distribution of the distance between the

inter-crystallite boundaries is noted. The theoretically assumed dependence of $\eta(\lambda)$ is very close to the measured value in solar cells with Si polycrystalline layers. In addition, the shape of the dependence of $\eta(\lambda)$ depends on the illumination intensity. Such a result corresponds to the 18% increase of $\eta(\lambda)$ for $\lambda = 0.875 \mu\text{m}$ obtained in experiments when the intensity of illumination increases.

A number of acquisitions in this field are of interest. Recombination effects at intergranular boundaries parallel to the plane of the p – n junction in the presence and absence of illumination were considered by Card and Hwang. Such fences also prevent the passage of the main cargo carriers. The theory of Card and Hwang was applied to flat and wide bandgap materials - mainly CuInSe_2 material, and the future improvement of polycrystalline solar cells as well as their application prospects were clarified. Green applied the equivalent scheme describing the three-dimensional flow of current and paid attention to the role of intergranular boundaries in the truncated region of the p-n junction [64].

In order to estimate j in $\text{Cu}_x\text{S} - \text{CdS}$ solar cells, it is assumed that these charge carriers do not add to j under the condition that the distance from the places where charge carriers are formed to the cylindrical intercrystallite boundary is smaller than the distance to the p – n junction. Despite such a simplified assumption, the inhomogeneity of the $d\Gamma/d\lambda$ generation rate, which is generally not considered in many theories, is taken into account in a real solar cell.

The three-dimensional problem of charge transport in a polycrystalline material is so difficult that an exact solution cannot be obtained. Since the models we consider make a number of assumptions, it is important to characterize the limitations inherent in such models.

1. The procedure of averaging the lifetimes and diffusion length of non-major charge carriers, by its very nature, makes it

impossible to estimate a number of important aspects of the charge transport process in the future.

2. As a rule, the operating conditions of solar cells are such that the analysis of the lifetime of charge carriers in crystallites cannot help to obtain accurate results.

3. In most models, the effect of straight slip on the quasi-neutral region, especially on the injection at the boundary of the truncated layer of the p-n junction, is not taken into account.

4. The calculation of U (taking into account the drift dependence of the collection of photogenerated charge carriers) is very approximate.

The effective rate of surface recombination at the intercrystallite boundary is calculated for two boundary conditions: with and without illumination, when the height of the wall at this boundary is significantly reduced. In light conditions, two options are available in turn: either the infinite value of the effective rate of surface recombination is used, or only strong excitation is used - in conditions where the effect of charges is not taken into account. A more rigorous consideration of intermediate states would be particularly useful for the diagnosis of polycrystalline material. A sufficient agreement of theoretical and experimental characteristics of solar cells based on polycrystalline materials in large grain sizes is observed. However, in the case of flat and wide-band materials, the values of U are usually smaller than those predicted by theory.

Despite the above-mentioned shortcomings, theoretical models have given a strong impetus to the improvement of the characteristics of polycrystalline solar cells. For example, according to the expression of the dependence of the recombination rate on the concentration of charge carriers, the useful work factor of solar cells increases significantly during concentrated radiation (in the range from 3 to 20 degrees of concentration). Although the possibility of using polycrystalline solar cells with systems with low levels of solar radiation

concentration is considered, such an application can be very economically advantageous. It is important to remember one more moment that for the increase of j , less addition of the light absorbing layer is required.

7.3. Formation technology and properties of microcrystalline silicon used in solar batteries

At the beginning of the 21st century, humanity faced the need to solve long-term energy problems as a result of the depletion of traditional energy sources and the deterioration of the Earth's ecological situation in the near future. In industrially developed countries, great attention is paid to the development of systems based on renewable energy, including solar energy sources.

The sun provides the Earth with a huge amount of energy, which is many times more than the demand of mankind. The use of this source is a difficult problem because solar radiation is a flood of energy that is heavily scattered on Earth. For the mass application of solar energy, it is necessary to ensure its effective use and improve the economic characteristics of solar cells. A promising approach to solving the problem of low-cost solar energy converters is the development of thin-film solar cells based on amorphous and microcrystalline silicon.

For the first time, microcrystalline silicon was obtained by hydrogen plasma and chemical transport at 600 °C. The interest in the element silicon increased after its highly doped layers were used in the production of $p-i-n$ structures of solar cells.

At present, the most common method of obtaining $\mu c-Si:H$ layers is the method of high addition of hydrogen to monosilane from glow discharge plasma at frequencies of 13.56 to 200 MHz and deposition at a relatively high power of the discharge (the ratio of materials used is $R = H_2/SiH_4 > 20$).

Figure 7.9 shows the diagrams explaining the acquisition of amorphous and monocrystalline layers depending on the amount of R and the thickness of the layer. At small values of the additive, when $R < 10$, only amorphous layers are obtained. At this time, the thickness of the layers has such a range that very rough layers begin to appear. Although the details of the diagram depend on the specific conditions of acquisition, the general picture remains the same.

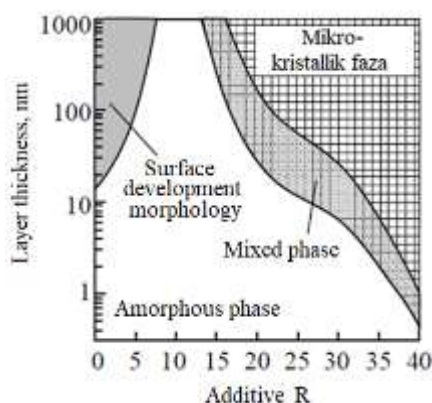


Figure 7.9. Dependence of the structure of silicon layers on the quantity R and layer thickness

Stable embryos necessary for monocrystalline growth of the layer are formed when the reaction at the plasma-layer boundary takes place under conditions close to equilibrium conditions. This condition is expressed by the following reaction in plasma:



In the plasma, monosilane is decomposed with the formation of radicals and SiH_n ions. In the straight direction, the reaction leads to the formation of the Si layer and hydrogen released into the plasma, while in the opposite direction, the

addition of the layer occurs as a result of the interaction of the plasma with the Si layer. The balance between the processes of deposition and erosion of the increased surface of the layer is the main factor that determines the characteristics of the structure of the material obtained at this time.

Under normal conditions of deposition of a-Si:H, the straight reaction is slow and the system is far from equilibrium. It is clear that a strong addition of hydrogen shifts the reaction in the opposite direction, and the rate of growth decreases even under conditions of increasing strength. The system approaches equilibrium and stable embryos are formed that stimulate further growth of the $\mu\text{c} - \text{Si:H}$ layer. A decrease in the growth rate leads to a significant increase in the average value of the grain size and the share of the crystalline phase.

Hydrogen etching plays a very important role in the formation process of $\mu\text{c} - \text{Si:H}$ structure. Elimination of energetically inefficient configurations, deformed bonds, due to etching leads to low-temperature crystallization. Such a mechanism of layer growth is called chemical plating, in which a monovalent element not only passivates the broken bonds in the Si-matrix, but also plays an important role in chemical reactions during the formation of the layer. The presence of fluorine enhances etching and helps to settle the equilibrium state.

When atomic hydrogen is penetrated into the deformed Si-bonds on the surface, hydrides are formed, which migrate along the surface and disintegrate during the collision, resulting in the formation of H_2 and Si - Si bonds. An increase in the frequency of incandescent discharge occurs at the same time as a 5-10 times increase in the rate of deposition of the layer.

In recent years, a number of new methods of deposition have become widespread. Thermocatalytic chemical deposition from the gas phase (one order of magnitude greater than the standard plasmochemical deposition method at high

frequencies) or the chemical deposition method with a heated wire from the gas phase is considered a promising method from the point of view of the possibility of significantly increasing the rate of growth of the layer. At the same time, the electron-cyclotron resonance method is also used. However, the deposition rate of the $\mu\text{c} - \text{Si:H}$ structure is too high for the wide practical use of this material, a maximum of $\sim 1\text{-}2 \text{ \AA}/\text{sec.}$ takes its price.

The resulting $\mu\text{c} - \text{Si:H}$ structural layers are amorphous - crystalline material. Hydrogen is concentrated in the regions of the grain boundaries in the amorphous matrix, which leads to effective passivation of the grain boundaries. The bonding of silicon with hydrogen is mainly mono- and dihydride bonds located on the surface of silicon crystallites.

Using the high frequency method (20 – 110 MHz), device-quality amorphous silicon is obtained at a lower substrate temperature and high deposition rate, which cannot be created by the standard method. As can be seen from figure 7.10, the deposition rate of $\mu\text{c} - \text{Si:H}$ layers increases more than the discharge frequency. The considered method is more effective in using coil technology of purchasing solar cells.

The layers are composed of crystallites with dimensions of 80 \AA (in polycrystalline silicon - 500 \AA and above). By changing the deposition conditions, it is possible to control the size of the crystallites to some extent. The share of the microcrystalline phase can be varied from a few percent to almost 100%.

Depending on the share of the microcrystalline phase, the electrical and optical properties of $\mu\text{c} - \text{Si:H}$ layers will be determined by either the amorphous or crystalline phase. The share of microcrystalline phase in device-quality $\mu\text{c} - \text{Si:H}$ layers reaches 90%. In such a material, the amorphous phase is mainly located in the intergranular space. The layers have a columnar structure with the orientation of the grains mainly 220.

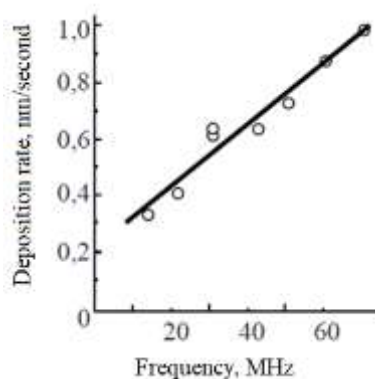


Figure 7.10. Dependence of the deposition rate of $\mu\text{c} - \text{Si:H}$ layers on the frequency of plasma excitation

The optical width of the forbidden zone of specific $\mu\text{c} - \text{Si:H}$, with a share of the microcrystalline phase exceeding 90%, is 1.1 eV. As the proportion of amorphous phase increases, the width of the forbidden zone increases.

Under normal production conditions, the undoped $\mu\text{c} - \text{Si:H}$ layer has n-type conductivity and a high value of dark conductivity of $10^{-5} \text{ Ohm}^{-1} \cdot \text{cm}^{-1}$. The Fermi level is located 0.4 eV below the bottom of the conduction band. Obtaining n-type high conductivity is explained by the presence of an oxygen admixture participating as a donor in the non-doped layers. Oxygen enters the $\mu\text{c} - \text{Si:H}$ structure from water vapor adsorbed on the walls of the reaction chamber or by means of gases transferred to the chamber.

Such material cannot be used as an active i-layer. In order to obtain a device-quality $\mu\text{c} - \text{Si:H}$ special layer, a special gas cleaning or microetching operation should be performed using an extremely high vacuum in the working chamber. In this case, it is possible to obtain a material with a Fermi level located in the middle of the forbidden zone.

A highly etched n - type μc - Si:H layer is obtained by introducing phosphine into the plasma. Diborane is added to the plasma to obtain the p - type μc - Si:H layer. In this case, the conductivity of the μc - Si:H layer first decreases due to the compensation of donors and the reduction of charge carriers. The Fermi level μc passes through the middle of the Si:H material (such materials are called compensated materials). Subsequently, an increase in conductivity is observed (up to $\sim 1\text{--}2 \text{ Ohm}^{-1}\cdot\text{cm}^{-1}$). To obtain a device-quality compensated μc - Si:H layer, it is necessary to perform microdoping (ie, adding a small amount of diborane to the glow discharge). The optimal microsizing regime for obtaining compensated material is very narrow and difficult to control.

μc - Si:H layers are mainly applied together with layers of amorphous materials. Highly doped layers are used as n- and p-type layers in solar cells. Such layers are added more effectively than layers created on the basis of amorphous materials and, therefore, have higher conductivity. This provides large values of no-load current and charge factor due to better field distribution in the active i-layer of the solar cell based on amorphous material. In addition, highly doped layers based on μc - Si:H are more transparent. As a result, when μc - Si:H is used as a p-type transparent window, large short-circuit current values are ensured.

Solar cells based entirely on μc -Si:H structures are of greater interest than α -Si:H structures due to their higher stability. Many characteristics of solar cells based on μc - Si:H are superior to those of α - Si:H and α - SiGe:H structures. Therefore, the considered material is more promising for use as the i-layer of the lower element in cascade solar cells. In addition, solar cells based on μc -Si:H have a higher form factor and are cheaper to manufacture than α -Si:H. One of the disadvantages of μc - Si:H layers is that the absorption coefficient is lower than that of α - Si:H structures, requiring

thicker layers (in the order of several microns) at low deposition rates. At the same values of short circuit $\mu\text{c} - \text{Si:H}$ based solar cells have lower values of no-load current voltage ($\sim 0.53\text{V}$) than $\alpha - \text{Si:H}$ based solar cells. At present, tandem solar cells have been developed, where $\alpha - \text{Si:H}$ plays the role of a wide-band i-layer, and $\mu\text{c} - \text{Si:H}$ plays the role of a narrow-band layer ($(\alpha - \text{Si:H})/(\mu\text{c} - \text{Si:H})$). Such solar elements are called miromorph elements (micromorph).

8. CARRIER TRANSPORT MECHANISMS AND DARK VOLT-AMPERE CHARACTERISTIC OF SOLAR CELLS

Measurement of the dark volt-ampere characteristics of solar cells (SE) makes it possible to find the prevailing transport mechanisms in solar cells, which determine the shape factor, as well as to estimate such important parameters as series and shunt resistances. In solar cells based on crystalline materials, two carrier transport mechanisms usually predominate: diffusion and recombination. In this case, the dark VAC of the SE can be described using a two-exponential model.

Taking into account the shunt and series resistances for the dark VAC of the SE, we obtain:

$$I_D = I_{01} \left\{ \exp \left[\frac{q(V - IR_{\Pi})}{n_1 kT} \right] - 1 \right\} + I_{02} \left\{ \exp \left[\frac{q(V - IR_{\Pi})}{n_2 kT} \right] - 1 \right\} + \frac{V - IR_{\Pi}}{R_{\text{ш}}},$$

where R_{ser} , R_{sh} are series and shunt resistances; n_1 , n_2 are ideality coefficients for diffusion ($n_1 = 1$) and recombination ($n_2 = 1-2$) transport mechanisms.

However, not always, especially for SE based on amorphous semiconductors, this model is applicable to describe the dark VAC, since it is necessary to take into account the presence of other transport mechanisms. In the scientific and technical literature it is noted that in this case the Poole-Frenkel effect and tunnelling can act. The presence of these transport mechanisms can increase the values of the ideality coefficient exceeding 2 [19,28].

The Poole-Frenkel mechanism represents the process of thermoexcitation of electron from traps to conduction zone accelerated by electric field. In this case, let us write the expression

$$I_{PF} \propto \exp \left[\frac{q\sqrt{\beta} \cdot \sqrt{E}}{2kT} \right] n_i W^* \left[\exp \left(\frac{qV}{2kT} \right) - 1 \right]$$

or

$$I_{PF} \propto T^{3/2} \exp \left[\frac{-E_g(T) + q\sqrt{\beta} \cdot \sqrt{E}}{2kT} \right] n_i W^* \left[\exp \left(\frac{qV}{2kT} \right) - 1 \right],$$

where E is the electric field in the recombination center region; $b = q/\rho e$ (e is the dielectric constant); n_i is the intrinsic carrier concentration; W^* is the effective thickness of the space charge region.

For SEs with high defect density, the tunnelling mechanism may be present. The tunnelling current is described by the relation

$$I(T) = I_{03} \cdot \exp(AV),$$

where $I_{03} = B \exp(aE_g(T))$ (B is the coefficient responsible for the tunnelling probability; a is the temperature-independent coefficient; $E_g(T)$ is the temperature-dependent forbidden zone width; A is the temperature-independent coefficient).

In Matsuura's works it was shown [39,40] that in heterostructures based on amorphous hydrogenated silicon the mechanism of multistage tunnelling with capture and emission of charge carriers prevails (fig. 8.1).

In this mechanism, holes from the valence band of c-Si p-type move into the amorphous semiconductor from one localised state to another, which differ in energy by the order of kT , due to multistage tunnelling processes. Such movement of carriers continues until the rate of tunnelling does not become less than the rate of emission of holes in the valence zone or the rate of recombination of holes with electrons from the conduction band of the amorphous semiconductor. The end point of hole tunnelling is near the edge of the depletion region of the amorphous semiconductor, where the tunnelling rate decreases due to a decrease in the electric field. In this case I_{03} in expression is defined as

$$I_{03} = B \left[\sigma_p v_{th} N_V \exp \left(-\frac{E_T - E_V}{kT} \right) + \sigma_n v_{th} N_C \exp \left(-\frac{E_C - E_F}{kT} \right) \right],$$

where B is a constant depending on the probability of carrier tunnelling; σ_p , σ_n - capture cross sections for electrons and holes, respectively; v_{th} - thermal velocity; N_V , N_C - effective densities of states in the valence zone and conduction zone of an amorphous semiconductor, respectively; E_T , E_V , E_C , E_F - energies corresponding to Fermi and trap levels, edges of the valence zone and conduction zone.

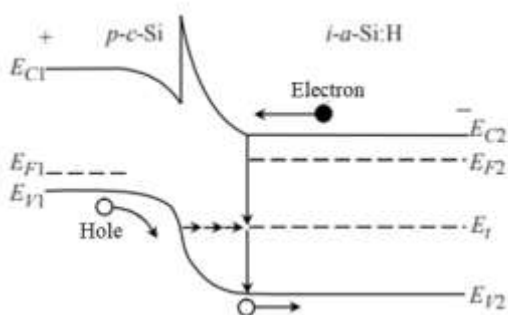


Figure 8.1. Model of tunnelling with capture and emission of charge carriers on localised states in α -Si:H/c-Si heterostructures

The first term in expression reflects the hole emission rate, and the second term reflects the electron trapping rate on the traps. In the case of n- α -Si:H/p-c-Si heterostructures studied by Matsuura, the tunnelling mechanism was limited by the hole emission rate.

The metal grid resistance, contact resistances, specific surface resistance, base and back contact resistances contribute to the series resistance of the SEs.

The shunt resistance of the solar cell is caused by various kinds of leakage currents (on the surface, peripheral regions, volume of the semiconductor SE, etc.).

The theoretical calculation of the volt-ampere characteristics of solar cells based on amorphous semiconductors is significantly complicated by the quasi-continuous distribution of electronic states in the mobility gap. In the forbidden zone of crystalline semiconductors there are only single discrete levels that act as recombination centers. Recombination processes in this case are described by the Shockley-Reed-Hall model. As a rule, the contribution of carriers to the total spatial charge trapped on states in the forbidden zone can be neglected due to the low density of states. In the mobility gap of amorphous silicon, there exists a quasi-continuous distribution of electronic states, which largely influence the electronic properties of the material. The contribution of carriers trapped on states in the forbidden zone to the total space charge can no longer be neglected. In addition, the lifetime of charge carriers depends to a large extent on the bias, since the number of states involved in recombination processes depends on it.

As a rule, the following assumptions are used in the mathematical description of the operation of devices based on amorphous silicon.

1. It is assumed that charge carriers are transported only along the propagated states.
2. There are sharp mobility boundaries separating carriers into propagated and localised states.
3. The filling of localised states is determined by free charge carriers. Only capture and emission processes between the propagated and localised states are taken into account, and the possibility of carrier exchange between localised states is neglected.

The above assumptions are valid at room and higher temperatures.

In almost all cases, one-dimensional device models are used. At the same time, real p-i-n - solar cell structures are

formed on a textured layer to enhance light scattering and absorption. As a result, the thickness of α -Si:H layers is not uniform in area. Electron and hole transport in a semiconductor is described by a system of equations: Poisson equation and continuity equations 110 for electrons and holes [59], which for the one-dimensional case are as follows:

$$\begin{aligned}\varepsilon \frac{\partial^2 U}{\partial x^2} &= -\rho(x); \\ \frac{1}{q} \frac{\partial J_p}{\partial x} &= G(x) - R(x); \\ \frac{1}{q} \frac{\partial J_n}{\partial x} &= G(x) - R(x), \quad J_n = q \left(n\mu_n E + D_n \frac{\partial n}{\partial x} \right),\end{aligned}$$

where ε is the dielectric constant; U is the potential; $G(x)$ is the generation rate; $R(x)$ is the recombination rate; q is the charge; J_n , J_p are the electron and hole current densities, respectively.

In an amorphous semiconductor, the charge q is determined by the concentration of donors and acceptors, free electrons n and holes p , and the charge of carriers trapped on states in the forbidden zone ρ_{trap} . Thus, $\rho = q \cdot (p - n + N_D^+ - N_A^-) + \rho_{\text{trap}}$.

In a general form for hole and electron currents

$$\begin{aligned}J_p &= q \left(p\mu_p E - D_p \frac{\partial p}{\partial x} \right); \\ J_n &= q \left(n\mu_n E - D_n \frac{\partial n}{\partial x} \right); \end{aligned}$$

where μ_p , μ_n are mobility of holes and electrons; D_n , D_p are diffusion coefficients of electrons and holes; E is electric field strength.

On the other hand, J_p and J_n are determined by the gradient of Fermi quasi-levels:

$$\begin{aligned}J_p &= \mu_p p \left(\frac{dE_{fp}}{dx} \right), \\ J_n &= \mu_n n \left(\frac{dE_{fn}}{dx} \right).\end{aligned}$$

In general, the volt-ampere characteristics of solar cells based on amorphous semiconductors can be obtained as a result

of solving the system of equations stated earlier. Further, the charge in the semiconductor, generation and recombination rates are theoretically analyzed, which is necessary to solve this system of equations.

8.1. Roll-to-roll technology for manufacturing solar cell modules

The characteristics of industrially produced modules, as a rule, are worse than those of solar cells (SE) produced in laboratories. This is primarily due to the fact that SEs produced in laboratories have smaller areas, higher quality of territorial grid organisation (TGO), semiconductors, high homogeneity of layers, low losses at sealing, shading, shunts. In the transition from R&D to large-scale flow production, the key points are homogeneity of deposition over large areas, deposition rate, gases used, yields, reproducibility, and the possibility of automation. An example of in-line production of SEs on a stainless-steel substrate is the roll-to-roll technology developed at Energy Conversion Devices, Inc. (ECD).

The essence of the technology is that the formation of the SE is performed on a steel sheet that is rolled up before the process starts, gradually unrolled during the processes at the entrance to the plant, and rolled up at the exit of the plant when finished. The steel sheet has a thickness of 125 μm , a width of 0.35 meters and a length of 750 meters. The production can be divided into two parts: deposition and assembly.

Deposition, in turn, consists of four stages, each involving roll-to-roll units:

- 1) substrate cleaning;
- 2) deposition of the back reflective layer;
- 3) deposition of $\alpha\text{-Si:H}$ and mc-Si:H ;
- 4) deposition of the top ITO layer.

The cleaning unit includes a module for ultrasonic washing in special washing solutions, brushing treatment, deionized water baths, infrared drying chamber. The cleaned steel sheet is twisted at the outlet together with a protective sheet. The steel sheet is then pulled through several modules with magnetrons at constant current to deposit Al or Ag layers as reflector and ZnO as buffer layer. The deposition is carried out on a heated substrate to ensure the formation of textured layers for enhanced light reflection. Next, the roll is fed into an HF PCS (nine-layer deposition) machine to form the n-i-p/n-i-p/n-i-p/n-i-p structure (deposition temperature 250-300⁰ C) as well as buffer layers on both sides of the α -SiGe:H layer. The deposition of all layers is done sequentially, but in one pass of the roll. To reduce defects in the film due to particle ingress, the layers are deposited from below. The feed rate of the steel sheet is ~30 cm/min. The chambers are isolated from each other dynamically with a gas shutter to prevent contamination, but the steel sheet is continuously moving. After deposition of the semiconductor structure, the coil is loaded into a TGO layer deposition unit. Either reactive evaporation of indium in an oxygen atmosphere or sputtering of an indium-tin oxide target in an Ar atmosphere is used.

The second part of production - assembly - involves the following steps. Firstly, the roll with the formed solar cell structure is cut into individual sheets of the required size. Next, an etching paste is applied around the perimeter of the sheet, which is activated in a conveyor oven to remove ITO. The selected samples are subjected to quality control. The SEs are then submitted to a shunt elimination operation. For this purpose, oxidation of TGO to dielectric in the electrolyte is performed in the area of shunt formation. The fabrication of the SEs is completed by forming a conductive grid using carbon paste or copper wire coated with carbon paste. The individual solar cells are interconnected, modules are fabricated, which are

covered with a transparent sealing layer of ethylvinylethylene and mounted on support structures.

Roll-to-roll production is large-scale yet simple and flexible. The steel sheet with the formed SE structure can be cut to any size from the small sizes required, e.g. for chargers, to the larger ones for installation on the roofs of buildings. The stabilized efficiency of modules produced by this technology is 8 %. A flexible Kapton substrate can be used instead of steel sheet.

An important aspect of a-Si:H-based solar cell production is safety. Despite the fact that there are no toxic substances in the final product, toxic, flammable and explosive gases are used in the production process - monogerman, phosphine, trimethylboron, monosilane, hydrogen, etc.

Figure 8.2. shows a solar cell on a glass substrate.

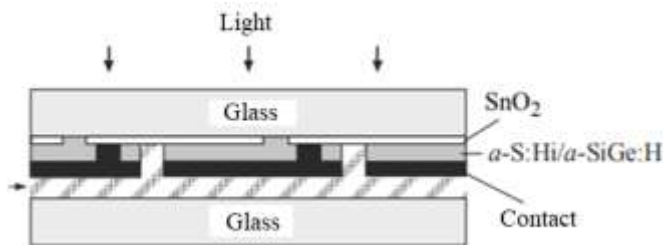


Figure 8.2. Solar cell on a glass substrate

For industrial production of SE modules based on amorphous semiconductors, glass substrates (thickness 3 mm, width 0.5 m, length 1 m) can be used on which a textured TGO (SnO₂) layer is deposited by chemical vapor deposition at atmospheric pressure. The TGO layer is then scribed into strips of the order of 9 mm width, and the substrates are loaded into a plasma chemical deposition unit to deposit semiconductor layers (six layers to form the p-i-n/p-i-n structure in the case of the α -

Si:H/ α -SiGe:H tandem solar cell). Next, a ZnO buffer layer is deposited and the next laser scribing is performed near the lines of the first scribing.

The laser power is selected so that the ZnO and semiconductor layers are removed, but the SnO_2 layer remains. Next, Al is deposited as a back reflective and contact layer and a third scribing is performed near the second one, completing the sequential joining of neighboring elements on the substrate, which allows reducing resistance losses by increasing the output voltage and reducing the SE current. Forming the junction of individual elements is easier on a glass substrate than on a steel substrate. A fourth laser perimeter scribing isolates the active region from the edges of the substrate. The panel formation is completed by soldering to another glass wafer using ethylvinylethylene ethylene (EVE) as shown in the figure.

The formation of flexible-based photovoltaic converters is interesting from a practical point of view. Such SEs are substantially lighter in weight than conventional ones and can be easily mounted on virtually any surface. They can repeat the surface of buildings and roofs, and due to the low weight, there is no need to reinforce supporting structures. Such technology can be used to create a special fabric with a formed photovoltaic converter, which can be used in the manufacture of sails and clothing. Such material can be used to make bags and covers, for example, for mobile phones, players, etc.

Representatives of the military industry are showing great interest in such technology. In modern conditions, the army uses a huge number of electronic devices, each of which requires electricity supply. The use of SE allows solving this problem. Lightweight solar cells on a flexible basis can be placed on the roof of tents, on backpacks, even uniforms can be made of them.

Currently, a technology is being developed that uses a plastic substrate as the base and an amorphous semiconductor as

the working layer. Metal layers are applied to both sides of the flexible plastic substrate, one of which is the metal electrode and the other is the back electrode. These layers prevent outgassing from the substrate and protect the semiconductor layers from degradation. Layers based on a-Si:H are deposited on the metal electrode followed by a layer of transparent conducting electrode based on indium and tin oxides. There are two types of holes in the formed SEs: one provides electrical contact between the transparent conducting electrode and the back electrode, and the other provides electrical contact between the metal electrode and the back electrode. ITO has a relatively high resistivity, which leads to an increase in the series resistance of the SEs. The first type of holes can reduce this resistance and increase the carrier collection efficiency. Laser scribing on both sides of the substrate makes it possible to form individual elements serially connected to each other. Using such a technique, modules were formed on a $40 \times 80 \text{ cm}^2$ flexible substrate based on tandem SEs with α -Si:H i-layers. The output voltage of the module was 200 V, efficiency = 10.5 %.

Formation of such SEs is possible using roll-to-roll technology. The original technology of manufacturing flexible photovoltaic converters is proposed by the Canadian company "Spheral Solar" (Cambridge, Ontario). The basis of such solar cells is a set of silicon beads located between two thin films of aluminum foil sealed in plastic. Each individual bead is a tiny SE that absorbs sunlight and converts it into electricity. Layers of aluminum foil give the whole structure the necessary strength and serve as electrical contacts.

Silicon from electronic waste is used to make the beads. It is melted and crystallized into spheres with a diameter of approximately one millimeter. The silicon spheres are further doped with boron to obtain p-type conductivity, and phosphorus is diffused into the near-surface layer, resulting in the formation of a p-n junction.

Silicon spheres made in this way are placed on a perforated sheet of aluminum, which creates contact with a surface having n-type conductivity. Then some part of the sphere surface is vented to the p-type conductivity core. A second layer of aluminum foil creates contact to the p-type core. The entire structure is then sealed with plastic. The uneven surface of the spheres allows for a larger area to absorb light.

For a photovoltaic converter with such a structure, an efficiency value = 11 % was obtained, which is comparable to the conversion efficiency of conventional SEs and significantly exceeds the efficiency of solar cells currently manufactured on a flexible basis. Such material can be placed on the surface of any shape and cover any structures and constructions.

8.2. Solar elements with p-i-n structure

The wide unalloyed i-region of α -Si:H ensures light absorption and, consequently, efficient operation of the cell. Unlike crystalline solar cells based on p-n junctions, where the charge carriers, having a large diffusion length (100-200 μm), reach the electrodes even in the absence of an electric field, in solar cells based on α -Si:H the charge carriers can reach the electrodes mainly only due to the internal electric field, i.e. due to the drift of charge carriers, since the diffusion length of holes in α -Si:H is very small (~ 100 nm).

The highest efficiency of solar cells was achieved using p-i-n - structures (fig. 8.3) [1-3].

Since in a simple p-n junction based on α -Si:H the region of strong electric field is very narrow and concentrated near the junction, and the diffusion length of charge carriers is small, there is no effective separation of charge carriers generated by light absorption in most of the solar cell. Consequently, in order to obtain efficient solar cells based on amorphous hydrogenated silicon, it is necessary to create a homogeneous and maximum

internal electric field in the entire optical light absorption region (i - region).

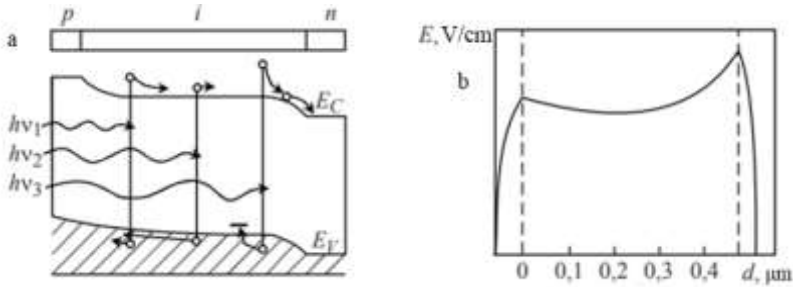


Fig. 8.2. Energy zone diagram of p-i-n - structure (a) and calculated electric field distribution (b)

Under conditions of thermodynamic equilibrium and absence of illumination, the p and n - layers in the p-i-n - structure have positive and negative charges, respectively, which leads to the formation of an electric field in the i - layer. When the p-i-n - structure is illuminated, light passes through the thin p-type frontal window, is absorbed in the thick i - layer, where it generates electron-hole pairs, the separation of which occurs by the electric field in the i - layer. Typically, the thickness of the i -layer is in the range of 200 to 500 nm and that of the p- and n-type layers is in the range of 10 to 30 nm. The holes and electrons generated by light in the n- and p-type layers do not contribute to the SE photocurrent due to the small carrier lifetime in the heavily doped α -Si:H layers [4-6]. Fig. 8.2 shows the energy band diagram of the p-i-n - structure and the calculated electric field distribution in the i - region of 0.5 μm thick α -Si:H. In this case, the electric field strength in the whole i-region exceeds 10^4 V/cm and the hole drift length $m\tau E$ ($m\tau = 3 \times 10^{-9}$ cm²/V) is 0.5 μm, i.e., commensurate with the size of the absorption region (i-region).

The tilt of the zones in the i - layer leads to the fact that the Fermi level in this layer in the region adjacent to the p - layer is shifted towards the valence band ceiling, and in the region adjacent to the n - layer - towards the bottom of the conduction band (see Fig. 1). As a result, some of the states in the optical slit in the i - layer near the p- and n - layers acquire positive and negative charges, respectively. These charged defects enhance the electric field near the p/i and n/i - interfaces. At the same time, the electric field in the volume of the i-layer decreases.

The properties of the p/i - interface have a significant influence on the characteristics of the SEs and their stability under illumination. The introduction of a layer of intrinsic wide-gap α -SiC:H at the p/i - interface increases the no-load voltages due to the reduction of recombination at the interface. The formation of a layer with varying C content and bandgap width further increases the no-load voltage and shape factor. However, the introduction of this layer is accompanied by additional degradation of the SE characteristics, since it affects the redistribution of the electric field under illumination [7].

The critical influence on the characteristics of the SE is exerted by the TCO/p-layer interface. Holes from the p-layer recombine at the TCO/p-layer interface with electrons from the highly doped (up to the degeneracy level) TCO n-type layer. Depending on the quality of the TCO/p - layer, a noticeable depletion of the amorphous p -layer can occur, which creates a barrier at the TCO/p - layer boundary.

The presence of zone tails in the α -Si:H layer leads to a decrease of the integrated field in the i-region and the no-load voltage of the SE compared to the theoretically estimated $U_{o,s}$ value from the zone energy diagram.

When manufacturing p-i-n - structures, solar cells with better parameters can be obtained when the p - layer is created first (fig. 8.3).

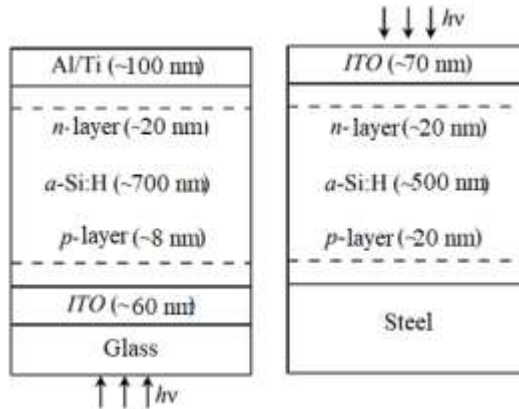


Fig. 8.3. p-i-n - structure on glass (a) and steel (b) substrate

This is explained by the fact that a small amount of boron ($< 10^{18} \text{ cm}^{-3}$) is used to obtain the p - layer, and thus no significant contamination of the unalloyed layer occurs. At the same time, if the n - layer is deposited first, the presence of residual phosphorus changes the properties of the i - layer. Creating a p - layer on the surface of a transparent conducting electrode provides good electrical contact with the electrode. However, it is recommended to create a sufficiently thin p-region (10 nm) so that most of the light is absorbed in the i -region. In addition, in this case, the path travelled by holes to the electrode is shortened and the efficiency of their collection is increased.

The second solar cell design (fig. 8.3b) differs from the first in that a metal foil, in particular stainless steel, is used as a substrate and illumination is performed from the side of a transparent electrode in contact with the n-region. This provides a higher short-circuit current density, which is achieved due to the reflectivity of the metal substrate and the lower optical absorption of light by phosphorus-doped α -Si:H films (n-region) compared to boron-doped layers.

The short-circuit current and power output of the solar cell are increased by introducing a reflective layer and using a textured substrate. This increases the absorption of that part of photons which is weakly absorbed by the i - layer. The rear reflective layer doubles the path travelled by a photon. A more noticeable effect is given by the use of a textured substrate. In this case, as a result of reflection from the textured surface of the substrate, conditions of total internal reflection are provided. The light is as if captured by the solar cell. In this way, the short-circuit current can be increased by up to 25 %.

In general, the front surface makes the main contribution to light scattering in the SE at wavelengths from 450 to 650 nm, while the rear surface - more than 650 nm. Thus, to enhance the effect of "sunlight capture" in the maximum wavelength range, it is necessary that the SEs have developed frontal and rear surfaces.

The properties of the transparent conducting oxide layer significantly affect the characteristics of the formed SE. Such layers should have high transparency to solar radiation, have low specific surface resistance to minimize series resistance losses, and provide low contact resistance to the p-type layer. High contact resistance results in lower V_{oc} and shape factor. The contact resistance between SnO_2 and α -SiC:H p -type layers is significantly affected by the deposition temperature. In addition, the TGO should be resistant to hydrogen reduction during plasma chemical deposition of other layers.

The transparent conducting oxides used to form the front electrode are $SnO_2:F$, $In_2O_3 - SnO_2$ (ITO) $ZnO:Al$. They have high transparency ($> 90\%$), large width of the forbidden zone (> 3.5 eV), low specific surface resistance (< 10 Ohm).

It is very effective to increase the efficiency of cascaded SEs by using TCOs, which provide increased absorption due to multiple internal reflection of sunlight. However, in highly textured layers, there is a decrease in the no-load voltage in SEs

with thinner i-layers due to an increase in the defect density in the i-layer. It is known that in a-Si:H based solar cells formed on SnO_2 layer, $U_{o,s}$ decreases with decreasing thickness of p - layer. A chemical vapour deposition method at atmospheric pressure and temperature 550°C is used to form textured tin dioxide. Zinc oxide and indium tin oxide (ITO) are deposited using sputtering or evaporation techniques at lower temperatures and are generally not textured. The uneven surface of zinc oxide can be obtained by etching in HCl. The use of zinc oxide results in a high contact resistance with α -Si:H. Layers of doped microcrystalline silicon can be used to obtain lower contact resistance.

ZnO is a promising material for TCO formation. The transparency of the SnO_2 layer deteriorates in the plasma due to its chemical reduction, which leads to a noticeable absorption in the layer. In addition, SnO_2 is less transparent in the visible region of the spectrum (transmittance is 94 %) than ZnO (transmittance is 97 %). This reduces the short-circuit current of SEs with SnO_2 -based TCO by 10 %. The problems of using ZnO are related to barrier formation at the ZnO/ α -SiC:H p -type contact, difficulty in providing clean laser scribing, and high shunt current.

Consider textured glass substrates with a TCO layer (fig. 8.3a). After the formation of the p-i-n - structure, a back reflective layer is deposited. Ag has the best reflective characteristics, and Al is also used. However, at the Si/Ag interface, the reflection deteriorates due to mutual diffusion of the elements. To prevent this, a buffer layer of ZnO is introduced between Si and Ag. To obtain a textured surface that scatters light, the deposition of Ag and ZnO layers is carried out at high temperatures: from 100 to 400°C . However, for SEs on glass substrate, the deposition temperature of the TGO back layer is limited due to the fact that the p-i-n structure is already formed. With time, the reflection of the ZnO/Ag contact deteriorates, resulting in a 3-4 % reduction of the short-circuit current. A

similar effect is not observed with the back reflecting ZnO/Al contact.

In solar cells fabricated on a stainless-steel substrate (fig. 2), a textured back reflective layer of Ag or Al is formed on which a back TGO layer, a p-i-n - structure and a front TGO layer are deposited. The formation of Ag metal mesh on the TGO layer reduces the specific surface resistivity.

For single SEs, the optimum optical slit width for the i-layer material is 1.7 eV. Using such a semiconductor, an idle voltage of up to 0.9 V and a shape factor of ~ 0.75 are obtained.

8.3. Effect of temperature and radiation on solar cell parameters

Thermophotovoltaic power generation is the conversion of long-wave (thermal) radiation, which, after heating the emitter material (radiator) to a high temperature (using concentrated solar radiation, burning natural gas, propane, petrol, hydrogen, etc.), is converted into electricity by a photovoltaic cell. Currently, the efficiency of such systems is not high and does not exceed 5 per cent, but they can operate around the clock, while ground-mounted solar cells usually operate less than 40 per cent of the time.

In any solar cell there are power losses due to parasitic resistances. In many cases, it is sufficient to introduce centred series resistance R_s and shunt resistance R_{sh} into the equivalent circuit (fig. 8.4). The diode and R_{sh} shunting the current source, as well as the resistance R_r included in series with them, should provide the output voltage U and current I [1,2].

The series resistance is due to the bulk resistance of the substrate, contact resistance on the front and back sides of the substrate. The shunt resistance is mainly caused by leakage currents across the p-n junction.

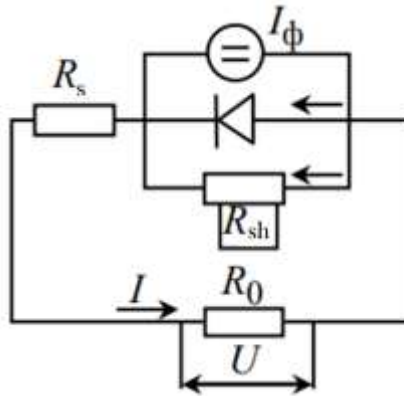


Fig. 8.4. Equivalent circuit of a real solar cell

Bulk leakage channels are created by foreign micro and macro inclusions in the p-n junction material. Surface leakage channels are formed by intensive recombination of electron-hole pairs through a continuous series of energy states on the semiconductor surface, arising due to the violation of valence bonds, as well as by current flow through impurities in the places where the p-n junction exits to the surface [3,4].

In order to obtain a more accurate picture, especially in the case of the use of thin films in devices that resist the flow of current, it is necessary to use various models of distributed resistance calculated by numerical and analytical methods.

Summing up the currents flowing in the branches of the equivalent circuit, we obtain the equation of the volt-ampere characteristic of a real photocell:

$$I = I_S \left[\exp \frac{e(U - IR_a)}{akT} - 1 \right] + \frac{U - IR_a}{R_{sh}} - I_f.$$

The series and shunt resistances cause losses in the SE, which lead to a decrease in the shape factor and no-load voltage. Therefore, knowledge of these parameters is very important for improvement of solar cell manufacturing technology.

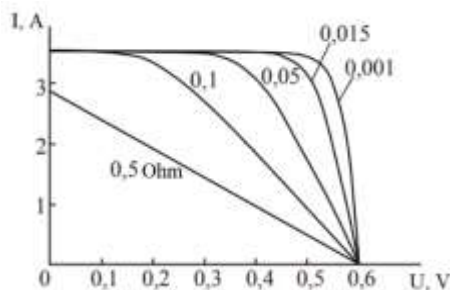


Fig. 8.5. VAC of solar cell with different value of resistance R_s

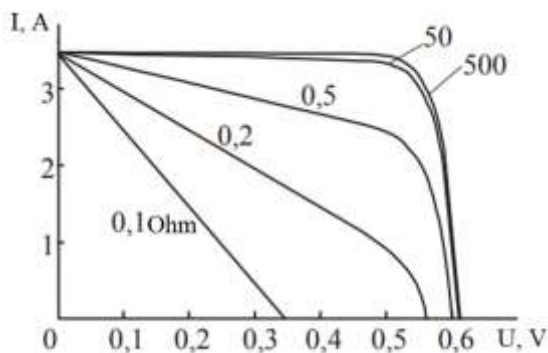


Fig. 8.6. VAC of solar cell with different value of resistance R_{sh}

As a rule, R_{sh} is large, so the second summand in equation (1) can be neglected.

The voltage drop across the series resistance has a much more significant effect on the volt-ampere characteristic than the voltage drops across the shunt resistance (figs. 8.5 and 8.6).

As can be seen from fig. 4, when the series resistance is increased from 0 to 5 ohms, the power decreases by more than 70%.

The permissible value of R_s , providing small power losses, can be approximated by assuming that the operating point of the cell characteristic corresponds to the maximum power mode, when the total losses can be represented as $J_m^2 \cdot R_s$ [5]. Then the share of power losses Z_s is defined as:

$$Z_s = J_m^2 \cdot R_s / (J_m \cdot V_m) = J_m \cdot R_s / V_m \approx J_{s.c} \cdot R_s / V_i.$$

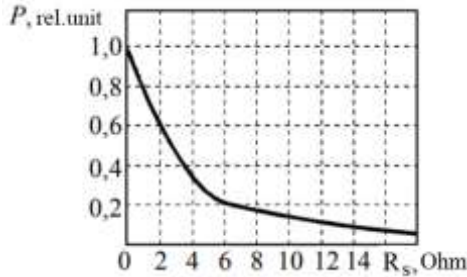


Fig. 8.7. Dependence of photocell output power P on series resistance R_s

Under the conditions of $J_{s.c} = 40 \text{ mA/sm}^2$ and $V_i = 0.6 \text{ V}$, for the loss fraction to be less than 3%, the series resistance of a square centimeters of element area should not exceed 0.5 Ohm.

Similarly, the power loss fraction of the shunt resistance is written as:

$$Z_{sh} = V_m^2 \cdot R_{sh} / (J_m \cdot V_m) = V_m / J_m \cdot R_{sh} \approx V_i / (J_{s.c} \cdot R_{sh}).$$

To keep the losses due to R_{sh} below 3%, the R_{sh} of each square centimeters of solar cell area must be greater than 500 Ohm. This approximate analysis provides reasonably accurate results with Z_s and Z_{sh} not exceeding 5%. For small power losses V_i and current $I_{s.c}$ are almost unchanged, and the most significant cause of these losses is the relative decrease in the shape factor.

With increasing temperature, the diffusion lengths in Si and GaAs increase as the diffusion coefficient does not change

or increases, and the lifetime of non-basic carriers increases with increasing temperature. The increase in the diffusion length of the non-basic carriers leads to an increase in $I_{s.c}$. However, this effect is small and is of the order of 0.07 %/K (fig. 8.8).

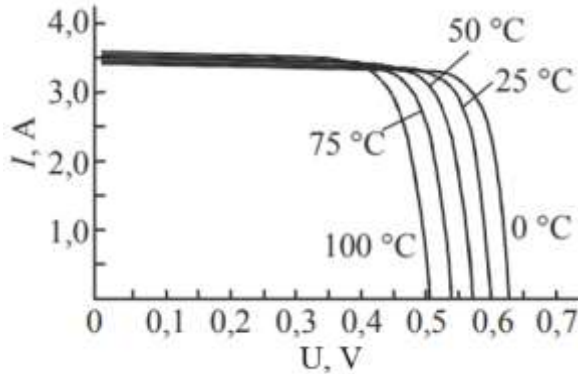


Fig. 8.8. VAC of a solar cell at different temperatures

Taking into account that $I_f \gg I_{01}$, and taking into account the law of acting masses for charge carriers:

$$n_i^2 = np = N_c N_v \exp\left(-\frac{E_g}{kT}\right)$$

we obtain the following expression for U_i :

$$U_i = \frac{E_g}{e} - \frac{kT}{e} \ln \left[\left(\frac{q N_v N_c A_j}{I_f} \right) \left(\frac{L_n}{n_n \tau_n} + \frac{L_p}{p_p \tau_p} \right) \right].$$

It follows from this equation that U_i decreases significantly with increasing temperature (see fig. 5), exceeds the increase of $I_{s.c}$ and is of the order of 0.4 %/K. In addition, the smoother shape of the volt-ampere characteristic at higher temperatures leads to a decrease in the shape factor. Therefore, in general, the increase in temperature leads to a decrease in conversion efficiency (fig. 8.9).

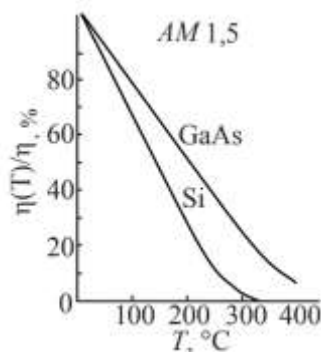


Fig. 8.9. Normalized conversion efficiency for ideal solar cells based on Si and GaAs

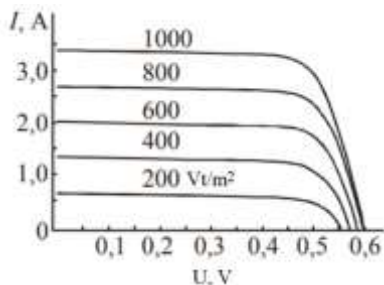


Fig. 8.10. VAC of a solar cell at different irradiation intensities

The photocurrent, and hence the short-circuit current $I_{s,c}$, is directly proportional to the irradiation intensity (fig. 8.10). At the same time, the no-load voltage U_i has a logarithmic dependence on the radiation intensity.

In space conditions, the output power of solar cells decreases due to the fact that irradiation by high-energy particles in remote orbits leads to the formation of defects in the semiconductor.

The photocurrent decreases with decreasing diffusion lengths L_n and L_p . The lifetime of excessive non-basic carriers at irradiation of semiconductor by high-energy particles changes according to the law:

$$\frac{1}{\tau} = \frac{1}{\tau_0} + K_1 \Phi, \quad (*)$$

where, τ_0 – initial lifetime; K_1 – constant; Φ – radiation dose.

It follows from expression (*) that the recombination rate of non-basic carriers is proportional to the initial concentration of recombination centres and their concentration introduced into the semiconductor during irradiation and proportional to the dose of particles hitting the semiconductor. Since the diffusion length is equal to $(D\tau)^{1/2}$, a D depends weakly on irradiation (or on the doping level), the relation (*) can be written in the form of:

$$\frac{1}{L^2} = \frac{1}{L_0^2} + K\Phi,$$

where, L_0 – is the initial diffusion length; $K = K_1/D$. To improve radiation resistance, lithium is introduced into solar cells, which easily diffuses and forms complexes with radiation point defects. Obviously, L_i neutralizes the defects and prevents lifetime degradation. To reduce the number of high-energy particles reaching the cell in outer space, a protective coating (e.g., cerium-containing thin paper) should be placed in front of the cell face.

Connection of individual solar cells Individual solar cells are not used in practice. An individual solar cell has low values of $I_{s.c}$ and U_i , in particular a silicon SE with an area of 2 cm^2 - an idle voltage of 0.5 to 0.6 V and a short-circuit current of 30 to 60 mA.

If high current values are required, parallel connection of solar cells is used (fig. 8.11). Volt-ampere characteristics of solar batteries with different number of parallel connected solar cells are shown in fig. 8.12.

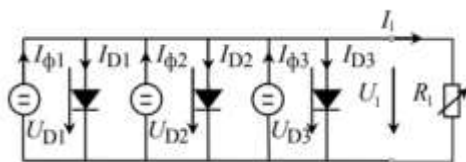


Fig. 8.11. Parallel connection of solar cells

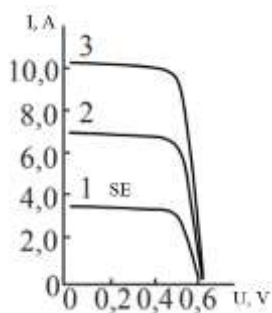


Fig. 8.12. VAC of SEs connected in parallel

To ensure high voltage values, solar cells are connected in series (fig. 13). Volt-ampere characteristics of solar batteries with different number of solar cells connected in series are shown in fig. 14.

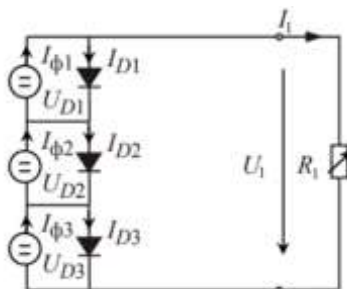


Fig. 8.13. Series connection of solar cells

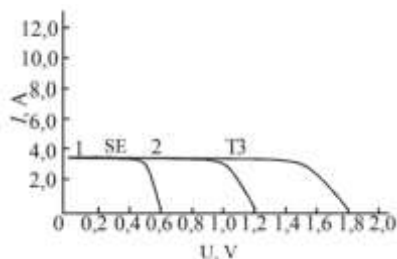


Fig. 8.14. VAC of SEs connected in series

The series-parallel connection of the elements in a larger battery allows for higher voltages and currents to be applied to the load simultaneously.

8.4. Increasing the stability of basic parameters of solar cells based on disordered semiconductors

Degradation of the efficiency factor (EF) of solar cells (SCs) based on a-Si:H is due to the fact that under the action of illumination a new metastable state arises due to defects [1-3]. The 2/3 decrease in efficiency is caused by the decrease in the shape factor and 1/3 by the decrease in the no-load voltage. The degradation of the short-circuit current under illumination is insignificant, but it is maximum when the SE operates in the no-load mode and minimum when the short-circuit state is closed.

Due to high temperatures in summer, the material properties improve (carrier lifetime increases, optical slit width decreases), which leads to an improvement of SE characteristics. This is also favored by the shift of the solar spectrum to the short-wave side associated with the decrease of AM. The most noticeable changes in the module based on single SEs are observed during the first two months of operation under illumination conditions. Complete stabilization occurs after two years of operation. In case of poor-quality sealing of the

modules, the degradation of SEs can increase due to corrosion of thin films.

Currently, to improve the stability of a-Si:H-based solar cells parameters, the technologies of forming individual layers and the SE design as a whole are being optimized.

Hydrogen dilution not only increases the efficiency of a-Si:H-based solar cells, but also reduces the degradation of SE parameters under illumination conditions [107]. In particular, in solar cells obtained with hydrogen dilution, the no-load voltage is less degraded compared to SEs in which the layers are obtained without hydrogen dilution.

The use of wide-area a-SiC:H buffer layers at the p/i-interface of p-i-n-structures, as already mentioned, increases the efficiency value of solar cells based on amorphous hydrogenated silicon. However, it has been shown in several works that the use of buffer layers reduces the conversion efficiency under illumination. Such a decrease in stability is due to the decrease in the no-load voltage and fill factor under illumination. Under illumination, the recombination current in the i-layer volume increases, increasing the dark current and reducing the no-load voltage of the solar cell. The decrease of the filling factor under the action of illumination is explained by the fact that the wide-gap semiconductor a-SiC:H has a high density of states in the middle of the mobility gap. When such a material is used as a buffer layer between the p- and i-layers, these states become positively charged (D^+ -states) because the Fermi level is near the valence band ceiling in this region of the SE. As a result, there is an increase in the electric field in the p/i-region and a decrease in the i-layer. Under illumination, the defect density in the i-layer increases and the electric field becomes insufficient to ensure effective separation of charge carriers, due to which the filling factor decreases [4].

Degradation of the SE parameters can be reduced by using a thin "gettering" layer in the i-layer. Such a layer can be

formed by increasing the RF power of the glow discharge by 3-4 times compared to the i-layer deposition mode. It has been established that in order to enhance the effect of reducing the degradation of SE parameters, it is necessary to use thinner gettering layers and to locate them near the p/i and i/n interfaces. This promotes the formation of a more homogeneous electric field near the i-layer interfaces and reduces the degradation of the no-load voltage and, consequently, the conversion efficiency [5].

The degradation problem of thin-film solar cells can be solved by using microcrystalline silicon, since it has almost no degradation of properties with time. However, the formation of mc-Si:H layers requires a strong dilution of SiH_4 with hydrogen, which leads to a significant reduction in the growth rate. In addition, since mc-Si:H is an indirect bandgap semiconductor, it has a low absorption coefficient and a layer of sufficient thickness must be used. All this restrains the widespread use of mc-Si:H as a thick active i-layer in solar cells.

The predominant transport mechanism in the i-layer SE is drift under the action of the embedded electric field. The embedded field in the i-layer of the SE is not uniformly distributed (see fig. 8.15 b).

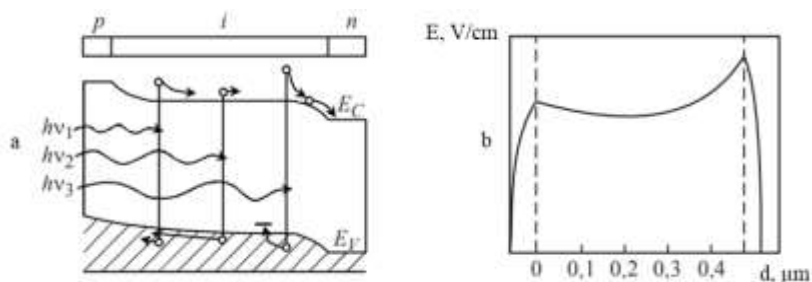


Fig. 8.15. Energy zone diagram of p-i-n-structure (a) and calculated electric field distribution (b)

If the layer is too thick or the material of the layer is of low quality and contains a large number of defects, the field may be practically absent in the middle of the i-layer and carrier transport will be due to diffusion. Since the diffusion length of carriers in a-Si:H is only 100-200 nm, the presence of a region with a small electric field will cause a sharp decrease in the carrier collection efficiency. Illumination by light leads to an increase in the additional number of broken bonds and density of states in the mobility gap, accompanied by a decrease in the electric field in the i-layer and an increase in losses in the SE due to recombination. If the thickness of the i-layer is small (< 250 nm), no appreciable degradation under illumination is observed in the SE because the drift path length of carriers is not smaller than the i-layer thickness. In addition, calculations show that as the thickness of the i-layer decreases, the minimum of the integrated electric field in the i-layer increases. Carrier collection can be promoted by forming the i-layer with increasing optical slit width from the n- to the p-layer. Practically, this can be achieved by varying the deposition temperature (increasing the deposition temperature leads to a decrease in the hydrogen content in a-Si:H and a decrease in its optical slit width).

Thus, by reducing the thickness of a-Si:H-based solar cells, the degradation of conversion efficiency can be reduced. As a rule, the maximum stabilized efficiency of a single SE is obtained with an i-layer thickness of ~ 200 nm. However, this also reduces the optical absorption of the structure. Therefore, it is necessary to use reflective layers on the back side and cascade structure of the solar cell. The use of cascade structures gives, on the one hand, the possibility to reduce the thickness of individual p-i-n-elements and thus provides greater stability, and on the other hand - a high value of efficiency due to the large thickness of the entire structure. It is also necessary to keep in mind that current matching in cascaded SEs assumes a minimum

thickness of the i-layer in the upper p-i-n-structure. As noted earlier, in this case also the degradation of this p-i-n element will be minimal. At the same time, this p-i-n-structure is a filter for the underlying structures, cutting off a part of the incident radiation. Reducing the intensity of the incident radiation on the lower p-i-n-elements, in turn, reduces the degradation of these elements. The dependence of the power generated by SEs on the time of operation (fig. 8.16) shows that after 1000 h of illumination the power generated by a solar cell with one p-n junction decreases by 30 %, and for SEs with three junctions the decrease is 15 %.

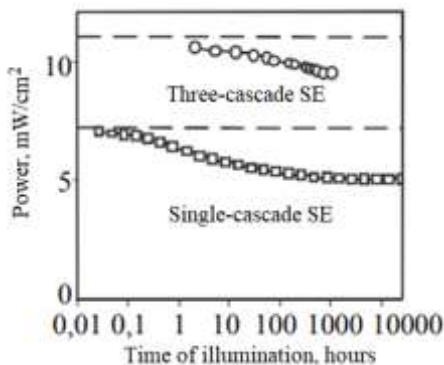


Fig. 8.16. Dependence of generated SE power on operation time

The application of a-Si:H/c-Si based structures opens wide opportunities for increasing the stability of solar cells. In such heterostructures there is practically no degradation of properties over time under illumination, which is promising in terms of their use not only for terrestrial but also for space purposes.

9. PHOTOELECTRIC PHENOMENON IN AMORPHOUS SEMICONDUCTORS

In disordered semiconductors, unlike crystalline semiconductors, there is no long-range order. At the same time it is established that in disordered semiconductors there is a near and middle order. For semiconductor materials with predominance of covalent type of chemical bonds, the short-range order is determined by the interaction of covalently bonded atoms and extends to the first and partially second coordination spheres. The middle order is determined by the interactions of electrons of unpartitioned pairs, van der Waals interaction and is formed by atoms that are partially included in the second coordination sphere and coordination spheres of higher orders.

Figure 9.1 shows the spectral dependence of the quantum yield for α -Si:H films obtained by the glow discharge method and at different temperatures [1].

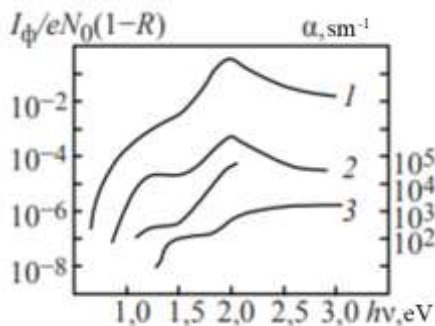


Fig. 9.1. Spectral dependence of quantum yield for amorphous silicon films obtained in glow discharge at different temperatures: 1 - $T = 500$ K; 2 - $T = 380$ K; 3 - $T = 350$ K; α - absorption coefficient of the film deposited at $T = 500$ K

Significant absorption is observed in the region where the quantum yield has small values (see fig. 9.1). The dependence of the quantum yield on temperature and wavelength can be explained as follows. Suppose that an electron is excited to an energy ΔE greater than the conduction band bottom energy. If the electron loses one photon quantum $\hbar\omega$ during the time $1/\omega$, it will diffuse to a distance before thermalization (i.e. when the binding energy is equal to $e^2/\varepsilon r$):

$$r_0 = \left\{ \frac{\Delta E + \left[\frac{e^2}{\varepsilon \cdot r_e D} \right]}{\hbar\omega^2} \right\}^{\frac{1}{2}},$$

where, ε – is the dielectric constant; D – is the diffusion coefficient.

If r_0 is greater than the Onzager radius r_e , defined by the formula:

$$e/(\varepsilon \cdot r_e) = kT,$$

then the particles will be released into the zone.

If r_0 is smaller than r_e , they will unite and form an exciton. There are two possibilities for the exciton:

1) recombination of an electron and a hole - the quantum yield at $r_0 < r_e$ has the form:

$$\eta = \frac{1}{1 + \exp\left(\frac{E_0}{kT}\right)},$$

where:

$$E_0 = \frac{e^2}{\varepsilon} \left[\frac{1}{r_e} - \frac{1}{r_0} \right],$$

2) electron and hole exit into the zones before recombination - in this case $\eta = 1$.

In the forbidden zone of amorphous silicon there are overlapping zones of acceptor E_x and donor E_y states (fig. 9.2).

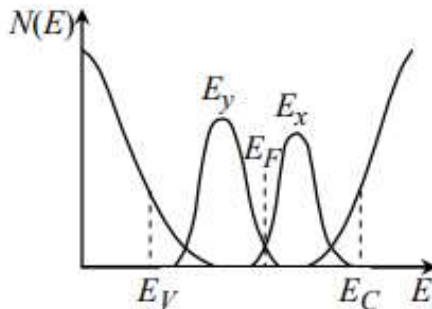


Fig. 9.2. Energy diagram of overlapping acceptor E_x and donor E_y states in the forbidden zone of amorphous silicon

The carriers trapped on them are released during the fly-through process under changing external conditions (field, temperature). This can be used to determine the carrier lifetime, or the time in which a carrier is lost due to its entrapment on a deep trap. The product $\mu D \tau$ (the distance that charge carriers are free to travel in a unit external electric field) is an important material parameter.

For α -Si:H film obtained in a glow discharge, it is assumed that in the region where the number of photogenerated charge carriers is greater than the dark concentration, holes are trapped by E_y -type centers (see fig. 9.2). If these centers are charged, they should be located in the overlap region with the E_x zone. It has been found experimentally that at room temperature the subsequent electron recombination is irradiation-free. The recombination rate $1/\tau$ depends on the number of excess carriers and hence on the product AF (A - absorption; F - photon flux incident on the sample).

It was found that for α -Si:H:

$$i_p = (AF)^\gamma,$$

where, $0,5 \leq \gamma \leq 1,0$ (the degree exponent γ does not depend on the photon flux when its value changes by several orders of magnitude, but is largely determined by temperature).

In accordance with the Mott-Davis-Street energy state distribution model, three mechanisms of charge carrier transfer in disordered semiconductors are possible [2-5]. If the Fermi level is located in the zone of localized states $N(E_f)$, then at low temperatures a hopping mechanism of conduction by states located near the Fermi level is possible. In this case, carriers tunnel between nodes that differ weakly in energy over a distance of variable length. This conduction mechanism has been termed hopping conduction with variable hopping length. Mott derived an expression for this mode of conduction:

$$\sigma = A \cdot \exp \left[- \left(\frac{T_0}{T} \right)^{\frac{1}{4}} \right], \quad (9.1)$$

where, $T_0 = \text{const.}$

The pre-exponential multiplier A is defined as:

$$A = \frac{1}{6} e^2 R^2 \nu_\phi N(E_f). \quad (9.2)$$

where, R – is the hopping length; ν_ϕ – is the phonon frequency of the order of $10^{13} \cdot \text{s}^{-1}$.

Thus, it follows from expressions (9.1) and (9.2) that the density of states at the Fermi level $N(E_f)$ can be determined from the dependence $\lg \sigma \sim (1/T)^{1/4}$ at low temperatures. The $T^{-1/4}$ dependence is observed in pure α -Si or in heavily doped samples of hydrogenated amorphous silicon, when the density of states near the Fermi level is large and is carried out with the first transport mechanism. At higher temperatures, the charge carriers can either be trapped on localized states of the valence band and conduction band tails, or end up in pervasive band states above the mobility threshold. The second mechanism of conduction at high temperatures is associated with the transfer of charge carriers on localized states on the tails of the zones. In this case, the mobility of charge carriers can be determined from the expression:

$$\mu_c = \nu_{ph} \frac{ea^2}{kT} \exp \left[- \frac{W}{kT} \right] \exp(-2\alpha R),$$

where $\exp[-W/kT]$ – is the Boltzmann factor; W is the difference of energies in the state before and after the jump or the activation energy of the jump; $\exp(-2\alpha R)$ – is a multiplier depending on the overlap of wave functions; R – is the distance covered by one jump, at energies close to E_c , the overlap is large and $\exp(-2\alpha R) \sim 1$.

As we see, the expression for the mobility of charge carriers includes an exponential multiplier related to the activation energy of the jump, which causes an exponential dependence of the drift mobility on temperature. In this case, the activation energy of conductivity includes the sum of the activation energies of concentration and drift mobility. If charge transfer is carried out along the localized states of the conduction band tail, the expression for σ will take the form:

$$\sigma = \sigma_0 \cdot \exp[-(E_A - E_F + W)/kT],$$

where, E_A – is the edge of the tail of the conduction zone.

The third mechanism is realized when charge transfer is carried out by delocalized states, and the free path length is less than the interatomic distance but comparable to it ($L \sim a$), conduction can be described by diffusive motion. In this regime, the electron mobility is determined by the formula:

$$\mu_c = \frac{1}{6} \cdot \frac{ea^2}{kT} \nu, \quad (9.3)$$

where, a – is the interatomic distance; ν – is the hopping frequency.

The value of $\mu_c = 1 - 10 \text{ sm}^2/(\text{V}\cdot\text{s})$.

Considering that $\mu_c \sim 1/kT$, the expression for electrical conductivity is transformed as:

$$\sigma = \sigma_M \cdot \exp[-(E_c - E_F)/kT], \quad (9.4)$$

where, σ_M – is the minimum metallic conductivity.

It is defined as the minimum non-activation conductivity. For the majority of disordered semiconductors, the value of σ_M lies in the range of $10-10^3 \text{ Ohm}^{-1}\cdot\text{cm}^{-1}$.

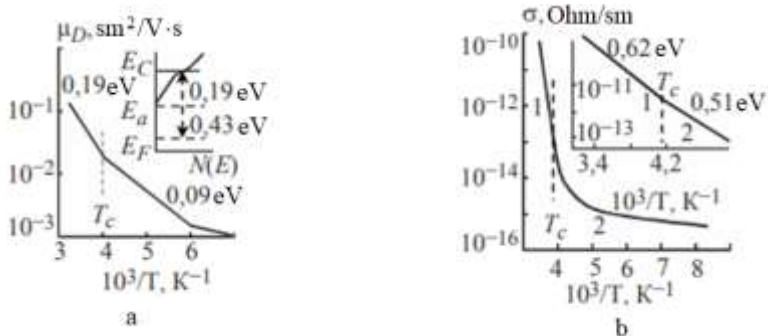


Fig. 9.3. Temperature dependence of electron drift mobility μ_D (a) and conductivity σ (b) for silicon film deposited in glow discharge at 500 K

It follows from expressions (9.3) and (9.4) that the mobility depends weakly on temperature when charge carriers are transported along the propagated states of the valence and conduction zones. The activation energy of conduction is determined by the activation energy of the concentration of free charge carriers.

Measurements of electron drift mobility in the sample deposited in the glow discharge at $T = 500$ K have shown that the temperature dependence curve has a kink at temperature T_c (~ 250 K), above which the activation energy is 0.19 eV and below which it is 0.09 eV (fig. 9.3a).

The temperature dependence curve of the conductivity (fig. 9.3b) also shows a slope change at the same temperature (~ 250 K).

The obtained dependences can be explained by the transport over non-localised states at $T > T_c$, and the activation energy of drift mobility is due to the capture of carriers in the region of small localised states at the edge of the conduction zone, as well as the hopping mechanism of transport over these states at $T < T_c$.

9.1. Study of optical properties of thin films by 4-probe method

InS_2 , CuGaS_2 and their solid solutions have been studied in detail in the absorption edge region. The data on the optical properties (bandgap width, type of interband transitions, etc.) of films of these materials obtained by different methods are very limited and contradictory, which is due to the high dependence of the composition and, consequently, the physical parameters of the films on the conditions of preparation. To investigate the optical properties of Cu(In,Ga)(S,Se)_2 films, the most promising is the study of the dispersion of optical constants n and k (real and imaginary components of the refractive index, respectively) in a wide spectral range, which makes it possible to obtain unambiguous information on the zone structure of films of these compounds.

The basis of the method is the study of interference phenomena in the substrate-absorbing film system at the incidence of a light beam close to the normal. The optical constants n and k are calculated by the method of successive approximations from the measured spectral dependences of the transmission coefficient $T(\lambda)$ and reflection coefficient $R(\lambda)$. The theory of the method and an improved calculation procedure are given in [1,2].

Taking into account all phenomena in the film-substrate system, including interference, leads to complex transcendental equations relating the real n and imaginary k components of the refractive index to the measured values of $T(\lambda)$ and $R(\lambda)$. Direct measurement of the dispersion dependence of $n(\nu)$ and $k(\nu)$ is not possible, so the transmission coefficients $T(\lambda)$ and reflection coefficients $R(\lambda)$ are measured and the dependences of $n(\nu)$ and $k(\nu)$ are reconstructed from them. The system of equations used to calculate the optical constants of thin films is derived in [3] and has the form:

$$T_{14} = \frac{1-R_{12}}{1-R_{12}R_{\alpha}}, \quad T_{14} = \frac{R_{12}T_{\alpha}}{1-R_{12}R_{\alpha}} + R_{\alpha}, \quad (9.5)$$

were

$$R_{12} = \frac{n^2-1^2}{n^2+1^2}, \quad T_{\alpha} = \frac{16n_2^2+k_2^2}{A}, \quad (9.6)$$

$$R_{\alpha} = \frac{C}{A}, \quad R'_{\alpha} = \frac{B}{A}, \quad (9.7)$$

where R_{12} is the Fresnel reflection coefficient at the film-air interface, A, B and C are the values expressing the relationship between the real and imaginary components of the refractive index of the investigated material, substrate and medium, T_{14} and R_{14} are the measured transmission and reflection coefficients of the film-substrate system. The refractive indices of the initial (n_1) and final (n_4) phases are equal to unity. The region of initial values of $n(v)$ and $k(v)$ is found by the method of successive approximations, in which only the interference transmission spectrum of the film-substrate system is used, and the values of the sought quantities are found at the points of extremums of T_{extr} .

The absorption index can be found by calculation using the formulae

$$\alpha = \frac{1}{t_2-t_1} \ln \left(\frac{T_1}{T_2} \right), \quad (9.8)$$

$$\alpha = \frac{1}{t} \ln \left(\frac{T}{1-R^2} \right), \quad (9.9)$$

where T_1 and T_2 are the transmission coefficients for two thin films of thicknesses t_1 and t_2 , respectively, t is the film thickness, T is the transmission coefficient, R is the reflection coefficient.

The width of the forbidden zone E_g is determined by extrapolation of the rectilinear part of the dependence $(\alpha \cdot hv)^2$ on the photon energy (hv) up to the intersection with the abscissa axis (fig. 9.4), related to E_g by the relation

$$\alpha hv = \frac{A}{hv} \sqrt{hv - E_g}. \quad (9.10)$$

The thickness of the films d can be determined from the displacement of interference lines at the boundary of the layers

$$d = \frac{\Delta m}{2\sqrt{n^2 - \sin^2\theta}} \cdot \frac{1}{\frac{1}{\lambda_1} - \frac{1}{\lambda_2}}, \quad (9.11)$$

where n is the refractive index (refractive index), θ is the angle of incidence, λ_1 and λ_2 are peaks or troughs ($\lambda_1 < \lambda_2$), Δm is the number of peaks or troughs between λ_1 and λ_2 .

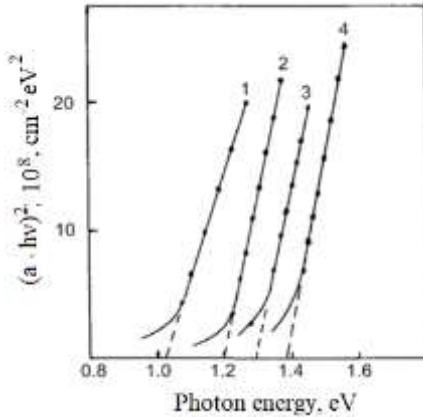


Fig. 9.4. Calculation of the forbidden band width E_g of $\text{CuIn}_x\text{Ga}_{1-x}\text{Se}_2$ films from the approximation of the dependence $(\alpha \cdot hv)^2 = f(hv)$

Optical measurements are usually made on films of varying thicknesses deposited on cleaned glass substrates.

One of the most important electrical measurements of the resulting films is the determination of their specific (ρ) and surface (R_s) resistances. For this purpose, it is most convenient to use the 4-probe method of measurement, which does not require the creation of ohmic contact to the sample under study. The only condition for measurements is the presence of a flat surface, the linear dimensions of which exceed the linear dimensions of the probe system [4]. The measurement scheme is shown in fig. 9.5.

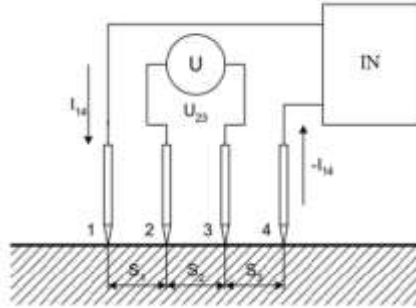


Fig. 9.5. Electrical scheme for measuring the resistivity and surface resistivity by 4-probe method VS - constant voltage source U - voltmeter

For a plate of infinite thickness

$$\rho = \frac{2\pi U_{23}}{I_{14} \left(\frac{1}{S_1} + \frac{1}{S_2 + S_3} - \frac{1}{S_1 + S_2} + \frac{1}{S_3} \right)}, \quad (9.12)$$

if $S_1 = S_2 = S_3 = S$, then

$$\rho = \frac{2\pi S U_{23}}{I_{14}} \quad (9.13)$$

in the case of in-line probes and

$$\rho = \frac{2\pi S U_{23}}{I_{14}(2 - \sqrt{2})} \quad (9.14)$$

when the probes are located at the vertices of a square with side S .

In the case of a thin plate with thickness w , the equations for resistivity are transformed by applying the correction function $g(w/S)$.

For a thin plate with a bottom conductive boundary:

$$g_1\left(\frac{w}{S}\right) = \frac{1}{1 + 4 \sum_{n=1}^{\infty} -1^n \left(\frac{1}{\sqrt{1 + \frac{4n^2 w^2}{S^2}}} - \frac{1}{\sqrt{4 + \frac{4n^2 w^2}{S^2}}} \right)}. \quad (9.15)$$

For a thin plate with two insulating boundaries:

$$g_2\left(\frac{w}{S}\right) = \frac{1}{1 + 4 \sum_{n=1}^{\infty} \left(\frac{1}{\sqrt{1 + \frac{4n^2 w^2}{S^2}}} - \frac{1}{\sqrt{4 + \frac{4n^2 w^2}{S^2}}} \right)}. \quad (9.16)$$

The values of the correction functions for these cases are given in table 9.1.

Table 9.1. Correction functions for thin plate g_1 - with conductive bottom boundary g_2 - with insulated boundaries

w/S	0.1	0.2	0.33	0.5	1.0	1.4	2.0	3.3	5.0	10.0
			3			14		33		
$g_1(w/S)$	1.9· 10 ⁻⁶	0.00 342	0.06 04	0.2 28	0.6 83	0.8 48	0.9 83	0.9 88	0.99 48	0.99 93
$g_2(w/S)$	13.8 63	6.13 9	4.15 9	2.7 8	1.5 04	1.2 23	1.0 94	1.0 22	1.00 7	1.00 045

Table 9.2. Correction functions for determining the surface resistivity of circular $f(d/s)$ and rectangular $f(a/b; b/s)$ plates with finite dimensions

b/s, d/s	f(d/s)	f(a/b, b/s)			
		a/b = 1	a/b = 2	a/b = 3	a/b ≥ 4
1.0				0.9988	0.9994
1.25				1.2467	1.2248
1.5			1.4788	1.4893	1.4893
1.75			1.7196	1.7238	1.7238
2.0			1.9454	1.9475	1.9475
2.5			2.3532	2.3541	2.3541
3.0	2.266	2.457	2.7000	2.7005	2.7005
4.0	2.929	3.114	3.2246	3.2248	3.2248
5.0	5.362	3.51	3.5749	3.575	3.575
7.5	3.927	4.0095	4.0361	4.0362	4.0362
10.0	4.172	4.2209	4.2357	4.2357	4.2357
20.0	4.436	4.4516	4.4553	4.4553	4.4553
40.0	4.508	4.512	4.5129	4.5129	4.5129
∞	4.532	4.532	4.5324	4.5325	4.5324

When measuring the surface resistivity, the sample should have infinite dimensions, but in the case of round or rectangular samples whose dimensions are comparable to the interprobe distance, the correction function $f(a/b; b/s)$ or $f(d/s)$ is introduced (see table 9.2).

This method can also be used to measure the surface resistivity. In this case, if $w/s > 0.4$, the latter is given by the formula

$$R_S = \frac{\pi U_{23}}{I_{14} \ln 2} = 4.53 \frac{U_{23}}{I_{14}},$$

otherwise, the correction function $f(w/S)$ is introduced, which is approximately equal to 1 for small w/S .

To measure the surface resistivity of thick films ($w/s > 0.4$), the correction function $f(w/s)$ is additionally introduced (see table 9.3):

$$R_S = f\left(\frac{w}{s}\right) f\left(\frac{a}{b}; \frac{b}{s}\right) \frac{U_{23}}{I_{14}}.$$

Table 9.3. Correction function for determining the surface resistivity of thick films using the 4-probe method

w/S	0.4	0.5	0.6	0.7	0.8	1.0	1.2	1.4	1.6	2.0
			25	143	333		5	286	66	
f(w/S)	0.995	0.974	0.989	0.979	0.960	0.921	0.849	0.793	0.725	0.636

Thus, the 4-probe method allows us to determine the resistivity and surface resistivity of the deposited films. In addition, it is promising for further study to remove the dependences $\rho(\Phi)$ and $\rho(\lambda)$ to determine the photosensitivity and spectral sensitivity of the deposited semiconductor films.

To estimate the contact resistance between a semiconductor and a metal contact, a special quantity called the specific contact resistance ρ_c [$\text{Ohm} \cdot \text{cm}^{-2}$] is used. The value ρ_c

$\rho_C = R_S \cdot L_T,$

where L_T is the transfer length (transfer length) – the distance from the contact at which the voltage value is attenuated by e times

where L_T is the transfer length (transfer length) – the distance from the contact at which the voltage value is attenuated by e times

$$\frac{U}{I} = \frac{R_S S}{z} + \frac{2L_T}{z} R_S coth\left(\frac{L}{L_T}\right) = R_{layer} + R_{contact}$$
$$U = IR + \frac{IR_S}{z}S + 2L_T,$$
$$L_T = \frac{\frac{zU}{IR_S} - S}{2},$$

$$\rho_S = R_S \frac{\frac{zU}{IR_S} - S}{4},$$

In the case of circular contacts of radius a , the contact resistance is described by the formula:

$$R_{contact} = \frac{R - \frac{R_{layer}}{2a}}{2} = \frac{R_{layer}}{S_{contact}},$$

$$R_{layer} = R_{contact} \cdot S_{contact},$$

where R is the resistance measured between the contacts R_{layer} is the film resistance, $S_{contact}$ is the contact area, $R_{contact}$ is the contact resistance.

The above techniques have been used to measure contact resistance in GaAs and Si-based solar cells and their application to the analysis of Cu(In,Ga)Se₂-based solar cells may encounter difficulties associated with both polycrystallinity of the structure and specific features of this material. The main technological difficulty of the measurement is the application of two rather large contacts ($L \gg L_T$) used in the research.

9.2. Theoretical calculation of photocurrent generated in silicon-based solar elements

Currently, the main material for making solar cells is crystalline silicon. The share of solar cells and modules produced on the basis of crystalline silicon in the photovoltaic market exceeds 90% in modern times, with approximately 2/3 being crystalline and 3/1 being polycrystalline. Such a wide application of crystalline silicon in photovoltaics is conditioned by the rapid development of silicon technology and, in general, the possibility of preparing solar cells based on crystalline silicon suitable for terrestrial use and with a more reasonable efficiency/price ratio. Therefore, the calculation of the photocurrent generated in solar cells (GE) is important.

If monochromatic light with wavelength λ and photon energy $h\nu \geq E_g$ falls on the upper surface of the solar cell (fig. 9.7), the dependence of the generation rate of electron-hole pairs on the distance x from the surface of the semiconductor is determined as follows [1]:

$$G(\lambda, x) = \alpha(\lambda)F(\lambda)[1 - R(\lambda)]\exp[-\alpha(\lambda)x],$$

where, $\alpha(\lambda)$ – absorption coefficient; $F(\lambda)$ – the density of the photon stream falling in a single spectral interval; $R(\lambda)$ is the share of photons reflected from the surface.

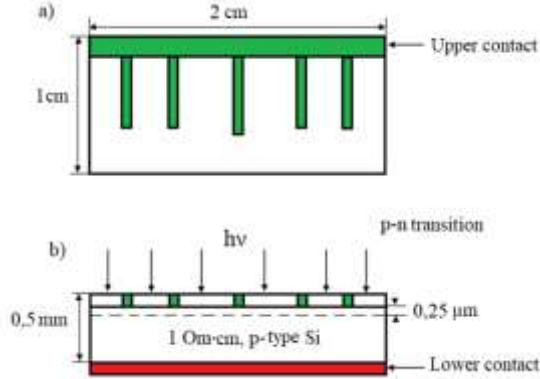


Figure 9.7. Schematic representation of p-n junction silicon solar cell: a – top view, b – side view

The photocurrent generated by light in a solar cell can be found from the continuity equation for excess charge carriers. The one-dimensional steady-state discontinuity equation for holes in an n-type semiconductor at the low level of injection will be:

$$G_p - \frac{p_n - p_{n0}}{\tau_p} - \frac{1}{e} \frac{dJ_p}{dx} = 0.$$

The continuity equation for electrons in a p-type semiconductor will be written as follows:

$$G_n - \frac{n_p - n_{p0}}{\tau_n} - \frac{1}{e} \frac{dJ_n}{dx} = 0.$$

In this case, the current density for holes and electrons is determined by the following equation:

$$J_p = e\mu_p p_n E - eD_p \frac{dp_n}{dx},$$

$$J_n = e\mu_n n_p E + eD_n \frac{dn_p}{dx}.$$

In these expressions, J_p and J_n are the hole and electron current densities, respectively. In a solar cell with a sharp p-n junction and a constant doping level along both sides of the junction (fig. 9.8), no electric field exists outside the junction region.

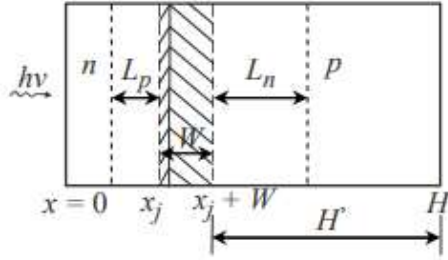


Figure 9.8. Solar cell dimensions and characteristic diffusion length of non-major charge carriers

From the above equations, we can get the equation describing the distribution of non-major charge carriers in the n region:

$$D_p \frac{d^2 p_n}{dx^2} - \frac{p_n - p_{n0}}{\tau_p} + \alpha F(1 - R) \exp(-\alpha x) = 0. \quad (*)$$

The general solution of this equation

$$p_n - p_{n0} = A \cosh(x/L_p) + B \sinh(x/L_p) - C \exp(-\alpha x)$$

is searched for. Here, $L_p = (D_p \cdot \tau_p)^{1/2}$ – diffusion length; A, B, C are constants.

Using the specific solution $p_n - p_{n0} = C \cdot \exp(-\alpha x)$ in equation (*) allows determining C:

$$C = \frac{\alpha F(1-R)\tau_p}{\alpha^2 L_p^2 - 1}.$$

The constants A and B are determined when using the boundary conditions in the frontal plane where recombination

occurs (when $x = 0$) and in the cascading region. The first condition can be obtained by noting that the diffusion current density at $x = 0$ is equal to the surface recombination current density:

$$D_p \frac{d(p_n - p_{n0})}{dx} = S_p(p_n - p_{n0}).$$

Here, S_p is the surface recombination rate.

The second boundary condition is true for the boundaries of the space charge region with few non-major charge carriers. Thus:

$$x = x_j \text{ olduqda } p_n - p_{n0} = 0.$$

Taking into account the boundary conditions in equation (*) allows us to obtain an expression for the excess concentration of holes:

$$p_n - p_{n0} = \left[\frac{\alpha F(1-R)\tau_p}{\alpha^2 L_p^2 - 1} \right] \left(\frac{S_p L_p}{D_p + \alpha L_p} \right) x \frac{sh \left[\frac{x_j - x}{L_p} \right] + e^{-\alpha x_j} \left[\left(\frac{S_p L_p}{D_p} \right) sh \left(\frac{x}{L_p} \right) + ch \left(\frac{x}{L_p} \right) \right]}{\left(\frac{S_p L_p}{D_p} \right) sh \left(\frac{x_j}{L_p} \right) + ch \left(\frac{x_j}{L_p} \right)} - e^{-\alpha x}.$$

Thus, the density of the hole photocurrent generated by photons of wavelength λ at the edge of the truncated region will be as follows:

$$J_p = -e D_p \left(\frac{dp_n}{dx} \right)_{x_j} = \left[\frac{e F(1-R) \alpha L_p}{\alpha^2 L_p^2 - 1} \right] x \left[\frac{\left(\frac{S_p L_p}{D_p + \alpha L_p} \right) - e^{-\alpha x_j} \left[\frac{S_p L_p}{D_p} ch \left(\frac{x_j}{L_p} \right) + sh \left(\frac{x_j}{L_p} \right) \right]}{\frac{S_p L_p}{D_p} sh \left(\frac{x_j}{L_p} \right) + ch \left(\frac{x_j}{L_p} \right)} - \alpha L_p e^{-\alpha x} \right].$$

At a given wavelength of the incident radiation, the photocurrent J_p accumulates on the upper side of the n-p junction of the p-based solar cell, since the lifetime of the charge carriers, their conductivity and the doping level are assumed to be constant in this region.

To determine the electron photocurrent collected in the substrate, it is necessary to use the expressions written above within the following boundary conditions:

$$x = H \text{ when } -D_n \frac{d(n_p - n_{p0})}{dx} = S_p(n_p - n_{p0}) \quad (**)$$

$$x = x_j + W \text{ when } n_p - n_{p0} = 0. \quad (***)$$

Here, H is the full thickness of the solar cell; W is the width of the truncated area. The condition in expression (***) indicates that the concentration of non-major charge carriers near the edge of the truncated region is zero, while the condition in expression (**) determines the rate of surface recombination near the ohmic contact on the rear surface. The use of such boundary conditions allows determining the electron current density generated at the edge of the truncated region of the p-base ($x = x_j + W$) by photons of wavelength λ :

$$J_n = eD_n \left(\frac{dn_p}{dx} \right)_{x_j+W} = \left[\frac{eF(1-R)\alpha L_n}{\alpha^2 L_n^2 - 1} \right] e^{[-\alpha(x_j+W)]} x \left[\alpha L_n - \frac{\left(\frac{S_n L_n}{D_n} \right) \left[ch\left(\frac{H_1}{L_n}\right) - e^{-\alpha H_1} \right] + sh\left(\frac{H_1}{L_n}\right) + \alpha L_n e^{-\alpha H_1}}{\left(\frac{S_n L_n}{D_n} \right) sh\left(\frac{H_1}{L_n}\right) + ch\left(\frac{H_1}{L_n}\right)} \right].$$

Here, H_1 is the thickness of the quasi-neutral region of the p-base. In addition to the diffusion component of the photocurrent collected in the n- and p-regions (above statements), it is necessary to take into account the drift component arising in the truncated region. Electron-hole pairs generated by light in the depleted region are removed from this region by the electric field before they have had the opportunity to recombine with each other. For this reason, the photocurrent of a truncated layer is equal to the number of photons absorbed in a single time in this layer in a single spectral interval:

$$J_{dr} = eF(1-R)\exp(-\alpha x_j)[1 - \exp(-\alpha W)].$$

Thus, the photocurrent generated in the solar cell by light of wavelength λ will be determined by the sum of above expressions:

$$J_L(\lambda) = J_p(\lambda) + J_n(\lambda) + J_{dr}(\lambda). \quad (\bullet)$$

The total density of the photocurrent flowing through a p-n-based element illuminated by sunlight with a spectral distribution $F(\lambda)$ can be obtained by integrating the expression:

$$J_f = \int_{\lambda_1}^{\lambda_2} [J_p(\lambda) + J_n(\lambda) + J_{dr}(\lambda)] d\lambda,$$

where λ_1 and λ_2 are the short- and long-wavelength limits of absorption, respectively.

$\lambda_1 = 0.3 \mu\text{m}$ for a typical solar cell based on p-n junction. The red limit of absorption is determined by the width of the band gap of the semiconductor. The relationship between the wavelength of the red limit of absorption $\lambda_{0s}(\mu\text{k})$ and the width of the band gap $E_g(\text{eV})$ of the semiconductor will be described by the following equation:

$$\lambda_{0s} = \frac{1,234}{E_g}.$$

For silicon ($E_g = 1.12 \text{ eV}$ at $T = 300 \text{ K}$), the red limit of absorption is located near $1.1 \mu\text{m}$.

Expression (\bullet) allows to calculate the spectral value of the solar cell (spectral value is the set of electrons corresponding to one incident photon of a given wavelength). SP – spectral value is equal to the photocurrent $J_L(\lambda)$ (expression \bullet) divided by the quantity eF (external spectral value, and when divided by the quantity $eF(1 - R)$ is the internal spectral value).

$$SR = \frac{J_p(\lambda) + J_n(\lambda) + J_{dr}(\lambda)}{eF(\lambda)[1 - R(\lambda)]}.$$

If the spectral value is known, the total density of photocurrent flowing when the element is illuminated by sunlight with spectral distribution $F(\lambda)$ will be as follows:

$$J_L = e \int_{\lambda_1}^{\lambda_2} F(\lambda)[1 - R(\lambda)]SR(\lambda)d\lambda.$$

The short-wavelength edge of the $Q(\lambda)$ spectral dependence is determined mainly by the collection of charge carriers from the frontal layer, and the long-wavelength edge from the base region.

In SE created on the basis of non-flat-band semiconductors, most of the radiation with energy $h\nu > E_g$ generates electron-hole pairs at a great depth of the base region, which is reflected in the long-wave spectrum of photolight due to the recombination of a part of the generated charge carriers in the volume of the base and on the back surface. determines the spectral dependence of the poled Q .

As a result of the sharp absorption edge in GE based on non-flat-band semiconductors, the value of Q has a sharp increase in the long-wavelength part of the spectrum. However, in this case, the surface absorption begins at large values of λ , as a result of which the value of Q decreases more rapidly due to the recombination of photogenerated charge carriers on the frontal surface with the decrease of λ [2,3].

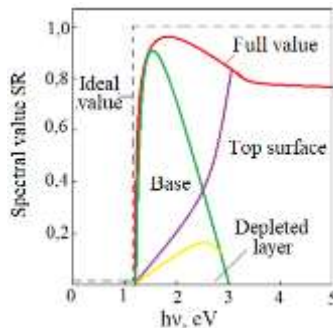


Figure 9.9. Calculated intrinsic spectral value of a p-base silicon element

For a silicon-based solar cell (p-based), the actual intrinsic spectral value differs significantly from the ideal step (figure 9.9).

During the calculations, the following parameters of the device should be used: $N_D = 5 \cdot 10^{19} \text{ cm}^{-3}$, $N_A = 1,5 \cdot 10^{16} \text{ cm}^{-3}$, $\tau_p = 0,4 \text{ mksec}$, $\tau_n = 10 \text{ mksec}$, $x_j = 0,5 \text{ }\mu\text{m}$, $H = 450 \text{ }\mu\text{m}$, S_p (front surface) $= 10^4 \text{ cm/sec}$, S_n (back surface) $= \infty$. Figure 9.9 shows the spectral dependences of the additions of all three components of the current. During the absorption of low-energy photons, the main share of charge carriers is generated in the base region, since the absorption coefficient in Si is small in this case. If the energy of the photons is greater than 2.5 eV, the additional photocurrent is taken from the surface.

When the energy of photons is greater than 3.5 eV, the value of α exceeds 10^6 cm^{-1} and the spectral value is determined exactly by the surface layer. Since the quantity S_p is assumed to be large enough, the surface recombination on the face surface of the element leads to a significant reduction of the spectral value compared to the ideal value. When $\alpha L_p \gg 1$ and $\alpha x_j \gg 1$ the spectral value asymptotically approaches the value determined by the junction face current, which is equal to the following expression:

$$SR = \frac{1 + \frac{S_p}{\alpha D_p}}{\left(\frac{S_p L_p}{D_p}\right) \text{sh}\left(\frac{x_j}{L_p}\right) + \text{ch}\left(\frac{x_j}{L_p}\right)}.$$

The surface recombination rate S_p strongly affects the spectral value, especially in the case of high-energy photons. Figure 9.10 shows the spectral values calculated for the device with that parameter (figure 9.9). At this time, S_p speed was changed in the range of $10^2 \dots 10^6 \text{ cm/sec}$. As can be seen, with the increase of S_p , the spectral value decreases sharply. From the expression, it is clear that at a given value of S_p , the spectral value L_p is more than the diffusion length. In general, it is considered appropriate to decrease S_n and S_p and increase L_n and L_p to increase the spectral value in the range of wavelengths used.

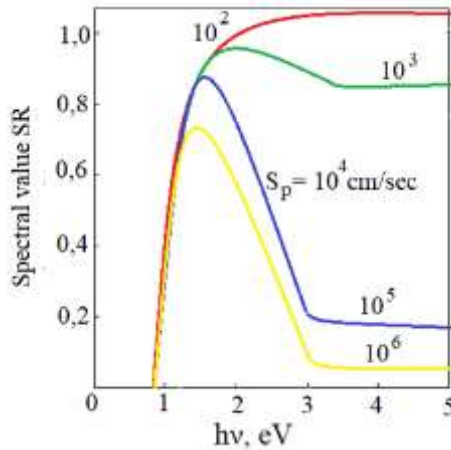


Figure 9.10. Calculated internal spectral value of p-base silicon element at different rates of surface recombination

Thus, it is observed that the collection coefficient drops sharply in the short-wave region as a result of the undesirable nature of the diffusion and recombination parameters of the opened layer [5]. Q can be increased by reducing surface recombination. This condition is achieved as a result of accurate processing of the semiconductor surface with the aim of eliminating recombination centers. In addition, the effective rate of surface recombination depends on the presence of a potential barrier, which in principle allows the reduction of recombination.

The surface recombination rate in gallium arsenide is significantly higher than in silicon. Growing a thin narrow zone layer of $\text{Al}_x\text{Ga}_{1-x}\text{As}$ ($x = 0.75-0.9$) solid solution on the surface of GaAs surface recombination due to the very close period of GaAs and AlAs lattices at the hetero boundary and the insignificance of broken valence bonds on the free surface of GaAs allows to reduce its speed sufficiently [6]. At the hetero boundary, the potential barrier prevents the charge carriers

generated in the narrow-band material from falling to the surface of the wide-band layer. Maintaining high photosensitivity at small ($< 0.1 \text{ } \mu\text{m}$) thicknesses of the considered layer will be possible even in the smallest wavelength region of the solar spectrum.

The second way to increase Q is to reduce the thickness of the doped layer in order to make the ineffective layer more transparent to photons of the solar spectrum [3]. However, the creation of small junctions is limited by the increase in resistance to current flows. In addition, the effect of recombination on the outer surface increases sharply in thin doped layers. For small junctions, there is the problem of creating metal contacts whose size is dictated by the formation of shunts, which limits the reduction of layer thickness. All the conditions we have considered create any optimal thickness of the top coated surface.

The third way is aimed at increasing the purity of the semiconductor layer, which will drastically reduce recombination in the absence of volume radiation. Technologies for purchasing high-quality primary materials and devices that do not spoil the initial parameters are required. At present, a significant deterioration of the parameters of the base occurs as a result of heat treatment of the elements. In addition, a large number of recombination defects are caused by the introduction of extraneous additives during the preparation of the p-n junction.

Finally, the fourth way to increase the collection of charge carriers is related to the creation of electric fields in the layers of the photoconductor, which causes the drift of non-main charge carriers towards the p-n junction. There is no doubt that the energy of the future for the comfortable existence of humanity is closely related to the efficient and effective use of the reactor called the Sun. Therefore, the study of solar cells based on different semiconductors is an important issue. As a

result of the research, the expressions obtained for the calculation of the currents generated in the solar cells are important from many points of view and reflect the reality of today.

9.3. Emission processes in α -Si:H based solar elements

Models of donor- and acceptor-like and amphoteric states in the α -Si:H carrier hole were used to estimate ρ_{trap} of charge carriers trapped in situations in the forbidden zone. States in the tail of the conduction band are assumed to be acceptor-like: these states are negative when they are occupied by electrons, and neutral when they are electron-free. At the tail of the valence band, the states behave as donor-like, while at the tail of the bands, the donor- and acceptor-like states have an exponential distribution.

In amorphous silicon, the Fermi quasi-levels lag behind the conduction band boundaries by more than $2kT$. For such a semiconductor, the Boltzman statistics are fulfilled and the concentration of free charge carriers can be determined by the following expression [1]:

$$\begin{aligned} n &= N_C \cdot \exp[(E_{fn} - E_C)]; \\ p &= N_V \cdot \exp[(E_V - E_{fp})]. \end{aligned}$$

Conditions caused by broken bonds are considered to be amphoteric in nature, that is, they can be either donor- or acceptor-like. This is explained by the fact that they can be in three charge states: positively charged (free of an electron), neutral (in which case there is one electron) and negative (there are two electrons). In this case, the broken bond results in the formation of two electrical levels in the hole: the $E^{+/0}$ level corresponds to the $+/0$ transition, and the $E^{0/-}$ level corresponds to the $0/-$ transition. The distance between two levels corresponds to the energy (E_U correlation energy) required for

the appearance of a second electron when it is already occupied by one electron. In the Mott and Davis model of the structure of the energy bands of amorphous semiconductors, states determined by broken bonds have a Gaussian distribution [2].

In this case, the load and donor- and acceptor-like cases will be determined as follows:

$$\rho_d = q \int_{E_V}^{E_C} N(E)[1 - f(E)]dE ;$$

$$\rho_a = -q \int_{E_V}^{E_C} N(E)f(E)dE,$$

where $f(E)$ is the probability of the energy level being filled with an electron.

In amphoteric cases, the charge is calculated as follows:

$$\rho_{at} = q \int_{E_V}^{E_C} N(E)[F^+(E) - F^-(E)]dE,$$

where, $F^+(E)$, $F^-(E)$ are the probabilities of finding cases in the free and doubly trapped state, respectively.

In a simple case - in the absence of light reflection from the back electrode, the rate of generation is expressed as:

$$G = G_0 \cdot \alpha(\lambda) \cdot \exp[\alpha(\lambda)x],$$

where, G_0 – intensity of incident radiation with wavelength λ ; $\alpha(\lambda)$ – absorption coefficient; x is the distance from the surface of the solar cell.

And generation during the reflection of light from the back electrode

$$G = \frac{G_0 \alpha(\lambda)}{1 - P} [\exp(-\alpha x) + P \exp(\alpha x)],$$

will be. Here, P is the release coefficient.

The recombination rate for an amorphous semiconductor can be calculated for all cases by integrating the recombination rate from the top of the valence band to the bottom of the conduction band. If the recombination efficiency $\eta_r(E)$ is defined as the rate of recombination per unit energy E .

Accepting that the capture and emission of charge carriers occurs only between diffuse and localized states allows using the Shockley-Reed-Hall statistics to describe recombination processes in donor- and acceptor-like states [3,4]. According to these statistics, capture of a discrete energy level is determined by two capture and two emission processes (fig. 9.11): r_1 , r_4 are electron and hole capture rates to the E_t level, and r_2 and r_3 are electron and hole emission rates.

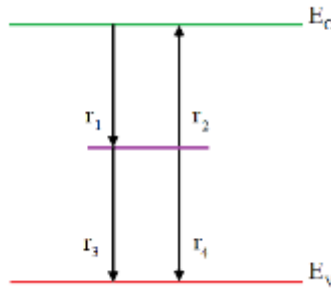


Figure 9.11. Discrete energy level capture and emission processes

Table 1 shows all emission and capture processes of electrons and holes in donor- and acceptor-like states. T_a and T_d in table 9.1 – acceptor and freeze-like states, respectively; v_{th} – heat rate of charge carriers, N_t – concentration of traps; σ_n^+ , σ_p^0 – capture cross section of trap for electron and hole, respectively; e_n^- , e_p^0 and are the emission coefficients of trapped electron and trap, respectively. The "+", "0" and "-" indices in the table indicate the load status of the trap.

In case of thermodynamic equilibrium $r_1 = r_2$ and $r_3 = r_4$ according to the principle of detail equilibrium. In this case, the probability of filling the state is described by the Fermi-Dirac function:

$$f = [1 + \exp(E_t - E_F)]^{-1}.$$

Table 1
Electron and hole capture and emission processes in
donor- and acceptor-like states

Process	Throughput	The speed of the process
Electron capture in the case of T_d^+	$T_d^+ + e \rightarrow T_d^0$	$r_1 = nv_{th}\sigma_n^+N_t(1-f)$
Electron capture in the case of T_a^0	$T_a^0 + e \rightarrow T_a^-$	$r_2 = nv_{th}\sigma_n^0N_t(1-f)$
Occupancy of holes in the case of T_d^0	$T_d^0 + h \rightarrow T_d^+$	$r_3 = pv_{th}\sigma_p^0N_tf$
Electron capture in the case of T_a^-	$T_a^- + h \rightarrow T_a^0$	$r_3 = pv_{th}\sigma_p^-N_tf$
Emission of an electron in the case of T_d^0	$T_d^0 \rightarrow T_d^+ + e$	$r_2 = e_n^0N_tf$
Emission of an electron in the state T_a^-	$T_a^- \rightarrow T_a^0 + e$	$r_2 = e_n^-N_tf$
Hole emission in the case of T_d^+ halında	$T_d^+ \rightarrow T_d^0 + h$	$r_4 = e_p^+N_t(1-f)$
Emission of holes in the case of T_a^0	$T_a^0 \rightarrow T_a^- + h$	$r_4 = e_p^0N_t(1-f)$

From this expression, the emission coefficients will be expressed as follows:

$$e_n^0 = v_{th}\sigma_n^+N_C \exp\left(\frac{E_t - E_C}{kT}\right),$$

$$e_n^+ = v_{th}\sigma_n^0N_V \exp\left(\frac{E_V - E_t}{kT}\right).$$

The overall rate of recombination is written as:

$$R = r_1 - r_2 = r_3 - r_4. \quad (*)$$

Taking the last expression and the expressions for the emission and absorption rates into account, we can get the eclipse function:

$$f = \frac{nv_{th}\sigma_n^+ + e_p^+}{nv_{th}\sigma_n^+ + pv_{th}\sigma_p^0 + e_n^0 + e_p^+}. \quad (**)$$

Considering the expression (*) in the equation for r_1 , r_2 , r_3 and r_4 , we can determine the recombination efficiency:

$$\eta_r = \frac{R}{N_t} = v_{th}^2 \sigma_n^+ \sigma_p^0 \frac{np - n_i^2}{nv_{th}\sigma_n^+ + pv_{th}\sigma_p^0 + e_n^0 + e_p^+}.$$

Taylor and Simmons showed that expression (**) can be approximated by the following expression:

$$f = \frac{nv_{th}\sigma_n^+}{nv_{th}\sigma_n^+ + pv_{th}\sigma_p^0 + e_n^0}. \quad (***)$$

The hole filling function is written as:

$$1 - f = \frac{pv_{th}\sigma_n^+}{nv_{th}\sigma_n^+ + pv_{th}\sigma_p^0 + e_n^0}.$$

Expression (***) can be transformed as follows:

$$f = \frac{n\sigma_n^+}{n\sigma_n^+ + p\sigma_p^0} \left[1 + \frac{e_n^0}{nv_{th}\sigma_n^+ + pv_{th}\sigma_p^0} \right]^{-1}.$$

In this case, the quantity in square brackets will be the Fermi-Dirac function. So:

$$f = \frac{n\sigma_n^+}{n\sigma_n^+ + p\sigma_p^0} \left[1 + \exp\left(\frac{E_t - E_{fnt}}{kT}\right) \right]^{-1}.$$

Fermi quasi-level for trapped electrons:

$$E_{fnt} = E_C + kT \ln \left(\frac{n\sigma_n^+ + p\sigma_p^0}{N_C \sigma_n^+} \right).$$

Analogously, the hole filling function:

$$1 - f = \frac{p\sigma_p^0}{n\sigma_n^+ + p\sigma_p^0} \left[1 + \exp\left(\frac{E_{fpt} - E_t}{kT}\right) \right]^{-1}.$$

Fermi quasi-level of trapped holes:

$$E_{fpt} = E_V - kT \ln \left(\frac{n\sigma_n^+ + p\sigma_p^0}{N_V \sigma_p^0} \right).$$

For the efficiency of recombination, we get:

$$E_t > E_{t0} \text{ when } \eta_r =$$

$$= v_{th} \frac{\sigma_n^+ \sigma_p^0 np}{n\sigma_n^+ + p\sigma_p^0} \left[1 + \exp\left(\frac{E_t - E_{fnt}}{kT}\right) \right]^{-1}$$

$$E_t < E_{t0} \text{ when } \eta_r =$$

$$= v_{th} \frac{\sigma_n^+ \sigma_p^0 np}{n\sigma_n^+ + p\sigma_p^0} \left[1 + \exp\left(\frac{E_{fpt} - E_t}{kT}\right) \right]^{-1}.$$

In these expressions, E_{t0} corresponds to the level where the emission coefficients of electrons and holes are equal:

$$E_{t0} = \frac{E_V + E_C}{2} - \frac{kT}{2} \ln\left(\frac{\sigma_n^+ N_C}{\sigma_p^0 N_V}\right).$$

Using the expression for η_r , approximating the Fermi-Dirac function, we can obtain the following expression for the recombination rate:

$$R = v_{th} \frac{\sigma_n^+ \sigma_p^0 np}{n\sigma_n^+ + p\sigma_p^0} \int_{E_V}^{E_{fpt}} N(E) dE.$$

In this case, the load captured in localized cases will be calculated by the following expression:

$$\rho = -q \left(\int_{E_V}^{E_{fpt}} N(E) dE + \frac{n\sigma_n^+}{n\sigma_n^+ + p\sigma_p^0} \int_{E_{fpt}}^{E_{fptn}} N(E) dE \right).$$

Recombination processes in amphoteric cases were theoretically studied by Sax and Shockley. Figure 9.12 shows the emission and capture processes of electrons and holes in such cases.

In table 9.2, D is the broken connection, F is the eclipse function, and the indices «+», «0» and «-» are the load case of the broken connection.

In this case, the emission coefficients will be expressed as follows:

$$e_n^0 = 0,5v_{th}\sigma_n^+N_c\exp\left(\frac{E^{+/0} - E_c}{kT}\right);$$

$$e_n^- = 2v_{th}\sigma_n^0N_c\exp\left(\frac{E^{0/-} - E_c}{kT}\right).$$

$$e_t^+ = 2v_{th}\sigma_p^0N_v\exp\left(\frac{E_v - E^{+/0}}{kT}\right);$$

$$e_n^0 = 0,5v_{th}\sigma_p^-N_v\exp\left(\frac{E_v - E^{0/-}}{kT}\right).$$

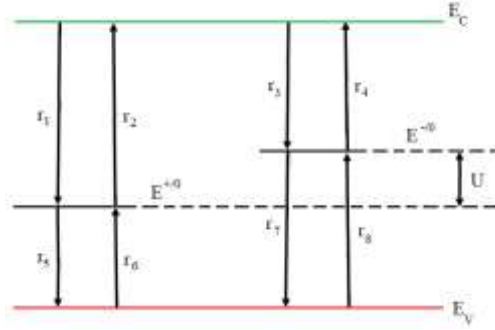


Figure 9.13. Electron and hole capture and emission processes in amphoteric cases

Table 9.2 explains the processes presented in figure 9.13.
Capture function for load cases:

$$F^+ = \frac{P^0P^-}{N^+P^- + P^0P^- + N^+N^0};$$

$$F^0 = \frac{N^+P^-}{N^+P^- + P^0P^- + N^+N^0};$$

where, $N^+ = n \cdot v_{th} \cdot \sigma_n^+ + e_p^+$; $N^0 = n \cdot v_{th} \cdot \sigma_n^0 + e_p^0$; $P^- = p \cdot v_{th} \cdot \sigma_p^- + e_n^-$; $P^0 = p \cdot v_{th} \cdot \sigma_p^0 + e_n^0$.

Using these expressions, we determine the recombination efficiency:

$$\eta_r = r_1 - r_2 + r_3 - r_4 = v_{th}^2(pn - n_i^2) \frac{\sigma_n^+ \sigma_p^0 P^- + \sigma_n^0 \sigma_p^- N^+}{N^+P^- + P^0P^- + N^+N^0}.$$

Table 9.2
Electron and hole capture and emission processes in
amphoteric states

Process	Throughput	The speed of the process
Electron capture	$D^e + e \rightarrow D^0$	$r_1 = nv_{th}\sigma_n^+ N_{DB} F^+$
Electron emission	$D^0 \rightarrow D^+ + e$	$r_2 = e_n^0 N_{DB} F^0$
Electron capture	$D^0 + e \rightarrow D^-$	$r_3 = nv_{th}\sigma_n^0 N_{DB} F^0$
Electron emission	$D^- \rightarrow D^0 + e$	$r_4 = e_n^- N_{DB} F^-$
Occupancy of hole	$D^0 + h \rightarrow D^+$	$r_5 = pv_{th}\sigma_p^0 N_{DB} F^0$
Hole emission	$D^+ \rightarrow D^0 + h$	$r_6 = e_p^+ N_{DB} F^+$
Occupancy of hole	$D^- + h \rightarrow D^0$	$r_7 = pv_{th} - N_{DB} F^-$

The average load corresponding to one broken connection is defined as:

$$Q = q \cdot (F^+ - F^-).$$

Since there are only discrete levels acting as recombination centers in the band gap of crystalline semiconductors, the recombination processes will be described by the Shockley–Reed–Hall model. As a rule, it is possible to ignore the cases caught in the prohibited zone to the general space cargo, due to the fact that the density of the cases has a low value. There is a quasi-continuous distribution of electronic states in the hole of amorphous silicon, which significantly affects the electronic properties of the material.

9.4. Optical absorption in amorphous hydrogenated silicon

Despite the fact that to date there is no unified theory of nanocrystalline materials, many optical and photovoltaic

properties can be explained on the basis of ideas about the zone distribution of energy states in amorphous semiconductors. However, the absence of long-range order leads to a significant difference in the structure of energy bands of crystalline and disordered semiconductors.

Before considering the optical absorption proper in amorphous semiconductors, it is necessary to present the features of the energy band structure in disordered semiconductors. There is no long-range order in them, so the main provisions of the zone theory of crystals in this case are inapplicable.

In the early 50s, A.F. Ioffe formulated an empirical rule, from which it follows that the near-order is responsible for the semiconductor properties in materials. Preservation of the near-order in disordered semiconductors explains the zone character of the distribution of energy states in them.

Amorphous materials, as well as ideal semiconductors, have delocalized states due to which electrons and holes can move freely. However, the lack of long-range order results in a much lower free path length for them than in a crystalline material. When this energy-dependent free path length becomes comparable to the interatomic distance, the charge carriers localize.

Studies on the electronic structure of amorphous semiconductors and the assumption of the presence of zone tails in nanocrystalline semiconductors were presented by A.I. Gubanov in 1963. [1].

Specific calculations and evaluation of real disordered systems were carried out in Mott's works [2,3]. According to Mott's ideas, in disordered semiconductors there should exist tails of localized states at the edges of the valence band and conduction band, as well as boundary energies separating localized states from common ones [4]. Based on these studies, several models for the structure of energy bands in disordered

semiconductors have been developed. According to Mott and Davis (fig. 9.14), the tails of localized states are rather narrow and extend into the forbidden zone by a few tenths of an electron Volt. The Fermi level is fixed in a narrow zone of compensated levels (near the middle of the forbidden zone), which owe their origin to defects in the random grid of atoms, i.e., broken bonds, vacancies, etc. The presence of zone tails is due to disordered structure, with increasing degree of disordered amorphous semiconductor they increase and, in the Mott-Davis model have an exponential distribution. The peak of deep states is described by Gaussian distribution.

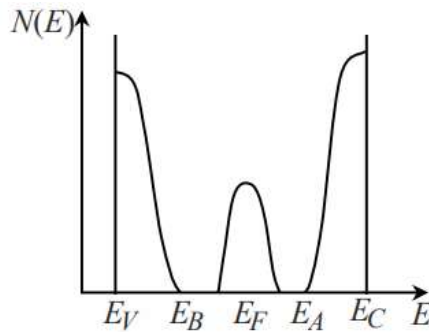


Fig. 9.14. Distribution of the density of states $N(E)$ in the forbidden zone of an amorphous semiconductor. Mott-Davis model: $E_B - E_V$ - tail width of the valence band; $E_C - E_A$ - tail width of the conduction band

In an ideal crystal, energy states cannot exist inside the forbidden zone, and in an amorphous semiconductor there are some localized states. Carriers can only move from localized states if they gain additional, significant energy. As a result, the ratio of charge carrier mobility across delocalized and localized states exceeds three orders of magnitude. Therefore, the range of energies from E_V to E_C is called the mobility gap in

amorphous semiconductors. It is this analog of the forbidden zone, energy gap in crystalline semiconductors that provides the presence of semiconducting properties in amorphous materials. In a crystal, the optical and electronic energy gaps are equal. In an amorphous material, the electronic properties are described by the mobility gap and the optical properties are related to the optical gap, which is usually smaller than the mobility gap by about 50-100 meV [5].

Due to the disordered structure and the presence of hydrogen in it, amorphous hydrogenated silicon differs significantly in optical properties [6] from crystalline silicon (fig. 9.15).

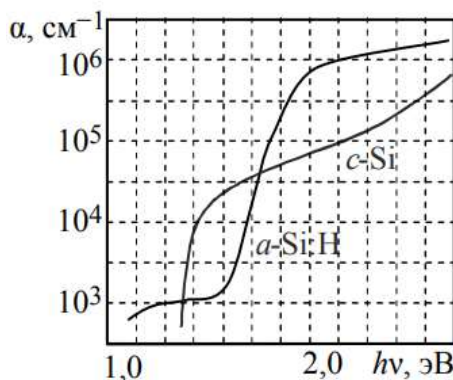


Figure 9.15. Dependence of the optical absorption coefficient α on the photon energy for c-Si and α -Si:H

The intrinsic, or fundamental, absorption is important for amorphous semiconductors because it determines the photovoltaic properties of the material in the visible region of the spectrum, and hence the efficiency of solar cells and the sensitivity of photodetectors.

Unlike crystals, the absorption edge in amorphous semiconductors does not have a sharp boundary. In the case of

amorphous hydrogenated silicon, an exponential growth of the coefficient α is observed, for which the empirical relation [7] is satisfied:

$$\alpha = \alpha_0 \exp \left[\frac{h\nu}{E_0} \right],$$

where α_0 – is the pre-exponential factor; $h\nu$ – is the photon energy; E_0 is the Urbach energy (parameter).

Near the absorption edge, optical transitions involving exponentially distributed states of the zone tails predominate. In this case, the value of the Urbach parameter E_0 is close to the value of E_{0v} , determining the extent of the valence zone tail, which is much wider than the conduction zone tail $E_{0v} > E_{0c}$. The undoped α -Si:H films obtained under optimal conditions are characterized by the minimum values of the Urbach parameter E_0 (≈ 50 meV). For doped films and ternary alloys α -SiX:H, where X = C, Ge, N, O, etc., the value of the Urbach parameter can exceed 100-150 meV.

The large difference between a-Si:H and crystalline silicon in optical absorption determines the corresponding difference in the values of the optical bandgap width: 1.7-1.8 eV for a-Si:H and 1.1 eV for crystalline silicon. The significant value of optical absorption of a-Si:H for photons with energy $h\nu \geq 1.7$ eV makes this material promising for the manufacture of devices operating in the visible range, where the photon energy takes values in the range from 1.7 to 3.0 eV (respectively red and blue radiation). This means that a-Si:H films only a few micrometers thick can be used in devices with high photosensitivity in the visible range, since they absorb all incident radiation.

The optical bandgap width for a-Si:H can be determined by the Tautz method from the relation:

$$(\alpha h\nu)^{\frac{1}{2}} = \text{const}(h\nu - E_g).$$

This dependence (fig. 9.16) is observed in amorphous semiconductors if the edges of their energy bands have a

parabolic dispersion shape and the matrix elements for optical transitions do not depend on energy. The optical bandgap width of a-Si:H films used in devices is usually 1.7-1.8 eV.

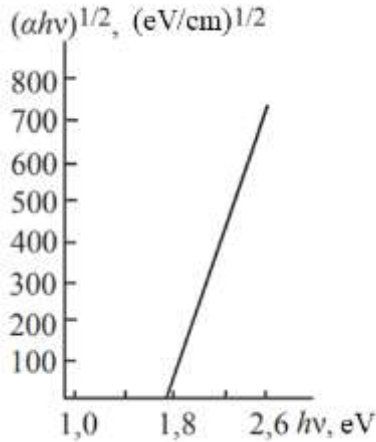


Fig. 9.16. Dependence of $(\alpha h\nu)^{1/2}$ on $h\nu$ for undoped a-Si:H films

A simplified method for determining the optical band gap is based on the assumption that E_g is equal to the energy of photons corresponding to the absorption coefficient $\alpha = 3 \cdot 10^3 \text{ cm}^{-1}$.

Presence of ~ 10 atoms. % hydrogen in a-Si:H increases the optical band gap from 1.5 to 1.7 eV compared to a-Si. When the hydrogen concentration increases to 50 atoms. % band gap of a-Si:H can reach 2.1 eV. However, in such a material it is difficult to control the passivation of broken bonds and maintain a low density of states near the middle of the bandgap. Thus, in a-Si:H films grown by chemical vapor deposition; a low density of states is ensured only in a material with a band gap of 1.7 to 1.8 eV. Therefore, a-Si:H films used in devices usually contain from 5 to 15 atoms. % hydrogen.

It is also possible to change the band gap and optical properties of a-Si:H by forming alloys: a-Si:Ge:H, a-SiC:H and a-SiN:H. Thus, by changing the germanium concentration from zero to 100%, it is possible to reduce the optical band gap from 1.7 to 1.1 eV. The introduction of additional carbon and nitrogen leads to an increase in the band gap from 1.7 to 3.0 and 5.0 eV, respectively.

In amorphous semiconductors, as in crystalline ones, it is possible to control the optical band gap by creating superlattices based on a-Si:H/a-Ge:H, a-Si:H/a-SiC:H, a-Si:H/ a-SiN:H multilayer structures. However, for these and other amorphous superlattices there are some limitations associated with the transport of carriers perpendicular to the layers, which is explained by the presence of heterojunctions.

In amorphous semiconductors, the levels of typical donors and acceptors (in a-Si:H - boron and phosphorus, respectively) are located quite deep in the band gap, and the corresponding optical transitions due to impurity absorption should be observed at room temperature. However, due to the high density of continuously distributed states of intrinsic defects, optical transitions caused by impurity ionization cannot be identified in absorption spectra. At the same time, the introduction of doping additives into a-Si:H can cause an increase in the concentration of dangling Si bonds in different charge states by several orders of magnitude. Thus, the effect of doping on the absorption spectrum is to increase absorption for energies 0.5–1.2 eV lower than the nominal value of the mobility gap.

A number of researchers have associated the presence of an Urbach “tail” in amorphous semiconductors with exciton absorption in them, but unambiguous evidence of this has not been obtained.

Analysis of the given data allows us to identify two features of the optical absorption process:

- the presence of a “tail” with an exponential dependence of the absorption coefficient, reaching energy values of up to 0.05–0.07 eV. This absorption tail is obviously caused by intrinsic states associated with disorder of the material structure;
- the existence of optical absorption even at relatively low photon energies ($h\nu \geq 1.2$ eV), due to localized states inside the mobility gap, which are created by unpaired electrons. These deep states play the role of recombination centers that limit the lifetime of photogenerated charge carriers.

9.5. Thin-film solar modules based on amorphous and microcrystalline silicon

The use of structures based on α -Si:H/c-Si opens up broad opportunities for increasing the stability of solar cells. In such heterostructures there is virtually no degradation of properties over time under illumination, which is promising from the point of view of their use not only for terrestrial, but also for space purposes.

The problem with traditional solar photovoltaics is the high cost of monocrystalline silicon solar cells, the main material in the solar energy market. The cost of solar panels (SP) and their efficiency affect the cost of electricity generated by solar power plants.

The ratio of the cost of “solar” and “grid” electricity determines the geography of cost-effective operation of solar power plants in countries with developed electrical networks. It is the excess of the cost of “solar” electricity over “grid” electricity (without taking into account special incentive tariffs for renewable energy) in developed countries that is holding back the active spread of solar energy.

It is possible to solve the problem of reducing the cost of solar electricity by switching to cheaper thin-film technologies for manufacturing solar cells.

A promising way to solve these problems is the use of heterostructural cascade photoelectric converters based on amorphous hydrogenated silicon and alloys based on it (fig. 9.17).

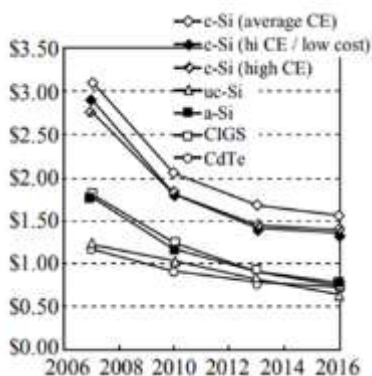


Fig. 9.17. Cost of 1 W of energy in a solar module obtained using various materials

The discovery in 1976 of the possibility of doping amorphous silicon with a-Si:H, obtained in a glow discharge plasma, marked the beginning of the use of its exceptional photoconductive properties associated with strong absorption in the wavelength region corresponding to the visible part of the spectrum. The discovery of technological routes for producing thin films of this material and other amorphous hydrogenated semiconductors has given a powerful impetus to the development of a new, much-needed technology in the field of renewable energy - the technology for creating low-cost solar cells.

The size of the solar cell market today is about 1 GW. Thin-film solar cells account for 15% and are experiencing faster growth in this market segment, which is primarily due to solving the main problem facing technologists - increasing the efficiency

of solar energy converters and reducing the cost of solar modules. Let us take for comparison crystalline silicon, the main material of modern solar energy, understanding that its cost determines the energy-intensive process of obtaining this material and its share in the solar cell itself. With this approach, it is difficult to expect a reduction in the unit cost of solar modules to less than 2.5 dollars/W.

The evolution of the basic technological principles for the production of thin-film silicon cells (low-cost technological processes, cheap substrates, different module designs, etc.) already today provides in laboratory conditions an efficiency comparable to elements based on polycrystalline silicon, and the rate of reduction in the cost of thin-film solar modules is much higher than modules based on crystalline silicon [1,2]. Currently, the real challenge for thin-film photovoltaics is to achieve a price of about 0.5–0.65 \$/W. The use of materials such as amorphous silicon carbide α -Si:C, amorphous silicon-germanium alloys α -SiGe:H, nanostructured and microcrystalline silicon, together with advances in technology for controlling the type of their conductivity and the creation of p–n junctions based on new structures, makes it possible to remove some fundamental limitations associated with the optical and electrophysical properties of previous materials open up the possibility of solving problems caused by increasing the efficiency of solar cells while simultaneously reducing their cost.

Experts predict that by 2030, solar photovoltaics will become a large economic sector worldwide. In Europe, photovoltaics will become a powerful industry with significant export potential. It is expected that the EU will create between 200 and 400 thousand jobs with an annual production of 20–30 GW.

Due to the fact that the main material of solar energy, silicon, is an indirect-gap semiconductor and its absorption

coefficient is low, to effectively absorb sunlight, the thickness of the manufactured solar cells must be hundreds of microns. This determines, along with the costly process of obtaining silicon, its significant consumption, and therefore the high cost of solar modules. The use of thin-film technology based on materials with a high absorption coefficient such as CdTe, Cu(In,Ga)Se, which are used in the form of polycrystalline films, can significantly reduce the consumption of the material used and its cost. These materials include amorphous hydrogenated silicon. But before we dwell on the presentation of the technology for producing solar modules based on it, let's consider their advantages and disadvantages.

Thin film nanotechnology CdTe. In Europe, one company is very active in this area (First Solar, www.firstsolar.com).

Advantages:

- High stable efficiency (production efficiency of the solar module is about 10%).
- Low production costs, resulting in very low cost solar modules.

Flaws:

- Great difficulty in controlling and reproducing processes (low output). At the same time, two components have to be controlled - Cd and Te, as well as their proper composition.
- Tellurium Te: A rare earth metal, about ten times rarer than In. There is a problem of guarantee of supply.
- Cadmium Cd: heavy metal. Environmental aspects must be taken into account. At the end of their service life, solar cells must be specially disposed of in heavy metal landfills (an expensive final procedure for returning and recycling solar cells, in which the manufacturer of these modules will have to bear the costs). Situation of solar cell failure during operation: when glass breaks, Cd can be absorbed and contaminate the soil. Thus,

additional expensive costs for installing the modules are required.

- The strip design of the module on a single substrate makes it difficult to provide gaps between individual strips.

Thin film technology of copper and indium diselenide CuInSe_2 (CIS) and $\text{Cu}(\text{In}_{1-x}\text{Ga}_x)\text{Se}_2$ (CIGS) There are approximately 20 companies (mainly German and US) working in this area. An example is “Würth Solar” (www.wuerthsolar.com) or “Avancis” (www.avancis.com).

- High stable efficiency (module production efficiency of about 11–13%).

- The technology for producing CuInSe_2 layers is simple and consists of sequential deposition by thermal evaporation of thin layers of Ga, Se and Cu onto the surface of the substrate and subsequent rapid thermal annealing.

Flaws:

- Extremely difficult to control and reproduce processes (low yield of suitable elements).

- Requires careful design of strips and gaps in the module, which is difficult to reproduce.

High temperature deposition process. To form CIS and CIGS, a number of methods are used (evaporation, atomization, gas transport, atomization followed by pyrolysis, electrochemical deposition, screen printing), which can be divided according to the selenization method:

- methods in which Se is introduced into the layer simultaneously with other elements of the compound;

- methods in which interaction with Se occurs as a result of deposition of layers of other elements of the compound. In both cases, either deposition onto a substrate heated to a temperature of 400–500 °C or annealing of the formed layer at these temperatures is used. During the reaction, a CIS layer 1.5–2 mm thick is formed.

- Indium and gallium: rare earth metals. To produce CIS thin-film solar cells capable of generating 1 GW of electricity, approximately 50 metric tons of indium are required. Guaranteed supply resources for India are about 2400 tons. The problem of guaranteeing supplies.

- Price movement. The price of one kilogram of indium in 2003 was 100 dollars; in 2005 it increased to \$1000. The problem of price stability for raw materials.

- Selenides. Environmental aspects and the cost of recycling must be taken into account.

The most significant in the world market in the field of thin-film solar cells based on amorphous silicon are foreign companies that have their own production of heterostructure thin-film photoconverters. The leading manufacturers of cascade thin-film silicon-based solar cells in the world are Sharp, BP Solar, Shell Solar, Sanyo, RWE Schott, Oerlikon Solar, Applied Materials, Santech, "Kaneka" All these companies have been producing thin-film photoconverters for solar modules for many years using the method of deposition of amorphous hydrogenated silicon in glow discharge plasma and advanced post-growth technologies.

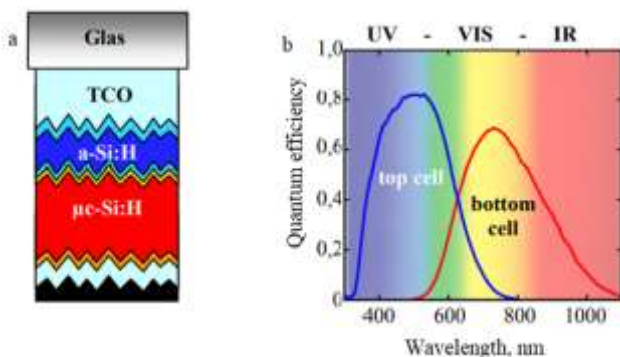


Fig. 2. Schematic representation of the tandem structure α -Si:H/ μ -Si:H (a) and its spectral characteristics (b)

A typical design of a heterostructural solar cell based on amorphous and microcrystalline, used in the mass production of solar modules, is shown in fig. 9.18.

The second stage performs two functions. It is made on the basis of a narrow-gap material (the width of the optical zone is about 1.1 eV), and this allows more efficient use of the long-wavelength part of the solar spectrum. On the other hand, microcrystalline silicon has higher conductivity, which has a positive effect on creating electrical contact and collecting current in solar cell panels.

9.6. Cyclic method of deposition of a-Si:H layers by processing in hydrogen plasma

One of the ways to obtain α -Si:H layers with high photosensitivity at fairly low temperatures of the substrate (250 °C) is to use an intermittent (cyclic) mode of drawing. At this time, the plasmochemical deposition cycle of a-Si:H layer with a nanoscale thickness of 0.3-25 nm in a monosilane environment alternates with processing in a hydrogen plasma. Another method of increasing the photosensitivity and stability of the layers is the plasmochemical deposition (PCD) method of a-Si:H layers with a small volume fraction of nanocrystalline connections at relatively high pressures of a gas mixture containing monosilane and hydrogen.

The method of layer-by-layer (cyclic) deposition in hydrogen plasma with intermediate plating is implemented in the "KONT" technological complex with two time relays added. A time relay ensures that the gas mixture in the chamber containing 20% SiH₄ + 80% Ar is changed to H₂ after given time intervals. Also, time relays determine the duration of deposition of a-Si:H nanoscale layers and their "finding" in hydrogen plasma [1-3].

Cyclic deposition of layers is a periodical alternation of plasmochemical deposition of a-Si:H layer on a fixed substrate in a rotating drum-substrate holder and deposition in a hydrogen plasma. The shift is carried out when the gas mixture in the chamber is permanently lit by the discharge. The deposition of nanoscale thick a-Si:H layers is carried out in a stable gas mixture (80% Ar + 20% SiH₄) in a technological regime optimal for pre-selected continuous deposition: substrate temperature – 250⁰ C; YT-discharge power – 55 mW/cm²; rotation speed of the drum-base holder - 4 revolutions/min.; gas mixture pressure – 25 Pa; deposition speed – 5-7 nm/min.

The thickness of the α -Si:H layer is varied during one cycle of deposition when the composition of the gas mixture is changed in the process of cyclic deposition and thermoprocessing in hydrogen plasma. For layers of small thickness in hydrogen plasma, the effect of deposition is relatively small - about 1-2 minutes. For this reason, during the experiments, the duration of soaking in hydrogen was fixed and was 2 minutes. It should be noted that the composition of the gas mixture was settled in the deposition and thermoprocessing process in a few tens of seconds - i.e., the same as the deposition and settling times. This condition has created a condition where the thickness of the layer continues to increase during the transition stage from deposition to thermoprocessing.

The parameters of the cyclic precipitation technological mode are given in table 1. The main parameter that was varied was the deposition time of one layer from 1 to 4 minutes. This caused the layer thickness *L* to change from 6 to 24 nm during one cycle (table 9.3). The thickness of the layer deposited during the cycle is determined by the ratio of the total thickness of the layer (for layers on a quartz substrate) to the number of cycles.

The study of structural properties was carried out for layers with a thickness of about 0.5 μ m on a silicon substrate. The substrates consisted of layers with a thickness of 16 nm

obtained by deposition in hydrogen plasma in a cyclic mode deposited during one cycle.

Table 9.3
Parameters of cyclic deposition of a-Si:H layers

Parameter	Deposition	Tab
Gas mixture	80 % Ar + 20% SiH ₄	H ₂
Time t, min.	1-4	2
The thickness of the layer deposited during the cycle is L, nm	6-26	—
Discharge specific power w, mW/cm ²	55	55
Pressure P, Pa	25	25
The temperature of the bases is T _s , °C	250	250
Deposition speed, nm/min	5-6	—
Thickness of layers d, nm	40-650	
The rotation speed of the base holder, rev/min.	8	
Bases	Sital, silica, quartz glass	

In the EM microphotograph of the layers, it is clear that they have a layered structure. The step between the layers corresponded to the thickness of the α -Si:H layer deposited during one cycle (fig. 9.17a). Dark bands are regions of amorphous hydrogenated silica with small concentration. Bright streaks are hydrogen-rich regions formed as a result of processing in a hydrogen plasma. Regions of high concentration of hydrogen have low density, as shown by electron-microscopic contrast in EM images.

The presence of nanocrystalline inclusions in the a-Si:H amorphous matrix is evidenced by the results of electron microscopy of the layer surface (fig. 9.17b).

Table 9.4
The thickness of layers obtained in different deposition modes

Deposition mode	Deposition time t, min.	The thickness of the layer deposited during the cycle, L, nm.	The number of cycles.	The total thickness of the layer, d, nm
Non-stop	96	470	-	470
Cyclic (4/2)	4	26	24	630
Cyclic (3/2)	3	16	32	515
Cyclic (2/2)	2	12	40	480
Cyclic (1/2)	1	6,5	96	620

The analysis of microphotographs allows not only to determine the sizes of nanocrystalline inclusions of silicon in the amorphous matrix, but also to build distribution histograms according to the sizes of the inclusions, to estimate the volume fraction occupied by the nanocrystalline phase (fig. 9.18a).

For a 16 nm thick α -Si:H layer obtained in cyclic mode using intermediate deposition in hydrogen plasma, the average cross-sectional area of the nanocrystals after deposition is $\sim 20 \text{ nm}^2$, and the average diameter is 4.5 nm (fig. 9.18b). For such a layer, the total volume fraction of nanocrystalline inclusions is less than 1%. Due to such a small volume fraction, it is not possible to detect the presence of the nanocrystalline phase in the Raman scattering spectra.

It should be noted that the thickness of the layer that can be seen by EM is 30-50 nm, so two to three layers are visible in the photomicrograph (fig. 9.18a). For this reason, it is only possible to estimate the volume fraction of the nanocrystalline

phase less than 1%. Due to the small volume fraction of the nanocrystalline phase, it is not possible to detect the presence of this phase in the Raman scattering spectra.

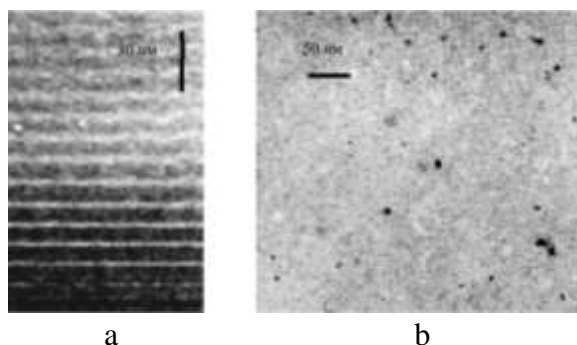


Figure 9.17. Photomicrograph of electron microscopy: a – cross-section and b – the surface of a-Si:H layer with a thickness of 515 nm (thickness L of the deposited layer during one cycle is 16 nm)

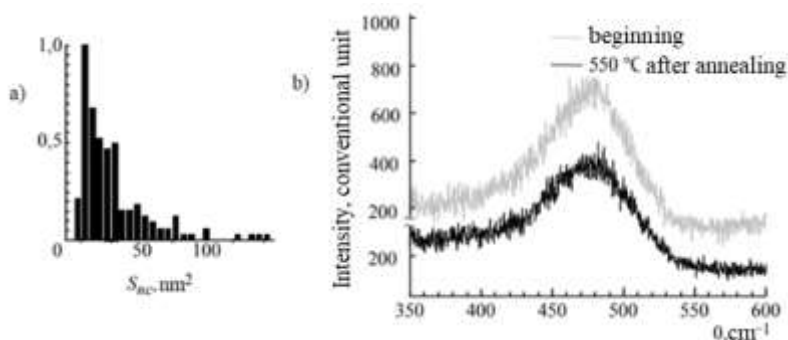


Figure 9.18. Histogram of the distribution of nanocrystallites in the cross-sectional area (a) for a-Si:H layer with a thickness of $L = 16$ nm obtained by the cyclic method, Raman distribution spectra in the initial state and after annealing at 550°C in vacuum

Figure 9.19b shows the Raman scattering spectra for the layered layer before and after annealing at a temperature of 550 °C. Only one broad maximum can be selected in the spectra at $\omega = 480 \text{ cm}^{-1}$, corresponding to amorphous silicon. When $\omega = 516\text{-}520 \text{ cm}^{-1}$ corresponding to nanocrystalline silicon, it is impossible to separate the peak [4,5].

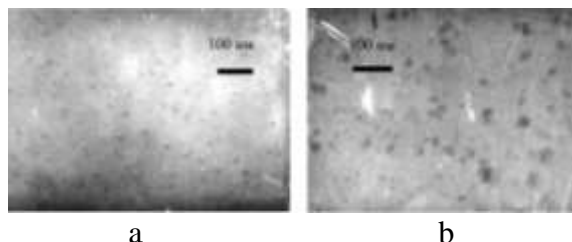


Figure 9.20. EM microphotographs: a – 40 nm thick a-Si:H layer after treatment in hydrogen plasma (12 minutes, 200 mW/cm²); b – Si:H layer obtained in cyclic mode (L = 12 nm, tann = 3 minutes, w = 100 mW/cm²).

In order to determine the mechanism of the formation of nanocrystalline connections in the process of cyclic deposition, the study of structural modifications of a-Si:H thin films (about 40 nm) in three different variants of processing in hydrogen plasma on a NaCl substrate was carried out:

1. Deposition of a-Si:H layer with a thickness of 40 nm under optimal conditions for continuous deposition with subsequent processing in hydrogen plasma [at the same temperature (250 °C) and the same pressure (25 Pa) of the gas mixture (80% Ar + 20% H₂), YT-discharge but with different values of specific power (55-200 mW/cm²) and in the settling time (8-12 min.)].

2. Cyclic deposition of three layers with intermediate deposition under continuous discharge conditions (L = 12 nm, deposition time 3 minutes, w = 100 mW/cm², P = 25 Pa, T_s = 250 °C).

3. Cyclic deposition with intermediate blowing under conditions of changing gas mixtures, that is, after the deposition cycle, the discharge is turned off, the silane is completely blown, then hydrogen is introduced and the discharge is started. Deposition is carried out under the following conditions: $L = 6\text{--}12\text{ nm}$, deposition time 3-9 minutes, $w = 100\text{--}200\text{ mW/cm}^2$, $P = 25\text{ Pa}$, $T_s = 250\text{ }^{\circ}\text{C}$, number of cycles – 3 for $L = 12\text{ nm}$, L and 6 for $L = 6$.

Homogeneous a-Si:H layers are maintained in hydrogen plasma during 8 minutes with a specific power of 55 mW/cm^2 . A weakly distinguishable contrast is observed in the layer during exposure for 12 minutes with a specific power of 110 mW/cm^2 . During 12-minute exposure with a specific power of 200 mW/cm^2 , nanoscale connections are formed in the layer. Figure 3a shows a bright contrast EM micrograph of such a layer. The layer has 3-4 nm-sized inclusions with an electron-microscopic contrast volume fraction of no more than 1% (fig. 9.20a). Most likely, the contrast in the photo is given by the nanocrystalline inclusions formed on the surface of the layer under the influence of hydrogen plasma deposition. However, the diffraction pattern obtained by the microdiffraction method for this layer is visually similar to that for the amorphous layer. Most likely, the small volume is determined by the size of the share and nanocrystallites.

The layer formation obtained by the cyclic method under constant discharge conditions had nanocrystalline connections that occurred in a short time and under hydrogen plasma conditions at low deposition power (fig. 9.20a).

However, in layers obtained in cyclic mode with intermediate sputtering, nanocrystalline junctions are not present even in hydrogen plasma deposition at a specific power of 200 mW/cm^2 and for 9 minutes.

Based on the obtained results, it can be said that the formation of nanocrystalline connections occurs due to

precipitation from a strong mixture of residual silane with hydrogen during plasma deposition. Changing gas mixtures takes about one minute. So, during cyclic deposition, we can divide the plasma deposition process into two stages:

- 1) formation of nanocrystalline connections due to precipitation from silane strongly mixed with hydrogen;

- 2) treatment of the surface of the layer with increasing thickness in hydrogen plasma, which leads to its saturation with hydrogen.

Thus, the use of the cyclic deposition method (with intermediate deposition in hydrogen plasma) allows obtaining α -Si:H layers with a layered structure caused by the uneven distribution of hydrogen. At this time, the size of nanocrystalline additives with a volume fraction of less than 1% was 4-5 nm.

9.7. Influence of thermal treatment on the properties of nanostructured films α -Si:H

To determine the effect of temperature treatment on the properties of layered films α -Si:H containing nanocrystalline inclusions, films with optimal $L = 16$ nm were annealed in vacuum for one hour at temperatures of 350, 450, 550 °C. Modification of the structure of layered films α -Si:H on a silicon substrate was investigated with the help of electron microscopy.

After annealing in a vacuum at 450 °C for one hour, the layered structure of α -Si:H films obtained in the cyclic mode is noticeably eroded (fig. 9.21a), and annealing at a temperature of 550 °C for an hour makes the film practically homogeneous on section (fig. 9.21b). Some increase in the size and number of nanocrystalline inclusions was observed for α -Si:H films annealed at temperatures of 450 and 550 °C (fig. 9.21).

Thus, after annealing at 450 °C, the average area increased from 20 to 60 nm², and after annealing at 550 °C – up to 75 nm².

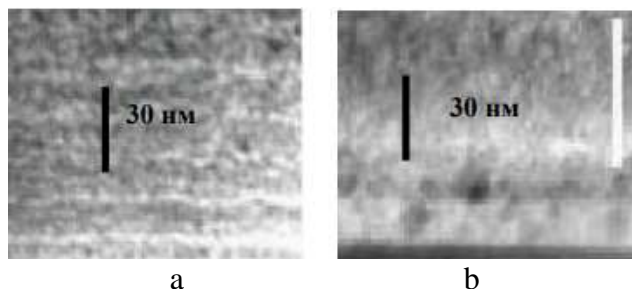


Fig. 9.21. TEM photograph in bright field contrast of the section of α -Si:H film deposited using intermediate annealing in hydrogen plasma after annealing in vacuum at 450 °C (a) and 550 °C (b) for one hour

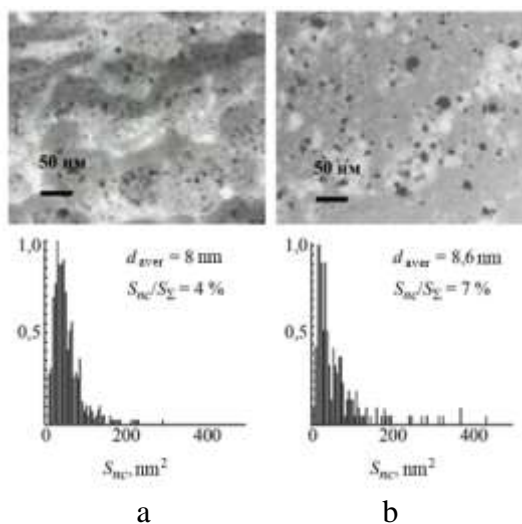


Fig. 9.22. TEM photographs in dark field contrast of the surface of a-Si:H films deposited using intermediate annealing in hydrogen plasma after annealing in vacuum at $T = 450$ °C (a) and 550 °C (b) and the corresponding histograms of the distribution of nanocrystallites over the area section

This corresponds to an increase in the average diameter of crystallites from 4–5 to ~ 8–9 nm, respectively. The process of crystallization in films is very difficult, as evidenced by a small change in the volume fraction of the nanocrystalline phase after temperature treatment. The share of the nanocrystalline phase increased from 1% for the unannealed film to 4% after annealing at 450 °C and to 7% at 550 °C (fig. 9.22). When estimating the volume fraction of the crystalline phase in the film after annealing at 550 °C, assuming that the nanocrystallites have the shape of a sphere, we get a value equal to approximately 2%. Such a small volume fraction of the nanocrystalline phase was also not detected by the Raman spectroscopy method.

It should be noted that with an almost two-fold increase in the volume fraction of nanocrystals after annealing the films at 450 and 550 °C, the nature of their distribution over the cross-sectional area, shown in the histograms (fig. 9.22), changes slightly and there is no significant shift in the density distribution towards larger sizes. This indicates that after annealing at 550 °C, the volume fraction of nanocrystals increases not due to the increase in the size of nanocrystals, but due to the increase in their number. Based on the obtained results, it was suggested that in layered films during vacuum annealing, the formation of crystallites occurs in layers of homogeneous amorphous hydrogenated silicon, and the growth of nanocrystallites is inhibited by interfaces with a high hydrogen content. This is confirmed by studies of structural modifications after vacuum annealing of thin free a-Si:H films deposited on NaCl substrates. Studies were conducted on two types of films:

- 1) films obtained in a continuous mode during 6 min with a thickness of ~ 40 nm (without annealing the layers in a hydrogen-containing plasma);

- 2) layered films obtained by the method of cyclic deposition with intermediate pumping when changing the gas mixture. Annealing of each of the three layers with a thickness

of 12 nm in a hydrogen-containing plasma was carried out for 3 minutes at a specific power of the HV-discharge – 200 mW/cm² and a pressure of the gas mixture (80 %Ar + 20 %H₂) – 25 Pa. In the initial state, nanocrystalline inclusions were not observed in the films.

The results of electron microscopic research of samples thermally annealed at 450 °C for 30 min are shown in fig. 9.23. After annealing at 450 °C, the formation of nanocrystalline inclusions, 10-12 nm in size, occupying an area of 1-2% is observed in both films. The appearance of the nanocrystalline phase in the a-Si:H films is reflected in the microdiffractograms (fig. 9.23). This allows us to judge the volume fraction of the crystalline structure, which is a single percent.

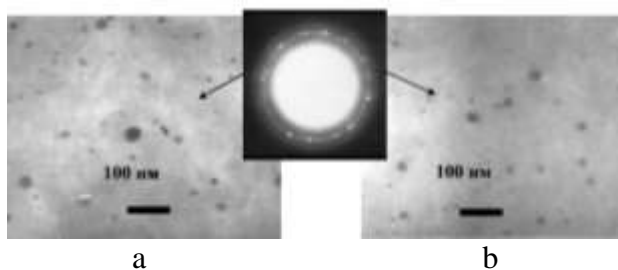


Fig. 9.23. Microphotographs and microelectrogram of transmission electron microscopy for α -Si:H films obtained in continuous (a) and cyclic (b) modes, after their annealing at $T = 450$ °C in vacuum

A further increase in the vacuum annealing temperature showed that after heat treatment at a temperature of 750 °C, silicon films obtained in modes 1 and 2 are characterized by a completely different structure (fig. 9.24). The film obtained by continuous plasma chemical deposition has a polycrystalline structure and consists of sufficiently large (1 μ m and more)

crystallites (fig. 9.24a). Reflections from individual crystallites are visible on the microdiffractogram. At the same time, the film obtained with the use of intermediate annealing in hydrogen plasma contains crystallites, the typical sizes of which are 10-12 nm (9.24b), and the absence of diffuse rings on the microdiffractogram indicates the predominant share of the nanocrystalline phase.

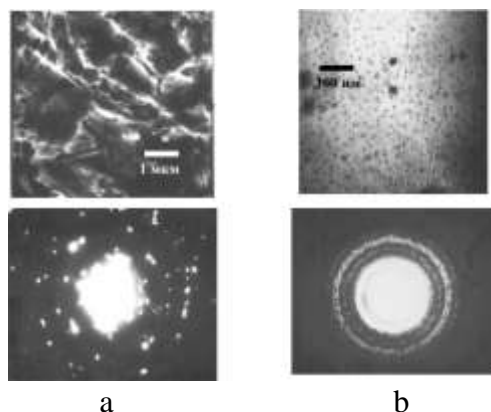


Fig. 9.24. TEM microphotographs and microelectrograms for a-Si:H films obtained in continuous (a) and cyclic (b) modes, after annealing in vacuum at $T = 750^{\circ}\text{C}$

It follows from the analysis of electron diffractograms that crystallites with [101] orientation normal to the surface prevail in polycrystalline silicon films. Thus, in layered films, the average size of crystallites does not exceed the thickness of the layer deposited per cycle. This allows you to control the size and proportion of nanocrystalline inclusions of silicon, which can be used when creating luminescent films.

The dependence of the dark and photoconductivity of layered films on the annealing temperature are presented in fig. 9.25. At annealing temperatures higher than 350°C , there is a

sharp increase in dark conductivity, a decrease in photoconductivity and, as a result, a decrease in the photosensitivity of α -Si:H films up to $8 \cdot 10^4$ (fig. 9.25).

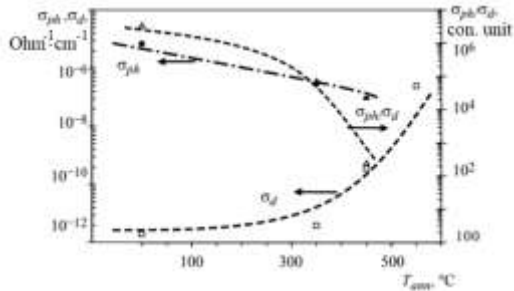


Fig. 9.25. Dependences of σ_d , σ_{ph} и $\sigma_{\text{ph}}/\sigma_d$ on the annealing temperature for the α -Si:H film obtained by the cyclic method with $L = 16$ nm

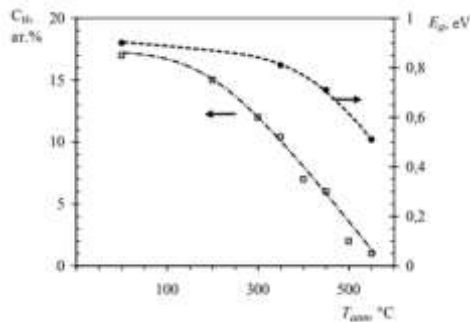


Fig. 9.26. Dependencies of C_H and E_a on the annealing temperature for a-Si:H film obtained by the cyclic method with $L = 16$ nm

After annealing at a temperature of 450°C , photosensitivity decreases to 10^2 , and after annealing at 550°C , photosensitivity is almost completely lost. It is obvious that such a small volume fraction of the nanocrystalline phase cannot lead to an increase in conductivity based on the representations of the

flow theory, and the increase in dark conductivity σ_d is apparently associated with an increase in the density of states in the α -Si:H film. As the heat treatment temperature increases, hydrogen effusion occurs, leading to an increase in the density of localized states. As can be seen from fig. 9.26, the concentration of hydrogen C_H in the α -Si:H film decreases from 17% in the original film to 10% after annealing at 350⁰ C, 6% at 450⁰ C, and at heat treatment temperatures above 500⁰ C it becomes less than 2% [1-3].

The hydrogen effusion process is accompanied by a decrease in the activation energy E_a from 0.9 to 0.71 eV after annealing at 450⁰ C, which is associated with a decrease in the width of the zone. At annealing temperatures higher than 500⁰ C, there is a change in the nature of the temperature dependence of the dark conductivity. На рис. 6 there are two sections [4-6]: in the region of temperatures greater than 380 K – the exponential section with an activation energy of 0.51 eV corresponds to band conductivity – at temperatures less than 380 K – jump conductivity is manifested by broken bonds near the Fermi level and the temperature dependence is described by the expression for jump conductivity:

$$\sigma_d(T) = A \exp \left[- \left(\frac{T_0}{T} \right)^m \right],$$

where, $A = 80 \text{ Ohm}^{-1} \cdot \text{cm}^{-1}$, $T_0 = 2.8 \cdot 10^6 \text{ K}$, $m = 0.325$. The dependence of dark conductivity is similar for films of amorphous silicon with a low hydrogen content (2–3%) and indicates a high degree of defectiveness of the material caused by the effusion of hydrogen from the film.

Annealing in vacuum a film obtained by the cyclic method with an optimal $L = 16 \text{ nm}$ makes it possible to further increase its stability. In fig. 9.27, which presents the results of photoinduced degradation for the same film before annealing and after annealing in vacuum at temperatures of 350 and 4500 C for one hour.

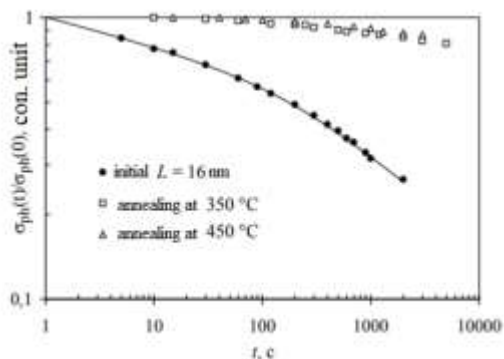


Fig. 9.27. Kinetics of changes in photoconductivity, normalized to the initial value, for an α -Si:H film obtained by the cyclic method with $L = 16$ nm in the initial state and after annealing at temperatures of 350 and 450 $^{\circ}$ C

From the data obtained, annealing at 350 $^{\circ}$ C is of practical interest, after which the stability of the films increases significantly while maintaining the σ_{ph}/σ_d ratio equal to $8 \cdot 10^4$. Films deposited in a cyclic mode directly at a temperature of 350 $^{\circ}$ C have a very low photosensitivity $\sigma_{ph}/\sigma_d = 6$ and an activation energy of 0.48 eV.

Conclusion

1. Using the cyclic deposition method, layered films of amorphous hydrogenated silicon were obtained containing nanocrystalline inclusions at the boundaries of the layers, with increased photosensitivity (the σ_{ph}/σ_d ratio reaches 10^7 at an illumination of 100 mW/cm 2) and stability (a change in photoconductivity of 2.5 times less after exposure to a radiation dose of 120 J/cm 2 compared to homogeneous films).

2. The increase in photosensitivity of α -Si:H layered films is due to a decrease in dark conductivity, which is associated with an increase in hydrogen concentration.

3. It has been shown that the formation of nanocrystalline inclusions in α -Si:H films occurs directly during annealing in plasma due to the deposition of silicon from residual monosilane diluted with hydrogen.

4. It was discovered that films produced by the cyclic deposition method are characterized by a nonuniform distribution of hydrogen throughout the thickness, which leads to the appearance of doublets in the photoconductivity spectra. The heterogeneity of the hydrogen distribution remains after annealing at a temperature of no more than 450⁰ C in vacuum, which is confirmed by a theoretical calculation of the redistribution of the concentration of hydrogen, which is in strong bonds with silicon.

5. It was revealed that the average size of nanocrystalline inclusions in layered films after annealing in vacuum up to a temperature of 750⁰ C does not exceed the thickness of the layers of a-Si:H films deposited in one cycle, which makes it possible to control the size and content of nanocrystalline inclusions in α -Si films :H.

6. Based on layered films of amorphous hydrogenated silicon containing nanocrystalline inclusions, photodetector structures with a Schottky barrier have been created that have a high spectral sensitivity (at least 0.04 A/W) in the range of 200-400 nm and a maximum sensitivity of 0.2 A/W at a wavelength of 480 nm.

9.8. Basic parameters of solar elements based on IrSi

The spectral sensitivity of a solar cell determines the range of wavelengths of optical radiation over which the cell in question can be practically used. The short-circuit current corresponds to the maximum current that can flow in the presence of illumination during self-closing of the photocell.

The volt-ampere characteristic of the photocell in case of illumination is determined by the following expression:

$$I = I_s \left(e^{\frac{eU}{kT}} - 1 \right) - I_f,$$

where, I_s is the saturation current of an ideal photovoltaic cell; I_f is the photocurrent.

If we assume $U = 0$ in this expression, the short-circuit current:

$$I_{q,q} = -I_f$$

will be.

Therefore, the short-circuit current is equal to the current photogenerated by the solar cell.

The no-load voltage of the solar cell $U_{y,r}$ corresponds to the voltage at the open terminals of the photocell ($R = \infty$). It is possible to obtain the $U_{y,r}$ value of the voltage in the no-load mode by assuming $I = 0$ in the first expression:

$$U_{y,r} = \frac{kT}{e} \ln \left[\left(\frac{I_f}{I_s} \right) + 1 \right].$$

It can be seen from the last statement that the value of the $U_{y,r}$ voltage can increase with the increase of the I_f/I_s ratio. This condition is achieved by reducing the dark current or increasing the lifetime of non-main charge carriers as a result of increasing the doping level of the substrate. An increase in the short-circuit current (previous expression) can also lead to an increase in the no-load voltage, but the effect will be less pronounced than in the case of a decrease in the dark current. In practice, increasing the value of $U_{y,r}$ is achieved by inserting a p^+ - layer on the opposite side of the board and creating a field as a result of the formation of a $p-p^+$ structure. Such a structure not only ensures that non-main charge carriers are reflected back to the $p-n$ junction region, but also reduces the contact resistance of the back electrode. As a result, all the main parameters of the solar cell - $I_{q,q}$, $U_{y,r}$, form factor, f.i.e. is getting better. For $p-n$ junction silicon solar cells, the no-load voltage depends on the

construction of the solar cell, the level of doping, etc. depending on it is in the range from 0.5 to 0.7 V [18,34].

The following expression applies to the photocurrent:

$$I_f = j_f S = \frac{e\gamma\beta S I_i}{h\nu},$$

where, j_f is the photocurrent density; S – area of p-n junction; γ – share of non-recombined pairs of charge carriers reaching the p-n junction; β – quantum output; I_i is the intensity of radiation. Given the previous statement:

$$U_{y,r} = \frac{kT}{e} \ln \left(1 + \frac{e\gamma\beta S I_i}{h\nu I_s} \right).$$

When the level of illumination is high, that is, when the condition $I_f/I_s \gg 1$ is satisfied, the following expression is obtained:

$$U_{y,r} = \frac{kT}{e} \ln \left(\frac{e\gamma\beta S I_i}{h\nu I_s} \right).$$

When the level of illumination is low, that is, when $I_f/I_s \ll 1$, dividing by the Taylor series, the following expression is obtained:

$$U_{y,r} = kT \frac{e\gamma\beta S I_i}{h\nu I_s}.$$

Thus, at a small level of excitation, the no-load voltage will be proportional to the light intensity. The maximum output power produced by the photovoltaic cell is indicated by the point P_m ($P_m = I_m U_m$, where I_m , U_m are the values of current and voltage corresponding to the maximum output power, respectively) in figure 9.28.

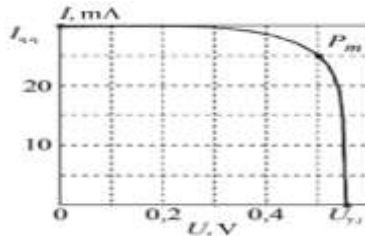


Fig. 9.28. VAC of the solar cell

The output power is defined as:

$$P = IU = I_s U \left(e^{\frac{qU}{kT}} - 1 \right) - I_f U.$$

The maximum output power condition can be found when $dP/dU = 0$. From here we get:

$$U_m \approx U_{y.r} - \frac{kT}{q} \ln \left(1 + \frac{eU_m}{kT} \right),$$

$$I_m = \frac{eI_s U_m}{kT} e^{\frac{qU_m}{kT}} \approx I_f \left(1 - \frac{kT}{eU_m} \right).$$

I_m and U_m quantities are in the ranges of $I_m = (0.85 - 0.95)I_{q,q}$, $U_m = (0.75 - 0.9)U_{y.r}$.

The maximum output power is determined by the following expression:

$$P_m = I_m U_m \approx I_f \left[U_{y.r} - \frac{kT}{e} \ln \left(1 + \frac{eU_m}{kT} \right) - \frac{kT}{e} \right] = I_f \left(\frac{E_m}{e} \right),$$

here:

$$E_m \equiv e \left[U_{y.r} - \frac{kT}{e} \ln \left(1 + \frac{eU_m}{kT} \right) - \frac{kT}{e} \right].$$

The quantity E_m corresponds to the maximum energy released in the load when a photon is absorbed under the condition that the photocell is optimally matched with the external circuit. Since the quantity E_m depends on I_s , this quantity also depends on the parameters of the material (for example, τ , D , doping level). The ideal conversion efficiency is realized when the optimal selection of the material parameters - i.e., the value of I_s is minimal [43].

An important parameter that characterizes the quality of solar cells is the shape factor or the filling factor ξ of the volt-ampere characteristic:

$$\xi = \frac{U_m I_m}{U_{y.r} I_{q,q}}.$$

From this statement:

$$P_m = \xi U_{y.r} I_{q,q}.$$

It is obtained from the last statements that the shape factor shows how many times the real VAC of the solar cell

differs from the ideal VAC, which is a rectangular step with voltage $U_{y,r}$ and current $I_{q,q}$.

The form factor for solar cells based on p-n junction silicon is in the range of 0.75...0.85, and for solar cells based on IrSi is in the range of 0.79...0.87.

Electron-hole pairs in solar cells can be generated both in the n- and p- region, depending on the depth of absorption of the energetic photon provided by solar radiation. The electric field near the p-n junction separates charge carriers and collects electrons in the n-region and holes in the p- region. However, some of the non-core charge carriers can be lost as a result of recombination. The efficiency of the collection process of photogenerated charge carriers is evaluated with the help of the charge collection coefficient Q . The accumulation factor of charge carriers is equal to the ratio of the number of electron-hole pairs separated by the electric field of the p-n junction to the total electron-hole pairs generated by light:

$$Q = \frac{j_{\phi}}{q\Phi_0},$$

where, Φ_0 is the density of the photon stream falling on the surface of the element.

The quantity Q strongly depends on the absorption coefficient, that is, on the wavelength of the radiation [5].

For semiconductors with a gap width E_g , the ideal spectral dependence of the charge carrier collection coefficient is step-like: the coefficient is 0 when $h\nu < E_g$, and 1 when $h\nu \geq E_g$. A real spectral characteristic is a curve with a maximum. In conventional converters, the maximum value of Q is close to unity and corresponds to $\lambda = 0.8\text{-}0.9 \mu\text{m}$ for silicon and $\lambda = 0.7\text{-}0.8 \mu\text{m}$ for IrSi. At sufficiently large wavelengths, the absorption coefficient decreases, and when $\alpha \rightarrow 0$, the quantity Q also approaches zero – so that $Q \sim \alpha$. At the limit of specific absorption, the spectral sensitivity and the absorption coefficient

of charge carriers become zero. The specific absorption edge for silicon is located at $\lambda = 1.1 \text{ } \mu\text{m}$, and for IrSi at $\lambda = 0.9 \text{ } \mu\text{m}$.

Finally, the conversion efficiency (or EF) of a solar cell is equal to the ratio of the maximum output power to the incident radiation power:

$$\eta = \frac{P_m}{P_{rad}} = \frac{U_m I_m}{P_{rad}} = \frac{\xi U_{y.r} I_{q.q.}}{P_{rad}}.$$

9.9. Radiation effects in IrSi-Si based microcircuits

With an increase in reverse voltage and a decrease in the concentration of additives in the base or epitaxial layer where the elements of integrated microcircuits are formed, the critical Q_{kr} value of the selected charge in their sensitive element increases. These effects are related to the formation of local regions with a sufficiently high density of electron-hole pairs in individual elements of the circuit.

Taking into account the very small size of modern integrated microcircuits (IMS), especially circuits with a high degree of integration, the formation of unbalanced charge carriers with a significantly higher concentration than the concentration of charge carriers related to the operation of the IMS in one element of the circuit, the malfunction of the circuit may result in This manifests itself mostly in the change of the logical state of a certain core of the digital IMS, as a result of which short-term interruptions in the operation of the circuit occur. Such breaks are usually called single breaks (SB). However, in some cases, the impact of charged high-energy particles can cause irreversible rejections in many IMS. Let's consider the processes that occur during the impact of high-energy charged single particles on the elements of the IMS.

A charged particle passing through the structure of the IMS loses its energy depending on the braking ability of the material and falls to (dE/dx) . The value of the braking ability of

a material is also called the linear energy transfer (LET) since it determines the energy loss of a particle per unit path length in a suitable material. At this time, with the increase in the mass of the particle and the decrease in its energy, the LET increases. However, the energy dependence of the LET is non-monotonic and has a maximum at sufficiently small energies. Thus, the maximum value of LET for α -particles corresponds to $\sim 1\text{MeV}$ and is $\sim 355\text{ keV}/\mu\text{m}$. When passing through a semiconductor material, a charged particle creates non-equilibrium electron-hole pairs in concentrations corresponding to the energy release along its rectilinear path (track). At this time, the energy dose absorbed from one particle in silicon along the axis of the track can be 10^6 rad for protons, and for heavy charged particles, for example, $10^8\div 10^9$ rad for ${}^{56}\text{Fe}$. After the particle has passed, the electron-hole plasma is thermalized within a cylindrical region with a radius of 1000 \AA in picosecond time. The concentration of electron-hole pairs in the plasma is $10^{18}\div 10^{19}\text{ cm}^{-3}$ and higher, which is much larger than the concentration of the main charge carriers in the substrates and epitaxial layers used in the creation of IMS [100].

If the particle passes through the p-n junction, which is one of the main elements of the IMS structure, the charge carriers generated in the space charge region (SCR) of the junction are collected. If the size of any region (for example, the substrate) that meets the p-n junction is greater than the diffusion length of the charge carriers located in it, then a pulse current determined by the diffusion length will flow.

Only the case of equal generation of pairs throughout the entire volume of the integrated circuit during gamma radiation is an exception, in which case the entire surface of the p-n junction contributes to the radiation current, the collection of charge carriers during the influence of a single charged particle is not from the entire area of the p-n junction, but from the charged particle. occurs at the intersection with the track.

However, when using such a model in practice, the value of the currents is significantly higher than the observed values. The reason for such a difference between the calculation and theoretical data is the presence of a high concentration of electron-hole pairs in the track of the charged particle, which leads to the "hanging" of the equipotential surfaces on the substrate in the track region (this effect is shown schematically for a reverse-shifted $n^+ - p$ junction in fig. 9.29). This effect is usually called the effect of the formation of a load wedge [92].

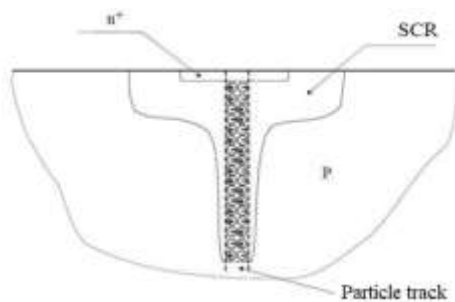


Figure 9.29. When a heavily charged particle passes $n^+ - p$ junction volume charge "hanging" effect

Initially, the electric field localized in the transition is transported to the substrate as a result of the high concentration of charge carriers located in the track when the charged particle passes. After thermalization, non-equilibrium charge carriers flow radially from the axis of the track due to ambipolar diffusion and axially due to drift in the electric field. Thus, the non-major charge carriers (in this case, electrons) drift towards the n^+ region, while the main charge carriers (in this case, holes) change their positions in the direction perpendicular to the axis of the track due to diffusion. At this time, in order to maintain electroneutrality in the track, the electrons must also change their places as they follow the holes towards the outer surface of

the cylinder. Otherwise, the spatial separation of electrons and holes leads to the creation of fields that prevent such separation. Separation from any part of the cylinder will be accompanied by separation of holes from that area. First, this phenomenon starts at the bottom of the cage, and the process shifts upwards, i.e., the space charge region of the junction is restored. Since the time of existence of the funnel is determined by the drift time of the non-core charge carriers, the collection of carriers from it gives a rather short-lived ($10^{-8} \div 10^{-10}$) current pulse, which is significantly larger than the generated current of charge carriers collected from the SCR junction [33].

It would be more convenient to evaluate the disturbances in the operation of the digital IMS under the influence of a single charged particle with the value of the collected charges. Thus, the false activation of the scheme during the energy release, which is smaller than the lifetime of the charge carriers, is characterized by the critical Q_{kr} value of the selected charge in the sensitive element of the IMS. This time:

$$Q_{kr} = \Delta V_{noise} \cdot C_{ef} ,$$

where, ΔV_{noise} – the noise continuity of the core, that is, the minimum value of the noise voltage – the ability to convert the circuit into another logical state; C_{ef} – is the effective value of the capacity of the IMS element.

Thus, by comparing the value of Q_{kr} with the value of the load Q_s collected by the element of the scheme, we come to a conclusion about the possibility of false operation of the scheme. When $Q_s \geq Q_{kr}$, the circuit stops once. Therefore, it is possible to determine the value of the accumulated charge caused by the passage of a charged particle through the IMS.

Let's look at another model of load collection. The total length of the track section where the charge is collected and directed perpendicular to the p–n junction of the charged particle is L_t . There is a linear density $N_0(z)$ of electron-hole pairs along

the track of the charged particle. The z coordinate coincides with the axis of the track. $N_0(z)$ is related to LET in the track:

$$N_0(z) = (1/E_C) \cdot (dE/dx)(z),$$

where E_C is the electron-hole pair formation energy. As a rule, the value of LET (dE/dx) increases with the increase of z , that is, with the penetration of the particle into the depth of the sample, so that the energy of the particle gradually weakens.

Q_s is defined as:

$$Q_s = q \int_0^{L_t} N_0(z) \cdot dz = q \cdot \overline{N_0} \cdot L_s,$$

where $\overline{N_0}$ is the average value of the linear density of electron-hole pairs equal to $\frac{1}{E_C} \left(\frac{dE}{dx} \right)$ in the interval L_s . The L_s quantity consists of two parts: SCR and qif, that is:

$$L_s = \overline{v_{n.m}} \cdot \tau + E_{SCR},$$

here, $v_{n.m}$ - the average drift speed of non-main charge carriers inside the mold; τ - drift period of non-main charge carriers along the axis of the sheath; E_{SCR} - p-n is the width of the space charge region of the junction.

In turn:

$$\overline{v_{n.m}} = \overline{\mu_{n.m}} \cdot \overline{E} = \overline{\mu_{n.m}} \cdot \frac{U + \varphi_k}{L_s} = \frac{U_0}{L_s} \overline{\mu_{n.m}},$$

where, $\overline{\mu_{n.m}}$ - the average value of the carriage of non-main cargo carriers; E - the average value of the intensity of the field inside the mold; The value of the reverse voltage applied to the U-p-n junction; φ_k - p-n is the contact potential difference in the junction.

From the last two equations, we get the following result:

$$L_s = 0,5 \cdot \left[E_{SCR} + (E_{SCR}^2 + 4 \cdot \overline{\mu_{n.m}} \cdot U_0 \tau)^{\frac{1}{2}} \right].$$

The last equation becomes somewhat simpler under the condition that $L_s \gg E_{SCR}$:

$$L_S = (\overline{\mu_{n.m}} \cdot U_0 \tau)^{\frac{1}{2}}.$$

Since the deviation of non-main and main charge carriers from the sleeve is determined by the same time period, let's determine the quantity τ – from the analysis of the process of movement of the main charge carriers from the sleeve in the direction perpendicular to the axis of the track, that is, along the radius of the cylinder, due to ambipolar diffusion. The change of the linear density N of the charge carriers due to diffusion along the radius inside the tube is related to the density $I_{m.c}$ of the stream of the main charge carriers. So, from the continuity equation, we know that the flow of the main charge carriers along the r – radius from the track axis causes their corresponding movement on the outer surface of the cylindrical part of the mold, where the concentration of the main charge carriers is equal to the concentration N_n of the additives in the base.

In such case:

$$\frac{dN}{dt} = -2\pi r(t) I_{m.c}.$$

In turn, the quantity $r(t)$ is determined by the distance from the axis of the cylinder, where the main charge carriers change their positions in the time period t due to ambipolar diffusion, i.e.:

$$r(t) = 2(D_a t)^{\frac{1}{2}}$$

where D_a is the ambipolar diffusion coefficient. The value of the density of the stream of main charge carriers is determined by the equilibrium concentration of the main charge carriers and their movement speed $v_{m.c}$ due to their ambipolar diffusion:

$$I_{m.c} = N_n \cdot v_{m.c}.$$

Considering the last three expressions, we get a differential equation with a separated variable:

$$\frac{dN}{dt} = -4\pi N_n v_{m.c} (D_a t)^{\frac{1}{2}}.$$

After solving the differential equation in the initial conditions $N = N_0$ and $t = 0$:

$$N(t) = N_0 - \frac{8}{3} \pi N_n v_{m.c} (D_a)^{\frac{1}{2}} t^{\frac{3}{2}}.$$

$N(t)=0$ when $t = \tau$. From here τ can be determined:

$$\tau = \left(\frac{3N_0}{8\pi N_c v_{m.c} D_a^{\frac{1}{2}}} \right)^{\frac{2}{3}}.$$

We can take the average speed of displacement of the main charge carriers due to ambipolar diffusion as $v_{m.c}$ - quantity:

$$v_{m.c} = \frac{r(t)}{\tau} = 2 \sqrt{\frac{D_a}{\tau}}.$$

Taking into account the last two expressions, the exact value of τ is determined:

$$\tau = \frac{3N_0}{16\pi N_c D_a}.$$

If we consider the value of τ from the last expression in the above equations, we can determine the last expression for L_s . Especially considering the last statement:

$$L_s = q \left(\frac{3N_0 \overline{\mu_{n.m}} v_0}{16\pi N_c D_a} \right)^{\frac{1}{2}}.$$

In general, the quantity N_0 varies along the axis of the track. Therefore, the quantity in the last equation is $\overline{N_0}$ the average price should be used. In this case, Q_s quantity will be determined by the following expression:

$$Q_s = q \left(\frac{3\overline{\mu_{n.m}} v_0}{16\pi N_c D_a} \right)^{\frac{1}{2}} \cdot (\overline{N_0})^{\frac{3}{2}}.$$

Thus, we can say that Q_s - quantity increases with the increase of the reverse voltage applied to the p-n junction and

the decrease of the concentration of additives in the base or epitaxial layer where the elements of integrated microcircuits are formed.

9.10. Energy diagram of the iridium silicide-silicium structure, problems of silicon nanoelectronics and their solutions

In this section, the electrical properties of the Schottky barrier were studied on the basis of IrSi-Si, and an energy diagram was constructed based on the obtained results. The IrSi-Si structure was obtained in a special device consisting of a gas main and a reaction chamber.

Solar cells are the main energy source of spaceships and satellites in long-term flights. Considering that the natural resources will be exhausted all over the world in about 60-70 years, interest in alternative energy sources, especially solar energy, is increasing day by day. For this purpose, research works related to the creation of cheap solar cells and solar lanterns based on them are intensively conducted [61, 82]. This is even more important for us if we take into account that there are about 300 sunny days a year in Azerbaijan.

There are currently a large number of options available for purchasing solar cells with higher FE. It is necessary to choose such a structure that the solar cells made on their basis are long-lasting, resistant to radiation, and resistant to temperature changes.

Solar cells operating on the basis of Schottky barriers sufficiently satisfy the conditions listed above. In the presented article, the electrophysical properties of the Schottky barrier based on the IrSi-Si contact were studied, and the energetic zone diagram of this structure was drawn up based on the experimental results.

The IrSi-Si structure was obtained with the help of a special device consisting of a gas main and a reaction chamber. The reaction chamber consists of tubes, a heater and a cassette for Si plates. Before heat treatment, the plates are subjected to chemical cleaning and 10^{-3} mm.c. the temperature in the pressurized chamber is maintained in the range of 200-700⁰ C with an accuracy of $\pm 2^0$.

The final current in the IrSi-Si Schottky junction is the same as in the p-n junction. Current caused by changes

$$J_D = q \cdot T(\lambda) \cdot F(\lambda) [1 - \exp(-\alpha \omega)]$$

is defined as Here, $T(\lambda)$ – is the emission coefficient, $F(\lambda)$ – is the photon flux density, and ω – is the width of the potential barrier. And the current created by electrons

$$J_n = qT(\lambda)F(\lambda) \left[\frac{aL_n}{aL_n + 1} \right] \exp(-a\omega)$$

happens. The full current is based on the last two relations:

$$J = qT(\lambda)F(\lambda) \left\{ 1 - \exp(-a\omega) + \left[\frac{aL_n}{aL_n + 1} \right] \exp(-a\omega) \right\}.$$

Voltammeter characteristics of solar cells based on Schottky barrier:

$$J = I_S \left[\exp\left(\frac{qV}{nkT}\right) - 1 \right] - I_L$$

$$I_S = AA^{**}T^2 \exp\left(-\frac{qU_B}{kT}\right)$$

will be.

Fermi – level

$$E_f = N_L \left[\exp\left(\frac{\xi}{kT}\right) \right]$$

is defined as The concentration of holes is $p = 1.5 \cdot 10^{15} \text{ cm}^{-3}$ and $N_0 = 1.04 \cdot 10^{19} \text{ cm}^{-3}$. Calculations show that $\xi = 0.04 \text{ eV}$, $\Delta\phi_B = 0.182 \text{ eV}$. By knowing the height of the potential barrier ($\Delta\phi_B$), the diffusion potential (u_d) and the width of the space charge region (ω) can be determined.

The energy distribution of the density of surface states (N_s) at the IrSi-Si boundary was found due to the dependence of the capacitance on the voltage $C = \rho(U)$. It was determined that N_s at the IrSi-Si boundary varies from $3.5 \cdot 10^{12} \text{ cm}^{-2} \cdot \text{eV}^{-1}$ to $1.4 \cdot 10^{10} \text{ cm}^{-2} \cdot \text{eV}^{-1}$. That is why, depending on the method of obtaining the IrSi-Si structure, the performance can vary, as with other metals and semimetals. On the other hand, in the absence of surface states:

$$\varphi_B = \varphi_m - \varphi_{n/n}.$$

If we consider that $\varphi_m = 4.8 \text{ eV}$ for silicon, $\varphi_{n/n} = 4.98 \text{ eV}$ for IrSi-Si, then $\varphi_B = 0.18 \text{ eV}$. Since the experimental error in determining the height of the potential barrier is 0.01 eV , the height of the real barrier is equal to 0.17 eV .

Figure 9.30 shows the energy band diagram of the IrSi-Si structure determined based on the experimental results. There are various values in the literature for the work done of the metal (Ir) incorporated into the structure you are looking at, and they differ dramatically from each other [32].

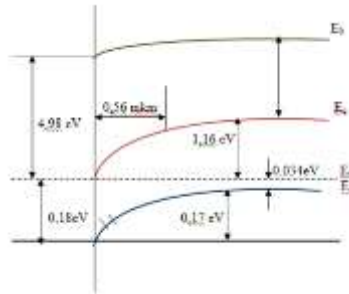


Figure 9.30. Energy band diagram of IrSi-Si structure

Naturally, the question arises that if we consider the height of the fence as a function of the output work, what value should be taken for the output work of the metal. For this reason, the value of output work previously found for IrSi - Si does not

coincide with experimental results. It should be noted that the output work can be determined according to the main parameters of the energy zone diagram, and the value of the output work determined by us is equal to 4.98 eV for IrSi.

Many problems arise as a result of shrinking the size of silicon field-effect transistors, mainly the current minimum channel length of 45 nm. A quantum-mechanical tunneling current is observed in a thin layer of silicon dioxide located under the control electrode. As a result, in order to obtain the necessary high values of the ratio of the currents in the closed and open states of the transistor, the working current flowing through the channel, the amount and distribution of additional atoms must be accurately controlled.

Controlling the displacement of an electron in an active nanodevice is of great interest from the point of view of ensuring ultra-low power consumption in nanoelectronic circuits. In a nanocapacitor, the transfer of even one electron from the external circuit to the small shirt of this capacitor leads to a redistribution of charges and an increase in the voltage ΔU in the shirts of the capacitor. In that case

$$\Delta U = e/C$$

where, e – is the charge of the electron; C – is the capacitance of the considered nanocapacitor.

Since the transition of the electron through the dielectric is realized by the tunneling method, the charged nanotube of the virtual nanocapacitor is called an "island" (fig. 9.31).

In order to obtain the effect, it is important to have large temperature fluctuations with a minimal change in energy [91,94]:

$$\Delta U_e \gg kT$$

where k – is Bolsman's constant and T – is ambient temperature.

Note that charge and voltage (islet potential) are quantized in the nanometric dimensions of the islet and the discrete nature of electric charges. It is clear that under certain

conditions it is possible to block the transition of the next electron to the islet - the electron prevents the transition of other electrons to the islet by means of the electrostatic repulsion field of its charge. This phenomenon is called coulomb blockade. Thus, the next electron can enter it only after the previous electron has left the island. Coulomb blockade can be determined by the lack of current due to coulomb repulsion when voltage is applied to the tunnel junction.

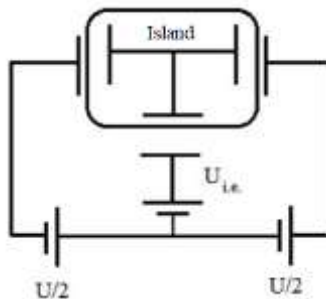


Figure 9.31. A one-electron field-effect transistor with two symmetrical tunnel junctions. Control electrode $U_{i.e.}$ voltage is given

Note that charge and voltage (islet potential) are quantized in the nanometric dimensions of the islet and the discrete nature of electric charges. It is clear that under certain conditions it is possible to block the transition of the next electron to the islet - the electron prevents the transition of other electrons to the islet by means of the electrostatic repulsion field of its charge. This phenomenon is called coulomb blockade. Thus, the next electron can enter it only after the previous electron has left the island. Coulomb blockade can be determined by the lack of current due to coulomb repulsion when voltage is applied to the tunnel junction. The voltage

applied to the switch to overcome Coulomb blocking is given by the following expression:

$$U_{C.b} = e/(2C)$$

The frequency of repeated f - transition of electrons to the island (quantum dot) is determined by the I - current passing through this one-electron system:

$$I = ef.$$

Such oscillation is called one-electron oscillation. The word "tunnel" is added in the case of a typical event such as tunneling of an electron to an island (transition through a quantum conductor is also possible). It can be seen from the last two statements that the following condition must be met for the effect to be observed [36]:

$$C \ll e^2/(2kT)$$

If we substitute the numerical values of the Boltzmann constant and the charge of the electron, it turns out that the required capacity at a temperature of 4.2 K will be $C \ll 2 \cdot 10^{-16}$ F, and at temperatures of 77 and 300 K it will be $C \ll 2 \cdot 10^{-16}$ F, respectively. Thus, the capacity needed to observe the one-electron effect should be in the order of attofarad (10^{-19} F).

It is concluded that there is a certain critical temperature above which the electron breaks the coulomb blockade and the structure does not work. This temperature is inversely proportional to the area of the junction. The resistance R of the transition is also considered its important characteristic. The opposite quantity – the conductance of the junction is significantly smaller than the quantum of conductance determined by Landauer's expression.

Finally, the operation of a single-electron device can be significantly affected by the parasitic capacitances of the contacts. Equivalent circuits of single-electron devices with one or two tunnel junctions are shown in figure 9.32a and b. A rectangle with a straight line in the center describes the tunnel passage.

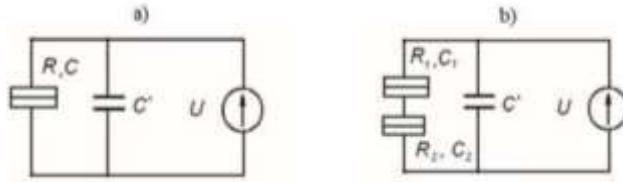


Figure 9.32. Equivalent circuit of a single-electron device with one (a) and two (b) tunnel junctions

C and R for a single-pass device, with two passes C_1, R_1, C_2, R_2 parameters are important for the device. Parasitic capacitance is denoted by C' . If C' parasitic capacitance than the capacitance of the switch is large, the system capacity of this shunt capacity will be determined by the price (figure 9.32a). In real devices, it is possible to get the shunt capacitance smaller than 10^{-15} F does not occur, which is a hundredth of the capacity required for single-electron tunneling even at helium temperature many times over. Two steps to solve this problem a device with (fig. 9.32b) is proposed. In that case parasitic capacitance does not shunt each tunnel link. In this case, the total electrostatic energy is calculated by the following expression [42]:

$$E = Q^2/2C_{\Sigma},$$

where Q is the load on the island; $C_{\Sigma} = C_1 + C_2$ – transitions is the sum of their capacities.

If the two junctions are symmetrical, their volt-ampere characteristic is smooth, as shown in figure 9.33 will have a description. It is possible to adjust the charge on the island by using the control electrode located near it. Tunneling electrons to the Heisenberg principle according to $\Delta E \Delta t \sim h$, capacitor energy $\Delta E = e^2/2C$ and capacitor charging time $\Delta t = R \cdot C$ is the resistance in the tunnel junction:

$$R \sim 2h/e^2 \text{ or } R > h/e^2$$

where h – is Planck's constant.

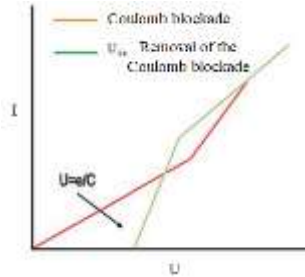


Figure 9.33. One-electron with two symmetric tunnel junctions field transistor volt-ampere characteristic

The rate of tunneling is different in different passages. The number of electrons entering and leaving the island is different. At each instant of time, the island will have a certain number of electrons depending on the value of the applied voltage. The more asymmetrical the transition, the sharper the steps in the volt-ampere characteristic will be. The amount of charge in expression is determined from the following equation:

$$Q = Q_0 - nq,$$

where, n is the integer number of electrons, Q_0 is the polarization charge of the island.

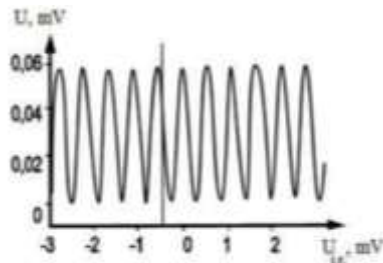


Figure 9.34. Dependence of the voltage at the quantum dot on the voltage at the control electrode at a constant current of $I = 300$ pA.

This load $U_{i.e.}$ changes continuously with the voltage change and the Coulomb blocking condition will be fulfilled periodically. Correspondingly, the current through the island or the stock and the stock, that is, the voltage drop between the contacts, will also change periodically (figure 9.34).

In systems with a large number of passages, more complex processes take place when there is an effect of external fields that change the height of the potential barrier, or when the shape and size of the island change.

Since single-electron transistors and circuits based on them are very small in size, as a rule, they use modern technologies, including - the purchase of thin layers, electronic lithography, etc. is used [55].

Another construction of a metal one-electron transistor is given in figure 5. The serial connection of several islands - to reduce the total capacity, that is, to increase the operating temperature of the device. The figure shows a structure with a size of 50 nm operating at liquid nitrogen temperature (77 K). For this purpose, a step was used in the dielectric (thermal silicon oxide with a thickness of 200 nm on the surface of a monocrystalline layer made of silicon). The metal strip (lighter in the picture) is made of titanium and applied to the top step of the staircase.

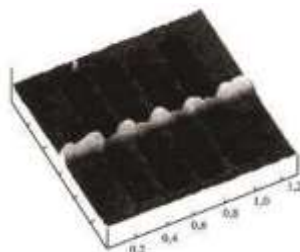


Figure 9.35. Atomic force microscope image of a metal single-electron transistor

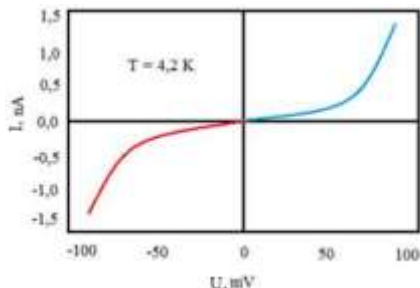


Figure 9.36. Volt-ampere characteristic of the one-electron transistor shown in figure 5

Before that, slits were opened on the surface of the layer (first by electron lithography, and later by ion implantation). Ion implantation is anisotropic up to a depth of 10 nm. The titanium scratch was obtained with the help of the second electron lithography method. After that, a titanium layer was formed and the 8-tunneled active part of the device was obtained by means of reverse lithography. Extraction of the electrical characteristics of the obtained one-electron transistor is carried out on a sample immersed in liquid nitrogen or helium. The volt-ampere characteristic of a transistor with a series of islands of 110 nm length at a temperature of 4.2 K is shown in figure 6. Coulomb blockade is observed at a voltage of ± 25 mV. Modulation is carried out by means of a control electrode located on the opposite side of the layer. The device generates Coulomb oscillation at a temperature of 77 K.

During the study of the active part composed of small chemical clusters, coulomb blockade was observed even at room temperature. Problems mainly arise on the opposite side of the layer, which requires a strict fixation of its potential.

As an example of the development of the idea of a single-electron transistor, a photomicrograph and a schematic of future quantum computers are shown in fig. 9.37 and fig. 9.38, respectively.



Figure 9.37. Photomicrograph of the structure for a quantum computer in a scanning electron microscope

These computers are better suited for systems with random events and ill-defined problems with probabilistic solutions, such as quantum mechanics. Quantum computers will find solutions to problems with a large number of mathematical calculations. For example, $5 \cdot 10^{24}$ operations should be performed to determine the prime factorization of a number with 300 signs. For this, a modern computer needs 150 thousand years. A quantum computer will do this process in just 1 second by performing $5 \cdot 10^{10}$ operations.

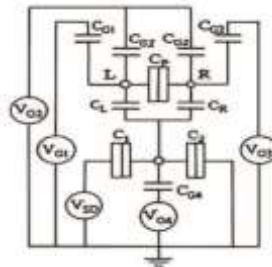


Figure 9.38. Equivalent circuit of the nanodevice shown in fig. 9.37

In figure 9.38, an isolated double quantum dot (IDQD) is connected to the control electrodes G_1 , G_2 , G_3 , SET and G_4 at

the capacitively coupled center. Transverse parasitic capacitances are ignored in the equivalent circuit for simplicity.

The idea of quantum computers is based on the achievements of quantum physics and quantum informatics. In computing, the quantum version of a bit corresponds to a qubit in quantum computers. However, it takes some time to build quantum computers. Many quantum systems strive to use such devices as element bases. This includes the state of the electron in the potential hole, the spin state of electrons and nuclei, individual atomic particles, multilevel states, etc. belongs to. The calculation process in a quantum computer is of an interference nature.

9.11. Effects of ionizing radiation on the parameters of semiconductors

Defects in the volume of semiconductors change the concentration of free charge carriers n , conductivity μ , lifetime τ and diffusion length L . The lifetime of non-major charge carriers in the volume of semiconductors is not determined by direct band-band recombination, but by energy levels of traps located in the bandgap. The formation of radiation defects leads to the formation of deep energy levels in the bandgap of the semiconductor, which increases the rate of volume recombination and, therefore, reduces the lifetime of charge-carrier pairs in a non-equilibrium state.

The nominal values of parameters of electronic devices can be realized only in their certain operating conditions. The operation of electronic devices must be carried out based on certain requirements and standards - instructions on the application of electronic devices and instructions for a specific class of devices.

The nature of defects in the crystal lattice of semiconductor materials caused by the effect of radiation does

not differ sharply from other defects. Despite the formation of a large number of levels in the band gap of a semiconductor, many of which are recombination levels, experiments show that the lifetime in an irradiated material is determined by one or two dominating recombination centers: if the concentration of recombination centers is sufficiently small compared to the concentration of charge carriers in equilibrium, the theoretical calculations show that the lifetime τ of charge carriers in the case of a dominating level is inversely proportional to the N_r concentration of recombination centers, which in turn is directly proportional to the integral flow of radiation [18,37]. So, the inverse value of the lifetime of charge carriers during irradiation

$$\Delta\left(\frac{1}{\tau}\right) = \frac{1}{\tau} - \frac{1}{\tau_0}$$

change is proportional to the concentration N_r of the recombination centers or the integral density of the stream of ionizing particles Φ (where τ_0 and τ are the lifetimes of non-major charge carriers before and after irradiation, respectively):

$$\Delta\left(\frac{1}{\tau}\right) = K_\tau \Phi,$$

where, K_τ is the radiative change coefficient of the lifetimes of non-main charge carriers, which depends on the concentration of the main charge carriers, the rate of formation of radiation centers and the degree of their filling with electrons.

Thus, with the increase of Φ , the life time decreases, the change of the inverse value of the life time $\Delta(1/\tau)$ increases, which is shown in fig. 9.39 for n-Si with specific resistance $\rho \sim 100 \text{ Ohm}\cdot\text{cm}$. Curve 1 - γ - with quanta; curve 2 - with electrons with energy $E_e = 2.5 \text{ MeV}$; curve 3 - with electrons with $E_e = 30 \text{ MeV}$; curve 4 determines the effect of irradiation with fast neutrons on the life span.

The analysis of the experimental results of the study of the influence of radiation on the mobility of charge carriers shows that the observed change in mobility is caused not only

by ionized atoms caused by radiation (decreasing right branches of curves 4, 5, 6 in fig. 9.40) but also by scattering from phonons caused by the drift effect of atoms (increasing left branches of curves 4, 5, 6 and curves 2, 3 in picture 9.40) [45].

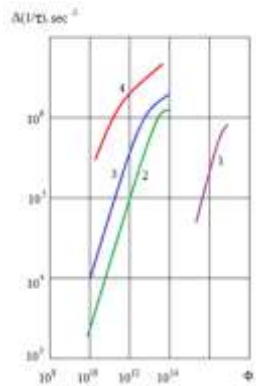


Figure 9.39. Dependence of the integral density Φ of the stream of ionizing particles on the change in the inverse value of the lifetime

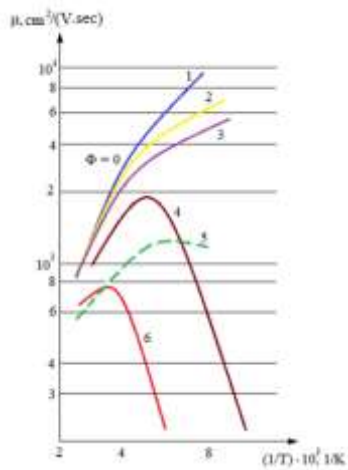


Figure 9.40. The effect of radiation on the mobility of cargo carriers

Curves 2 and 4 show neutrons with intensity $\Phi_N = 1.6 \cdot 10^{14} \text{ cm}^{-2}$ and $\Phi_N = 3.3 \cdot 10^{15} \text{ cm}^{-2}$, curve 3 shows intensity $\Phi_e = 10^{15} \text{ cm}^{-2}$, curves 5 and 6 show $\Phi_{pr} = 10^{14}$, respectively. cm^{-2} , $\Phi_{pr} = 6 \cdot 10^{14} \text{ cm}^{-2}$ intensity and energy $E_{pr} = 660 \text{ MeV}$ was obtained when irradiated with a flood of protons. At low temperatures, a noticeable decrease in conductivity during irradiation (a large value of $1/T$) is due to the appearance of ionized atoms and atomic complexes compared to the initial state. Radiation increases the number of immobile charged particles, which leads to an increase in the probability of coulomb collisions of free charge carriers with ions and a corresponding decrease in drag. Since the physical mechanisms of the interaction of the radiation stream with the substance of the semiconductor are of a different nature, they can be quite different in terms of quantity and quality (see the table) [52].

Cədvəl

Maddənin 1 sm^3 -da sürüşmüş atomların sayının
şüalanmanın növü və enerjisindən asılılığı

Material	Neytronlar $E_n = 2$ MeV	Protonlar		Elektronlar $E_e = 2$ MeV
		$E_p = 2$ MeV	$E_p = 5$ MeV	
Silisium $E = 12,9 \text{ eV}$	42	341	148	2,8
Germanium $E = 14,5 \text{ eV}$	62	482	213	1,2

For each type of radiation flood, the change in conductivity in silicon will be different. This is clearly shown in figure 9.41 (1 curve γ – quanta, 2 curve electrons with energy of 10 MeV , 3 curve fast neutrons). The change in the concentration of free charge carriers in silicon occurs at a small level of doping and more strongly when $\Phi_N > 10^{14} \text{ neutrons/cm}^2$ are irradiated with a stream of neutrons.

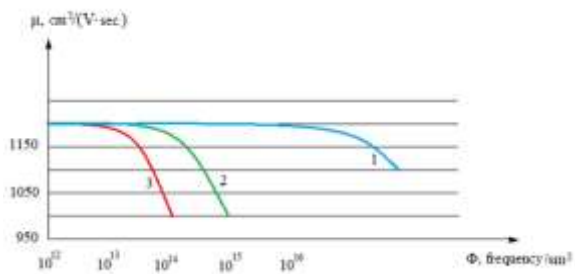


Figure 9.41. Variation of mobility of charge carriers in silicon

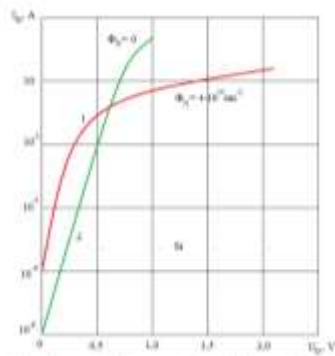


Figure 9.42. VAC in a wide range of values of direct currents when irradiated with neutrons

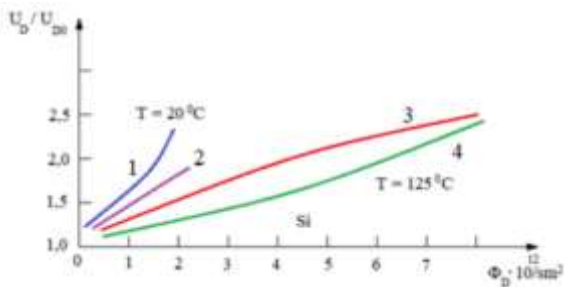


Figure 9.43. The variation of the flat voltage

At present, radiation effects in rectifier diodes have been studied in more detail. In silicon diodes, under the influence of any type of ionizing radiation with a sufficiently large energy, its valve properties due to the increase in reverse conductivity and decrease in forward conductivity are degraded. The rate of degradation is mainly determined by the width W of the base, its specific resistance ρ_B and the value of the direct current I_d . In addition, radiation energy, concentration of dopants in the emitter region, concentration gradient and lifetime τ_p of holes in the base (for a base with electronic conductivity) have a significant effect. In many cases, the straight branch of VAC undergoes the largest change during irradiation in silicon diodes. Therefore, the radiation resistance of diodes is evaluated by doubling the direct voltage U_d at a given value of direct current I_d .

The main electrophysical parameters of semiconductors that determine the change of VAC during irradiation are τ_p , N , ρ_B and W . The variation of the life time τ_p , which is a function of the parameters N , ρ_B and W of the holes in the base of the diode in a wide range of values of I_d during different types of radiation, can be estimated by the above formula [66].

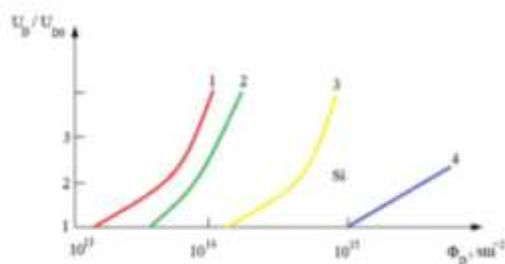


Figure 9.44. Effect of radiation on different types of diodes

Variations of the direct voltage VAC and U_d in a wide range of values of direct currents of silicon diodes during

neutron irradiation are given in figures 9.42 and 9.43, respectively.

In figure 9.43, curve 1 was obtained when $\Phi_N = 0$, that is, when there was no radiation, and curve 2 when $\Phi_N = 4 \cdot 10^{14}$ neutrons/cm². In figure 9.44, when $\Phi_N = 0$, U_{d0} is the flat stress, while the remaining regions between curves 1 and 2, 3 and 4 show deviations from the U_d/U_{d0} value for different additives (eg, B, Al). Boron-doped diodes have greater radiation resistance than aluminum diodes.

Irradiation of diodes at high temperatures causes a rather small change in their properties as a result of partial thermal processing of radiation defects. The effect of radiation on different types of diodes is given in figure 9.45.

Here, curves 1 and 2 were obtained by different brands of rectifiers, and curves 3 and 4 were obtained during the irradiation of pulse diodes. When $\Phi_N = 0$ across the diode, U_{d0} is the forward voltage.

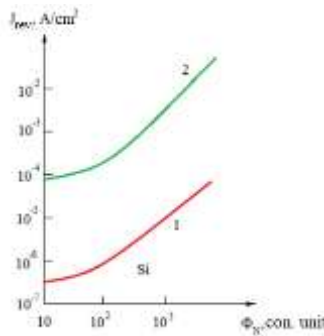


Figure 9.45. Dependence of countercurrent density j_{dep} on neutron flux

The effect of radiation on the opposite branches of the VAC of silicon diodes is mainly determined by the processes occurring in the p-n junction. Irradiation changes the effective

distribution of uncompensated dopants near the p–n junction, i.e. affects the junction thickness. This is due to the fact that the effective concentration of charge carriers in the base region changes during irradiation. The change in the concentration of the main charge carriers in the emitter can be ignored. So, since $N_a \gg N_D$ for the $p^+ - n$ transition, the increase in the thickness of the transition occurs mainly on the base side during irradiation. In addition, the presence of sufficiently large concentration gradients of additives in the junction leads to the fact that during irradiation, a significant change of the concentration gradients of free charge carriers and, therefore, the currents flowing through the junction can be observed.

For silicon diodes with a specific resistance of $\rho_B = 2.5$ Ohm·cm, when $U_{dep} = 300$ V, the dependence of the reverse current density on the neutron flux is given in figure 9.45. 1 curve $t = 18$ °C; curve 2 was obtained at temperatures $t = 100$ °C. It is clear that the change in the width of the passage during irradiation will also change the capacitance of the barrier.

Conclusion

Taking into account the above, we can classify the processes occurring on the surface of semiconductors during irradiation as follows: - creation of new fast surface states that increase the speed of surface recombination; - capture of charge carriers generated as a result of radiation by traps or excitation of surface states, which change the charge of surface states and the value of surface potential; - ionization of the gas in the body of the semiconductor-based device and deposition of charged ions on the surface of the crystal, which causes a change in the surface potential.

REFERENCES

1. Ковалев А.В., Федчишин В.Г., Щербаков М.И. Тепловидение сегодня. Специальная техника, 1999, №3, с.13-18.
2. Алфёров Ж.И. Перспективы электроники в России. Гетероструктурная электроника и акустоэлектроника. // Электроника: наука, технология, бизнес. 2004, № 6, с. 90-93.
3. Алфёров Ж.И. Двойные гетероструктуры: концепция применения в физике, электронике и технологии. Нобелевская лекция по физике // УФН. 2002, т. 172, № 9, с.1068-1086.
4. Алфёров Ж.И. и др. Наноматериалы и нанотехнологии // Микросистемная техника. 2003, № 8, с. 3-13.
5. Ангина Н.Р. и др. Многоэлементные фотоприемники ИК-излучения на диодах с барьером Шоттки // Зарубежная электронная техника. 1986, №5, с. 3-37.
6. Андреев Д.А., Грушко Н.С. // Микроэлектроника. 2002, т. 31, №2, с. 142-146.
7. Андреевский Р.А., Рагуля А.В. Наноструктурные материалы. М.: Академия. 2005, 192 с.
8. Антоненко С.В., Малиновская О.С., Мальцев С.Н. «ЖЭТФ», 2007, т. 132, №1, с. 230-232.
9. Бабаев Н.А., Багиров М.А., Имангулиев Г.А. и др. / Всесоюзная научно – техническая конференция “Приборы с отрицательным сопротивлением и интегральные преобразователи на их основе”. Баку, 1991, с. 71.
10. Бабаев Н.А., Имангулиев Г.А., Казымов Н.Ф. К технологии изготовления водородочувствительных кремниевых барьерных структур. Сообщения НПО Космических исследований. Баку: «Элм», 1990, с. 222.
11. Бабаев Н.А., Имангулиев Г.А., Казымов Н.Ф. и др. Водородочувствительный элемент в интегральном исполнении. Всесоюзная научно – техническая

конференция” Приборы с отрицательным сопротивлением и интегральные преобразователи на их основе”. Баку, 1991, с. 72.

12. Баранов В.В., Ануфриев Л.П., Глухманчук В.В. и др. / Тр. VIII Междунар. научн.-техн. конф. "Актуальные проблемы твердотельной электроники и микроэлектроники". Таганрог. 2002, ч.1, с. 157-159.

13. Баранов В.В., Соловьев Я.А., Тарасиков М.В. и др. Диоды Шоттки на основе силицида платины // Изв. Белорус. инж. акад. 2003, №1, (15)/4, с. 89-91.

14. Барыбин А.А., Сидоров В.Г. Физико-технологические основы электроники. СПб. Изд-во „Лань“, 2001, 272 с.

15. Беляев А.Е., Болтовец Н.С., Капитанчук Л.М. и др. // Материалы и технология изготовления приборов СВЧ. 2009, № 2, с. 31.

16. Бессонов Л.А. Теоретические основы электротехники. Электрические цепи. Гардарики, М.: 2002, с. 638.

17. Бобровский Ю.Л., Корнилов С.А., Кратиров И.А. и др. Электронные, квантовые приборы и микроэлектроника.: Под ред. проф. Н.Д. Федорова М.: Радио и связь, 1998.

18. Бойцов С.К., Иванов В.Г., Моисеев Ю.И. и др. Матричный ФППЗ на основе фотодиодов с барьерами Шоттки из PtSi/Si с числом элементов 256x256 / Тез. докл. IV конф. "Приборы с зарядовой связью и системы на их основе" ПЗС-92. М.: 1992, с. 45.

19. Бушуев В.А. Исследование влияния лазерного отжига на структуру приповерхностных слоев ионно-имплантированного кремния методом рентгеновской дифрактометрии // Физика твердого тела. 1993, т. 35, № 2, с. 355-364.

20. Быкина Н.К. и др. Влияние технологии формирования омического контакта на параметры ПТШ на арсениде галлия. “Электронная техника”, сер. 1. Электроника СВЧ. Вып 9/433, 1990, с. 57.

21. Быков В.А. Приборы и методы сканирующей зондовой микроскопии для исследования и модификации поверхностей. Диссертация на соискания ученой степени доктора технических наук. Москва. 2000, с. 376-393.
22. Валенко В.С. Полупроводниковые приборы и основы схмотехники электронных устройств: под. ред. Ровдо А.А. М.: Издательский дом «Додэка XXI», 2001, с. 368-372.
23. Васильев В.А., Голенков А.Г., Дворецкий С.А., и др. Фотоприемники на основе гетерозепитаксиальных слоев CdHgTe, для среднего и дальнего ИК-диапазонов// Микроэлектроника. 2002, т. № 6, с. 31-35.
24. Вейко В.П., Петров А.А. Введение в лазерные технологии. Издание СПбГУ ИТМО, 2009.
25. Внукова Н.Г., Бондаренко Г.В., Чурилов Г.Н. Методы и средства контроля. Определение элементного состава вещества: Метод указания Красноярск: ИПЦ КГТУ. 2005, с. 23-35.
26. Войцеховский А.В., Несмелов С.Н., Кульдичкий Н.А. Материалы 16 Междунар. симп. «Тонкие пленки в электронике». М.: Техномаш, 2004, с. 141-147.
27. Горбунов Г.Г., Егорова Л.В., Еськов Д.Н. и др. Новые применения Фурье-спектрометров, Оптический журнал, 2001, т. 68, №8, с. 87.
28. Громов Д.Г., Климовицкий А.Г., Мочалов А.И. и др. Материалы для металлизации кремниевых СБИС // Электронная промышленность. 2002, № 1, 60-66 с.
29. Громов Д.Г., Мочалов А.И. Материалы и процессы формирования систем металлизации кремниевых интегральных схем. Учебное пособие. М.: МИЭТ 2006, с. 180.
30. Громов Д.Г., Мочалов А.И., Сулимин А.Д. и др. Металлизация ультрабольших интегральных схем // Учебное пособие, под ред. Чаплыгина Ю.А. /М.: Бином, 2009, с. 253-277.

31. Гуртов В.А. Твердотельная электроника. Учебное пособие (Петрозаводск, ПетрГУ, 2004), гл 3, с. 108 (175) 52.
32. Гуртов В.А. Твердотельная электроника: учебное пособие. 2-е изд., доп. М.: Техносфера, 2005, с. 408-412.
33. Гусаров А.В. Перенос излучения в слоях металлических порошков при лазерном формировании // Квантовая электроника. 2010, т. 40, №5, с. 451-459.
34. Данилов А.А. Специализированные аналоговые микросхемы: Операционные усилители с уникальными функциями и параметрами // Электронные компоненты. 2007, №12, с. 85-89.
35. Денисов В.М., Истомин С.А., Подкопаев О.И. и др. Кремний и его сплавы. Екатеринбург: УрО РАН, с. 2005, 467.
36. Джафарова Р.Г., Казымов Н.Ф. Электрофизические свойства контакта, полученные методом ионно-плазменного распыления / Материалы VII научно – технической конференции молодых ученых и специалистов. Баку, 1990, с. 48.
37. Джеффри Тревис LabVIEW для всех. Перс. англ. Клушин Н. А. М.: ДМК Пресс, 2005, с. 544.
38. Домашевская Э.П., Юраков Ю.А., Кашкаров В.М. Твердофазно взаимодействие в тонкоплёночной структуре Pt-Si (111) по данным ультрамягкой рентгеновской эмиссионной спектроскопии и рентгеновской дифракции // Перспективные материалы. 1997, № 3, с. 35-40.
39. Дьячков П.Н. Углеродные нанотрубки. Строение, свойства, применение. М.: Бином. Лаборатория знаний, 2006, с. 293.
40. Екимов А.И., Онущенко А.А. Размерное квантование энергетического спектра электронов в микроскопическом полупроводниковом кристалле // Письма в ЖЭТФ, 1984, т. 40, с. 337.

40. Екимов А.И., Онущенко А.А. Размерное квантование энергетического спектра электронов в микроскопическом полупроводниковом кристалле // Письма в ЖЭТФ, 1984, т. 40, с. 356.
41. Ельяшевич М.А. Атомная и молекулярная спектроскопия, Изд. Эдиторал УРСС, 2001, с. 896
42. Жукова С.А., Обижаев Д.Ю., Демичева О.В. и др. Нано- и микросистемная техника, 2007, № 4, с. 60-64.
43. Закамов В.Р., Чеченин Ю.И. // Прикладная физика. 2012, № 3, с. 101 (247) 69.
44. Зи С. Физика полупроводниковых приборов: В 2-х кн. Кн. 1. Пер. с англ. М.: 1984.
45. Ибрагимов Г.Б. Керимов Э.А. Фотоэлектрические свойства фотодиодов // Вестник Московского Городского Педагогического Университета Серия «Естественные науки» № 2 (14) Москва 2014 с. 6-15.
46. Ибрагимов Г.Б., Керимов Э.А. Фотоэлектрические свойства фотодиодов на основе силицида металла-кремний // Известия. АНАКА, 2014, т. 17, № 1, с. 42-47.
47. Ибрагимов Г.Б., Керимов Э.А. Фотоэлектрические свойства фотодиодов // Вестник Московского Городского Педагогического Университета, Москва, 2014, №2(14), с. 15.
48. Иванов В. Г., Иванов Г. В., Каменев А. А. Многоэлементные ИК-приемники на основе барьеров Шоттки, чувствительные к излучению с энергией квантов меньше высоты потенциального барьера // Оптический журнал. 2008, № 8, с. 53-59.
49. Иванов В.Г., Иванов Г.В. Фотоприемная матрица детекторов на основе барьеров Шоттки с чувствительностью в субмиллиметровом диапазоне длин волн: Пат. 2304826 Российской Федерации от 20.03.2006.
49. Иванов В.Г., Иванов Г.В., Каменев А.А. Многоэлементные ИК приемники на основе барьеров

Шоттки, чувствительные к излучению с энергией квантов меньше высоты потенциального барьера // «Оптический журнал», т.75, №8, 2008, с. 53-56.

50. Иванов В.Г., Иванов Г.В., Каменев А.А. Способ увеличения граничной длины волны ИК-детектора с барьером Шоттки, ИК-детектор и фотоприемная матрица, чувствительная к ИК-излучению: Пат. 2335823 Российской Федерации от 23.10.2006.

51. Иванов В.Г., Панасенков В.И., Иванов Г.В. Квантовая эффективность фотодиодов с барьером Шоттки вблизи длинноволновой границы // ФТП, 1997, том 31, выпуск 6, с. 735.

52. Ивановский А.Л. Квантовая химия материаловедения. Нанотубулярные формы вещества. Екатеринбург: УрО РАН, 1999, с. 132-140.

53. Иевлев В.М., Куцев С.Б., Руднева И.Г. и др. Фазовый состав, ориентация и субструктура пленок силицидов Ir, синтезированных в процессе вакуумной конденсации металла на Si. "Неорганические материалы" М.: 2003, v. 39, № 5, с. 1-5.

54. Каламейцев А.В, Романов Д.А., Ковчавцев А.П. и др. Природа отрицательного дифференциального сопротивления неидеального барьера Шоттки на основе арсенида индия // ФТП, 1997, т. 31, № 3, с. 370.

55. Канагеева Ю.М., Мошников В.А., Arnold M. и др. Электрофизические свойства фотодиодов на основе эпитаксиальных слоев для среднего ИК-диапазона // Вакуумная техника и технология. 2008, т. 18, № 1, с. 3-8.

56. Керимов Э.А. Электрофизические свойства контактов с барьером Шоттки на основе IrSi – Si // Bulletin of Kemerovo State University, Journal of theoretical and applied research. Founded in 1999, 2013, №3 (55), v. 1, p. 165-169.

57. Керимов Э.А. Разработка тестового кристалла и исследование проводимости углеродных нанотрубок /

Наука и образование в современном мире, Сборник научных трудов по материалам Международной научно – практической конференции, часть I, Москва 31 мая 2013, с. 17-23.

58. Керимов Э.А. Технология получения мощных диодов Шоттки на основе силицида Pt/Ni // Известия НАНА т. XXXI, №2, 2011, с. 166-168.

59. Керимов Э.А. Фоточувствительные структуры с барьером Шоттки на основе контакта силицид никеля – кремний. Тенденции и перспективы развития современного научного знания / Материалы VII международной научно – практической конференции, 29 июня 2013, Москва 2013, с. 7-15.

60. Керимов Э.А. Фоточувствительные структуры с барьером Шоттки на основе контакта силицид платины – кремний / The materials of IV international distance research and training conference, Scholarly discussion: problems of mathematics physics, chemistry, biology, Moscow, 2013, p. 53-60.

61. Керимов Э.А. Фоточувствительный элемент на основе контакта IrSi –Si // Известия НАНА т. XXXI, №5, 2011, с. 158-161.

62. Керимов Э.А. Шумы фотоприемных устройства на основе диодов Шоттки // Электронный научный журнал «ФИЗ-МАТ», Выпуск 1(15)/ Январь – март 2014, стр. 3-8.

63. Керимов Э.А., Асадуллаева М.М., Байрамова Ш.А. и др. Механизм токопереноса в контактах силицид палладия – кремний // Научные сочинение НАА, 2010, № 2, с. 108-114.

64. Керимов Э.А., Байрамова Ш.А., Мехтиев Э.В. Вольт - фарадные характеристики контакта PdSi – Si. Известия АНАКА, 2010, т. 13, №1, с. 56-58.

65. Керимов Э.А. // Приемники изображения с барьерами Шоттки на основе контакта IrSi –Si // Intellectual Archive, 2013 september, №5, v.2, p. 7-13.

66. Керимов Э.А. Физические основы повышения квантовой эффективности фото – диодов на основе IrSi - Si // European Applied Sciences . #8 - 2013, с. 112-117.
67. Керимов Э.А. Шумы фотоприемных устройств на основе диодов Шоттки // Электронный научный журнал «ФИЗ-МАТ» Выпуск 1. (15), Январь-март 2014, с. 3-8.
68. Керимов Э.А. Investigation of change of the height of potential barrier of the contact IrSi – Si // The Recent Trends in Science and Technology Management, 09-10 May 2013, London, p. 341-345.
69. Керимов Э.А. Методика получения тонких контактов IrSi – Si и формирование наносистем // Science and world № 1(1), с. 18-21.
70. Керимов Э.А. Физические свойства контактов с барьером Шоттки на основе силицид иридия - кремний // Микроэлектроника. Москва, 2015, т.44, №3, с. 1-4.
71. Керимов Э.А. Физические основы работы фотодиодов с барьером Шоттки // Вестник МГПУ, серия «Естественные науки», №1 (17), Москва 2015, с. 35-39.
72. Керимов Э.А. Фотоэлектрические и оптические свойства фотодиодов с барьером Шоттки на основе IrSi – Si // Микроэлектроника. Москва, 2016, т.45, №2, с. 1-7.
73. Кобаяси Н. Введение в нанотехнологию. Москва, 2008, с. 30-42.
74. Кулев М.О., Барышникова Е.В., Павлов А.Н. и др. Оценка влияния неоднородной чувствительности ячеек ПЗС на погрешность датчика координат очага возгорания // Ползуновский Вестник 2007, №3, с. 56-58
75. Курбанов М.А., Султанрахмедова И.С., Керимов Э.А. и др. Плазменная кристаллизация композитов полимер – сегнетопьезоэлектрическая керамика и их пьезоэлектрические свойства. Физика Твердого Тело, 2009, т. 51, вып. 6, с. 1154-1160.

76. Кущев С.Б., Руднева И.Г. Фазовый состав, структура и ориентация пленок силицидов иридия, полученных при вакуумной конденсации металла на подогретые подложки кремния / 3-й Всерос. Семинар "Нелинейные процессы и проблемы самоорганизации в современном материаловедении". Воронеж. 2000, с. 26.
77. Ландау Л.Д. Теоретический физика. М.: наука, 1989, т. 3, 768 с.
78. Латышев А.В., Асеев А.Л. Моноатомные ступени на поверхности кремния. Новосибирск: Изд. СО РАН, 2006, 242 с.
79. Левин М.Н., Бормонтов Е.Н., Волков О.В. и др. Анализ распределения заряда в диэлектрике МДП-структуры по спектральным зависимостям фотоэмиссионного тока // ЖТФ. 2001, т. 71, вып. 3, с. 44-52.
80. Литвинов В.Г., Гудзов В.В., Зубков М.В. и др. Автоматизированный измерительно-аналитический комплекс токовой релаксационной спектроскопии глубоких уровней. Рязань: Рязанский ЦНТИ, информационный листок о НТР №, 61-081-02, 2002, с. 4.
81. Магарилл Л.И., Энтин М.В. Письма в ЖЭТФ 80, 6, 477, 2004.
82. Макунин А.В., Бачурин К.Е., Воробьева Е.А. и др. Морфологические различия строения углеродных наноструктур, синтезированных различными методами. НИИ ядерной физики им. Скобелева Д.В. МГУ, Москва. Физика и химия обработки материалов 2011, №4, с. 66-70.
83. Макунин А.В., Чеченин Н.Г., Сердюков А.А. и др. Технологические аспекты синтеза наноструктур электродуговым и газопиролитическим методами. Физика и химия обработки материалов, 2010, № 6, 38-41 с.
84. Макунин А.В., Бачурин К.Е., Воробьева Е.А. и др. Лаборатория нанотехнологий и наноматериалов НИИЯФ МГУ: цели и перспективы. Доклад на 18-ой

Международной конференции по электростатическим ускорителям и пучковым технологиям. Обнинск 19-22 октября 2010 г.

85. Немудров В.Г., Мартин Г. Системы на кристалле. Проблемы проектирования и развития. М.: Техносфера, 2004, с. 203-216.

86. Овсяк В.Н., Курышев Г.Л., Сидоров Ю.Г. и др. Матричные фотоприемники инфракрасного диапазона. Новосибирск: Наука, 2001, с. 376.

87. Овсяк В.Н., Курышев Г.Л., Сидоров Ю.Г. Матричные фотоприемные устройства инфракрасного диапазона. Новосибирск: Наука, 2001, с. 252.

88. Орешкин П.Т., Дорджин Г.С., Лактюшкин О.Н. и др. Резонансный релаксационный спектрометр глубоких уровней / Материалы VII Международной конференции по микроэлектронике. 1990, т. 1, Минск, с. 287.

89. Питанов В.С., Якименко А.В. Природа «мягкого» поведения обратного тока в Шоттки – структурах Mo/n-Si // Вестник ВГУ. Серия физика, математика, 2001, №2, с. 33-41.

90. Родерик Э.Х. Контакты металл-полупроводник. М.: Радио и связь, 1982, 208 с.

91. Родерик Э.Х. Контакты металл-полупроводник: Пер. с англ. // Под ред. Степанова Г.В. М.: 1982, 89-95 с.

92. Рыков С.А. Сканирующая зондовая микроскопия полупроводниковых материалов и наноструктур / Под ред. Шика. А.Я – СПб. «Наука», 2001, 52 с.

93. Рюхтин В.В., Добровольский Ю.Г., Шимановский А.Б. «Кремниевые р-п фотодиоды для ультрафиолетовой области спектра» // Proc. SRRE, 2011, v. 782, с. 93-98.

94. Самсонов В.М., Харечкин С.С., Гафнер С.Л. и др. // Кристаллография. 2009, т. 54, с. 530.

95. Alemany L., Zhang L., Zeng L. et al. SolidState NMR Analysis of Fluorinated Single-Walled Carbon Nanotubes:

Assessing the Extent of Fluorination // Chemistry of Materials. 2007, v. 19, No 4, p. 735-744.

96. Ando T. Theory of electronic states and transport in carbon nanotubes // Phys J. Sok. Japan. 2005, v. 74, p. 777.

97. Baca A. Fabrication of GaAs devices. London, United Kingdom: The Institution of Electrical Engineers, 2005, p. 350.

98. Balan N., Gruzdev A., Nevsky A. / Books of abstracts, International conference "Micro- and nanoelectronics 2005", October 3rd –7th, 2005, Moscow, Zvenigorod, Russia. p. 1–11.

99. Barrow J. Reducing Ground Bounce in DC-to-DC Converters—Some Grounding Essentials, Analog Dialogue. 2007, v. 41–2, p. 2–7.

100. Belin T., Epron F. Characterization methods of carbon nanotubes: a review // Materials Science and Engineering B. 2005, v. 119, No 2, p. 105-118.

101. Benton J., Kimerling L. Capacitance transient spectroscopy of trace contamination in silicon // J. Electrochem. Soc. 1982, v.129, No 9, p. 2098-2102.

102. Bhattacharya P., Properties of III-V quantum wells and superlattices, U.S.A., 1996.

103. Brintlinger T., Chen Y., Durkop T., et al, Melingailis J. RaRRd imaging of nanotubes on insulating substrates // Appl. Phys. Lett. 2002, v. 81, p. 2454-2456.

104. Bulusheva L., Okotrub A., Guesel A. et al. Molecular Nanostructures. XVII Int. Winterschool / Euroconf. on Electronic Properties of Novel Materials / Eds Kuzmany H., Fink J., Mehring M., Roth S.. AIP Conf. Proc. 685, 2003, p. 108.

105. Chang C., Segmüller A. Huang H., et al. // Electrochem J. Soc. 1986, v. 133, № 6, p. 1256–1260.

106. Chen Y., Fitzgerald J., Chadderton L., Of Metastable and Nanocrystalline Materials. 1999, v. 2, No 6, p. 375-380.

107. Choi H., Ihm J., Louie S., et al, Phys. Rev. Lett. 84, 2000, p. 17-29.

108. Davies A. and Graighean H. Ballistic-Electron-Emission Microscopy Characteristics of Reverse-Biassed Schottky Diodes. Appl. Phys. Lett., 1994, 64 (21), p. 2833 – 2835.
109. Derrien J. Properties of Metal Silicides, edited by Maex K. and Van Rossum M. (IEE INSPEC, 1995), p. 164.
110. Derycke V., Martel R. Controlling doRRng and carrier injection in carbon nanotube transistors // Appl. Phys. Lett. 2002, v. 80, No 15, p. 2773-2775.
111. İbrahimov H.B., Kerimov E.A. // European Science Review, № 1 2014, January-Februrar p. 163-167.
112. Ivanenko L., Shaposhnikov V., Filonov A. et al // Thin Solid Films. 2004, v. 461, p. 141-147.